Stony Brook University

Understanding Direct Metal-Metal Bonding in Rare Earth Molybdates

A Dissertation Presented

by

Diane Marie Colabello

to

The Graduate School

in Partial Fulfillment of the

Requirements

for the Degree of

Doctor of Philosophy

in

Chemistry

Stony Brook University

August 2015

Stony Brook University

The Graduate School

Diane Marie Colabello

We, the dissertation committee for the above candidate for the

Doctor of Philosophy degree, hereby recommend

acceptance of this dissertation.

Peter G. Khalifah – Dissertation Advisor
Associate Professor, Department of Chemistry, Stony Brook University

John B. Parise - Chairperson of Defense
Distinguished Professor, Department of Chemistry and Geosciences, Stony Brook University

Robert B. Grubbs – Third Member of Defense
Associate Professor, Department of Chemistry, Stony Brook University

Tyrel McQueen – Outside Member of Defense
Associate Professor, Department of Chemistry, Johns Hopkins University

This dissertation is accepted by the Graduate School

Charles Taber
Dean of the Graduate School

Abstract of the Dissertation

Understanding Direct Metal-Metal Bonding in Rare Earth Molybdates

by

Diane Marie Colabello

Doctor of Philosophy

in

Chemistry

Stony Brook University

2015

Transition metal oxides possess a number of useful physical properties that have allowed compounds belonging to this class to serve as functional oxides in a variety of high-tech applications. The range of physical properties among this family is strongly related to the transition metal *d* orbital splitting, predicted by ligand field theory, and the nature of the transition metal *d* electrons. This dissertation is focused on the specific subset of transition metal oxides that contain direct metal-metal (*M*-*M*) bonds. To date, transition metal oxides with *M*-*M* bonds have been largely explored in terms of crystal structure characterization, with little work done to characterize the effects of *M*-*M* bond formation on the electronic structure and resultant physical properties of these compounds. *M*-*M* bonding will lead to *d* orbital splitting that deviates from the orbital splitting predicted by ligand field theory, and result in electronic structure configurations that more closely resemble narrow *f* electron states. In turn, this means compounds with *M*-*M* bonds should have physical properties that differ from the same

compounds without *M-M* bonds. *M-M* bonding is characterized by a *M-M* distance shorter than the distance between atoms in the pure metal, with Mo known to form the largest number of clusters and nuclearities. Due to the large number of known lanthanum molybdenum oxides with Mo-Mo bonds that could be explored further, study began with attempts to synthesize and investigate known lanthanum molybdates. Work extended to include other known and novel rare earth molybdenum oxides with Mo-Mo bonds using a comprehensive approach that incorporated the study of relationships between crystal structures, electronic structures, and physical properties in these systems.

The tetragonal compound $La_4Mo_2O_{11}$ is a rare example of a solid state oxide with direct metal-metal bonding, as reflected in the short Mo-Mo bond distance of 2.59 Å. The Mo cations are located in isolated Mo_2O_{10} octahedral dimers, which represent one of the simplest geometries in which to study metal-metal bonding. Although a d^1 electron configuration is expected for the pentavalent Mo cations based on electron counting arguments, this compound is found to be diamagnetic ($S = 0$) in magnetic susceptibility measurements and non-metallic in electronic transport measurements. Diffuse reflectance measurements show that $La_4Mo_2O_{11}$ absorbs light well into the infrared spectrum (observed onset energy of ~ 0.5 eV), though the present data do not permit the precise determination of a band gap due to the many component features observed in the optical spectra. When the band gap of $La_4Mo_2O_{11}$ is investigated by density function theory (DFT) studies, a band gap of 0.9 eV is predicted by LDA methods (which are known to underestimate band gaps) and a 2.2 eV band gap is predicted using HSE methods typically produce more accurate estimates of band gaps. Both of these DFT-calculated gaps are significantly larger than the activation energy obtained by fitting electronic transport data. This suggests that electronic conduction likely occurs through a polaronic or other defect-driven

mechanism with activation energy of 0.25 eV, and is very consistent with the transport behavior previously observed for the closely related compound La_2MoO_5. Furthermore, the DFT results indicate that the strong infrared absorption observed in experimental measurements is associated with phenomena other than just simple excitations across the band gap. It is demonstrated that the typical t_{2g} and e_g states expected for isolated MoO_6 octahedral are split by the Mo-Mo bonding in $La_4Mo_2O_{11}$ into ten non-degenerate states. These states can be readily rationalized using a molecular orbital approach, and are believed to be the source of the observed diamagnetism and small band gap behavior of this phase.

The structure of the novel compound La_2MoO_5 has been solved from powder X-ray and neutron diffraction data and belongs to the tetragonal space group *P4/m* (no. 83) with a =12.6847(3) Å and c = 6.0568(2) Å and with Z = 8. It consists of equal proportions of bioctahedral (Mo_2O_{10}) and square prismatic (Mo_2O_8) dimers, both of which contain direct Mo−Mo bonds and are arranged in 1D chains. The Mo−Mo bond length in the Mo_2O_{10} dimers is 2.684(8) Å, while there are two types of Mo_2O_8 dimers with Mo−Mo bonds lengths of 2.22(2) and 2.28(2) Å. Although the average Mo oxidation state in La_2MoO_5 is 4+, the very different Mo−Mo distances reflect the fact that the Mo_2O_{10} dimers contain only Mo^{5+} (d^1), while the prismatic Mo_2O_8 dimers only contain Mo^{3+} (d^3), a result directly confirmed by density function theory calculations. This is due to the complete disproportionation of Mo^{4+}, a phenomenon which has not previously been observed in solid-state compounds. La_2MoO_5 is diamagnetic, behavior which is not expected for a nonmetallic transition-metal oxide whose cation sites have an odd number of *d* electrons. The resistivity displays the Arrhenius-type activated behavior expected for a semiconductor with a band gap of 0.5 eV, exhibiting an unusually small transport gap relative to other diamagnetic oxides. Diffuse reflectance studies indicate that La_2MoO_5 is a

rare example of a stable oxide semiconductor with strong infrared absorbance. It is shown that the *d* orbital splitting associated with the Mo_2O_8 and Mo_2O_{10} dimeric units can be rationalized using simple molecular orbital bonding concepts.

Among oxide compounds with direct metal-metal bonding, the $A_5B_2O_{12}$ family of compounds has a particularly intriguing low-dimensional structure due to the arrangement of bioctahedral dimers into one-dimensional edge-sharing chains along the direction of the metal-metal bonds. Furthermore, these compounds can have a local magnetic moment due to the non-integer oxidation state (+4.5) of the transition metal, in contrast to the conspicuous lack of a local moment that is commonly observed when compounds with direct metal-metal bonding have integer oxidation states (due to the lifting of orbital degeneracy typically induced by the metal-metal bonding). Although a monoclinic *C2/m* structure has been previously proposed for $Ln_5Mo_2O_{12}$ (*Ln* = La-Lu, Y) members of this family based on prior single crystal diffraction data, it is found that the average structural model misses many important structural features. Based on synchrotron powder diffraction data, it is shown that the *C2/m* monoclinic unit cell represents a superstructure relative to the base orthorhombic *Immm* subcell, and that the superstructure derives from the ordering of nearly-interchangeable Mo_2O_{10} and LaO_6 building blocks. The superstructure for this reason is typically highly faulted, indicated by the breadth of superstructure diffraction peaks. Finally, it is shown that oxygen vacancies can occur when *Ln* = La, resulting in an oxygen deficient stoichiometry of $La_5Mo_2O_{11.55}$ and an approximately 10-fold reduction in the number of unpaired electrons due to the reduction of the average Mo valence from +4.5 to +4.05, as confirmed by magnetic susceptibility measurements. These oxygens are removed from the bioctahedral Mo_2O_{10} dimers, resulting in an atypical local coordination environment for the Mo cations involved in Mo-Mo bonding. Based on the results of DFT

calculations, the lifting of the *d* orbital degeneracy of $Ln_5Mo_2O_{12}$ compounds is explained within a simple molecular orbital picture. It is found that this absorption gives rise to strong visible light absorption and infrared absorption that is not typically seen for 4*d* transition metal oxides.

Dedication Page

To my family

Table of Contents

List of Figures

List of Tables

List of Abbreviations

BVS – Bond valence sum

DFT – Density functional theory

DOS – Density of states

DR – Diffuse reflectance

FC – Field-cooled

IR - Infrared

KM – Kubelka-Munk transform

LDA – Local density approximation

LMTO – Linear muffin tin orbital

M-M – Metal-metal bond

MO – Molecular orbital

PPMS – Physical property measurement system

TGA – Thermogravimetric analysis

TOF – Time-of-flight

VSM – Vibrating sample magnetometer

V.U. – Valence units

XRD – X-ray diffraction

ZFC – Zero-field-cooled

Acknowledgments

I would first like to thank my advisor Dr. Peter Khalifah for his sharing his time, and providing his knowledge, guidance, and support to me during my time as a PhD student. You have provided me with wonderful opportunities to learn, collaborate, and travel, and for that I am grateful. I would like to also extend my gratitude to Dr. John Parise, Dr. Robert Grubbs, and Dr. Michelle Millar for serving as my committee members, as well as sharing their time and advice with me throughout this process.

Past and present members of the Khalifah group, thank you for your friendship and support during my time at Stony Brook University. Thank you for your encouragement, suggestions, and assistance in and outside of the laboratory. A special thank you to Huafeng Huang and Elizabeth Sobalvarro for their contributions to this project.

I would like to extend my deepest appreciation to my collaborators, in particular Dr. Mark Hybertsen. Thank you for your efforts in calculating and analyzing the higher level DFT data included in this dissertation. Thank you for spending hours sharing your knowledge of theory and contributing to this research. Dr. Fernando Camino, thank you for your help in acquiring resistivity data, your input on experimental setups, and providing us with sample stages. Thank you to those scientists, Dr. Ashfia Huq, Dr. Andrew Payzant, Dr. Mikhail Feygenson, and Dr. Joerg Neuefeind, at the Spallation Neutron Source for your help acquiring data that was vital for properly analyzing these oxides systems.

I cannot thank Dr. Alexandra Reinert enough for sharing an office and friendship with me. Your constant encouragement was very much appreciated. Last, but not least, thank you to my greatest supporters, my family and my fiancé Alex, for their patience, love, and encouragement. I could not have done this without you.

Publications

D. M. Colabello, F. E. Camino, A. Huq, M. Hybertsen, P. G. Khalifah, "Charge Disproportionation in Tetragonal La_2MoO_5, a Small Band Gap Semiconductor Influenced by Direct Mo−Mo Bonding" *J. Am. Chem. Soc.*, 2015, 137, 1245.

D. M. Colabello, F. E. Camino, A. Huq, M. Hybertsen, P. G. Khalifah, "Strong infrared absorption in $La_4Mo_2O_{11}$ enabled by Mo-Mo bonding within Mo_2O_{10} dimers" (submitted)

Chapter 1

Introduction

1.1 Motivation

Transition metal oxides comprise an extremely varied and complex class of materials whose many useful properties are derived from the behavior of the transition metal *d* electrons. A specific subset of transition metal oxides that have drawn interest are those compounds with direct metal-metal (*M-M*) bonds. *M-M* bonding tends to shift *d* orbital splitting away from the typical splitting predicted from ligand field theory, and towards a configuration that more closely resembles narrow *f* electron states. The unusual *d* electron states will impact the electronic structure and physical properties of these compounds, possibly leading to large Seebeck coefficients, small band gaps, and other desirable properties for technological applications. A short *M-M* bond distance, closer than the distance between atoms in the pure metal, is the clearest sign of a direct *M-M* bond. Rhenium, ruthenium, and molybdenum are among those transition metals known to form direct *M-M* bonds, with molybdenum known to form the largest variety of clusters and nuclearities. While there are number of known compounds, only some have been explored beyond synthesis and crystal structure characterization. Based on the number of known rare earth molybdenum oxides that could be explored further, it was the goal of this research to study known and novel rare earth molybdenum oxide compounds with direct Mo-Mo bonds using a systematic and comprehensive approach that incorporated the investigation of relationships between crystal structures, electronic structures, and physical properties.

1.2 Transition metal oxides

Transition metal oxides make up a wonderfully diverse class of materials that can crystallize in a wide variety of structure types and exhibit a broad range of physical properties. Compounds of this class have shown physical phenomena of interest such as high-Tc superconductivity, multiferroicity, and colossal magnetoresistance.[1-3] For this reason, a number of transition metal oxides have served an important role in high-tech applications, including, but not limited to, battery, laser, and information storage applications. What sets transition metals apart from the rest of the elements in the periodic table is a partially filled *d* orbital subshell. In transition metal oxides, it is the overlap of rather localized *d* electron states with O 2*p* states that gives rise to the wide range of physical properties. This is because the small amount of overlap between the transition metal and oxygen states results in bandwidths smaller than most metal compounds, 1-2 eV compared to 5-15 eV respectively (Figure 1.1).[1,4] Due to these narrow states, the effects of electron correlations become increasingly important in these systems. Described by ligand field theory, the transition metal oxidation state, coordination number, and polyhedral environment play a major role in determining the type and amount of the previously mentioned orbital interactions.[5,6] As such, the number of *d* electrons, and the coordination environment of the transition metal in an oxide complex will have a significant impact on properties like electrical resistivity and magnetic susceptibility.

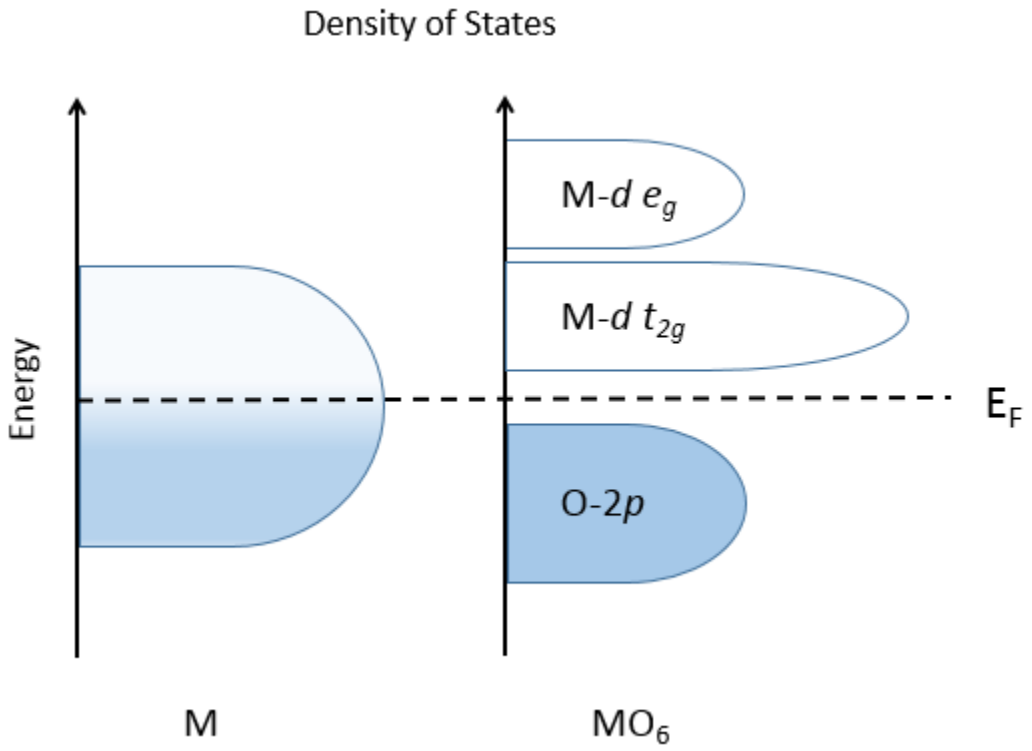

Figure 1.1. Qualitative density of states picture for a metal (left) and a transition metal oxide phase with transition metal octahedral coordination (MO_6, right) ligand field splitting, highlighting the typical differences in bandwidth around the Fermi level (E_F).

As a class, transition metal oxide compounds exhibit a full spectrum of electrical resistivity behaviors, ranging from metallic to insulating and more complex. Ultimately, the transport properties are related to the *d* orbital splitting and the number of *d* electrons present to fill those orbitals, as this will impact the overall degree of localization or delocalization of charge carriers within the unit cell.[1,7] For example, TiO (Ti^{2+}, d^2) is a metallic compound with low electrical resistivity (high conductivity) due to the delocalization of electrons in partially filled t_{2g} bands. Contrastingly, NiO (Ni^{2+}, d^8) is insulating with high electrical resistivity (low conductivity) due to localization of the *d* electrons in e_g orbitals which point at oxygen anions and prevent overlap with adjacent Ni^{2+} ions. Different degrees of electron localization can also result in semiconducting behavior. Examples of semiconducting transition metal oxides include

CuO, TiO_2, and a number of other transition metal oxides. The orbital splitting and amount of delocalization associated with the *d* electrons, in turn, plays a significant role in the magnetic behavior of transition metal oxide compounds. In systems where the electrons are not localized or unpaired the result is diamagnetic (MoO_3, WO_3) or Pauli paramagnetic behavior, whereas localized electrons can give rise to paramagnetic and more complex magnetic susceptibility behavior, such as ferrimagnetism (Mn_3O_4, Fe_3O_4) and antiferromagnetism (Co_3O_4, FeO).[8]

Transition metal oxides have served the role of functional oxides in a number of high-tech applications due to the range of accessible electrical and magnetic properties. For example ferrite and garnet phases are used as active components in magnetic storage media, switched-mode power supplies, magnetic field sensors, resistance random access memory, and circulators for radar systems and mobile phones.[9] In these applications, device function is dependent on the physical properties of the transition metal oxide compound, and it is the degree of response of the functional oxide material to a stimuli that will act as the limiting factor to device performance. Simply stated, device performance and technological progress is correlated to the physical properties of an active material, and to further technology in any field, better, faster, more efficient, and more resilient materials that can meet or surpass required demands are needed. Since the physical properties of transition metal oxides are strongly dependent on the coordination environment of the transition metal and nature of the associated *d* electrons, research has focused on studying structure-property relationships to develop materials with more desirable properties. So called "crystal engineering" has been used to exercise some degree of control over physical properties by manipulating sample composition and fabrication methods to purposely produce materials with desired traits.[10,11] However, one must consider that crystal structures do not directly control physical property behaviors, but rather the crystal structure will

influence the electronic structure of a given material. It is the electronic structure that will be the best indicator of physical properties in solids, and furthermore, the ability to manipulate or tune the electronic structure will provide the best control over functionality. A powerful approach to gaining deeper insights into a chemical system, is to combine experimental and theoretical methods to study the relationships between the crystal structure, electronic structure, and physical properties. The collected information and understanding from such studies can be used as an indicator of physical properties in novel materials and will also serve as a means to drive technological progress.

This dissertation focuses on the specific subset of transition metal oxides that contain direct metal-metal (*M*-*M*) bonds. The formation of the direct *M*-*M* bond leads to orbital splitting that is not predicted from ligand field theory, and this greatly impacts the electronic structure and physical properties of materials within this class. While it has been observed that the *M*-*M* bonds can lead to unusual electronic states caused by the *d* orbital splitting associated with formation of the *M*-*M* bond, the majority of known phases have only been the subject of synthesis and structural characterization studies. These phases are of interest because the non-typical electronic states produced from *M*-*M* bonds will lead to electronic structures with more narrow bandwidths than compared to the general class of transition metal oxides with previously mentioned bandwidths of 1-2 eV.[12] The *d* electron states in these systems are more likely to resemble narrow *f* electron states, which has the potential to effect physical properties, as does the tendency for this type of bonding to produce smaller bandgap materials. The combination of these factors means that compounds with *M*-*M* bonds, compared to transition metal oxides without such bonds, will have unique, and possibly advantageous, physical properties which, to date, have not been explored to the fullest extent. This dissertation is motivated by the study of

transition metal oxides with the distinct crystal structure feature of direct *M-M* bonds for the purpose of expanding the knowledge base of how crystal structures influence the electronic structures, and ultimately physical properties in this family of solids. More information about compounds with direct *M-M* bonds and possible applications are found in the following sections.

1.3 Canonical examples of *M-M* bonding

Metal-metal bonding is most notably characterized by a short distance, on the order of less than 3 Å, between two metal atoms. This distance is shorter than those distances between metal atoms in the pure metal and far shorter than metal – metal distances in compounds without direct *M-M* bonds. As a concept, this is quite simple, but without the proper experimental techniques for detection, direct *M-M* bonds were not recognized for many years. Some of earliest compounds mentioned in scientific literature, specifically $Cr(RCO_2)_2$-type compounds, that are now known to contain *M-M* bonds, date back to the mid to late 19th century. From the primary observation of these compounds to later studies in 1950, all that was known of the Cr-acetate hydrate compounds was that they possessed different coloring and magnetic properties from other known Cr complexes at the time. In 1950, scientists could only go so far as to speculate that a different type of bonding must be occurring in regards to the Cr atoms. It would not be for another 20 years that the realization of direct Cr-Cr bonds in this class of compounds was truly understood. Similar work followed in the early 20th century for bridged halide metal complexes such as Mo_3Cl_6, for which tungsten and tantalum analogs also exist, as scientists tried to make the behavior of these compounds fit the established ideas of "one-center" coordination chemistry set forth by Alfred Werner.[13,14] Not until more discrete methods of verifying the presence of *M-M* bonds, particularly X-ray diffraction, did more work begin to emerge about compounds with this type of bonding, and the idea could be established that transition metals can also have

"multi-center" coordination chemistry. The main experimental methods now utilized for detection of *M-M* bonding are highlighted in Figure 1.2.

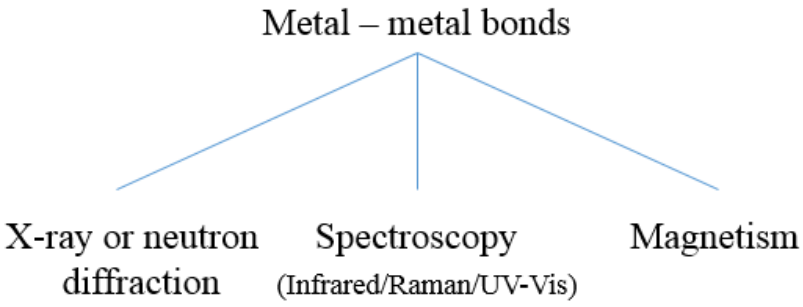

Figure 1.2. Experimental techniques effective for verifying a direct *M-M* bond, with X-ray and neutron diffraction being the most definitive.[15]

Cyrill Brosset, in the late-1940s, used X-ray scattering techniques to determine that the distance between Mo atoms in $Mo_6Cl_8^{4+}$ type inorganic complexes was roughly 2.6 Å, shorter than the distance of 2.725 Å between Mo atoms in pure Mo metal, which must be indicative of a direct Mo-Mo bond. Similar studies about *M-M* bonding followed for MoO_2 and WO_2, and other distorted rutile-type compounds. Later, the work of Cotton *et al.*, prominently established the ground breaking concept of a quadruple bond with the study of the $[Re_2Cl_8]^{-2}$ anion. The distance between Re atoms in this structure is 2.24 Å. Compared to bridged complexes, such as the previously mention Mo_3Cl_6, the Re-Re bond in $[Re_2Cl_8]^{-2}$ is not supported by any bridging ligands. This provided strong evidence that the short Re-Re distance is due to a direct bond between the Re atoms. Cotton was able to rationalize the extremely close Re-Re distance as well as the eclipsed configuration of the Cl atoms, using the concept of a quadruple bond built up from one σ, two π, and one δ components (Figure 1.3). From this work stemmed the reevaluation of many Re based complexes and further exploration of other transition metal based complexes with *M-M* bonds, much of which is now reported in books and literature.[13,16,17]

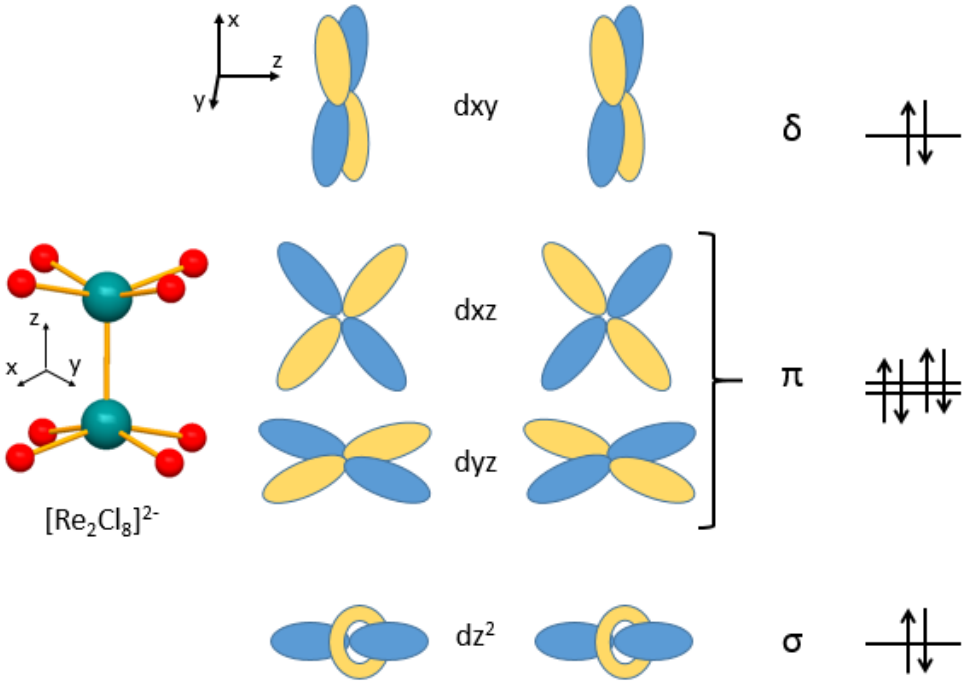

Figure 1.3. Positive overlap of *d* orbitals forming a quadruple bond between Re atoms, each d^4, in the $[Re_2Cl_8]^{2-}$ anion. The dx^2-y^2 orbitals (not pictured) participate in ligand bonding.

1.4 Binary and ternary transition metal oxides with *M-M* bonds

Based on the contributions of Cotton and others, many molecular compounds with *M-M* bonds have been identified and studied. Comparatively, a much smaller number of solid state oxide compounds with *M-M* bonds have been discovered and well characterized. As a result, many opportunities exist for exploring synthesis techniques and crystal structure-electronic structure-physical property relationships among this family of solids. Based on the correlations between *M-M* bond formation with the *d* electron count and *d* orbital radial extension, *M-M* bonding is more likely to occur in early 4*d* and 5*d* reduced transition metal elements which will have unpaired electrons available for *M-M* bond formation.[12] This point is illustrated by the ternary diagram (Figure 1.4) of known La-Mo-O phases, for which a relatively large number of compounds with Mo-Mo bonds have been discovered. The diagram is constructed in such a way that the Mo oxidation state can be easily identified. As expected, compounds with Mo-Mo bonds, represented by red dots in Figure 1.4, are only observed in the reduced molybdate phases.

Of solid state oxides known to contain this type of bonding, several binary transition metal oxides phases with *M-M* bonds have been discovered. Some of the most studied binary oxide systems consist of V, Nb, Mo, Re and W oxides with the formula MO_2.[12,18-20] The structure adopted by each transition metal oxide phase is a variation of a low symmetry rutile structure, and *M-M* bonds are observed in chains of edge sharing MO_6 octahedra that alternate short and long *M-M* distances. The *M-M* bonds lead to a zig-zag off-centered displacement of the transition metal atom towards the direction of the other transition metal atom participating in the bond and away from the second atom with which it does not share a bond. This is depicted for the compound WO_2 in Figure 1.5. Due to the number of d-electrons in each system, MoO_2 and WO_2 are described as having a double *M-M* bond and exhibit metallic behavior, while VO_2 and NbO_2,

which have a single *M-M* bond, both undergo metal to insulator transitions in conjunction with a phase change upon a change in temperature.

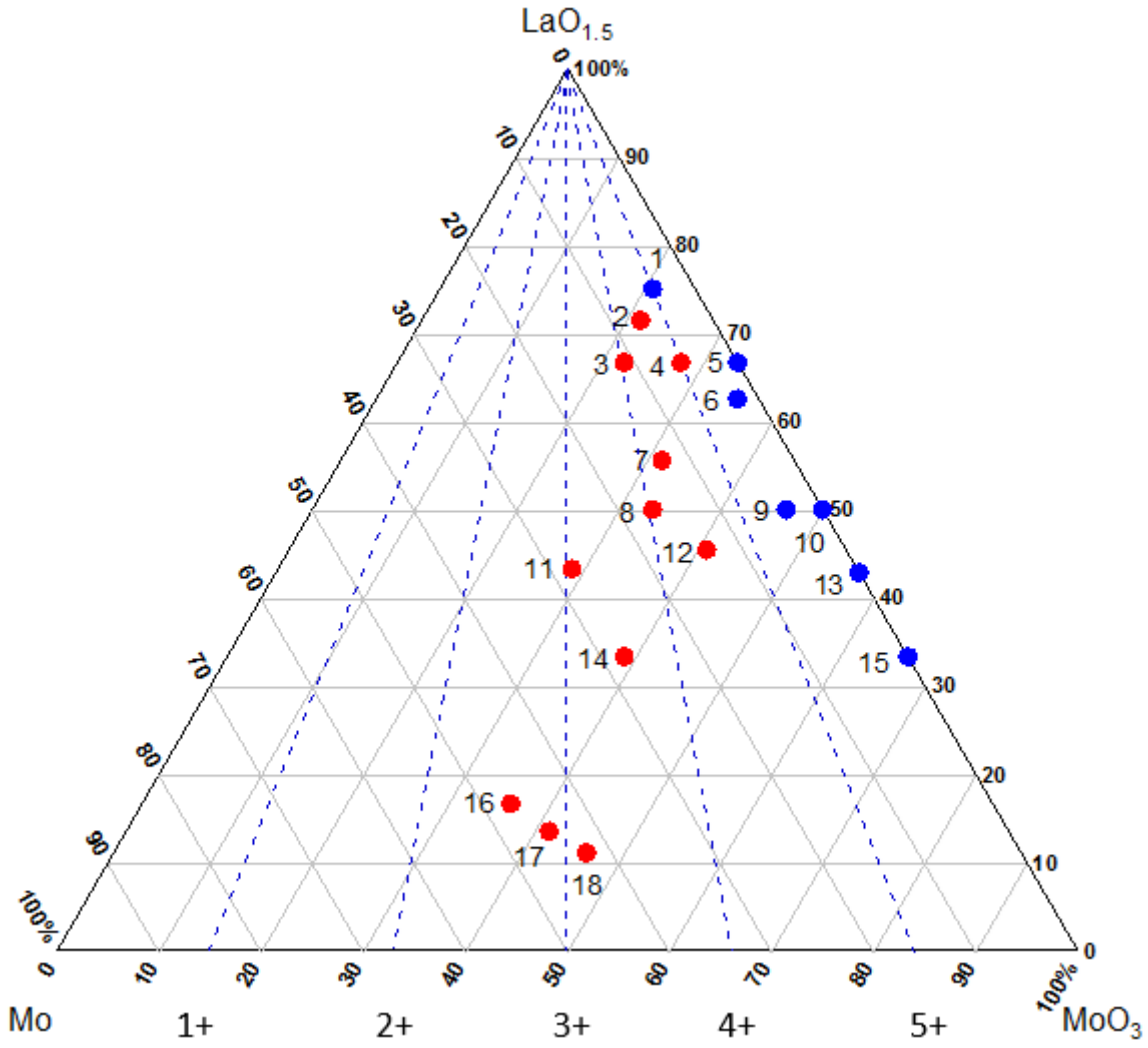

Figure 1.4. Ternary diagram representing known La-Mo-O phases. Phases represented with red dots are known to contain one or more Mo-Mo bonds. La-Mo-O phases without Mo-Mo bonds are represented by blue dots. The Mo oxidation state boundaries are represented by dashed blue lines ranging from 0 (Mo) to 6+ (MoO_3). (1) La_3MoO_7, (2) $La_5Mo_2O_{12}$, (3) La_2MoO_5, (4) $La_4Mo_2O_{11}$, (5) La_2MoO_6, (6) $La_5Mo_3O_{16}$, (7) $La_5Mo_4O_{16}$, (8) $La_2Mo_2O_7$, (9) $La_7Mo_7O_{30}$, (10) $La_2Mo_2O_9$, (11) $La_{16}Mo_{21}O_{56}$, (12) $La_5Mo_6O_{21}$, (13) $La_6Mo_8O_{33}$, (14) $LaMo_2O_5$, (15) $La_2Mo_4O_{15}$, (16) $LaMo_5O_8$, (17) $La_5Mo_{32}O_{54}$, (18) $LaMo_8O_{14}$.

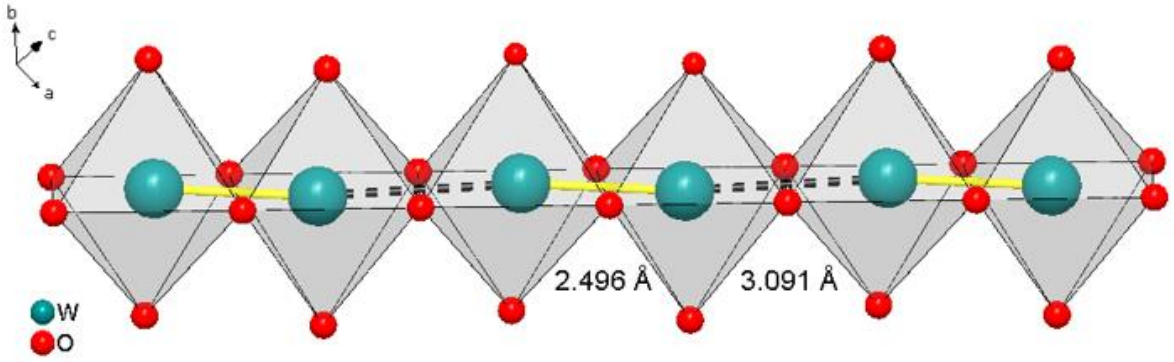

Figure 1.5. A chain of WO_6 octahedra alternating short (yellow) and long (black) W-W bond distances in the compound WO_2 is displayed.

More complex in terms of crystal structures and physical properties are those compounds belonging to the class of ternary transition metal oxides with *M-M* bonds. This group largely consists of rare earth transition metal oxides with a significant number of Mo, Re and Ru compounds found to contain direct *M-M* bonds. Little work has been completed to characterize the physical properties or electronic structure of these phases, but the crystal structures and *M-M* bonding environments within these compounds have been characterized, revealing a rich coordination chemistry in terms of *M-M* bound dimers and extended cluster units. Of the transition metals that form *M-M* bonds, molybdenum is known to form the largest variety of clusters.[21-23]

The *M-M* bonded units in rare earth transition metal oxide phases can exist as isolated dimers or form extended transition metal oxide polyhedral networks with higher dimensionality (1D - 3D) throughout the unit cell. Some examples of ternary Mo, Re, and Ru oxide compounds showing the range of structure types and *M-M* bonding networks are shown in Figure 1.6. As displayed in the corresponding figure, $Nd_4Re_2O_{11}$ (Re^{5+}) contains isolated (0D) Re_2O_{10} units with Re atoms separated by 2.43 Å.[24] $Eu_5Ru_2O_{12}$ ($Ru^{4.5+}$) has 1D chains of edge sharing Ru_2O_{10}

octahedra with alternating short and long Ru-Ru distances of 2.78 and 3.09 Å, respectively.[25] In $La_2Mo_2O_7$ (Mo^{4+}), Mo atoms are separated by 2.48 Å. The Mo_2O_{10} edge sharing octahedral units share corners with adjacent dimers in both the *a* and *c* axis directions, building a 2D framework of MoO_6 polyhedra.[26] $La_5Mo_6O_{21}$ (average $Mo^{4.5+}$) contains Mo_3O_{13} cyclotrimer (triangles) units with Mo atoms separated by about 2.56 Å and connected in a 3D framework of MoO_6 polyhedra.[27] These four compounds only provide a small sampling of the range of crystal structure types and metal cluster environments that are known to be accessible. There are still ample opportunities to explore physical properties and electronic structures among compounds of this type.

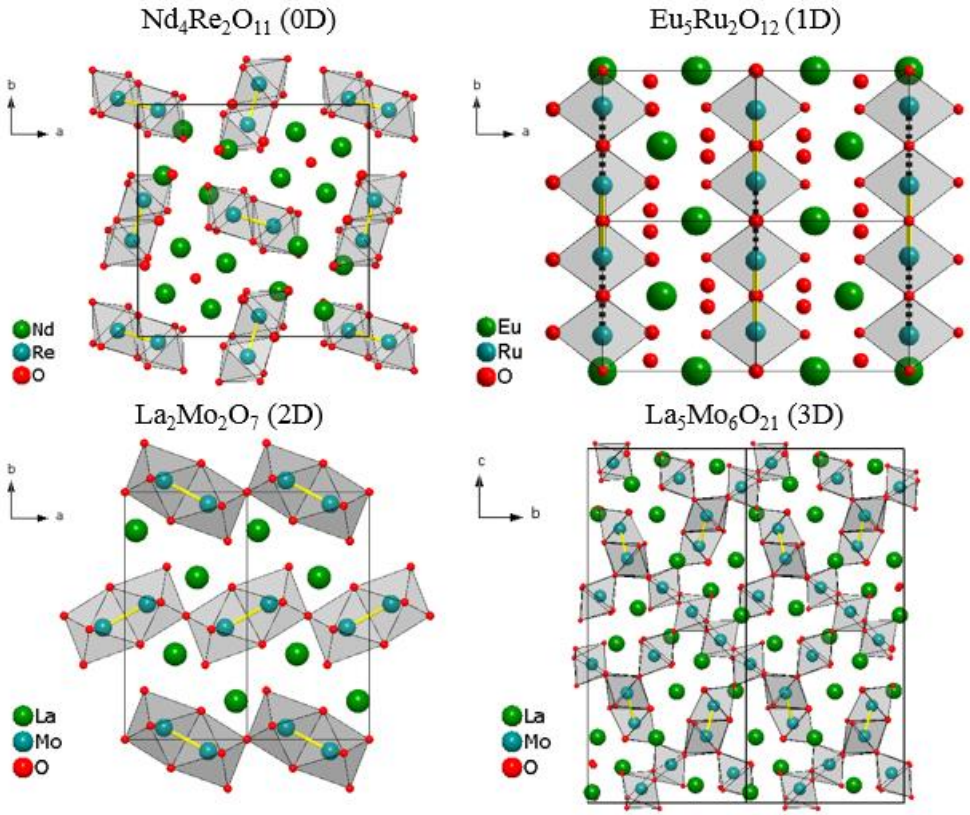

Figure 1.6. Four rare earth transition metal oxide compounds containing *M-M* bonds built up from different transition metals with varying dimensionality are shown for reference. The *M-M* bonds are highlighted by yellow sticks between metal atoms. Dashed black lines displayed in $Eu_5Ru_2O_{12}$ represent non-bonded metal atoms.

1.5 Ternary molybdenum oxide phases with Mo-Mo bonds

This dissertation was motivated by the study of rare earth transition metal oxides with direct Mo-Mo bonds, and establishing a method to understand the relationships between crystal structures, electronic structures, and physical properties among this class of compounds. Being that most known compounds have only been the subject of structural studies, rare earth molybdenum oxides were chosen based on the diversity of observed Mo-Mo cluster units and the number of known compounds which could be explored further. Table 1.1 provides a listing of ternary rare earth molybdenum oxides with Mo-Mo bonds. The reported crystal structures of the compounds listed in Table 1.1 have been resolved mainly through the use of X-ray diffraction studies, and reflect the variety of crystal structures that can be found across the family of oxides with Mo-Mo bonds. Previously stated, the distance between Mo atoms in pure molybdenum metal is 2.725 Å, and the Mo-Mo bond distances of compounds listed in Table 1.1 are clearly shorter than this distance, indicating the presence of the direct Mo-Mo bond.

In terms of variety, the Mo-Mo bonding environments of the cluster units in these compounds span from Mo_2 dimers to Mo_{10} based clusters (Figure 1.7). Linear Mo_2 units can be observed as isolated clusters within the unit cell, as in $La_4Mo_2O_{11}$, or forming one dimensional chains with alternating long and short Mo-Mo bond distances as is found in $Gd_5Mo_2O_{12}$.[28,29] Higher dimensionality with Mo_2 based units has also been studied in compounds like $La_2Mo_2O_7$, described and pictured previously in Figure 1.6.[26] Mo_3 and Mo_4 based clusters can be described as trigonal or rhomboidal units respectively. Mo_6 octahedral, Mo_8 bicapped octahedral and Mo_{10} bioctahedral units have also been reported.[27,30] For some ternary molybdate compounds, multiple units can be found in a single crystal structure. For example, $Ln_4Mo_{18}O_{32}$ is characterized by the

presence of Mo_2, Mo_4, and Mo_6 based clusters that form complex chains along the *b* axis of the unit cell.[23]

Table 1.1. Ternary molybdenum oxides with Mo-Mo bonds. The average Mo oxidation state and the shortest Mo-Mo bond distance are provided for reference.

Formula	*Ln*	Space group	Avg. Mo Valence	*d* electron count	Mo-Mo length (Å)	Ref.
$Ln_4Mo_2O_{11}$	La	$P4_2/n$	5	d^1	2.59	[28]
$Ln_5Mo_6O_{21}$	La	$P2_12_12_1$	4.5	$d^{1.5}$	2.55	[27]
$Ln_5Mo_2O_{12}$	Y, Gd	$C2/m$	4.5	$d^{1.5}$	2.50	[29]
$Ln_5Mo_4O_{16}$	La	$C2/m$	4.25	$d^{1.75}$	2.41	[31,32]
$Ln_2Mo_2O_7$	La	$Pnnm$	4	d^2	2.48	[26]
Ln_2MoO_5	La	$P4/m$	4	d^2	2.22	[33]
$LnMo_8O_{14}$	La, Ce	$Pbcn$	3.125	$d^{2.88}$	2.59	[22]
$LnMo_8O_{14}$	Nd, Sm	$Aba2$	3.125	$d^{2.88}$	2.59	[22]
$LnMo_8O_{14}$	Pr	$Pbca$	3.125	$d^{2.88}$	2.59	[22]
$LnMo_2O_5$	La	$P6_3mc$	3.5	$d^{2.5}$	2.57	[34]
$Ln_{16}Mo_{21}O_{56}$	La-Nd	$P12_1/c1$	3	d^3	2.61	[35]
$Ln_5Mo_{32}O_{54}$	La-Nd	$P12_1/c1$	2.9	$d^{3.1}$	2.56	[36]
$Ln_4Mo_{18}O_{32}$	Y, Gd-Yb	$P12/c1$	2.89	$d^{3.11}$	2.51	[23,37]
$LnMo_5O_8$	La-Nd, Sm-Gd	$P12/c1$	2.6	$d^{3.4}$	2.75	[38]
$Ln_4Mo_4O_{11}$	Y, Nd-Tm	$Pbam$	2.5	$d^{3.5}$	2.59	[30]

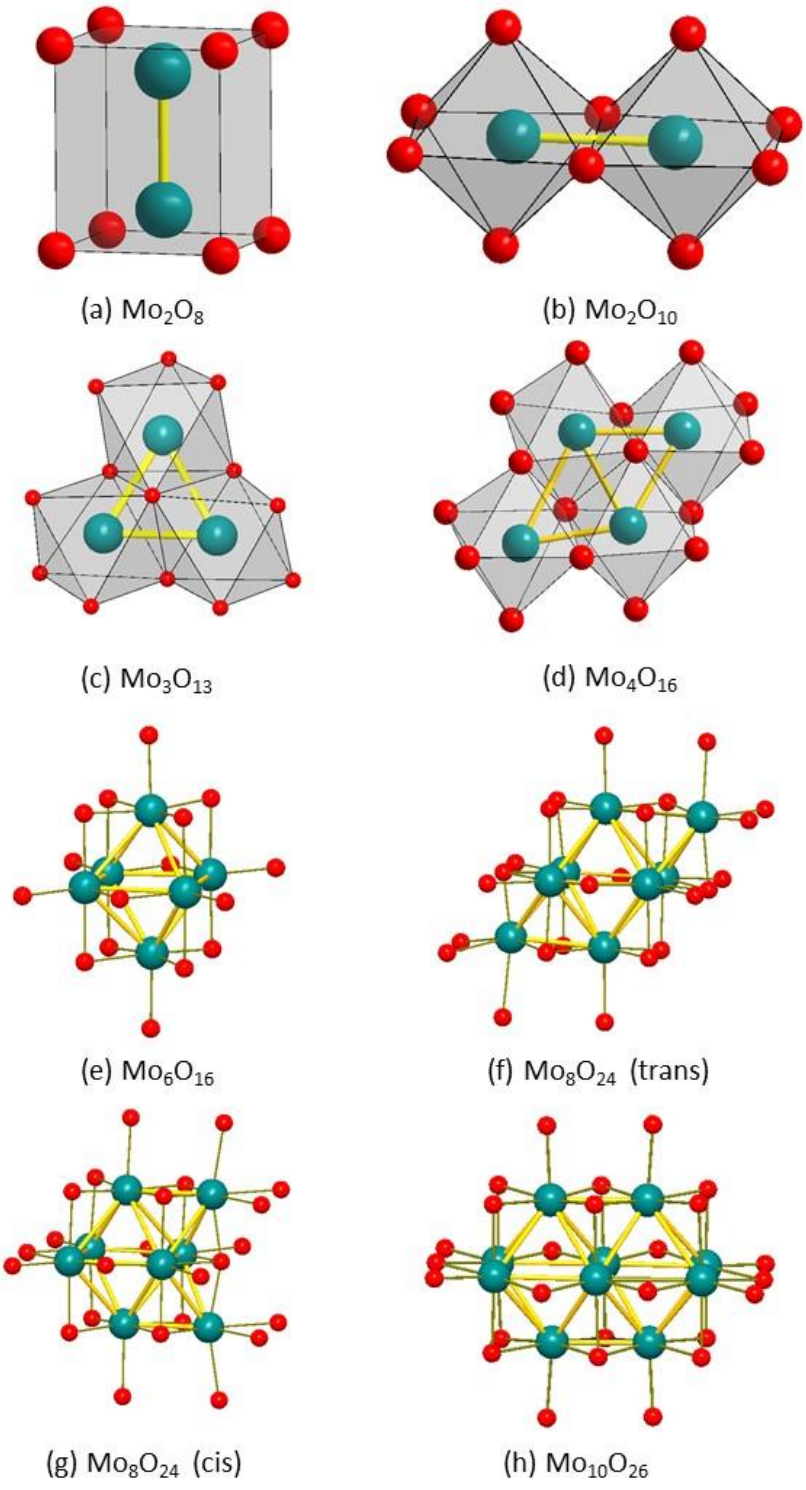

Figure 1.7. Examples of Mo-Mo bound cluster units ranging from Mo_2 to Mo_{10} based clusters. (a) La_2MoO_5, (b) $La_4Mo_2O_{11}$, (c) $La_5Mo_6O_{21}$, (d) $Gd_4Mo_{18}O_{32}$, (e) $Y_4Mo_4O_{11}$, (f, g) $LaMo_8O_{14}$ (h) $LaMo_5O_8$

The wide variety of Mo-Mo bonding environments and range of available Mo oxidation states poses a difficult task to studying this class of compounds systematically. The number of *d* electrons available for Mo-Mo bonding, the type Mo-Mo cluster unit, and the resulting electronic structure will have a significant bearing on physical properties. While the majority of known compounds have only been the focus of synthesis and crystal structure solution, a range of transport and magnetic properties have been observed for those compounds that have been explored beyond structural investigations. $Y_4Mo_{18}O_{32}$ has metal to insulator transition around 120 K and magnetic susceptibility studies show a nearly temperature independent response, indicating that the Mo sub-lattice does not contribute to the magnetic susceptibility in this phase or for isostructural phases with a magnetic rare earth ion.[37] $Gd_5Mo_2O_{12}$ and the isostructural $Y_5Mo_2O_{12}$, with Mo_2O_{10} edge sharing octahedral units, are reported to be *n*-type semiconductors.[29] For these compounds Mo is in the 4.5+ oxidation state ($d^{1.5}$) and the measured magnetic susceptibility was in agreement with the predicted S = 1/2 response corresponding to 1 unpaired electron per Mo dimer. $Ln_{16}Mo_{21}O_{56}$ compounds exhibit insulating behavior, with a measured resistivity on the order of 10^6 Ω·cm at RT, and the Mo_{10} based clusters in the unit cell are found not to contribute the overall magnetic response of the phase.[35]

So while some work has been done to characterize the physical properties of select compounds, there are still many known compounds, and possible novel phases, that have not been fully characterized for molybdate and other transition metal oxide phases with this type of bonding. This would include electronic structure calculations to describe the *d* orbital splitting associated with the formation of direct Mo-Mo bonds. Studies of this kind can aid in predictions of physical properties of analogous or novel phases. Establishing a method of study to characterize not only the crystal structure, but electronic structures and physical properties

among this class of materials would serve to better understand how *M-M* bonding will impact the functionality and applications of all solid state materials containing *M-M* bonds. Research conducted in this manner will be useful for making predictions about novel compounds from crystal structure information and simple density functional theory (DFT) type calculations.

1. 6 Properties and applications of oxide compounds with M-M bonds

Most of the work surrounding compounds with direct *M-M* bonds has focused on discovery, synthesis, and structural characterization. Crystal structure investigation in conjunction with electronic structure calculations and physical property studies will be valuable to property optimization and for making predictions about physical properties in novel phases. Despite the influence *M-M* dimer or cluster formation will have on transport properties and magnetic susceptibility, few studies include these types of measurements. From reports of compounds with *M-M* bonds that do include magnetic and electrical transport data, usually over a limited temperature range (80-300 K), it can be inferred that *M-M* bonds are often detrimental to magnetic susceptibility and will also likely result in small band gap materials.[39-43] Since the formation of a direct *M-M* bond tends to lead to an increase the transition metal *d* orbital splitting, with fewer degenerate states, when compared to the same type of compound in the absence of *M-M* bonding, there is a greater likelihood that electrons will pair in a single orbital, resulting in a reduction of the transition metal magnetic moment. More data, and data at lower temperatures, will be of benefit to future studies of compounds with *M-M* bonds, making predictability of property behaviors more accurate as well as increasing the understanding of crystal structure effects on physical properties. As with magnetic and electrical transport studies, few DFT calculations to characterize electronic structures have been carried out for these types of compounds.

From the limited physical property and theoretical studies reported in literature, it is understood that *M-M* bonding tends to shift *d* orbital splitting away from the typical splitting predicted from ligand field theory. In the single ion picture, an isolated transition metal atom has a set of 5 completely degenerate *d* orbitals. When the transition metal is located in an octahedral coordination environment, MO_6, the *d* orbital splitting predicted by ligand field theory is the familiar set of triply degenerate t_{2g} states with the doubly degenerate e_g states lying higher in energy (Figure 1.8). In the solid state picture, the t_{2g} and e_g states are represented by two broad sets of bands in the electronic band structure and density of states profiles.[5] *M-M* bonds will alter the characteristic *d* orbital electronic structure of a transition metal centered octahedra when, for example, two octahedra share an edge and a direct *M-M* bond (M_2O_{10} unit). This is exemplified in the compounds $Y_5Re_2O_{12}$, for which ReO_6 octahedra share an edge and a Re-Re bond distance of 2.447 Å, and $La_4Ru_6O_{19}$, which also forms edge sharing Ru_2O_{10} octahedral units with Ru atoms separated by a short distance of about 2.5 Å. A simple DOS calculation for $Y_5Re_2O_{12}$ (Figure 1.8) reveals, that although Re atoms are found in an octahedral coordination environment, the Re *d* orbitals contribute to more than two peaks (e_g/t_{2g}) in the DOS due to the formation of the Re-Re bond across the Re_2O_{10} units.[44] Comparatively, in studies of $La_4Ru_6O_{19}$, density functional theory calculations were used to explicitly probe the electronic band structure and DOS, with an additional "fatbands" analysis to calculate how specific *d* orbitals contributed individually to the electronic band structure. In this compound the 3 t_{2g} states of each Ru atom in the Ru_2O_{10} unit hybridize to 6 non-degenerate states, forming the σ, π, δ, δ*, π*, σ* components of the Ru-Ru bond (Figure 1.9).[45,46] The tendency for reduction in orbital degeneracy, for these two examples and other *M-M* bonded compounds, increases the likelihood that electrons will pair and result in a diamagnetic response in the presence of a magnetic field.

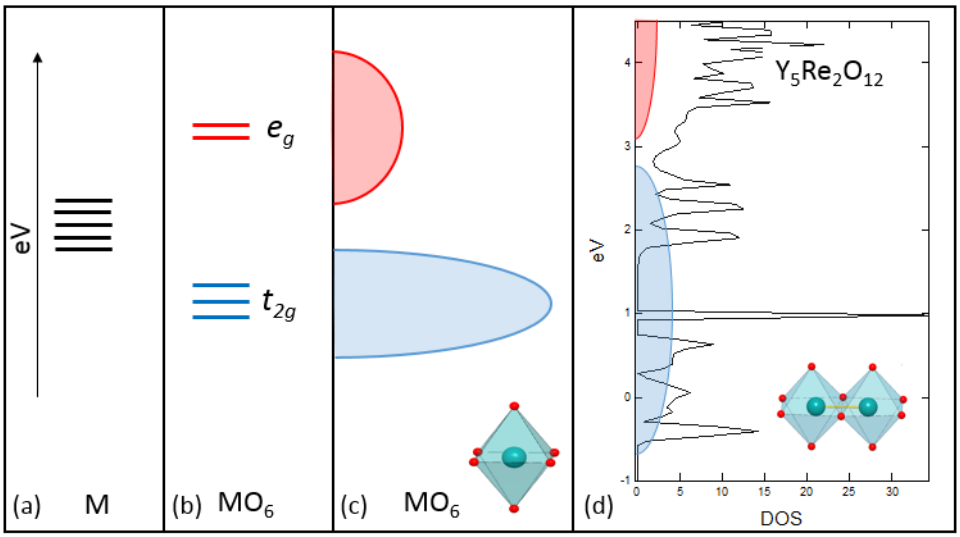

Figure 1.8. Typical *d* orbital energy levels. (a) An isolated transition metal with 5 degenerate *d* orbitals. (b) Octahedra crystal field splitting of the doubly degenerate (e_g) and triply degenerate (t_{2g}) *d* orbitals for molecular compounds. (c) The DOS distribution of e_g (red) and t_{2g} (blue) *d* orbital energy levels in a solid with octahedral coordination. (d) $Y_5Re_2O_{12}$ contains Re_2O_{10} edge sharing octahedra dimers with a Re-Re distance of 2.447 Å. The calculated DOS (black) for $Y_5Re_2O_{12}$ and the partial DOS for the Re *d* orbital contribution (red/blue) show that the *d* orbital splitting deviates from the crystal field prediction for an isolated ReO_6 octahedra.

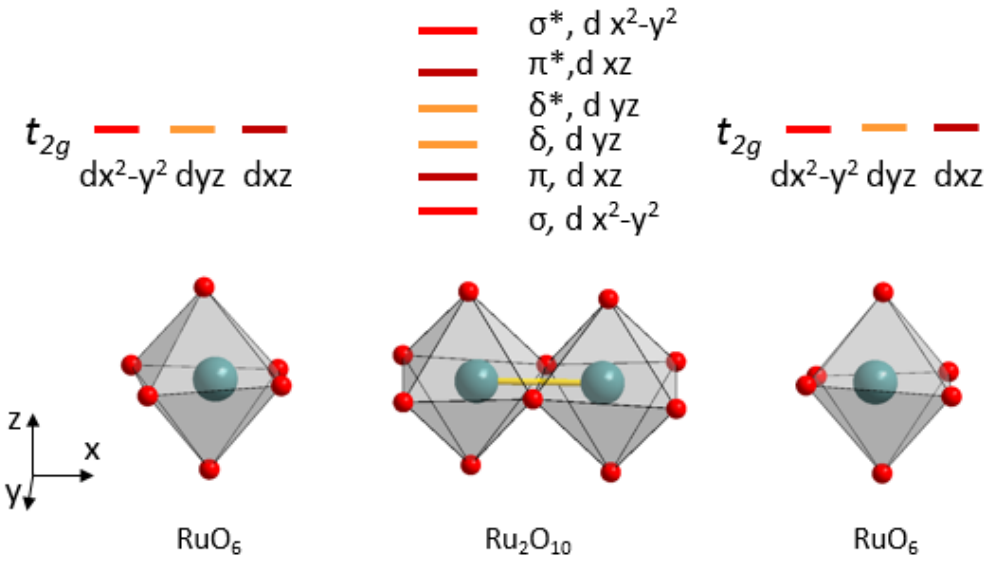

Figure 1.9. Hybridization of Ru t_{2g} states forming the σ, π, δ, δ*, π*, σ* components of the Ru-Ru bond in $Lu_4Ru_6O_{19}$ determined from the results of DFT-type calculations.

In addition to the general effects on electronic structure and magnetic susceptibility, this type of *d* orbital splitting has possible implications for other physical properties, which have not been explored in a systematic way across the transition metal elements that are known to form *M*-*M* bonds or the type of *M*-*M* bonding environments that result from the formation of the direct bond. As depicted for $Y_5Re_2O_{12}$ in Figure 1.8, the lowering of the *d* orbital degeneracy will tend to result in sharp contributions to the DOS over a narrow energy range (0.2-0.5 eV) as well as an increased likelihood for small band gaps.[12] These two effects, small band gaps and narrow bandwidths, hint at possible technological applications for compounds with *M*-*M* bonds, which have not yet been explicitly studied. While most semiconductor technology makes use of larger band gap materials, there are niche uses for small band gap materials, specifically for infrared (IR) applications.[47] Currently, the small band gap semiconductor materials utilized for IR detector applications include later *p*-block elements such as In, Ga, As, Pb, and Sb. These elements are often toxic and typically are not air stable. Due to their stability in air and lower toxicity, small band gap oxide semiconductors may offer advantages over the current *p*-block materials used for IR applications. Since research into transition metal oxides with *M*-*M* bonds indicate that this type of bonding tends to lead to small band gaps, these compounds might offer nontoxic, air stable, alternatives for IR detector applications over traditional materials such as InGaAs.[48]

Sharp, localized peaks that span over a narrow energy range in the DOS was the second general electronic structure feature highlighted for oxide compounds with *M*-*M* bonds. Based on theoretical studies that will be discussed, this feature in the DOS suggests that compounds with *M*-*M* bonds might be useful for thermoelectric applications. Thermoelectric devices offer a means to convert thermal energy into electric energy (Seebeck effect) or electric energy into a

thermal gradient (Peltier effect). The potential for waste heat recovery systems for cars and industrial processes, that can increase device efficiency without greenhouse gas emissions, is a promising technology. Thermoelectric small scale solid state refrigeration holds possibilities for efficient cooling of high power electronic devices, whose components typically operate at temperatures close to the edge of their reliability. Current thermoelectric devices operate at low efficiencies (< 10%) which has reduced use of these devices to niche applications.[49,50]

Thermoelectric device efficiency is strongly correlated to the efficiency of materials used to comprise the module, and therefore better materials will directly result in better device performance. Efficiency is judged by the dimensionless figure of merit Z which is evaluated for a specific operating temperature and more often referred to as ZT. ZT is related to the Seebeck coefficient ($S = \Delta V/\Delta T$), the electrical conductivity (σ), and thermal conductivity (κ) such that $ZT=S^2\sigma T/\kappa$. A good thermoelectric material will have a large absolute Seebeck coefficient (> 150 μV/K), and strong electrical conductivity ($\approx 10^3\ \Omega^{-1}cm^{-1}$), and a low thermal conductivity (< 2 W/mK), so as to keep charge carriers mobile while maintaining a thermal gradient across the device.[51] The parameters S, σ, and κ are intimately related to the electronic structure of a compound, and theoretical studies have been completed to address what features of the electronic structure will give rise to the largest ZT materials. The solution to the transport distribution function, which considers S, σ, and κ as integrals of a single function, found that materials with a large contribution to the density of states, over a narrow energy range, near the chemical potential of the system will have a large thermoelectric efficiency. Theoretically, the ideal solution is the Dirac delta function (0 for $x \neq 0$ and infinite at $x = 0$), but this type of response is not found in real systems. For real materials, these types of electronic states are commonly found in strongly correlated *f* electron systems.[52] Additionally, the correlation between a steep slope in

the DOS (n) near the Fermi level (E_F) and a large Seebeck (S) coefficient is also described by the Mott relation, $S = \frac{1}{n(\varepsilon)}\left(\frac{\partial n}{\partial \varepsilon}\right)_{\varepsilon=\varepsilon_F}$. Based on the transport distribution function and the Mott equation, the best thermoelectric materials are strongly expected to have an electronic structure with intense and narrow peaks in the DOS profile near the Fermi level of the system.

It has been shown that for oxide compounds with *M–M* bonds that the *d* orbital degeneracy is reduced as *d* orbitals from each metal atom hybridize to form bonding and anti-bonding states. The lack of *d* orbital degeneracy results in an electronic structure with features that more closely resemble narrow *f* electron states, as opposed to typical *d* orbital states for transition metal oxides without *M-M* bonds. Based on the results of the transport distribution function and Mott equation, this would indicate that the tendency for small band gaps and the *d* orbital splitting imposed by *M-M* bonds should lead to materials with a strong electrical conductivity, a large Seebeck coefficient, and therefore a high thermoelectric efficiency. Since oxide materials typically possess good thermal stability in air, this provides additional evidence that transition metal oxides with *M-M* bonds would be ideal candidates for thermoelectric applications.

While the physical properties of most oxide compounds with *M–M* bonds remain unexplored, the family of *Ln*Mo_8O_{14} (*Ln* = La, Ce, Pr, Nd, and Sm) compounds with Mo_8 cluster units has been investigated for possible thermoelectric applications.[22] Typical of compounds with *M-M* bonding, the electronic structure of *Ln*Mo_8O_{14} reveals many sharp and narrow peaks contributed by the Mo *d* orbitals to the DOS (Figure 1.10). Electrical resistivity studies characterize the compounds as narrow band gap *n*-type semiconductors ($LaMo_8O_{14}$, E_g = 0.05 eV). As predicted by the transport distribution function and Mott relation, *Ln*Mo_8O_{14} compounds

possess relatively large Seebeck coefficients. The combination of small band gaps and large Seebeck coefficients result in power factors, σS^2, (Figure 1.10) that rival some of the best thermoelectrics, such as Bi_2Te_3 (35 $\mu W/mK^2$ – 300 K).[53] Further exploration of other oxide compounds with *M–M* bonds are predicted to reveal similar properties, but a systematic method of study for transition metal oxides with *M-M* bonds has not been established.

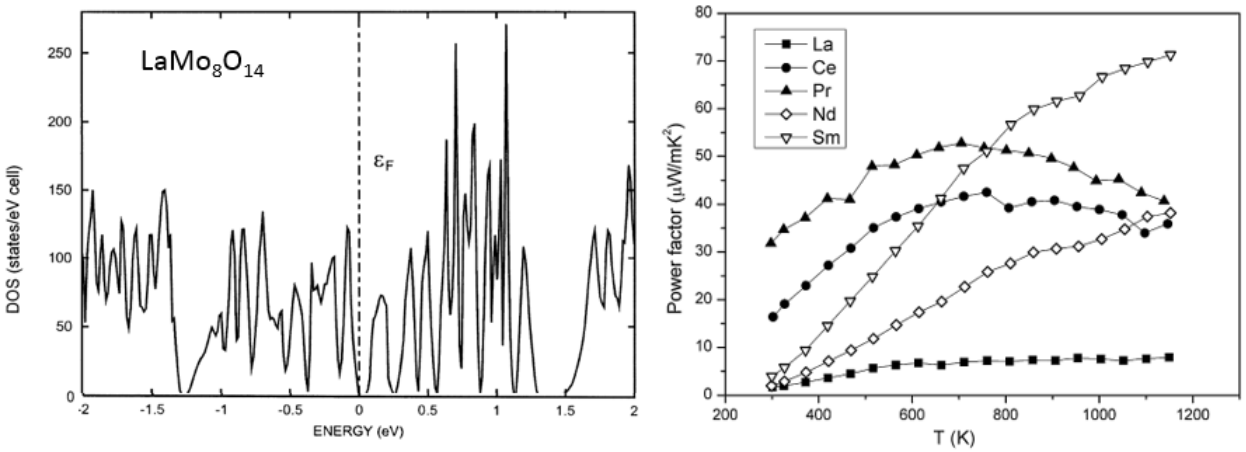

Figure 1.10. (Left) The DOS plot for $LaMo_8O_{14}$, a compound with Mo-Mo bonds. The Mo *d* orbital contribution to the DOS (-1.5 to 1.5 eV) resembles certain features of the Dirac delta function and *f* electron systems in terms of the intense contribution over a narrow energy region to the DOS. (Right) The power factor as a function of temperature for $LnMo_8O_{14}$ (*Ln* = La, Ce, Pr, Nd, and Sm) compounds.[22]

1.7 Research objectives

This research is based on the extensive characterization of select rare earth molybdenum oxide phases with direct Mo-Mo bonds. The unusual electronic states in these compounds, imposed by the formation of direct Mo-Mo bonds, can induce physical properties that may be of potential interest for high tech applications, including, but not limited to, thermoelectric and infrared technologies. Up to date, most known compounds in this class have been the subject of crystal structure characterization, with little work done to characterize or manipulate physical properties. It was, therefore, a goal of this work to study and contribute to the knowledge of

crystal structure - electronic structure – physical property relationships among this class of compounds. This type of characterization allows for intelligent predictions about physical properties to be drawn from crystal structure and electronic structure information, and through this work, strategies for the control of functionality can be developed and directed towards technological needs. Crystal structures of both known and novel rare earth molybdenum oxides were investigated with X-ray and neutron diffraction studies, electronic structures were probed with both lower level and higher level DFT-type calculations, and physical properties (absorbance, magnetism, and electrical resistivity) were measured using appropriate techniques, of which the general methodology and importance will be discussed below.

1.8 Experimental techniques

1.8.1 Powder synthesis

Powder synthesis, referred to as the ceramic method, is a simple, effective, and widely used technique in the preparation of solid state compounds. Desired amounts of starting materials are ground together with an agate mortar and pestle to ensure homogeneity, small grain size, and maximum contact among starting materials. A large surface area and good contact between starting materials is paramount because in a solid state synthesis the majority of the reaction is occurring at the surface of the powders with some, but not as much, diffusion occurring as well.[10] Once the mixture is ground, it can either be reacted as a loose powder or pressed into a pellet before heating. A pellet will increase the contact of reagents while minimizing the contact between the sample and the crucible. Crucibles can be made of alumina, carbon, steel, metal, or quartz. Additionally, samples can be sealed either under vacuum or a particular gas, if necessary for the synthesis. The sample, in a suitable vessel, is then heated to high temperatures in either a

box furnace if the reaction is taking place in air, or a tube furnace if the reaction requires a special atmosphere. In the case of the later, compressed gases such as N_2, O_2, Ar, NH_3, or 5%H_2 / 95%N_2 can be flowed over the sample to create the desired atmosphere for the reaction. For this work, a box furnace was used to dry starting materials before being weighed. Over the course of these studies either a Lindberg/BlueM Mini-Mite furnace with a 1" quartz tube and compression fittings, or a Mellen SV Series mullite tube (3.5" diameter) furnace were used to carry out solid state syntheses at elevated temperatures under 5%H_2 / 95%N_2, as a reducing atmosphere was required to produce the desired phases. A flowmeter and bubbler filled with mineral oil were used to ensure the gas continued to flow through the setup at a steady rate of approximately 60 mL/min. The synthesis progress and phase purity of samples were studied with powder X-ray diffraction experiments at intermediate points throughout the synthesis and after reaction completion. If a reaction had not reached completion, evidenced by the indexing of phases present in the X-ray diffraction data, then the sample was reground to create new contacts between phases in the reaction mixture before being returned to the furnace for further heating under the appropriate reaction conditions.

With the primary goal of this research being to study both known and novel phases of molybdates with direct Mo-Mo bonds, the knowledge of phases readily accessible through simple solid state reactions was of utmost importance. To establish this library of compounds that are not only readily synthesized, but readily synthesized single phase, many powder synthesis reactions were carried out. Investigation began with the synthesis of compounds in the La-Mo-O family, as there are already several compounds known to contain direct Mo-Mo bonds. La_2O_3 and MoO_3 were often used for starting materials. The starting ratio of La:Mo^{6+} was varied and several reaction temperatures were tested. As Mo-Mo bonding is found in reduced

molybdates, all reactions were run under flowing 5%H_2 / 95%N_2 to promote the reduction of molybdenum. Both known and novel phases were synthesized from this approach, and this method was later extended to the study other rare earth molybdates (Y, Sm, Eu, and Lu).

1.8.2 Powder X-ray diffraction

Powder X-ray diffraction (XRD) is a powerful tool for solid state chemists that is utilized for both its qualitative and quantitative applications in the characterization of crystalline materials. Qualitatively, XRD is used to identify the composition of phases, including impurity phases, present within a powder sample. Quantitatively, XRD is used to obtain phase fractions and detailed information about lattice and atomic parameters necessary to describe or solve crystal structures. Powder XRD is very appealing due to the ease of sample preparation, as only a few milligrams of sample are required and only a short amount of time is needed to acquire data. Useful information can often be obtained in a matter of minutes.

X-rays fall on the electromagnetic spectrum between γ-rays and the ultraviolet region. They have a wavelength of approximately 1 Å, which is important for diffraction because it is on the same order of magnitude as the distance between scattering objects. In a crystal lattice this distance ranges from about 0.5-2.5 Å. The X-rays that are used for diffraction experiments are usually produced from a molybdenum or copper source, with Cu the typical choice for laboratory powder diffractometers. X-rays are produced when a high energy beam of electrons is accelerated and allowed to hit the metal Cu target. The incident electrons ionize the electrons in Cu 1s orbital (K shell), and an electron from an outer orbital quickly fills this vacancy. The transition energy of the 2*p* or 3*p* electron falling into the vacant 1*s* orbital is released in the form of X-radiation. For Cu there are two characteristic wavelength energies to describe this

transition, K_α and K_β. K_α, the result of a $2p \rightarrow 1s$ transition, has a wavelength of 1.5418 Å, which is the average of the $K_{\alpha 1}$ (1.5404 Å) and $K_{\alpha 2}$ (1.5443 Å) transition energies. K_β, which occurs less frequently and is less intense than K_α, is the result of a $3p \rightarrow 1s$ transition. The characteristic wavelength for the K_β transition is 1.3922 Å, and is often eliminated with the use of a Ni filter. The relative position and intensities of the full Cu emission spectrum are shown in the Figure 1.11. Due to the greater frequency and intensity of the Kα transition, this type of radiation utilized in diffraction experiments.[10,54]

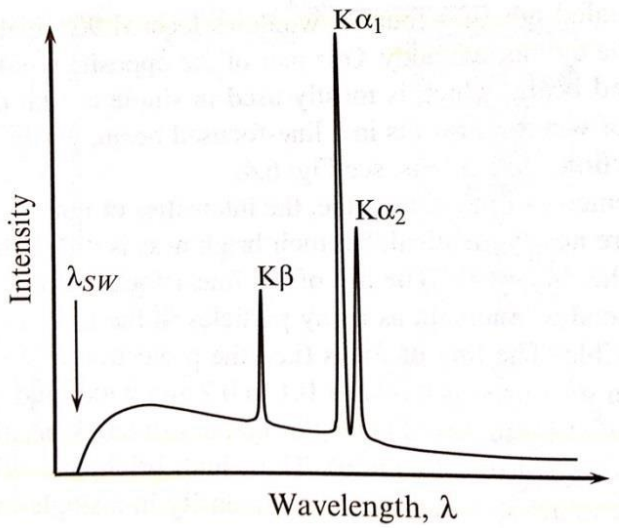

Figure 1.11. Cu X-ray emission spectrum showing the wavelengths associated with $K_{\alpha 1}$, $K_{\alpha 2}$ and K_β transitions.[54]

Compared to standard laboratory diffractometers with a Cu K_α source, higher resolution data with a lower FWHM can be obtained with the use of synchrotron radiation. Synchrotron radiation involves the acceleration of high energy electrons into a storage ring whose path is controlled by a strong magnetic field. As electrons orbit the storage ring, the use of insertion devices and bending magnetics (BM) actually creates a round-cornered polygon shape rather than a perfect ring. Beamlines extend at various tangential points off of the storage ring. The properties and energy of X-rays, as well as the experimental applications, for each beamline will

depend whether they originate from the storage ring at a bending magnet or an insertion device. Some powder XRD data included and analyzed in this dissertation comes from data collection at the 11-BM powder diffraction beamline at the Advanced Photon Source located at Argonne National Laboratory. The radiation wavelength associated with those data collections was approximately 0.4 Å which allows for the collection of higher resolution data when compared to laboratory Cu K_α based XRD experiments.

The use of X-rays to study solid state compounds is based in principle on Bragg diffraction, which is effective for describing the long range average structure in solids. This is because crystalline materials are comprised of repeating units of atoms and it is this periodicity which is necessary for Bragg scattering to occur. When an incident beam of X-rays with a certain wavelength (λ) interacts with the sample, the X-rays are scattered from each element's electrons and, in turn, the collective electron density that is spread out over the lattice of the unit cell. The response is gathered by the detector of the instrument. Because X-rays interact with electrons, atoms with a larger Z (more electrons) will scatter X-rays more effectively than atoms with a lower Z (fewer electrons). Diffraction of the crystalline sample occurs at specific angles, Bragg angles, when the reflected beams radiating from the sample are in phase and interact constructively. If the beams are out of phase, destructive interference and cancellation will occur. This information is summarized by the Bragg's Law equation $2d \sin\theta = \lambda$, where *d* refers to the spacing between parallel planes of the crystal, θ is the angle between the incident beam and the plane, and λ is the wavelength of the incident beam (Figure 1.12). Diffraction will occur when Bragg's law is satisfied. Bragg's law also determines the lowest *d* spacing resolution that can be achieved for a particular radiation source.[54] The lowest *d* spacing that can be probed by a source with wavelength λ is set by λ/2, when $\sin\theta_{max}$ is equal to 1 (θ = 90°). For a Cu source with a

wavelength of about 1.54 Å this limit is about 0.8 Å, whereas for the synchrotron experiments with a wavelength of about 0.4 Å, the lowest *d* spacing that can be theoretically investigated is closer to 0.2 Å.

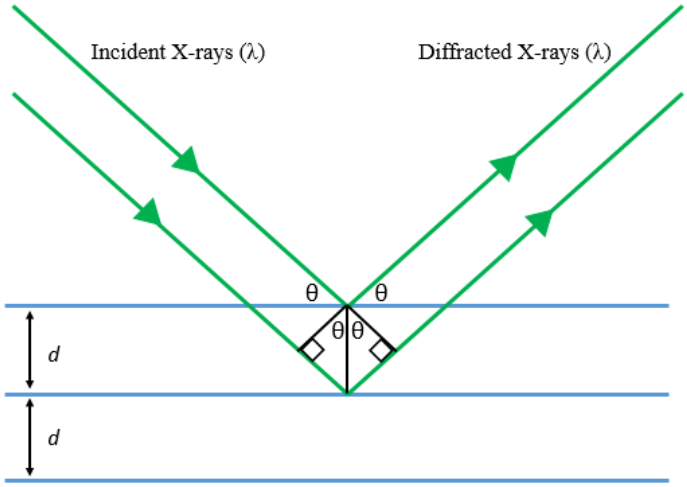

Figure 1.12. Depiction of Bragg's Law.

The XRD pattern, the result of a Bragg diffraction experiment, contains two important pieces of information. The first is the Bragg angles at which peaks appear, and the second significant piece of information is the intensity associated with those peaks. The position of the peaks corresponds to the *d* spacing of the unit cell, via Bragg's law, and therefore provides information about the crystal class and unit cell lattice parameters (a, b, c, α, β, γ) of the measured sample. The *d* spacing of a sample is unique because the unit cell size and shape will create distinct variations in the *d* spacing formula (a function of the lattice parameters and *hkl* Miller indices). As much information as the position of peaks tell about a crystallite sample, the absence of peaks can be just as powerful. In the case of an unknown sample, systematic absences, due to the centering of the unit cell or a symmetry element, can sometimes be used to discern one space group over another. The position of peaks in a powder XRD pattern can

therefore be used to determine the lattice parameters and in some, but not all, experiments the space group of the material being analyzed. Characteristic peak positions are also associated with fingerprint regions for crystallite phases and aid in the buildup of solid state databases for faster indexing of a powder structure.

The intensity of peaks reveals additional information about a solid state crystal structure, as the intensity of a peak is related to the elements that compose a unit cell, as well as the atomic position within the unit cell. This is associated with the fact that X-rays interact with electrons. Heavier elements, with more electrons will have more scattering power than lighter elements. The result is that with X-rays it is more difficult to locate lighter elements in the unit cell especially when heavier atoms are also present. As such, it can be very useful to study the same sample with more than one source of incident radiation, such as neutrons.[54]

1.8.3 Powder neutron diffraction

Powder neutron diffraction is an important analysis technique for studying solid state samples. Whereas with X-rays it can be difficult to analyze a sample that contains both heavy and lighter elements in one unit cell, this is not a problem for neutron experiments depending on sample composition. The scattering factor of an element is not dependent on the number of electrons for a neutron diffraction experiment. Incident neutrons interact with the nuclei of each atom in the unit cell rather than the electron cloud, resulting in scattering lengths that are not dependent on an element's atomic number. Neutron experiments related to the studies discussed in this dissertation were performed at the Spallation Neutron Source at Oak Ridge National Laboratory. Spallation neutrons are produced from negatively charged hydrogen ions that are injected into a linear particle accelerator. At high energies, the charged atoms are passed through

a foil which strips the hydrogen atom of its electrons and leaves the proton to pass on to an accumulator ring. The protons are released from the ring in bunches as a pulse at a rate of 60 Hz and spallation occurs when the protons are allowed to hit a target of liquid mercury. The neutrons are then slowed down and filtered through a series of choppers as they are guided down the beamline. As opposed to an XRD experiment with a fixed wavelength of incident radiation and a changing Bragg angle, spallation neutron diffraction experiments involve the collection of data at varying wavelengths but at a fixed angle. The data are collected as a function of the neutron time-of-flight.[55] For elements relevant to work presented in this dissertation, mainly La (Z = 57), Mo (Z = 42), and O (Z = 8), there are large differences among the X-ray scattering factors. Combining X-ray and neutron diffraction experiments were particularly useful for studying novel phases, as the neutron scattering lengths were comparable for each element, 8.2, 6.7, and 5.6 respectively. This allowed for increased sensitivity, easier detection, and placement of oxygen atoms within the unit cell of novel phases.

1.8.4 Rietveld analysis

The Rietveld method of analysis, developed by Hugo Rietveld[56], is used to extract information about the crystal structure of a sample from X-ray or neutron diffraction data. A Rietveld refinement employs a nonlinear least squares approach, and is typically performed after a Pawley or Le Bail fit has been executed. A Pawley fit involves a full pattern decomposition using a least squares minimization where the peak intensities are treated as free least square parameters during the calculation. The Pawley or Le Bail fit is concerned with peak positions, lattice parameters, and peak profiles (Gaussian, Lorentzian) being modeled correctly. Unlike the Pawley or Le Bail fit, a Rietveld refinement requires a more complete unit cell model, including coordinates of atoms within the cell. A Rietveld refinement allows for the atomic positions,

occupancies, and displacement parameters to vary in order to achieve the closest fit between the calculated and observed powder pattern. Peak intensities will be influenced by varying these parameters. Being a full pattern refinement, Rietveld refinements consider every point during a calculation, and when done properly will give further insight into atom positions, occupancies, atomic displacement parameters, and bond lengths within the unit cell.[54] Rietveld refinements can also be used to generate Fourier difference maps which are useful for evaluating the validity of the crystal structure model or placing atom positions for crystal structure solutions of novel phases. Rietveld refinements, based on both X-ray and neutron diffraction data, were used to model and solve crystal structures of rare earth molybdate compounds with Mo-Mo bonds using the Bruker program TOPAS (V4.2).

1.8.5 Thermogravimetric analysis

Thermogravimetric analysis (TGA) is an experimental technique that can be used to track physical changes in a sample as a function of increasing temperature. In particular, TGA is useful in tracking mass changes associated with reduction, oxidation, or loss of absorbed moisture.[57] A TA Instruments Q5000 IR instrument was utilized for TGA experiments described in this dissertation. To run a TGA experiment two small sample pans (alumina or Pt - 100 μL) are required. One, pristine pan, serves as a reference and the second holds the powder sample, usually on the order of 10-20 mg. During the experiment, the sample pan is housed in a furnace and depending on the desired reaction, different gases can be flowed over the sample. As the temperature changes according to the set program, the precision balance of the instrument tracks the sample mass change. It is important to eliminate the effects of buoyancy when analyzing results, and as such the sample mass should be compared by holding for extended periods of time at the same temperature before and after the highest reaction temperature. For this work, TGA

experiments were used to probe the Mo oxidation state of synthesized samples. Metal-metal bonding is found in reduced molybdates and an important part of sample analysis was determining the Mo oxidation state and comparing it to the oxidation state calculated from the sample formula. To do so, samples containing Mo in a reduced oxidation state were heated under flowing oxygen. The percent mass was compared at a hold temperature of about 150 °C before and after heating to an elevated temperature of about 800 °C, where upon Mo was fully oxidized (Mo^{6+}). The Mo oxidation state in the reduced compound with Mo-Mo bonds was calculated by comparing the change in percent mass at extended isothermal holds of 150 °C before and after complete oxidation of the sample. The products of the TGA experiments were also characterized with X-ray diffraction studies.

1.8.6 Magnetic susceptibility measurements

Magnetic susceptibility is a measure of the magnetic response for a given material in the presence of an applied magnetic field. The degree of magnetization strongly depends on the electron configuration and the presence of unpaired electron spins. When electrons with opposite spins pair in a single orbital the result will be a net cancellation of the magnetic moment from each electron (diamagnetic). A material which is considered diamagnetic will be repulsed by an applied magnetic field. Systems with unpaired electrons or partially filled orbitals are considered paramagnetic and will be attracted to a magnetic field. It is possible in a paramagnetic system that the magnetic moment associated with each unpaired electron will point in different or random directions resulting no net magnetization for the overall sample. However, in the presence of a magnetic field, the magnetic moments for each electron can line up resulting in a positive magnetic response. Additionally, this is can be temperature dependent being that at elevated temperatures random thermal motions will make it challenging to maintain alignment of

the magnetic moment for each electron in the system. Materials with different types of magnetism, including, ferromagnetism, antiferrromagnetism, and ferrimagnetism, play an important role in many high tech applications. The type of magnetism exhibited by a material will depend on the elemental composition of a sample, the crystal structure, and the resulting electronic structure and electron configuration. The crystal structures of compounds with direct *M-M* bonds will have a strong impact on the electronic structure of a material, and therefore will also have a large effect on magnetic susceptibility behavior.[5] This can make it difficult to predict magnetic behavior strictly from sample stoichiometry and electron counting. Due to the relatively low number of studies about *M-M* oxides that include magnetic susceptibility data, often over a limited temperature range (80-300 K), data collected at lower temperatures, will be of benefit to future studies of compounds with *M-M* bonds. Results of studies conducted over a wider temperature range and in varying field strengths will make predictability of magnetic behavior in *M-M* bonded systems more accurate, and will serve to increase the understanding of crystal structure effects on magnetic susceptibility.

A Quantum Design Physical Properties Measurement System (PPMS) was utilized to carry out the majority of magnetic susceptibility studies presented in this dissertation. The specific PPMS utilized is capable of creating a magnetic environment of up to 9 T over a temperature range of 1.9 - 400 K. The low temperature conditions are made possible by the instrument setup which includes a liquid helium dewar encased in a liquid nitrogen- jacketed-dewar. The liquid nitrogen jacket works to insulate the liquid helium, and helps the PPMS consume less helium overall. A vibrating sample magnetometer (VSM) was used to carry out both field-cooled and zero-field-cooled measurements of powder samples in varying magnetic fields over a temperature range of about 2 - 350 K. The VSM utilizes a linear transport motor

(head) to vibrate the sample near a pickup coil which can detect magnetization changes less than 10^{-6} emu at a data collection rate of 1 Hz. The VSM operates on the theory that a changing magnetic flux induces voltage in the pickup coil. This voltage is time-dependent and follows the equation $V_{coil} = \left[\frac{d\varphi}{dz}\right]\left[\frac{dz}{dt}\right] = \left[\frac{d\varphi}{dt}\right]$, where φ is the magnetic flux of the pickup coil, *z* is the vertical position of the sample relative to the coil, and *t* is time.

For use of a VSM, the sample is attached to the bottom of the sample rod which is then inserted into the PPMS, and a sequence of the desired operations is programmed into the computer. The basic VSM setup is shown in Figure 1.13. The sample is attached to the end of the rod that is then inserted into the PPMS. The rod and sample are driven by the VSM head in a sinusoidal manner, which will induce a detectable voltage in the pickup coil. When the sample is moving in a sinusoidal fashion the voltage in the coil is based on the equation, $V_{coil} = 2\pi f C m A \sin(2ft)$, where *f* is the frequency of oscillation, *C* is a coupling constant, *m* is the DC magnetic moment of the sample, and *A* is the amplitude of oscillation.[58]

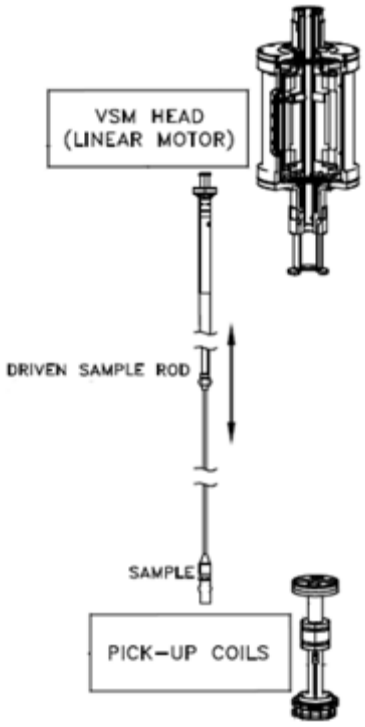

Figure 1.13. Setup for use of a vibrating sample magnetometer to collect magnetic susceptibility data is depicted.[58]

The importance of sample position and displacement are reflected in the sequence file of a VSM measurement. A sequence file usually consists of centering operations for every few degrees in temperature the sample environment changes over the course of the measurement. This gives a greater accuracy to the data because measurements require the sample to oscillate in the center of the coil ± 0.1 mm. The PPMS will determine the center of the sample via a touchdown operation. During a touchdown the motor will lower the sample rod until the bottom of the sample holder makes contact with a puck inside the PPMS. Because the PPMS knows the exact location of the puck, the sample within the holder, and center of the coil, the motor can then raise the sample rod to position the center of sample at the coil's center.[58] VSM measurements can take up to several days to complete depending on the programmed sequence.

Field-cooled and zero-field-cooled sweeps in varying field strengths were conducted as part of this study.

1.8.7 Electrical resistivity measurements

Electrical resistivity is a measure how much a material opposes the flow of electronic current. Given the symbol ρ, electrical resistivity is a function of the concentration and mobility of charge carriers in a system, and is inversely related to electrical conductivity, σ, such that $\rho = 1/\sigma$.[5] In general, transition metal oxides show a range of electrical resistivity properties. Some materials exhibit metallic behavior while others are strong insulators.[1] Some compounds in the class, such as VO_2, can have a temperature dependent metal to insulator behavior transition. For studies included in this dissertation concerning molybdate compounds with Mo-Mo bonds, it was of interest to focus on how this type of bonding influences electrical transport properties and activation energies.

Four-probe resistivity measurements were carried out on bar-shaped cross sections cut from a ½" diameter pressed sintered pellets that were then affixed to a custom sapphire stage with double sided Kapton tape. Four thin Pt wire leads were attached to the sample with a silver epoxy, as shown in the Figure 1.14. Two leads at each end of the of the bar were used to source current and the remaining leads were positioned at two points on top of the bar to measure the drop in voltage across the sample. This experimental set up was housed in a MBE Komponenten GMbH controlled atmosphere rapid thermal annealing chamber. Metal-to-metal pressure contacts were used to connect the copper contacts on the sample stage to a Keithley 2636 source meter. The measurements took place under an Ar atmosphere over the temperature range of 30 to 300 °C. Ohm's law was then used to calculate the sample resistance via the equation R = V/I

where R is the resistance in ohms, I is the current in amperes, and V is the potential difference in volts measured across the sample. The electrical resistivity behavior was calculated from the collected data and studied as a function of temperature. If it is determined that the material is behaving like a typical thermally activated semiconductor with Arrhenius behavior, then the band gap can be extracted by fitting the data using following the relationship $\boldsymbol{\rho = \rho_0 e^{-E_{g/2kT}}}$, where ρ is the electrical resistivity, E_g is the band gap, k is the Boltzmann constant, and T is the temperature.

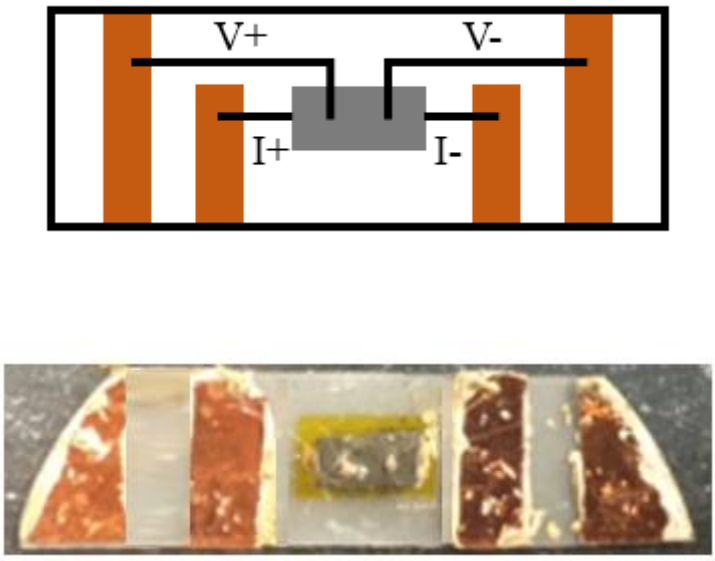

Figure 1.14. The set up for a four-probe electrical resistivity measurements is shown. The bar shaped sample (gray) is mounted on a sapphire stage with double sided Kapton tape. The Cu pads (orange) are connected to the sample via thin Pt (black) wires and silver epoxy. Each Cu pad is connected to an external source meter using metal-to-metal pressure contacts. The actual experimental setup is also displayed.

1.8.8 Diffuse reflectance spectroscopy

Diffuse reflectance describes the reflection of an incident ray of light from a surface such that the reflected light is spread over many angles, as opposed to specular reflection in which the light is reflected back at a single angle (Figure 1.15). Diffuse reflection is not strictly light

reflected from the surface but rather light that has penetrated the surface of a material and scattered internally. Light that is not absorbed by the material eventually makes its way to the surface again and is reflected at a number of different angles. This type of spectroscopy is utilized to study the optical properties of a compound, and is particularly useful for measuring the properties of powder samples. UV-Vis absorption spectroscopy is another method by which to study the optical properties of powders, but involves dispersing the sample in some type of liquid media. This can cause complications interpreting the absorption spectrum if the particle size of the sample too big and precipitates out of solution. Diffuse reflectance spectroscopy has ease of sample preparation, powder pressed into a metal holder with a quartz window, without the complications associated with liquid dilution. Kubelka and Munk developed the theory to describe the way light travels through a light-scattering specimen and relate the total diffuse reflection from a given material to its scattering and absorption properties. This is described by the Kubelka-Munk transform, $f(R) = (1 - R)^2)/2R$ = α/s, where R is the absolute reflectance, α is the absorption coefficient, and s is the scattering coefficient.[59] Powder samples are typically measured against a highly reflective standard, such as $BaSO_4$, for which α is very close to zero. The spectra collected from a diffuse reflectance experiment can in most cases be used to unambiguously assign the band gap energy of a solid state compound and help determine the possible optoelectronic applications. Optical absorbance measurements included as part of this work were done using a two-beam Perkin Elmer Lambda 950 UV/VIS/NIR spectrometer with a 60 mm diameter Spectralon-coated integrating sphere to collect diffuse reflectance data.

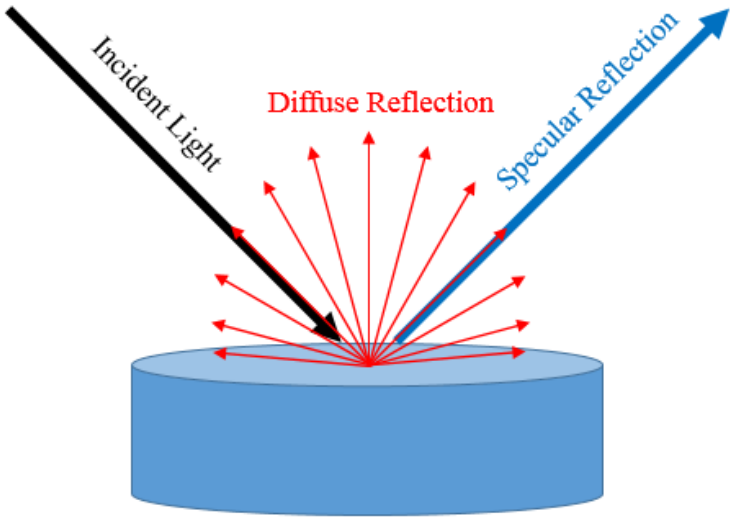

Figure 1.15. Depiction of diffuse and specular reflectance from a surface.

1.8.9 Density functional theory-type calculations – LMTO method

Density functional theory (DFT) is a widely applicable computational modelling method used in physics and chemistry to study the ground state electronic structure in many-body systems. There are many functionals, often described as the ABCs of DFT or a zoo of functionals, which have been developed to deal with the particulars of modeling different chemical systems. These methods vary in their applicability and computational costs. For work included in this dissertation, a linear muffin tin orbital (LMTO) approach was used for lower level DFT-type calculations using the LMTO47c code developed by Andersen and coworkers.[60] The LMTO47c-TB-ASA program uses a LMTO approach within a tight-binding (TB) approximation, and an atomic sphere approximation (ASA) to model voids within the unit cell using empty spheres.[60,61] Results can be used to predict band gaps and molecular orbital splitting, as well as magnetic susceptibility.

LMTO is based on local density approximation (LDA), which is a function dependent upon the local electron density at each point in space within the modeled system. LDA provides a self-consistent solution to the one electron Schrödinger equation. When utilizing an LDA approach to DFT-type calculations, there are two main methods that can be followed, both having their own advantages and disadvantages. The first is the fixed basis set method where the wave-function is determined as an expansion in some set of fixed basis functions and which has the advantage of being computationally simple. For example, linear combinations of atomic orbitals (LCAO) and plane waves are based in this method. The main drawback of this approach is that the basis set may be too large to reasonably complete. Plane waves also do not contain chemical information, so some post processing is necessary. The second method is the partial wave method utilized by augmented plane waves and the Korringa-Kohn-Rostoker (KKR) method. Here, the wave function is expanded in a set of energy and potential dependent partial waves. To do so, a set of equations with a complicated non-linear energy dependence must be solved, making this method computationally heavy. Advantages include the use of a minimal basis set and the fact that partial waves can be applied equally well to every atom of the periodic table. The LMTO approach is the linearized version of KKR, and combines the desirable features of the fixed basis set and partial wave methods.

LMTO calculations start with a muffin tin (MT) sphere approach where the potential energy is presumed to be spherically symmetrical close to the ion core and flat in between atoms. Inside the MT sphere the solution to the Schrodinger equation is modeled with partial waves, while outside the MT sphere the solution is modeled with plane waves. The completed solution is obtained by matching the solution inside and outside the MT spheres. Next an envelope function is applied and this introduces the structure matrix. Screening is then performed to

localize some of the functions that are associated with the solutions calculated outside the MT spheres. Screening can be augmented (MTO) or linear (LMTO). A depiction of this is shown in Figure 1.16. The MTO method is based on energy dependent partial waves and results in a KKR problem. LMTO is an energy independent eigenvalue problem. This is easier to solve than an MTO problem, making LMTO one of the faster computational DFT methods.[61]

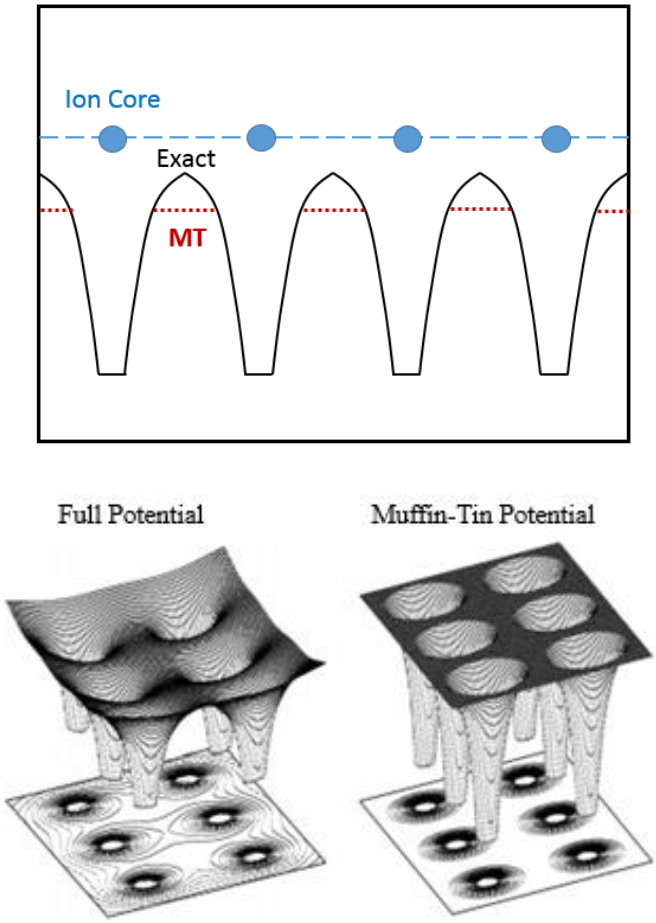

Figure 1.16. (Top) Diagram comparing the actual potential energy landscape to the muffin-tin (MT) modeling approach. (Bottom) 3-dimensional representation of the top figure comparing the full or exact potential energy and the resulting MT landscape.[62]

For the work described here, LMTO calculations were used to model the density of states (DOS) and electronic band structure for several rare earth molybdate systems with direct Mo-Mo

bonds. Fatband type calculations were computed for each of the five Mo *d* orbitals (*d*xy, *d*xz, *d*yz, dx^2-y^2, dz^2) and result in a broadening of the bands where the specified *d* orbital contributes to the electronic band structure. Projection of fatbands on to the total band structure were used to assign Mo *d* orbital contributions to the electronic structure and density of states, and to model the molecular orbital splitting of the ten *d* orbitals within Mo-Mo bound dimers of the modeled systems.

Chapter 2

Strong infrared absorption in $La_4Mo_2O_{11}$ enabled by Mo-Mo bonding within Mo_2O_{10} dimers

2.1. Introduction

While direct metal-metal (*M-M*) bonding has been structurally characterized for a number of oxide compounds, the influence of *M-M* bonding on the physical properties and electronic structure of these oxides is much less well understood.[34,39,44,63-65] Early density functional theory work found that the direct *M-M* bonding can lead to a lifting of the *d* orbital degeneracy, resulting in narrow bands and to sharp features in the electronic density of states that are reminiscent of *f* electron systems.[45,46] The unusual electronic states of compounds with *M-M* bonding have motivated the present efforts to understand and control the electronic states in this broad class of compounds with the goal of unlocking the potential of these materials for technological applications. A deeper understanding of the effect that crystal structure has on electronic structure and physical properties will enable the rational design of functionality for compounds with *M-M* bonding.

Metal-metal bonding occurs most often with 4*d* and 5*d* transition metals, with molybdenum known to form the largest variety of clusters and nuclearities.[66,23] Some ternary molybdenum oxides known to have Mo-Mo bonds are listed in Table 2.1, and are sorted by the number of Mo cations linked through direct *M-M* bonding. In addition to the size of the cluster varying, the geometry and coordination environment for each Mo cation can also vary. For instance $La_2Mo_2O_7$ and $Y_5Mo_2O_{12}$ both have dimeric bonding (Mo_2 cluster type), but $La_2Mo_2O_7$ contains edge sharing Mo_2O_{10} octahedral units connected into a two-dimensional (2D) network

via corner shared oxygen atoms, whereas $Y_5Mo_2O_{12}$ also contains Mo_2O_{10} dimers but these dimers are instead arranged into 1D chains of edge sharing octahedra that alternate between short and long Mo-Mo distances.[26,29] Another example of the geometrical variety is found in structures containing Mo_8 clusters, which are known to form both cis and trans-edge shared octahedral clusters.[66]

Table 2.1. Mo cluster types found in molybdates.

Cluster type		Compound	Mo avg. valence
Mo_2	linear	$Gd_4Mo_{18}O_{32}$ [23]	2.89
Mo_2	linear	$La_2Mo_2O_7$ [26]	4.00
Mo_2	linear	MoO_2 [18]	4.00
Mo_2	linear	$La_5Mo_4O_{16}$ [31]	4.25
Mo_2	linear	$Y_5Mo_2O_{12}$ [29]	4.50
Mo_2	linear	$La_4Mo_2O_{11}$ [28]	5.00
Mo_2	linear	$Mo_{17}O_{47}$ [67]	5.53
Mo_3	trigonal	$La_5Mo_6O_{21}$ [27]	4.50
Mo_4	rhomboidal	$La_4Mo_{18}O_{32}$ [23]	2.89
Mo_6	octahedra	$Y_4Mo_4O_{11}$ [30]	2.50
Mo_6	octahedra	$Gd_4Mo_{18}O_{32}$ [23]	2.89
Mo_6	octahedra	$LaMo_2O_5$ [34]	3.50
Mo_8	bicapped octahedra	$LaMo_8O_{14}$ [22]	3.13
Mo_{10}	bioctahedra	$NdMo_5O_8$ [38]	2.60
Mo_{10}	bioctahedra	$Pr_{16}Mo_{21}O_{56}$ [35]	3.05

In the present work, the known compound $La_4Mo_2O_{11}$ was chosen for more detailed study due to its simplicity. The *M-M* bonding occurs in the form of isolated Mo_2O_{10} octahedral dimers embedded in a non-magnetic host framework with high crystallographic symmetry. Furthermore, the valence of Mo is 5+, leading to a nominal d^1 configuration for each Mo cation. $La_4Mo_2O_{11}$ has previously been synthesized in the form of single crystals with the main focus of prior work being crystal structure determination.[28] In the present study, a deeper characterization of this compound (magnetic, resistivity, and optical measurements complemented by electronic structure calculations using density functional theory) has been carried out in order to obtain more substantial insights into the valence electrons and into the influence of *M-M* bonding on the electronic states of this compound.

2.2. Experimental

2.2.1. Synthesis

La_2O_3 (99.99%, Alpha Aesar) and MoO_3 (99.95%, Alpha Aesar) were used as starting materials. La_2O_3 was dried at 900°C for several hours before weighing to eliminate absorbed moisture. Stoichiometric amounts of the starting oxides were ground together using an agate mortar and pestle, placed in a dense alumina crucible (CoorsTek), and heated in air at 950 °C for about 12 hours to synthesize La_2MoO_6 as a precursor for subsequent reactions. $La_4Mo_2O_{11}$ (~10 g) was subsequently synthesized by heating La_2MoO_6 at 900 °C in a reducing atmosphere of 5% H_2/95% N_2 (60 mL/min) in a Mellen SV Series mullite tube (3.5” diameter) furnace for about 10 days with intermediate grindings. The final product was dark gray in color.

2.2.2. Powder diffraction

Laboratory X-ray diffraction data were collected using a Bruker D8 Advance laboratory diffractometer. A nickel-filtered Cu K_α source was used to measure over a 2θ scan range of 7-140° using a step size of 0.02°, a fixed divergence slit of 0.3°, and Soller slit widths of 2.5°. Time of flight (TOF) neutron powder diffraction measurements were collected at 12 and 300 K (FERNS sample environment) on the POWGEN beamline located at the Spallation Neutron Source (SNS) at Oak Ridge National Laboratory (ORNL) during the 2012-A run cycle. Silicon powder (Gem Dugout, 200 mesh) was incorporated into the sample to act as an internal standard. Samples (~ 4 g) were loaded into 8 mm vanadium cans. Data were collected over a *d*-spacing range of 0.41 – 3.61 Å using a repetition rate of 60 Hz in frame 1.75 with a total proton charge of 3.6 to 7.2 x 10^{12} (1 – 3 hrs collection time). Diffraction data were analyzed using the TOPAS software package (V4.2, Bruker AXS).

2.2.3. Magnetic susceptibility measurements

Magnetic susceptibility measurements were collected with a Quantum Design Physical Property Measurement System (PPMS) using the vibrating sample magnetometer (VSM) attachment. The magnetic response was measured over a temperature range of 2 – 350 K in applied magnetic fields of 1, 10, 50, and 90 kOe with both field cooled (FC) and zero field cooled (ZFC) sweeps.

2.2.4. Diffuse reflectance spectroscopy

Diffuse reflectance data were collected over the range of 200 – 2500 nm using a two-beam Perkin Elmer Lambda 950 spectrometer equipped with a 60 mm diameter Spectralon-coated integrating sphere. Powder samples were packed ~10 mm deep in black sample holders

with a 1.5 mm quartz window (16.6 mm in diameter). Ground $BaSO_4$ powder (Alfa Aesar, 99.99%) was used for both the initial baseline correction and as a 100% reflectance reference. Raw data were transformed using the Kubelka-Munk formula to calculate the relative absorbance from the collected reflectance data by the relationship $\alpha_{KM} = \alpha/s = (1\text{-}R)^2/(2R)$, where α_{KM} is a relative absorbance, α is the absolute absorbance, s is an generally unknown scattering coefficient, and R is the reflectance measured by the spectrometer.

2.2.5. Electrical resistivity measurements

Four-probe resistivity measurements were conducted on bar-shaped samples cut from a sintered 0.5 inch diameter pellet. Four copper pads were attached to a custom sapphire stage, and silver epoxy (EPOTEK, H20E) was used to connect Pt wires (0.0025 mm) between the sample and pads. The Pt wire was connected to the sample at each end of the bar and the remaining two leads were attached at points in the middle of the bar so as to measure the voltage drop across the sample. Metal-to-metal pressure contacts connected the stage to a Keithley 2636 source meter which provided an applied voltage of about 25 V. The sample stage was mounted in a MBE Komponenten GmbH controlled atmosphere rapid thermal annealing chamber that maintained an inert Ar atmosphere. A typical measurement involved allowing the temperature to stabilize at 30 °C, ramping up to 300 °C in 30 minutes, holding for 10 minutes, and ramping down 30 °C at the same programmed rate.

2.2.6. Thermogravimetric analysis

Thermogravimetric analysis (TGA) was carried out using a TA Instruments Q5000 IR instrument. A powder sample (10-20 mg) was heated in a 100 μL alumina pan under flowing O_2 (25 mL/min) to 950 °C using ramp rate of 5 °C/min with a additional holds at 250 °C. In order to

avoid errors due to buoyancy and absorbed moisture, the change in sample mass was calculated by comparing the masses measured at 250 °C before and after heating.

2.2.7. Theoretical calculations

Density functional theory (DFT) studies to calculate the electronic structure and density of states were performed using the LMTO47c code.[60] This program uses a linear muffin tin orbital (LMTO) approach within a tight-binding approximation. Lattice parameters and atomic positions determined by Rietveld refinement were used as input for the calculations, and integration over *k* space was performed with 77 irreducible *k* points on a 6 x 6 x 12 grid. Analysis of the electronic structure with a "fatbands" approach was used to assign the molecular orbital contributions to individual Mo *d* orbitals. To probe the dipole allowed optical transitions, further DFT calculations were performed using the VASP code[68,69] with the projector augmented wave (PAW) method[70] and the local density approximation (LDA).[71,72] The imaginary part of the dielectric function was calculated in the random phase approximation in which the impact of exciton effects (electron–hole interaction) are not included.[73] The VASP code was also used to calculate the band gap using the HSE functional, a screened hybrid functional that often yields more accurate energy gaps in semiconductors and insulators than the simple LDA, though with a higher computational cost.[74,75]

2.3. Results and Discussion

The compound $La_4Mo_2O_{11}$ belongs to the $Nd_4Re_2O_{11}$ structure type, and is illustrated in Figure 2.1.[24,76] Very early studies on $Nd_4Re_2O_{11}$ incorrectly described this phase as β-$Nd_2ReO_{5.25}$.[42] Later, single crystals were used to solve the structure and establish the stoichiometry. $Nd_4Re_2O_{11}$ crystallizes in the space group $P4_2/n$ (#86) and contains isolated edge-

sharing Re_2O_{10} octahedral pairs with Re atoms separated by just 2.42 Å. Single crystals of $La_4Mo_2O_{11}$ were previously found to share the same tetragonal structure as $Nd_4Re_2O_{11}$.[28]

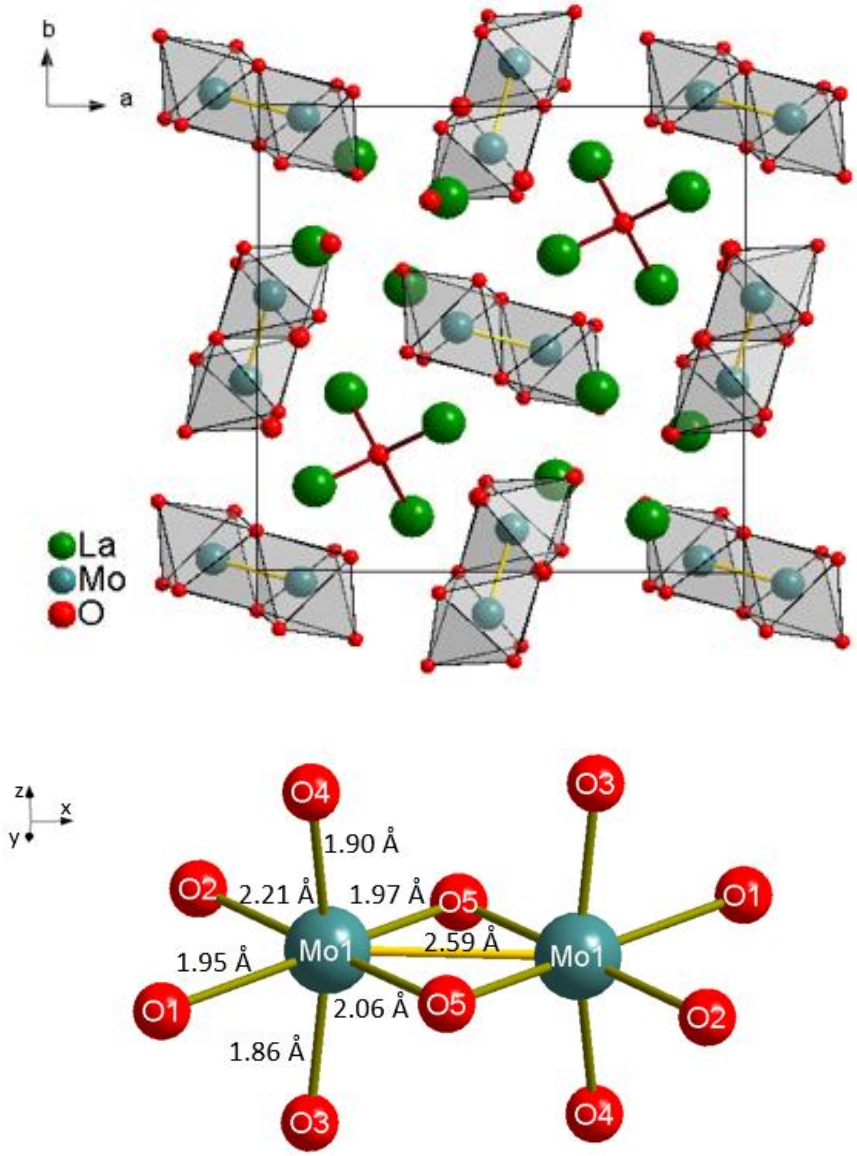

Figure 2.1. Polyhedral representation of the structure of $La_4Mo_2O_{11}$, with the tetragonal unit cell shown in gray. A close-up of a single Mo_2O_{10} dimer with Mo-O and Mo-Mo bond distances labelled is also given.

In the present work, a simple hydrogen reduction synthesis procedure was developed to for the first time produce single phase powders of $La_4Mo_2O_{11}$ using fully oxidized La_2MoO_6 as a precursor. Rietveld refinements utilizing X-ray and time of flight (TOF) neutron powder diffraction data were used to study the crystal structure and phase purity of these powder samples (Figure 2.2). $La_4Mo_2O_{11}$ belongs to the space group $P4_2/n$ (# 86) with a = 12.9901(4) Å and c = 5.6532(2) Å. The full structural data from these refinements is provided in the Supporting Information (Appendix 1: Tables S1 and S2), while selected bond distances are given in Tables 2.2 and S3. The present neutron structure is in very close agreement with the previously reported structure from single crystal X-ray diffraction data (all bond distances agree within ~0.01 Å).

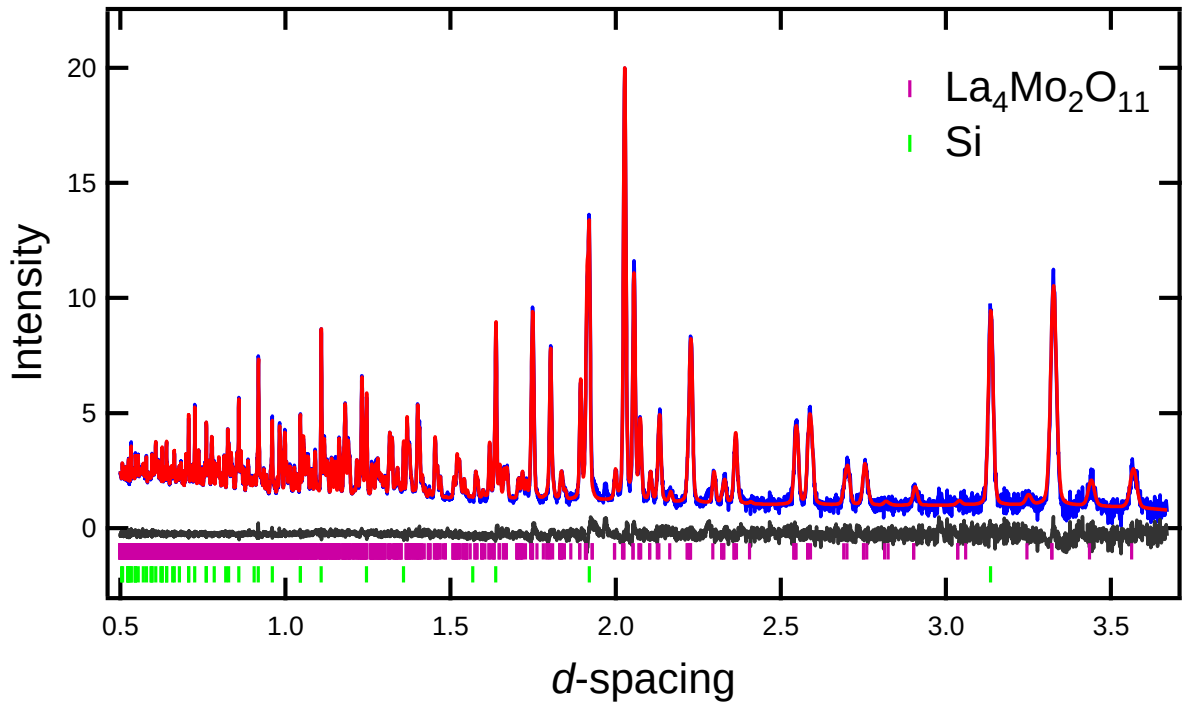

Figure 2.2. Rietveld refinement of $La_4Mo_2O_{11}$, with neutron diffraction data shown in blue, intensities calculated from the structural model in red, and the difference pattern in black. Expected peak positions of the main phase (purple) and Si internal standard (green) are also indicated.

$La_4Mo_2O_{11}$ contains isolated Mo_2O_{10} dimers built from two distorted octahedra that share a common edge. The Mo atoms within the dimer are separated by 2.59 Å, a short distance indicative of a direct Mo-Mo bond. Based on electron counting arguments, this Mo-Mo bond is expected to be a single bond in $La_4Mo_2O_{11}$ while the substantially shorter Re-Re bond in $Nd_4Re_2O_{11}$ is expected to correspond to a double bond. The Mo-O bond distances within the Mo_2O_{10} dimers range from 1.86 to 2.21 Å. This wide range reflects both the displacement of Mo cations from the center of the octahedra and a non-ideal octahedral arrangement of the coordinating oxygen ligands. The displacements result in each Mo atom being pulled slightly closer to the center of the dimer, and also moving away from the middle of the equatorial plane that contains six oxygen ligands. The octahedral Mo_2O_{10} dimers are separated from each other by equal amounts of distorted LaO_8 polyhedra built around La1 sites and OLa_4 tetrahedra in which the ligands are La2 sites.

Table 2.2. Selected bond distances in $La_4Mo_2O_{11}$.

Atom1	Atom2	Bond Length (Å)
Mo1	O3	1.860(3)
	O4	1.900(3)
	O2	1.951(3)
	O5	1.968(3)
	O5	2.056(3)
	O1	2.207(3)
Mo1	Mo1	2.591(4)

While the octahedral coordination of Mo at first glance may look typical, a closer examination shows that the Mo-O bonding in $La_4Mo_2O_{11}$ is weaker than in analogous molybdates without Mo-Mo bonding. The Mo-O bond lengths can be used to calculate the apparent Mo valence using bond valence sum (BVS) methods. In this approach, the Mo site valence (v) is calculated from the sum of the i individual valences (s_i) associated with each of the Mo-O bonds through the relationship $v = \sum_i s_i = \sum_i e^{(R_0 - R_i)/b}$. The only information needed to carry out this site valence calculation is the experimentally determined bond lengths (R_i) and the two empirical parameters R_0 and b which have been tabulated for most cations based on an analysis of many literature compounds with well-defined valences.[77-80] The detailed results of these calculations are provided in Tables S4-S6.

When BVS calculations for the Mo site in $La_4Mo_2O_{11}$ are carried out using the two best sets of literature values of R_0 and b,[79,80] the calculated valence for this site is only about 4.5+, a value which is far (~0.5 valence units, v.u.) below the formal valence of 5+. This is reflected in the fact that the average experimentally determined Mo-O bond length, 1.99 Å, is substantially longer than the ideal Mo-O bond length of about 1.94 Å for an oxide with Mo in the 5+ valence state with a coordination number of 6. These longer bonds are indicative of a decrease in the strength of the Mo-O bonding relative to a typical pentavalent molybdenum oxide.

Although the neutron diffraction data leave little doubt about the 5+ oxidation state of Mo in $La_4Mo_2O_{11}$, further experimental confirmation of this valence was obtained through thermogravimetric analysis (TGA), as shown in Figure 2.3. In order to avoid errors due to buoyancy and absorbed surface moisture, the mass of the sample was compared at 250°C before and after heating at 950°C under flowing oxygen gas. The observed mass change of 1.71% is in close agreement with the expected mass change of 1.73% for $La_4Mo_2O_{11}$ being fully oxidized to

La_2MoO_6. X-ray diffraction studies found no evidence of phases other than La_2MoO_6 in the oxidized product. This Mo oxidation state of 5+ will lead to one valence electron per Mo atom (d^1), although it can also be thought of as resulting in two total valence electrons per dimer.

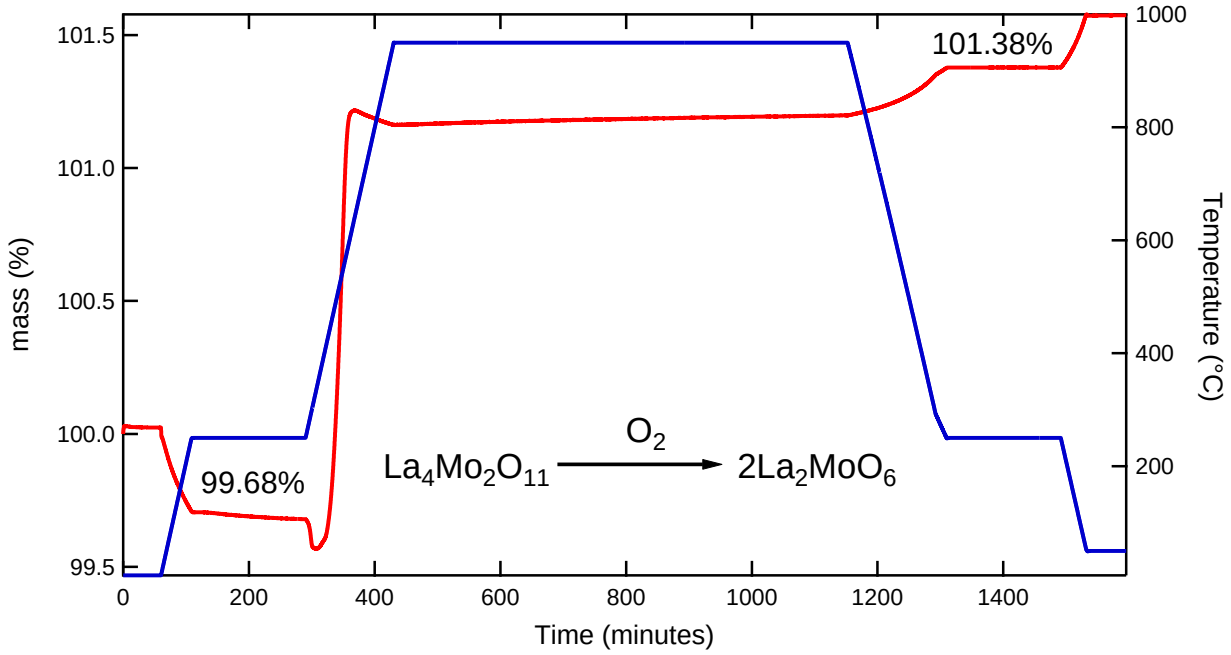

Figure 2.3. TGA data following the changes in mass (red) as $La_4Mo_2O_{11}$ is thermally oxidized to La_2MoO_6 over the temperature profile (blue) of this experiment. The sample % mass at 250°C before and after oxidation is indicated.

The actual electron configuration of $La_4Mo_2O_{11}$ should be reflected in physical property measurements, especially in magnetic susceptibility measurements for which the response scales with the number of unpaired electrons. The measured magnetic susceptibility of $La_4Mo_2O_{11}$ (Figure 2.4) is temperature independent over the studied range and thus $La_4Mo_2O_{11}$ is shown to be diamagnetic and lacking unpaired electrons with an estimated susceptibility of -1.1×10^{-4} emu/mol. The response of $La_4Mo_2O_{11}$ is far weaker than expected for the S = ½ paramagnetic susceptibility normally expected for Mo 5+ (d^1). The direct Mo-Mo bonds thus are providing a mechanism for pairing the single electron contributed from each Mo cation within the dimer.

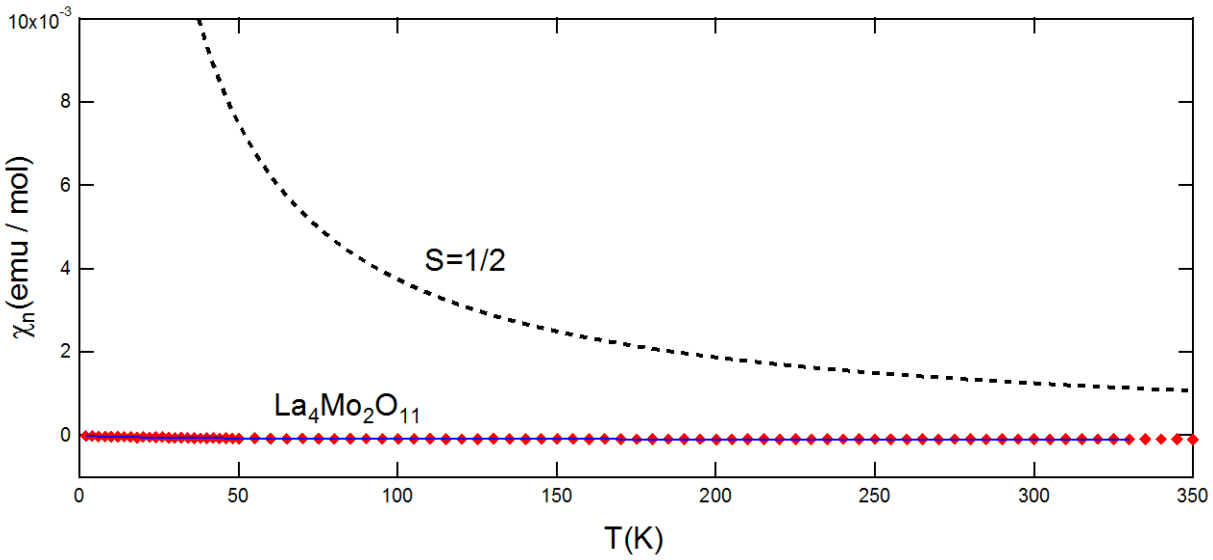

Figure 2.4. Magnetic susceptibility data for $La_4Mo_2O_{11}$ collected during a zero-field cooled measurement with an applied field of 90,000 Oe. The response expected for S = ½ Mo ions (dashed lines) is also shown for comparison.

Further insights into the electronic states of $La_4Mo_2O_{11}$ are obtained from temperature dependent resistivity measurements (Figure 2.5). A very large resistivity of 3.1 x 10^4 Ω·cm is observed at room temperature. As expected for a semiconductor, the resistivity decreases with increasing temperature and is reduced to 3.4 x 10^2 Ω·cm by 300 °C. Arrhenius-type activated behavior is seen in the linearity of plots of log ρ against 1/*T*. Fits to the data find a band gap of 0.49 eV when this compound is assumed to be behaving as a conventional thermally activated semiconductor following the relationship $\rho = \rho_0 e^{-Eg/2kT}$, though it should be noted that the same activated behavior could be due to different activated processes (which would then have activation energies of 0.25 eV). The latter case is judged to be more likely based on DFT calculations which will be discussed later, though in either case the behavior is atypical for an oxide semiconductor, and represents another manner in which *M-M* bonding leads to unusual properties.

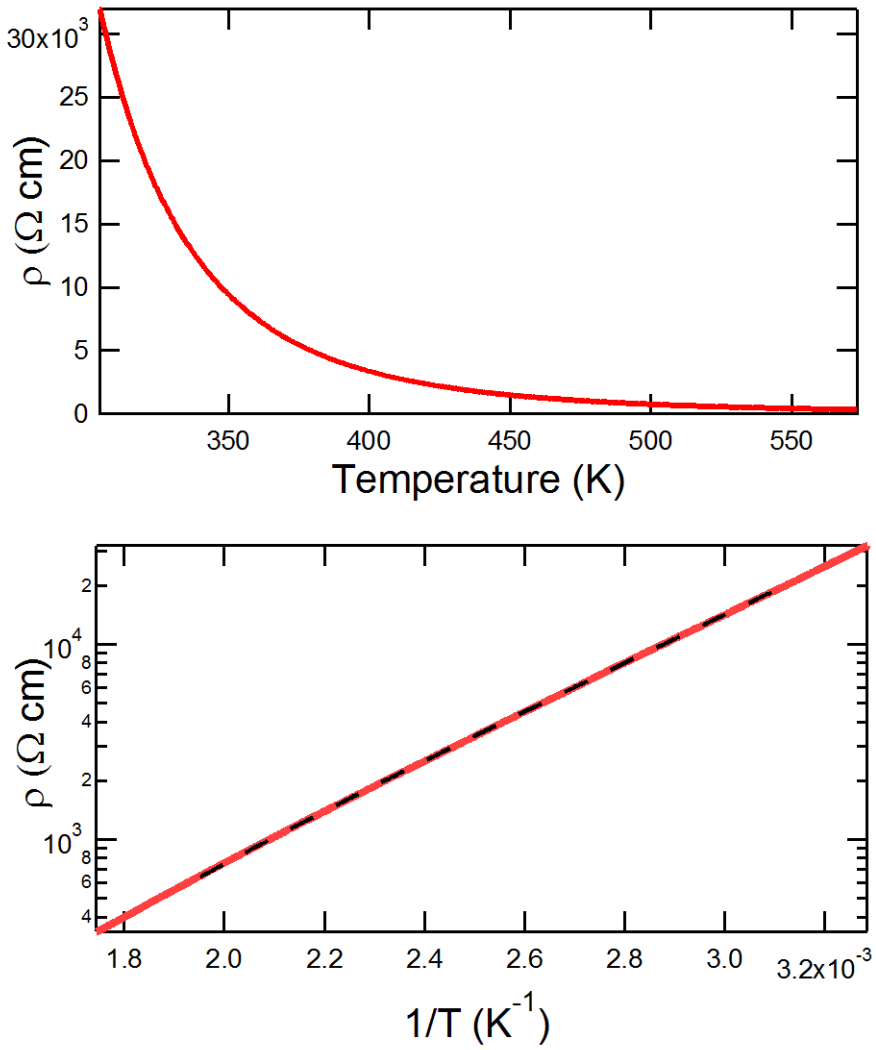

Figure 2.5. The temperature-dependent resistivity of $La_4Mo_2O_{11}$.

Diffuse reflectance measurements were used to study the absorption behavior of $La_4Mo_2O_{11}$ over the energy range of 0.5 to 5 eV (Figure 2.6). From this data, it is clear that the onset of absorption occurs around 0.5 eV. However, this onset is gradual and cannot be clearly attributed to absorption across a band gap (which typically follows a functional form in which α/E scales as $E^{0.5}$ for an indirect optical transition or as E^2 for a direct optical transition) rather than to other types of optically active transitions (such as those for internal *d-d* transitions)

whose energies are unrelated to the band gap energy. The absorption profile of $La_4Mo_2O_{11}$ is rather complex, but it is clear that there is substantial absorption at energies below 1 eV not related to free carriers – something that is rarely seen for oxide semiconductors with fully paired electrons. Oxide materials are usually transparent in this energy range due to the lack of available excitations. There are many different transitions in the optical response of $La_4Mo_2O_{11}$, suggesting that the underlying electronic structure of this material is quite complex.

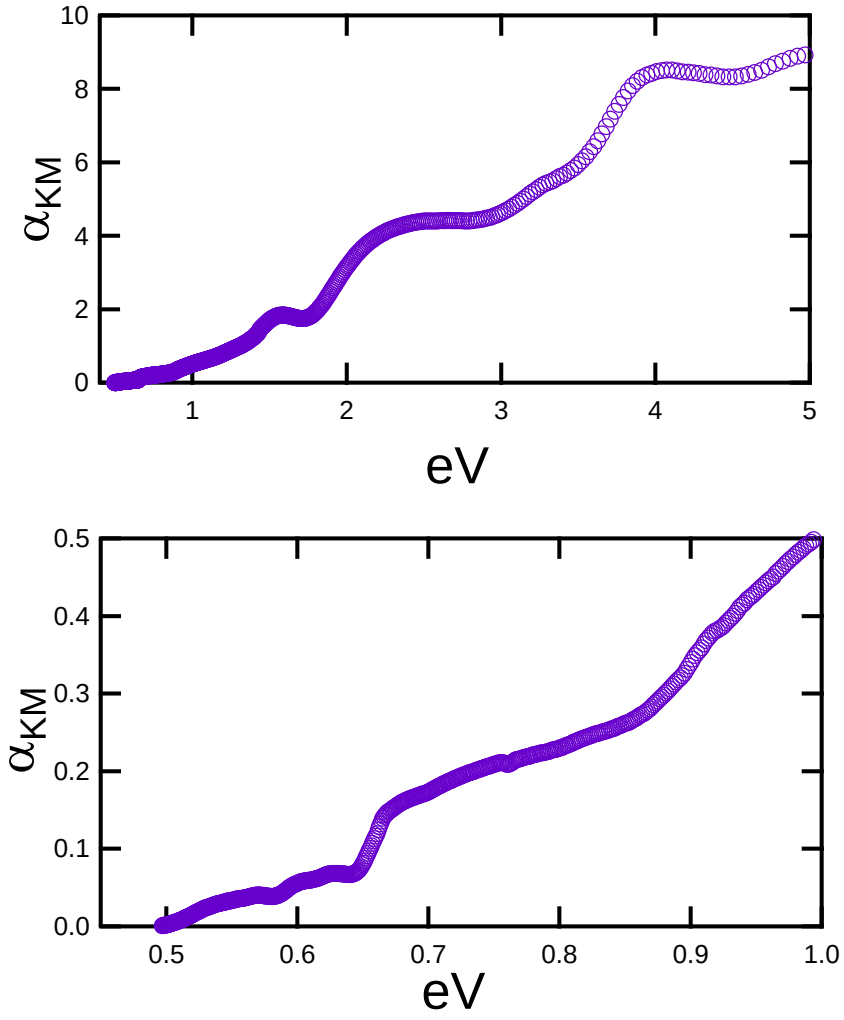

Figure 2.6. Relative absorbance spectra of $La_4Mo_2O_{11}$ obtained from a Kubelka-Munk transform of diffuse reflectance data shown in full (top) and with an expanded view of low energies (bottom).

The electronic structure of $La_4Mo_2O_{11}$ was directly investigated through density functional theory (DFT) calculations, which were initially carried out using the LMTO47c code in order to investigate the orbital contributions. From the resulting density of states (DOS) (Figures 2.7) and band structure (Figure 2.8), it is clear that the Mo *d* orbital splitting is far different from the familiar e_g and t_{2g} splitting of isolated MoO_6 octahedra. In DOS plots, six sharp peaks associated with the Mo *d* orbitals can be distinguished over the span of -0.5 to 2.5 eV relative to the top of the valence band. An analysis of the integrated DOS indicates that each sharp peak in the DOS has room for only 1 electron per Mo, or alternatively 2 electrons per dimer. The latter description is the most sensible one, and indicates that the degeneracy of the octahedral states expected in the single-ion picture has been lifted due to the presence of Mo-Mo bonding. This is the origin of the small calculated band gap of 0.98 eV, with *d* orbital derived states comprising both the valence and conduction band.

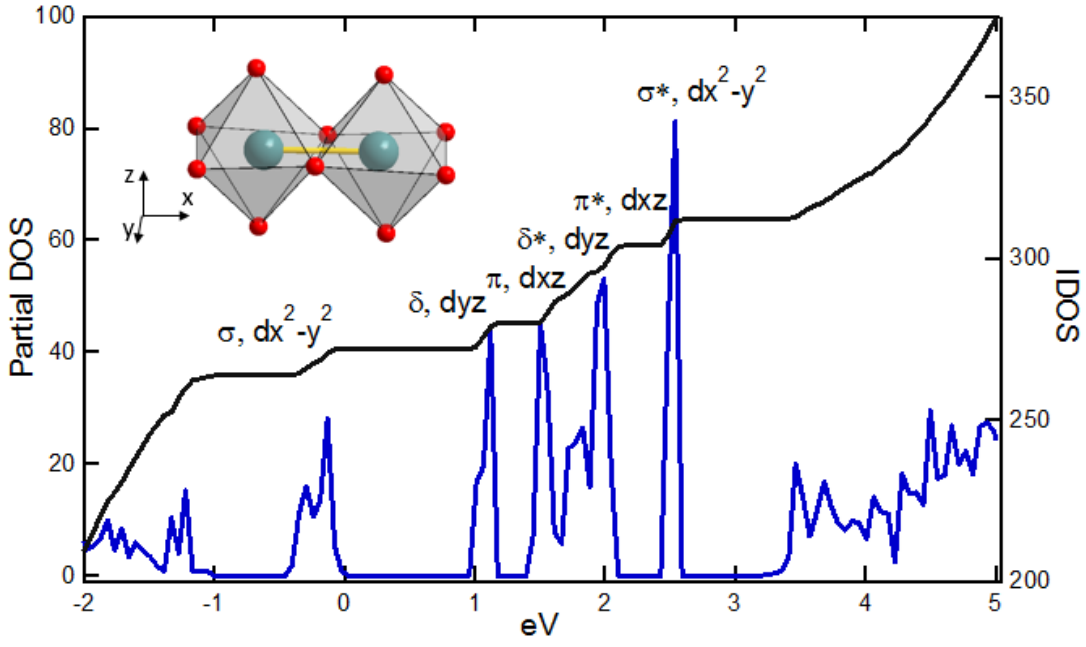

Figure 2.7. Partial DOS representing the contributions of Mo *d* orbitals. Labels are assigned based on Figures 2.8 and S2. The energy zero is set to the top of the highest occupied band.

A better understanding of the nature of the bonding in $La_4Mo_2O_{11}$ can be achieved by closely examining the orbital character of the *d* electron states in this compound. The five individual "fatbands" calculations used to aid in this assignment are provided in Figure S1. In this analysis, bands are projected on the five *d* orbitals associated with each octahedral Mo cation (*d*xy, *d*yz, *d*xz, dx^2-y^2, and dz^2), though non-standard coordinate axes were used to describe these orbitals (as in the shown in the inset to Figure 2.7). Having identified the relationship between specific bands and supporting *d* orbitals, a complete assignment of the states has been made, as is illustrated in Figure 2.8. For the energy bands near the gap region (-1 eV to +3 eV in Figure 2.8), these states manifest in the solid as distinct bands. For higher energies (above 3 eV), substantial mixing with continuum states broadens out the bands, although the character of the contributions from the Mo *d* orbitals in that region can still be identified (Figure S1). It can be seen that each of these five primary *d* orbitals is split into bonding and anti-bonding (*) pairs, resulting in ten non-degenerate orbitals which can be labelled using the conventions of molecular orbital theory as having σ, π, and δ symmetry. The σ / σ * splitting is largest and the δ / δ * splitting smallest, in accord with the maximum degree of overlap possible for orbitals of these types.

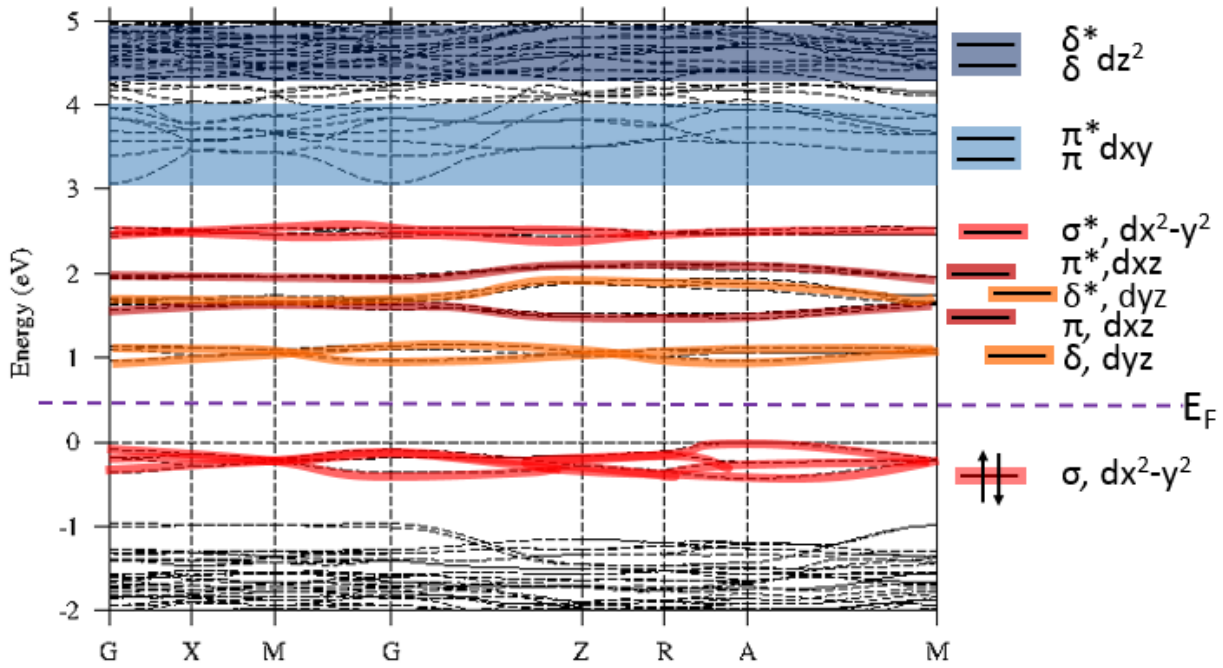

Figure 2.8. Electronic band structure of $La_4Mo_2O_{11}$, with the bands associated with Mo *d* orbitals colored to indicate there origin, as labelled in the legend. Energies are relative to the top of the highest occupied band. States associated with 10 non-degenerate *d* orbitals can be resolved.

The relationship of the ten non-degenerate molecular orbital states to the t_{2g} and e_g states expected for isolated MoO_6 octahedra is schematically illustrated in Figure 2.9. It can be seen that the simple procedure of starting with the single-ion octahedral levels and then splitting them to a degree proportional to the amount of orbital overlap between bonded Mo cations (~2 eV for σ, ~1 eV for π, ~0.5 eV for δ) results in a reasonable predictions for the complex electronic states associated with the Mo_2O_{10} dimers of $La_4Mo_2O_{11}$. A further refinement of the predictions can be achieved by noting that the MoO_6 octahedra in this compound are compressed in the *z*-axis direction, causing the ideal octahedral symmetry to be broken even in the single-ion picture. This will result in a partial lifting of the degeneracy of the octahedral e_g ($dxy < dz^2$) and t_{2g} (dx^2-$y^2 < dyz$, dxz) states. The repulsive interactions of Mo *d* electrons with electrons in the neighboring MoO_6 octahedron in the dimer provides an additional symmetry breaking along the

axis of the Mo-Mo bond (*x*-axis), and this raises the energy of the *d*xz states relative to the *d*yz states. Thus all of the primary features of the complex electronic structure of $La_4Mo_2O_{11}$ can be deduced from the experimentally determined local Mo_2O_{10} coordination environment by applying simple chemical bonding principles.

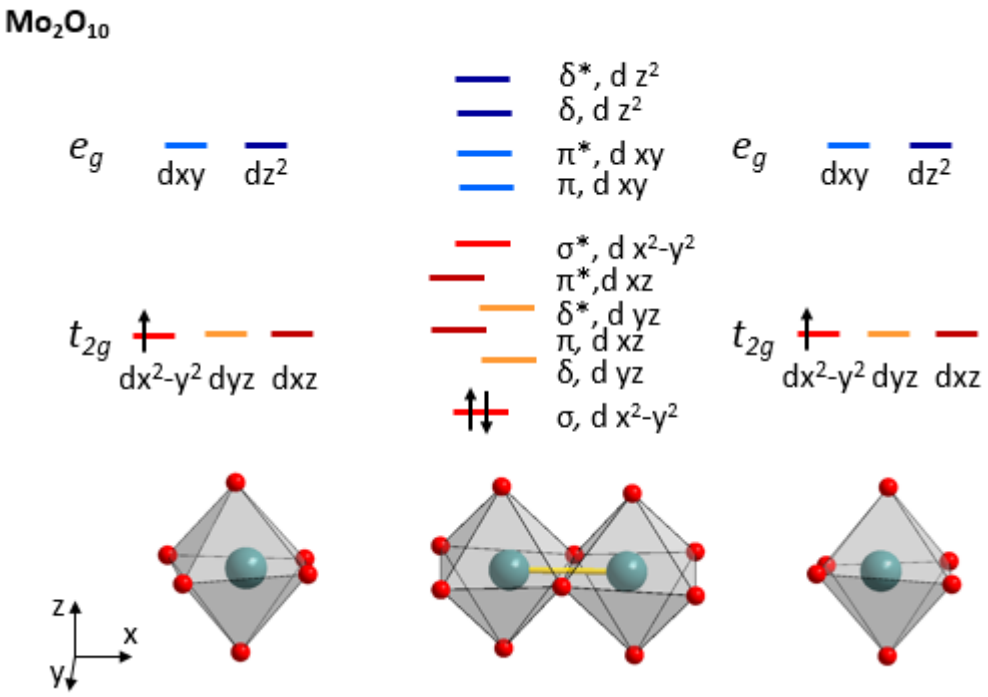

Figure 2.9. Schematic illustration of the relationship between the *d* orbital states in a single-ion MoO_6 octahedron (left, right) and those assigned for the Mo_2O_{10} dimers based on the results of DFT calculations and a simple MO analysis.

The absorption spectrum of $La_4Mo_2O_{11}$ was calculated using projector augmented wave methods in VASP, and is shown in Figure 2.10. The onset of absorption due to dipole allowed transitions is slightly above the minimum direct gap energy, which is about 1 eV in the LDA. The lowest lying *d*-*d* transitions (between 1 and 2.5 eV) all only exhibit weak dipoles. The first strongly dipole allowed transitions between 2.5 eV and 3.25 eV are also *d*-*d* transitions, but are associated with a symmetry-allowed σ-σ* transition involving states that are attributable to dx^2-

y^2 orbitals. Although this *d*-*d* transition would be forbidden for an isolated octahedron, it can be seen that the symmetry of each individual octahedron along the *x*-axis direction of the Mo-Mo bond is broken within the Mo_2O_{10} dimers of $La_4Mo_2O_{11}$, enabling this particular *d*-*d* transition to be symmetry-allowed.

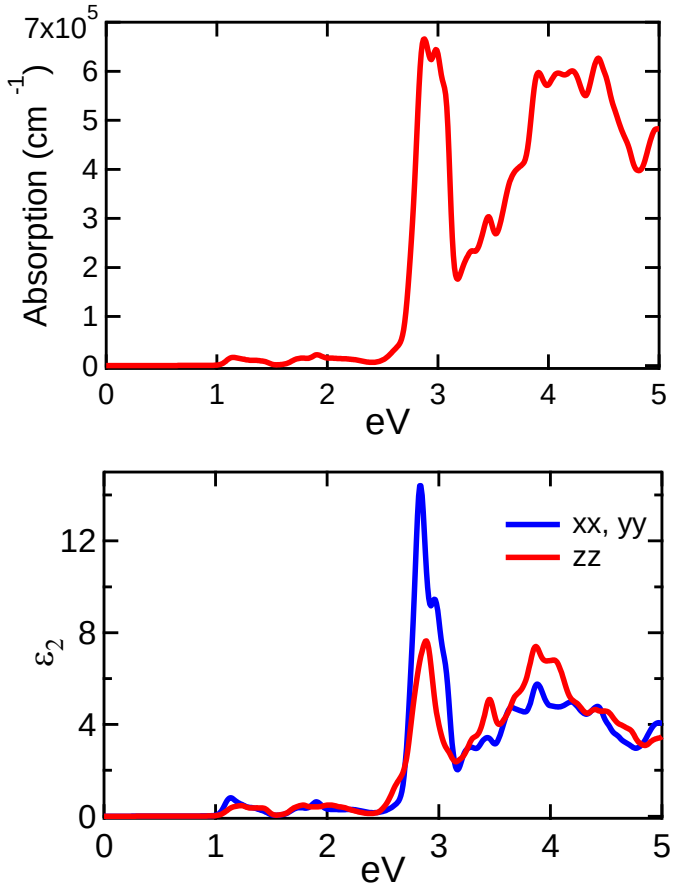

Figure 2.10. Calculated absorption spectrum (top) and imaginary dielectric constant (bottom) for $La_4Mo_2O_{11}$ in the random phase approximation with LDA-based energy bands. The strong transition at 2.5 – 3.25 is associated with σ-σ* excitations which are oriented along the axis of the Mo-Mo bond. Since the dimers are tilted out of the *ab*-plane of the tetragonal cell, this oscillator will be seen in probes of both the in-plane (*xx*, *yy*) and out-of-plane (*zz*) optical response.

All semiconductor absorption spectra calculated using density functional theory within both the local density (LDA) and the random phase approximation (RPA) are expected to suffer

from three limitations. First, the calculated energy gap in the LDA is substantially underestimated for non-metallic phases. To explore the magnitude of this effect, additional DFT calculations were carried out using the screened hybrid HSE functional which has been previously shown to more closely reproduce experimental band gaps in simpler semiconductor systems whose optical properties have been well characterized.[74,75] The 2.2 eV HSE band gap for $La_4Mo_2O_{11}$ is substantially increased relative to the band gap of 0.9 eV previously calculated within the LDA. The computational cost of this method constrained the present $La_4Mo_2O_{11}$ calculation to utilize a relatively sparse sampling of the Brillouin zone and the full HSE-calculated optical spectrum was therefore not plotted in comparison to the LDA result (Figure 2.10), though it should be noted that the strong dipole-allowed σ-σ* transition also increased in energy by about 1 eV (from 3 eV to 4 eV), a similar magnitude of change as for the band gap. A second limitation of the LDA/RPA approach is that excitonic effects are neglected in these calculations.[73] Based on some recently reported DFT results which included exciton effects (through solution of the Bethe-Salpeter equation) for some representative 3*d* transition metal oxides,[81] we would expect a partial shift of oscillator strength to the lower energy side of each absorption band. However, the calculated onset energy for optical transitions is not expected to be strongly influenced by this limitation.

The third limitation of the LDA/RPA approach used in the present $La_4Mo_2O_{11}$ calculations is that only electric-dipole derived optical transitions are included in the calculated optical spectrum, and this limitation presents the greatest challenges in relating calculated and observed optical spectra. DFT calculations therefore neglect transitions associated with electric quadrupoles, magnetic dipoles and all other processes not associated with electric dipoles. Although these alternative transitions are typically weaker than those associated with electric

dipoles, they can lead to observable features in the experimentally measured optical spectrum at energies below the minimum optical gap calculated using LDA/RPA methods. A well-known example of experimentally observable optical transitions not captured even in state-of-the art DFT calculations for 3*d* transition metal oxides are the optical transitions of NiO that occur in the range of 1 – 3.5 eV, substantially below the accepted band gap and photoconductivity onset of NiO (~4 eV). These lower energy optical excitations are due to internal (intratomic) *d-d* excitations that are not dipole allowed[82] and are clearly not associated with transitions between energy bands, as can be seen in the persistence and lack of a substantial energy shift of the peaks associated with these *d-d* transitions when the Ni ions are diluted to a minority component through the formation of a $Ni_xMg_{1-x}O$ solid solution.[83] These types of *d-d* transitions are captured in neither the random phase approximation used here nor in the state-of-the-art Bethe-Salpeter approach for DFT calculations of optical responses (as has been recently discussed by Rodl and coworkers[81]), though classic ligand-field models can provide good insights into the energies of these transitions for transitional metals with octahedral (or other common symmetrical polyhedral) ligand environments.[5,84-86]

In addition to the three specific limitations of DFT methods in calculating optical responses discussed above, it should also be recognized that DFT calculations are commonly carried out using the static, zero-Kelvin structure of materials in which the vibrationally-driven displacement of atoms away from their average positions is ignored. At room temperature, the thermal displacement of atoms away from their average positions is expected to be on the order of 0.1 Å at any snapshot in time, based on a survey of experimentally refined displacement parameters obtained through conventional crystallographic techniques (powder and single crystal diffraction experiments). These transient dynamic displacements are comparable in magnitude

to the static distortion of the Mo-O bond lengths in $La_4Mo_2O_{11}$ (Table 2.2) away from their average value of 2.0 Å that would be expected for an ideal MoO_6 environment with perfect octahedral symmetry. Neglecting these dynamic distortions will therefore be expected to substantially degrade the ability of static DFT calculations to accurately model the oscillator strength of optical transitions which are symmetry-forbidden, as the intensity of such transitions will be very sensitive to the magnitude of atomic displacements away from their ideal high-symmetry positions. When viewed from the perspective of a periodic solid, phonon-assisted transitions can open up new absorption channels that can be significant in the spectral range where the band gap is indirect or when the direct transitions have zero or weak dipole matrix elements. When DFT investigations were previously compared to experiment,[81] it was found that thermal broadening can also significantly spread out narrow features, thus reducing the apparent peak heights as a result of this energy broadening.

The comparison of the LDA-calculated optical response (Figure 2.10) with the experimentally measured room-temperature diffuse data (Figure 2.6) should therefore be carried out with these considerations in mind. As expected, some clear differences are apparent. First, the LDA-calculated optical response has a strong peak at 3 eV associated with the σ-σ* transition that has no obvious analogue in the experimental spectrum. This suggests that DFT calculations are predicting this feature to be too narrow, perhaps due to the neglect of thermal vibrations and the finite temperature vibronic coupling associated with them.[81] The ~1 eV difference between the HSE and LDA band gap suggests that this transition might be expected to occur at an energy of ~4 eV in the experimental pattern, and there is indeed a resolvable peak in the experimental spectrum at this energy.

There are also clear differences between the onset of absorption in the experimental and DFT-calculated spectra. Within the LDA, the optical response is predicted to begin near the intrinsic band gap of 0.9 eV calculated using this method. However, the larger band gap of ~2.2 eV calculated using HSE methods is more likely representative of the true band gap of $La_4Mo_2O_{11}$, and it appears that the experimentally measured absorption spectrum of $La_4Mo_2O_{11}$ is dominated by optical transitions not associated with the band gap over the approximate energy range of about 0.5 – 2.0 eV, despite the substantial measured intensity of absorption at these energies. One likely possibility is that this absorption results from internal *d-d* transitions. Another viable possibility is that the low energy onset of absorption is associated with a native defect in the crystalline material, and may thus represent the energy scale of exciting a carrier out of a trap or of activating polaronic hopping. If it is the latter, it is likely that the onset energy of absorption is closely linked to the activation energy of carrier transport.

A third significant difference between the calculated and observed optical response is that the calculated optical response is weak at energies as much as 2 eV above the band gap, followed by a rapid increase in the strength of absorption at higher photon energies as the allowed σ-σ* transition and the slightly higher energy allowed *p-d* transitions are accessed. This suggests that in experimental measurements, the intrinsic absorption associated with the band structure of $La_4Mo_2O_{11}$ should be weak until an energy of 3 or 4 eV, depending on whether the true band gap for this compound is closer to the LDA value (0.9 eV) or the HSE value (~2.2 eV). In contrast, the experimental data show a nearly linear increase in absorption coefficient from 0.5 to 5.0 eV. One possibility for this difference is that the LDA-calculated response is severely underestimating the strength of the forbidden *d-d* transitions that occur at energies just above the band gap due to the neglect of thermal vibrations. This hypothesis could be tested either

experimentally (carry out variable-temperature measurements) or theoretically (investigate structural models beyond that of the 0 K structure). Another possibility is that the internal *d-d* transitions which cannot be described by band theory are strong relative to the optical transitions associated with the $La_4Mo_2O_{11}$ band structure. This hypothesis is more challenging to ascertain, but is perhaps best approached through optical measurements on single crystal samples which are interpreted using ligand field methodologies that capture these internal *d-d* transitions. The linked Mo_2O_{10} dimers are clearly more complex than the isolated polyhedra more commonly treated in ligand field studies, and a study of this type will therefore be non-trivial.

The electronic structure of $La_4Mo_2O_{11}$ is clearly quite complex, and the interpretation of both experimental and theoretical data is correspondingly found to be very challenging. While it is clear that this compound has a very substantial absorption in the infrared (< 1.5 eV) and visible (< 3.2 eV) portions of the electromagnetic spectrum, it is not yet clear which of the many features observed in experimental optical spectrum represent responses inherent to (rather than external to) the band structure of this compound, and further work will be required to resolve this. While the lowest gap energies measured in both the optical spectrum and the electronic transport measurements generically have the potential to reflect the intrinsic band gap of $La_4Mo_2O_{11}$, these energies in both cases are substantially lower than the calculated band gaps (2.2 eV by HSE, 0.9 eV by LDA). As such, it is quite likely that neither of these measurements provide direct insights into the band gap of $La_4Mo_2O_{11}$. It is deemed likely that the electronic transport in $La_4Mo_2O_{11}$ is polaronic, and as such, the transport-derived activation energy reflects the energy scale of polarons rather than the band gap energy. Similarly, the many infrared energy optical features (0.5 – 1.5 eV) in $La_4Mo_2O_{11}$ are most likely expected to be associated

with internal *d*-*d* configurational changes, though other contributors (polaronic excitations or other defects states) cannot be ruled out as additional contributors.

2.4. Conclusion

It is demonstrated that direct Mo-Mo bonding within the isolated Mo_2O_{10} octahedral dimers of $La_4Mo_2O_{11}$ is responsible for completely lifting the *d* orbital degeneracy of these units. This produces a very complex electronic structure as well as unusual physical properties (diamagnetism for d^1 Mo^{5+}, a small Arrhenius gap in electronic transport measurements, and strong absorption in the infrared and visible portions of the electromagnetic spectrum). Despite its complexity, it is demonstrated that most features of the electronic structure can be rationalized through simple chemical bonding rules. However, further work is required to conclusively determine the size of the intrinsic band gap of this material (estimated as 0.9 eV in LDA calculations and 2.2 eV in HSE calculations), and to assign the precise origin of the optical features observed at infrared and visible energies.

Chapter 3

Charge disproportionation in tetragonal La_2MoO_5, a small band gap semiconductor influenced by direct Mo-Mo bonding

3.1. Introduction

Transition metal oxides comprise a multifunctional class of materials whose many useful properties are generally derived from the behavior of their *d* electrons, which can strongly hybridize with oxygen 2*p* states.[1] While ligand field theory generally provides a good framework for understanding the electronic states of transition metal oxides,[6] we are broadly interested in a special subset of transitional metal oxide compounds which contain direct metal-metal (*M*–*M*) bonds that have the potential to introduce radical changes in the electronic structure of oxides that may lead to enhanced functionality. Direct *M*–*M* bonds are most commonly found in early 4*d* and 5*d* transition metals (with M = Mo, Re or Ru) that have a small number of electrons in *d* orbitals (d^1 – d^4). Some examples include the compounds $LnMo_8O_{14}$ (*Ln* = La, Ce, Pr, Nd, Sm)[66-22], $LnMo_5O_8$ (*Ln* = La, Ce, Pr, Nd, Sm, Eu, Gd)[38], $Nd_4Re_2O_{11}$[24], $Ln_4Re_6O_{19}$ (*Ln* = La, Pr, Nd)[87], and $La_4Ru_6O_{19}$[45-46]. The clearest signature of direct *M*–*M* bonds is the short distances between the metal participating in the bonding, as these bond lengths are far shorter than the *M*–*M* distances that are typically seen for the same compounds in the absence of *M*–*M* bonding (> 3 Å). The shortest *M*–*M* bond distance reported is a Cr-Cr bond, 1.8028(9) Å, found in a molecular dinuclear chromium diazadiene complex.[88] Other short bond lengths, typically 2.0-2.2 Å, are observed in canonical molecular inorganic compounds with quadruple and quintuple bonds.[89-90] While *M*–*M* bonding in molecular compounds has been extensively studied, only handful of solid state oxide compounds with *M*–*M* bonds have been discovered, most of which include the

early transition metals Mo or Re. An overview of the electron configuration and experimentally determined bond lengths for solid state oxides of Mo and Re with dimeric *M-M* bonding is provided in Table 3.1. These compounds represent an intriguing interface between the science of molecular compounds and that of extended solids.

Table 3.1. Examples of dimeric *M-M* (M = Mo, Re) bonding.

Compound	Valence	d^n	*M-M* (Å)	Dimer
$La_4Mo_2O_{11}$ [28]	5+	d^1	2.5905(5)	Mo_2O_{10}
$Y_5Mo_2O_{12}$ [29]	4.5+	$d^{1.5}$	2.496(1)	Mo_2O_{10}
$La_5Mo_4O_{16}$ [31]	4.25+	$d^{1.75}$	2.406(1)	Mo_2O_{10}
$La_2Mo_2O_7$ [26]	4+	d^2	2.478(4)	Mo_2O_{10}
$La_3Re_2O_{10}$ [91]	5.5+	$d^{1.5}$	2.484(1)	Re_2O_{10}
$Nd_4Re_2O_{11}$ [24]	5+	d^2	2.421(1)	Re_2O_{10}
$La_6Re_4O_{18}$ [92]	5+	d^2	2.456(5)	Re_2O_{10}
$Ho_5Re_2O_{12}$ [39]	4.5+	$d^{2.5}$	2.436(2)	Re_2O_{10}
$La_4Re_6O_{19}$ [93]	4.33+	$d^{2.67}$	2.422(7)	Re_2O_{10}
Sm_2ReO_5 [94]	4+	d^3	2.251(1)	Re_2O_8
$La_6Re_4O_{18}$ [92]	4+	d^3	2.235(6)	Re_2O_8
La_2ReO_5 [63]	4+	d^3	2.259(1)	Re_2O_8

The physical properties of compounds with direct *M–M* bonding can strongly differ from those of conventional oxides with similar electron counts. For example, *M–M* bonds can suppress paramagnetism in non-metallic compounds. The compound Ln_2ReO_5 (*Ln* = Sm, Eu Gd) contains Re_2O_8 dimers, with Re-Re bonding within the dimer.[95] The average Re valence is 4+, resulting in a d^3 configuration that is generally expected to lead to unpaired electrons and paramagnetism. However, this non-metallic compound is observed to be diamagnetic. Unusual properties for the metallic members of the general class of compounds with *M–M* bonding have also been reported. The compound $La_4Ru_6O_{19}$ was the first oxide compound reported to exhibit non-Fermi-liquid behavior, an effect ascribed in part to the exceptionally high density of states (very reminiscent of *f* electrons) that results from the direct *M–M* bonding.[45,46] While there have been a number of reports of intriguing properties for compounds with *M–M* bonds[30,35,91], a general framework for comprehensively understanding the influence of these bonds on the overall electronic structure remains elusive.

The present work is concerned with the compound La_2MoO_5, which has an average valence of Mo^{4+}. Another lanthanum molybdate with a 2:1 cation ratio is La_2MoO_6, which contains fully oxidized Mo^{6+} cations, and can be readily synthesized in air.[96] This compound has isolated MoO_4 tetrahedra and crystallizes in the tetragonal space group $I4_1/acd$ with a = 5.80 Å and c = 32.04 Å. There have been a few prior reports of reduced compounds with the general composition of Ln_2MO_5 (*Ln* = La, Y, Ce-Lu; M = Mo, Re), though most of these studies were carried out decades ago.[42,97,98,40,41] The original report of Ln_2MO_5 phases with the α-Nd_2ReO_5 structure type suggested a body-centered tetragonal cell with a = 8.81 Å and c = 5.89 Å for Nd_2ReO_5. The atomic arrangement of this structure type remained unknown until the growth of crystals allowed the structure of La_2ReO_5 to be solved using single crystal X-ray diffraction

techniques.[63,76] In prior work, this lanthanum compound was referred to as $La_4[Re_2]O_{10}$ to emphasize the Re_2O_8 square planar dimers in this structure. Later, other types of molybdate Ln_2MoO_5 compounds were also discovered.[41,40] These compounds were either reported in a cubic fluorite-type unit cell ($a \sim 5.7$ Å)[99], or in a more complex monoclinic unit cell which has curiously been ascribed to both Ln_2MoO_5 and $Ln_5Mo_2O_{12}$ compositions.[29,100] A recent investigation of the fluorite-related structure type by powder neutron diffraction and thermogravimetric analysis found a variable stoichiometry ranging from $Ln_2MoO_{4.8}$ to $Ln_2MoO_{5.2}$, with good oxygen anion conductivity at elevated temperatures resulting from the abundant oxygen vacancies relative to the ideal fluorite composition of Ln_2MoO_6.

In the present work, a novel polymorph of La_2MoO_5 is reported and its structure has been solved from powder diffraction data. This compound is demonstrated to adopt a new structure type which is crystallographically related to that of tetragonal La_2ReO_5. The physical properties of this compound have been measured, and are unexpected for a compound whose average Mo valence is 4+. The band gap of this compound is much smaller than for other semiconducting molybdates, resulting in the substantial absorption of infrared light. Density function theory studies have been carried out to understand the role of *M*-*M* bonding in determining both the novel structure type and the unexpected physical properties, and the observed physical properties of this phase can be readily understood in terms of its electronic structure. It is shown that the DFT-calculated energy levels can be simply rationalized in terms of bonding and anti-bonding orbitals generated through a molecular-orbital analysis of the dimeric units in La_2MoO_5.

3.2. Experimental

3.2.1. Synthesis

La_2O_3 (99.99%, Alpha Aesar) and MoO_3 (99.95%, Alpha Aesar) were used as starting materials, with La_2O_3 dried at 900°C for several hours before being weighed to eliminate absorbed moisture. La_2MoO_6 was prepared by grinding stoichiometric amounts of the starting materials using an agate mortar and pestle. This powder was then placed in a dense alumina crucible (CoorsTek) and reacted in air in a box furnace at 950°C for about 12 hours. La_2MoO_5 was synthesized by heating a ~1 gram ½" pellet of La_2MoO_6 in a 1" ID quartz tube under a flowing gas mixture of 5% H_2/95% N_2 (60 mL/min, passed through a line drier) in a Lindberg/BlueM Mini-Mite furnace at temperatures of 900 – 950 °C for about 3 days with intermediate grinding. Upon completion of the reaction, the powder was slate gray in color.

3.2.2. Powder diffraction

Laboratory X-ray diffraction data were collected using a Bruker D8 Advance diffractometer with a nickel-filtered Cu K_α source. Data were collected over a 2θ scan range of 7-140° using a step size of 0.02°, a fixed divergence slit of 0.3°, and Soller slit widths of 2.5°. Synchrotron X-ray diffraction were collected at the APS 11-BM beamline. Powder samples were packed into 0.8 mm Kapton capillaries. A wavelength of 0.41333 Å was used to collect data over a 2θ scan range of 1-50° using a step size of 0.001°. Time of flight (TOF) neutron powder diffraction measurements were collected at both 12 and 300 K on the POWGEN beamline located at the Spallation Neutron Source (SNS) of Oak Ridge National Laboratory during run cycle 2013A. Samples, approximately 2 g in mass, were loaded into an 8 mm diameter vanadium can which was placed in the FERNS cryogenic sample changer. Data were collected

using a repetition rate of 60 Hz in frame 1.5, corresponding to a *d*-spacing range of 0.28-3.09 Å, with a total proton charge of 3.6 to 7.2 x 10^{12} (1 – 3 hrs collection time). All diffraction data were analyzed using the TOPAS software package (V4.2, Bruker AXS).

3.2.3. Magnetic susceptibility measurements

Magnetic susceptibility measurements were done in a Quantum Design Physical Property Measurement System (PPMS) using a vibrating sample magnetometer (VSM) attachment. The magnetic response was measured over the temperature range of 2-350 K with applied magnetic fields of 1000, 10000 and 50000 Oe. Both field-cooled (FC) and zero-field-cooled (ZFC) sweeps were conducted.

3.2.4. Diffuse reflectance spectroscopy

Optical absorbance measurements were done using a two-beam Perkin Elmer Lambda 950 UV/VIS/NIR spectrometer with a 60 mm diameter Spectralon-coated integrating sphere to collect diffuse reflectance data. Undiluted samples were packed about 10 mm deep into black metal sample holders with a 1.5 mm thick quartz window (16.60 mm in diameter). Ground $BaSO_4$ powder (Alfa Aesar 99.99%) was used as a 100% reflectance standard. The Kubelka-Munk transform was used to calculate relative absorbances from the reflectance data through the relationship $\alpha_{KM} = \alpha/s = (1-R)^2/(2R)$, where α_{KM} is a relative absorbance, α is the absolute absorbance, s is an generally unknown scattering coefficient, and R is the reflectance measured in the spectrometer.

3.2.5. Electrical resistivity measurements

Four-probe resistivity measurements were carried out on bar-shaped samples cut from a sintered ½" diameter pellet. The most distant ends of the bar were coated with silver epoxy (EPOTEK, H20E) to provide the current contacts, while voltage was measured on two in-line point contacts on the top of the sample. A custom sapphire stage with Cu pads was used to support the sample during measurements. Pt wires (0.025 mm) were used to connect the sample to the stage with contacts made using silver epoxy, while metal-to-metal pressure contacts connected the stage to external cables leading to the Kiethley 2636 source meter used to control the resistivity measurements (which were typically done at an applied voltage of about 25 V). The sample stage was mounted inside a controlled-atmosphere rapid-thermal-annealing chamber (MBE Komponenten GmbH) in which an inert Ar atmosphere was maintained. A typical sweep was performed by first stabilizing the sample temperature at 30°C for several minutes, ramping up to 300°C in 30 min, holding for 10 min, and finally ramping down to 30°C at the same rate.

3.2.6. Thermogravimetric analysis

Thermogravimetric analysis (TGA) was used to determine the Mo valence in La_2MoO_5 using a TA Instruments Q5000 IR instrument. A powder sample (10-20 mg) was heated in a 100 µL alumina pan under flowing O_2 (25 mL/min) with a continuous ramp rate of 1°C/min during both heating and cooling, and with additional holds at 150°C (2.5 h) and 950°C (4 h). In order to minimize errors due to buoyancy and surface-adsorbed moisture, the mass change was determined by comparing the sample mass at 150°C before and after cooling.

3.2.7. Theoretical calculations

Density functional theory (DFT) calculations using the LMTO 47c code were carried out in order to obtain an understanding of the metal-metal bonding through a "fatbands" analysis of orbital contributions.[60] The program uses a linear muffin tin orbital (LMTO) approach within a tight-binding approximation, and an atomic sphere approximation to model voids within the unit cell using empty spheres. Lattice parameters and atomic positions taken from Rietveld refinement results were used as input for the calculations and integration over k space was performed with a 6 x 6 x 12 grid of 77 irreducible k points.

Further DFT calculations were performed with the projector augmented wave method[70] as implemented in the VASP code [68,69] using the local density approximation (LDA) [71,72] and with the LDA+U method.[101] For the latter, the U and J parameters were applied to the Mo *d* states with values 3.0 and 0.3 eV.[102] Initial lattice parameters and atomic positions were taken from the experimental structural refinement. Electronic and optical characteristics were calculated following internal relaxation of the atomic positions with lattice parameters held fixed. Structural properties were assessed by performing total energy calculations for a series of cell volumes over a range of approximately -24% to +12% relative to the measured cell volume while allowing the c/a ratio and internal coordinates to relax at each point. Final cell parameters were determined by a fit to the Murnaghan equation of state.[103]

3.3. Results and discussion

In the course of materials discovery efforts within the La-Mo-O phase space, it was discovered that the high temperature reduction of the precursor phase La_2MoO_6 resulted in the formation of a novel reduced lanthanum molybdate. The powder XRD pattern for this new

phase (Figure 3.1) could not be indexed using the cell parameters previously reported for known phases such as cubic or monoclinic La_2MoO_5, but was found to closely resemble the XRD pattern of tetragonal La_2ReO_5, which crystallizes in the tetragonal space group *I4/m* (#87) with unit cell dimensions of a = 8.935 Å and c = 6.011 Å. As illustrated in Figure 3.1, this La_2ReO_5 structure contains isolated Re_2O_8 square prisms which have very short Re-Re bond lengths of 2.26 Å, reflecting the strong metal-metal bonding in this phase.[63]

All of the major diffraction peaks in the lanthanum molybdate diffraction pattern could be well modeled in both Le Bail and Rietveld fits using the analogous La_2ReO_5 structural model as a starting point, suggesting that the stoichiometry of this novel phase is La_2MoO_5. The refined molybdate lattice parameters using this *I4/m* structural model were a = 8.9587(2) Å and c = 6.0518(1) Å, with additional crystallographic parameters given in Appendix 2 Table S1. However, there are some subtle indications that this proposed structure is incorrect. While an R_{wp} of 5.37 can be achieved through a Le Bail fit, the best Rietveld fit with this model gave an R_{wp} of 6.98, suggesting that peak intensities were not optimally modeled. A close look at long scans collected in a laboratory X-ray diffractometer with a good signal-to-noise ratio indicated the reproducible presence of additional weak peaks (marked with asterisks) that cannot be indexed using the La_2ReO_5-type structural model or by plausible impurity phases, a result which was confirmed in follow-up high-resolution synchrotron diffraction studies with reduced peak widths and improve signal-to-noise ratios. These peaks could, however, be fit with a $\sqrt{2} \times \sqrt{2}$ x 1 superstructure of the *I4/m* symmetry cell. Furthermore, when the Mo valence was calculated from the Mo-O bond distances in this La_2MoO_5 structural model using bond valence sum methods, the resulting Mo valence of 3.15+ was not consistent with the expected stoichiometry.

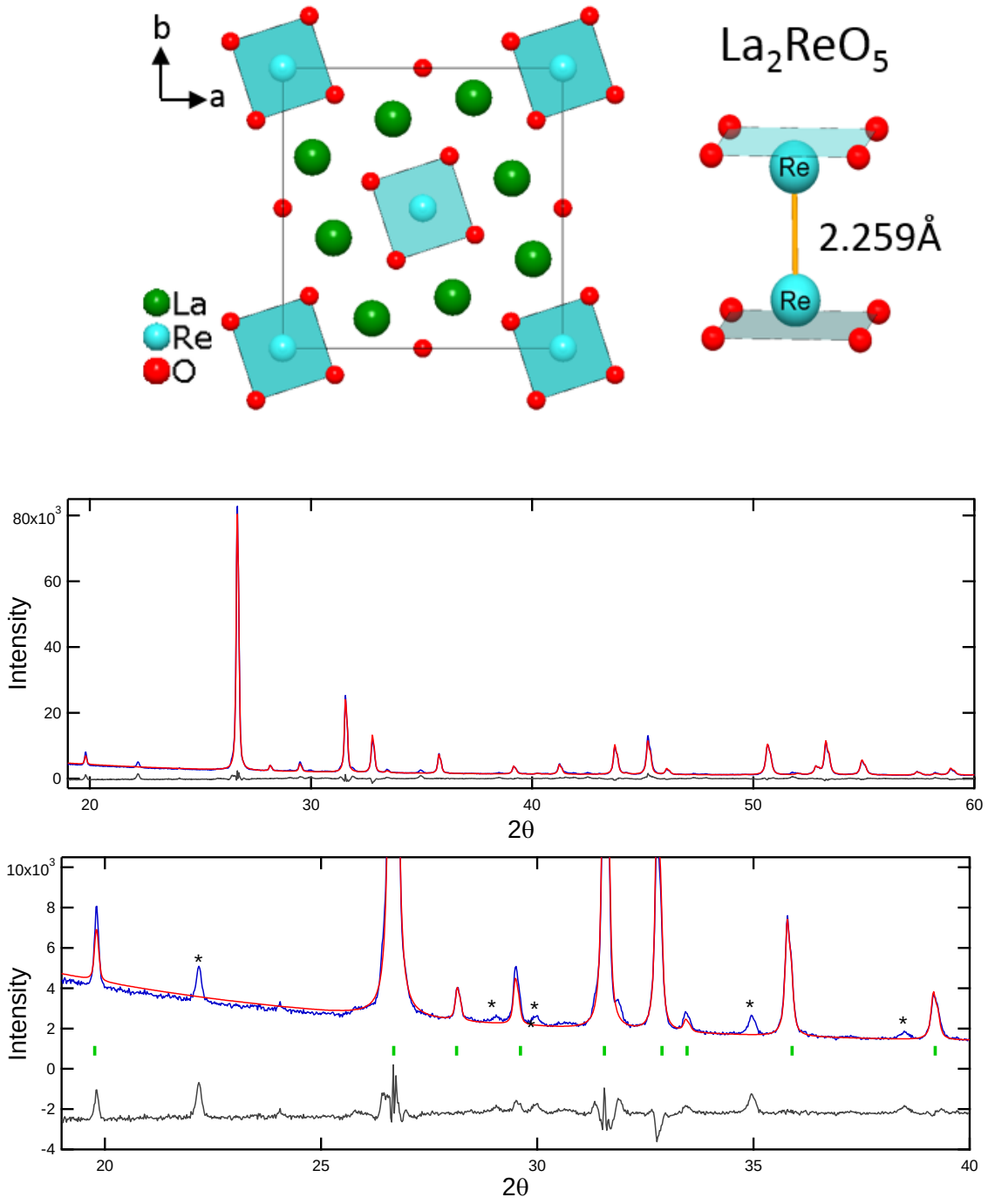

Figure 3.1. Top: Structure of La_2ReO_5, with an isolated dimeric Re_2O_8 square prism also shown to illustrate the short Re-Re bond distances. Bottom: Two different views of the Rietveld refinement of laboratory powder X-ray diffraction data for La_2MoO_5 using the La_2ReO_5 (*I4/m*) approximant structural model, with refined lattice parameters of a = 8.96 Å and c = 6.05 Å. Data are shown in blue, the modeled intensities in red, the difference pattern in grey, and the predicted reflection positions in green. The fit is very good in most aspects, but misses a series of weak peaks (*) that can be fit in the true $\sqrt{2} \times \sqrt{2}$ x 1 superstructure (*P4/m*).

Thermogravimetric analysis (TGA) oxidation experiments (Figure 3.2) were used to directly probe the oxidation state of Mo, and to thereby probe the composition of this phase. The mass gain during oxidation was calculated from the difference in masses during extended holds at 150°C before and after thermal oxidation to eliminate potential errors from both buoyancy and from surface-adsorbed water. The final product after oxidation at 950 °C was found by XRD (Figure S1, Table S2) to consist of single phase La_2MoO_6, confirming that there was no cation volatility during the original synthesis or during the subsequent TGA oxidation experiments. The observed mass change (3.53%) is in good agreement with the expected mass change (3.42%) for a sample with the stoichiometry La_2MoO_5 and an average Mo valence of 4+.

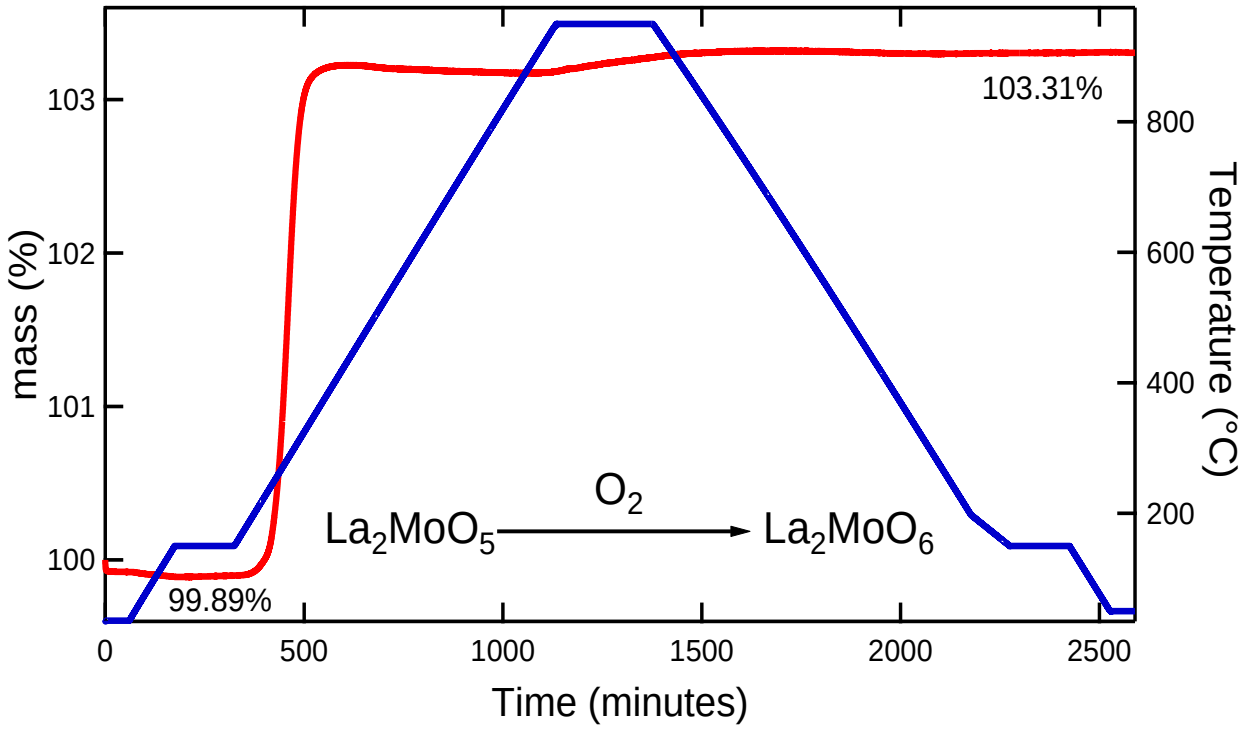

Figure 3.2. TGA data showing the mass changes (red) as La_2MoO_5 is thermally oxidized to La_2MoO_6 over the programmed temperature profile (blue). The sample % mass at 150°C before and oxidation is indicated.

With this basic knowledge, structure determination was then attempted. Charge flipping methods were used to first assign the heavy atom (La and Mo) positions using synchrotron X-ray diffraction data. Peaks positions and intensities from a Le Bail fit were used as input and trial calculations were performed both with and without symmetry constraints. The SUPERFLIP symmetry analysis indicated that the highest of the three possible space group symmetries consistent with the diffraction data (*P4/m*) was preferred, and this space group was used throughout the remainder of the structure solution process.[104] It was found that the heavy atom positions in La_2MoO_5 were essentially unchanged relative to the La_2ReO_5-type subcell. Next, oxygen positions were determined from neutron data and Fourier difference maps. All atomic sites were found to be fully occupied. The final structure refinements were carried out using only neutron diffraction data (which provided good sensitivity to all atoms) in space group *P4/m*, since the lower symmetry space groups (*P4* and $P\bar{4}$) with the same systematic absence conditions were found to produce negligible improvements in the refinement quality while exhibiting substantially increased statistical uncertainties in atom positions reflecting the correlation effects that occur when symmetry-equivalent atoms are independently refined. The final refinement results are presented in Table 3.2, while selected bond distances are given in Tables 3.3 (for Mo) and S3 (for La). Similar quality fits were also obtained using synchrotron diffraction data (Table S4), and the refined synchrotron lattice parameters of a = 12.66871(6) Å and c = 6.05048(3) Å are expected to be more accurate than those of the neutron diffraction data due to the parallel beam and fixed diffractometer geometry used in the synchrotron data collection.

Table 3.2. La_2MoO_5 crystallographic parameters and atomic sites (*P4/m*).

Crystal system		Tetragonal
Space group		*P4/m* (#83)
Z		8
Radiation		Neutron (TOF)
Temperature		300K
λ (Å)		1.066 (center)
Range of collection		0.28 < d < 3.09
Lattice parameters (Å)	*a*	12.6684(4)
	c	6.0526(2)
Cell volume ($Å^3$)		971.37(7)
P_{calc} (g/cm^3)		6.2054(5)
R_{bragg}		2.48
R_{wp}		3.39

Atom	Wyck	*x*	*y*	*z*	B_{eq}
La1	4j	0.2041(4)	0.1093(4)	0	0.73(8)
La2	4j	0.3005(4)	0.3901(4)	0	0.39 (6)
La3	4k	0.2719(4)	-0.0961(4)	½	0.51(6)
La4	4k	0.3871(4)	0.2220(4)	½	0.51(5)
Mo1	2g	0	0	0.316(2)	0.55(9)
Mo2	2h	½	½	0.312(2)	0.44(8)
Mo3	4i	0	½	0.2217(7)	0.51(4)
O1	8l	0.3518(4)	0.5417(4)	0.7561(6)	0.58(5)
O2	8l	-0.0433(5)	0.8533(4)	0.7711(5)	0.76(7)
O3	8l	0.2546(4)	0.7555(4)	0.2532(5)	0.59(4)
O4	8l	0.0497(4)	0.6378(4)	0.2528(5)	0.93(6)
O5	4j	0.4616(5)	0.8894(5)	0	0.73(7)
O6	4k	0.4655(6)	-0.0976(5)	½	0.74(7)

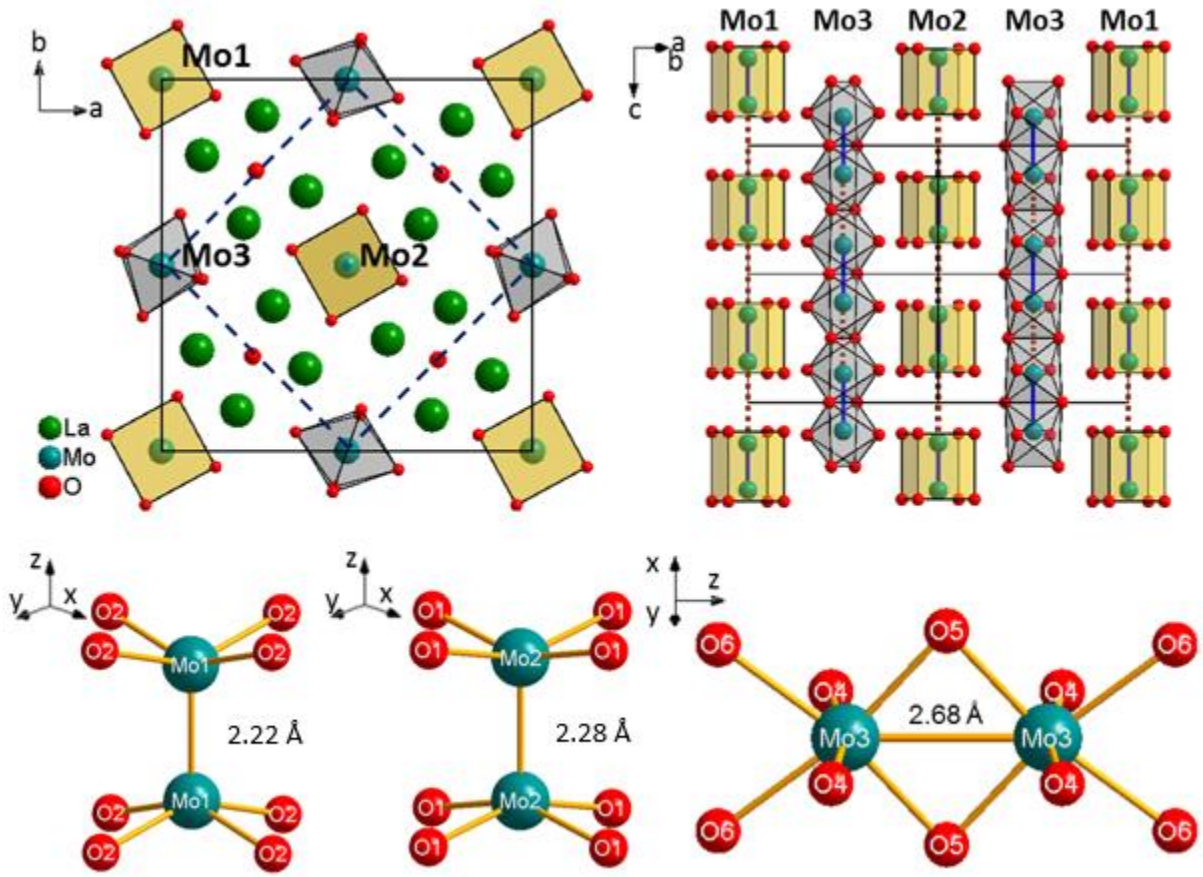

Figure 3.3. Top left: The tetragonal *P4/m* La_2MoO_5 unit cell is displayed with the boundary of the *I4/m* subcell of La_2ReO_5 (dashed lines) superimposed. Top right: Chains of Mo_2O_8 (Mo1 and Mo2 site) and Mo_2O_{10} (Mo3 site) dimers in La_2MoO_5 are shown with Mo-Mo bonds drawn with solid blue lines and non-bonding Mo-Mo neighbors connected with dashed orange lines. Bottom: Local geometry of the three Mo sites and the non-standard coordinate axes used to define their *d* orbitals.

Table 3.3. Mo-O and Mo-Mo bond distances.

Atom 1	Atom 2	Mult	Distance (Å)
Mo1	O2	x 4	2.010(6)
	Mo1 (short)	x 1	2.22(2)
	Mo1 (long)	x 1	3.83(1)
Mo2	O1	x 4	1.994(5)
	Mo2 (short)	x 1	2.28(2)
	Mo2 (long)	x 1	3.78(1)
Mo3	O4	x 2	1.866(5)
	O5	x 2	2.000(6)
	O6	x 2	2.135(5)
	Mo3(short)	x 1	2.684(8)
	Mo3(long)	x 1	3.369(6)

The final refined structure of La_2MoO_5 is shown in Figure 3.3. Although the arrangement of heavy atoms (La, Mo) is essentially the same as in the La_2ReO_5 structure, a set of new Mo coordination environments are observed due to some oxygens moving to significantly different positions (~2 Å away from the analogous positions in La_2ReO_5) in the superstructure. This results in La_2MoO_5 having two different types of coordination polyhedra (Mo_2O_8 square prisms, and Mo_2O_{10} edge-sharing bioctahedra present in equal amounts), in contrast to La_2ReO_5, which has only Re_2O_8 prisms. The alternating pattern of these two building blocks gives rise to the $\sqrt{2} \times \sqrt{2}$ superstructure of La_2MoO_5.

While there are only two different types of Mo bonding environments, there are three different crystallographic Mo sites. The Mo1 and Mo2 sites sit at the 2g and 2h Wykoff positions which both have 4-fold rotational symmetry along the Mo-Mo bond axis, resulting in perfectly square arrangements of oxygens around these square prismatic sites. These two sites are found in separate Mo_2O_8 dimers with Mo-Mo bond lengths of 2.22(2) and 2.28(2) Å, respectively. The Mo3 site (4i Wykoff position) has a lower 2-fold rotational symmetry, as four-fold rotational symmetry is not compatible with the formation of the octahedra in these edge-sharing bioctahedral Mo_2O_{10} dimers. These octahedral dimers have much longer Mo-Mo bond lengths of 2.684(8) Å, an indication that the Mo-Mo bond order is reduced in the Mo_2O_{10} octahedral dimers relative to the Mo_2O_8 prismatic dimers. Since all of the Mo-Mo bonds in both the octahedra and in the square prisms are oriented parallel to the *c*-axis, the structure can be considered to have chains of both types of polyhedral units running parallel to the *c*-axis, as illustrated in Figure 3.3. The sum of the Mo-Mo bond length and the non-bonded Mo-Mo distance is necessarily equal to the *c*-axis length for both the prismatic and octahedral chains.

The two crystallographically distinct types of Mo_2O_8 square prisms both have a single type of Mo-O bond length due to the 4-fold symmetry of the structure, and this length is ~2.00 Å for each site. In contrast, the Mo_2O_{10} octahedral dimers have a wider distribution of Mo-O bond lengths (1.87, 2.00, and 2.13 Å) that may either be indicative of a second-order Jahn-Teller distortion[105] of the central Mo cation or might just reflect the symmetry breaking caused by the alternating short and long Mo-Mo distances in the octahedral chains. An additional important building block within the La_2MoO_5 structure is the OLa_4 tetrahedra, which have an O3 site at their center. The bond distances within OLa_4 tetrahedra are in general known to be shorter than typical O-La bonds, and indeed short bond distances of ~ 2.4 Å are found for these tetrahedra. If

La cations are drawn at the center of coordination polyhedra, environments of distorted LaO_8 cubes or LaO_7 monocapped trigonal prisms are observed. The bond distances in these polyhedra are generally short (2.4 – 2. 7 Å).

It is well established that the experimentally determined bond lengths can be utilized to obtain reasonable estimates of ion valences through the bond valence sum method.[77,79,78] The contribution of each individual bond to the total valence of a Mo cation can be obtained through the relationship: $\boldsymbol{v_i = e^{(R_0 - R_i)/b}}$, where the valence contribution from the i^{th} ligand can be calculated from its bond distance, R_i, based on two parameters R_0 and b for which tabulated values are typically available based on empirical analyses of the prior crystallographic literature. The experimental bond distances (R_i) for La_2MoO_5 were determined through Rietveld refinement of neutron powder diffraction data (Table 3.3). The best choice of R_o and b is not clear since these parameters are often valence-specific, and the thus the choice of an expected valence will affect the valence calculated using BVS methods. When a variety of BVS parameters suggested for Mo cations are investigated (Tables S5, S6), it is robustly found that there is a very large difference (1.5 – 2 valence units, v.u.) in the valence predicted for the prismatic and octahedral sites. This suggests that charge disproportion is occurring, with the average Mo valence of 4+ not observed for any site. Instead, the prismatic sites are found to have Mo^{3+} (d^3), while the octahedral sites have Mo^{5+} (d^1). Final valences (Table 3.4) were therefore calculated using Mo^{3+} BVS parameters for the prismatic sites and Mo^{5+} BVS parameters for the octahedral site (Mo3), and the difference in valence between the two sites when calculated in this manner was 2.0, a value which suggests complete disproportionation. This represents the first example of the disproportionation of Mo^{4+} within any solid state structure.

Table 3.4. Bond valence sum analysis.

Mo site	O site	Bond length	Site type	Valence/ bond	Valence/ site
Mo1	O2	2.010	Prism	0.62	2.49
Mo2	O1	1.994	Prism	0.65	2.59
Mo3	O4	1.866	Oct	1.03	4.51
	O5	2.000	Oct	0.72	
	O6	2.135	Oct	0.50	

The bond valence sum analysis also highlights another unusual aspect of bonding within this system. The calculated valence of all three Mo sites is reduced relative to the formal oxidation state by about 0.5 valence units. This is a very large and systematic difference that indicates significant variations in the observed Mo-O bond lengths relative to those generally expected for other compounds with the same Mo valence and coordination number. The BVS parameters can also be used for the reverse process of predicting what the average bond length should be for a given valence (Table S7-S9), and it can be seen from this analysis that the Mo-O bonds in La_2MoO_5 are about ~0.05 Å longer than would normally be expected based on their oxidation state (Table 3.5). This demonstrates that the presence of metal-metal bonding results in a substantial weakening of Mo-O bonds within these dimeric units relative to expectations for isolated polyhedra. Metal-metal bonding therefore offers the opportunity to tune bond strength in a manner that may be useful for applications such as catalysis, where performance in many cases directly correlates with bond strength.

Table 3.5. Refined *vs.* ideal Mo-O bond lengths (Å).

	Refined distance	Ideal distance (BVS)	Δ(distance)
Mo1	2.01	1.94-1.97	+0.04-0.06
Mo2	1.99	1.94-1.97	+0.02-0.05
Mo3	2.00	1.94-1.95	+0.05-0.06

Although disproportion of ions in the solid state is uncommon, it is in many cases associated with intriguing functionality. We first note that even though the change in oxidation state is often referred to as "charge disproportionation", the term "charge" is very misleading as changes in oxidation state need not be accompanied by changes in the electrostatic charge associated with ions[106,107], as has been very effectively demonstrated in some recent theoretical investigations.[108] Instead, disproportionation refers to a change in the integer "formal charge" of ions, which is more commonly called an oxidation state, and thus should be thought of as "formal charge disproportionation". The oxidation state of ions is often the same as their valence state (which corresponds to the number of orbitals involved in chemical bonding), though this need not be the case as has been described in a recent overview.[106] The actual charge of ions can only be clearly assigned integer values for isolated gas phase ions, and as such it is not sensible to think of solid state compounds in terms of integer charges.

Typically, disproportionation is driven by an energetic impetus to satisfy Hund's rule, which specifies that closed shell electron configurations are particularly stable, and that half-filled shells are next most stable. The energetic advantages conferred by achieving a closed shell are clearly seen in the stable valences of many *p*-block cations, such as Bi^{5+}/Bi^{3+}, Pb^{4+}/Pb^{2+},

Tl^{3+}/Tl^{+}, Sb^{5+}/Sb^{3+}, and Sn^{4+}/Sn^{2+}. These valence states can co-exist in a single compound, as exemplified by the compound Sb_2O_4 which contains only Sb^{3+} and Sb^{5+}, which can be considered to be an example of disproportionation since the average Sb oxidation state is 4+.[109] Sb_2O_4 is therefore necessarily an example of a mixed valence compound in which different valences states of the same element co-exist in a compound. Interestingly, it has been reported that the intermediate 4+ oxidation state of Sb and Bi can be stabilized by dilution[106], and it has been hypothesized that the strong tendency of electrons in the nominal 4+ state of these ions to disproportionate leads to a tendency for electrons to pair in a manner that facilitates the superconductivity at temperatures up to 30 K in perovskite compounds such as $Ba(Pb_{0.75}Bi_{0.25})O_3$ (T_c ~ 12 K)[110], $Ba_{0.6}K_{0.4}BiO_3$ (T_c ~ 30K)[111], as and $Ba(Pb_{0.75}Sb_{0.25})O_3$ (T_c ~ 3K)[112]. There has been resurgent interest in halide analogues of this system[113] due to the prediction of superconductivity at about 20 K and 30 K for $CsTlCl_3$ and $CsTlF_3$, respectively.[114]

Unlike the *p*-block elements, disproportionation in transition metals can be driven by the electron configuration rearranging so that the resulting electronic states are either half-filled or completely filled (or a combination of these two cases for the two different valences that result from disproportionation). The electron configurations which lead to disproportionation will vary with the local geometry of the transition metal due to the different degrees to which ligand field effects can lift the native five-fold degeneracy of *d* orbitals expected for an isolated atom, and is of course affected by the spin state (high spin / low spin) of the cation as well. Thus the tendency of the high spin octahedral d^4 configuration to disproportionate drives both the $2\ Fe^{4+} \rightarrow Fe^{3+} + Fe^{5+}$ speciation in the unusual solid state compound $CaFeO_3$,[115] as well as the well-known instability of Mn^{3+} ions in aqueous solution, which is relevant to the modern design of oxygen evolution reaction (OER) electrocatalysts.[116] Disproportionation is also known to occur for

octahedral d^7 ions, resulting in the 2 $Ni^{3+} \rightarrow Ni^{2+} + Ni^{4+}$ speciation in perovskites such as $NdNiO_3$.[117] Although octahedral disproportionation examples are probably most common due to the predominance of this coordination environment, disproportionation can occur in non-octahedral geometries such as the trigonal prismatic d^6 Co^{3+} sites in $Sr_5Co_4O_{15}$.[118] Although examples for the later 4*d* and 5*d* transition metals are less common than for the 3*d* transition metals described above, examples such as AgO[106] and $CsAuCl_3$[119] are known.

While Hund's rule typically provides the driving force for transitions between integer valence states, similar speciation processes have been reported for transition metals in non-integer valence states, such as the 2 $Fe^{2.5+} \rightarrow Fe^{2+} + Fe^{3+}$ speciation reported for Fe_2BO_4 [120-122] and the 2 $Ir^{3.5+} \rightarrow Ir^{3+} + Ir^{4+}$ speciation reported for $CuIr_2S_4$,[123,124] and of course the classic Verwey transition of Fe_3O_4 whose precise nature has been much debated.[125-127] Such compounds are often said to be "charge ordered", though of course the same qualifiers on the use of the term charge apply. These compounds do not represent the disproportionation of ions (as the ground state of an atom does not have a half-integer number of electrons). These speciation reactions are better considered to be an example of a thermally driven transition between a mixed valence state (where electrons are localized on one ion) and an intermediate valence state (where electrons are delocalized over multiple ions), with the former state being enthalpically favored and the latter being entropically favored. As such, these transitions are perhaps better thought of as the "charge disordering" of the native mixed valence ground state.

In this context, the compound La_2MoO_5 is a particularly interesting example of charge disproportionation given the scarcity of other examples among the early 4*d* and 5*d* transition metals. Furthermore, even though the Mo^{3+} and Mo^{5+} sites that result from disproportionation could be equivalent in a hypothetical compound in which all Mo cations possessed the average

4+ state (as is the case for the Re^{4+} cations in the closely related structure of La_2ReO_5), the coordination of the two Mo cations in disproportionated La_2MoO_5 is completely different as these cations are either square planar (CN 4) or octahedral (CN 6) in their local geometrical environment even though the stoichiometric ratio of Mo:O atoms is identical in both the prismatic and octahedral columns. This difference in geometry is structurally accommodated by the motion of two oxygen anions by about 1.5 Å, a massive structural rearrangement. As such, it seems likely that any dynamic changes in valence caused by the motion of electrons will necessarily lead to strong changes in local coordination environments, giving rise to exceptionally strong coupling between the lattice and electronic degrees of freedom in this compound and likely leading to polaron formation. It is therefore expected that the disproportionated state cannot easily be disrupted, and physical properties measurements (discussed next) show no evidence for transitions out of the disproportionated state up to the maximum temperature studied (300 °C).

It is of great interest to understand both the crystal chemical forces that permit the stabilization of the mixed valence structure of La_2MoO_5, and the manner in which the mixed valence ions will influence the electronic structure of this compound as well as the dependent physical properties, such as resistivity, magnetic susceptibility, and optical absorption. Magnetic susceptibility measurements generally provide a robust method of probing the number of unpaired electrons at transition metal sites. The measured magnetic susceptibility (Figure 3.4) is essentially temperature-independent and indicates that La_2MoO_5 should be considered to be diamagnetic. There is a very weak paramagnetic signal which is about 50 times weaker than that expected for a single unpaired electron (S = ½) which obeys the Curie law, and is therefore attributed to contributions from a minor impurity phase. When explicitly fit to a Curie-Weiss

law of the form $\chi = \chi_0 + C / (T - \Theta)$, the refined value for the temperature independent susceptibility χ_0 is 1.3 x 10^{-5} emu / mol, the Curie constant C is 1.18 x 10^{-2} emu / mol K and the Curie-Weiss Θ is -7.4 K, supporting this assignment. As shown in Fig. 3.4, this diamagnetism is very different from the expectations for a d^1 cation in octahedral coordination (S = ½) or for a d^3 ion in square planar coordination (S = ½), and indicates that the direct metal-metal bonding must strongly impact the electronic structure of La_2MoO_5 and provide a mechanism for pairing all of the valence electrons.

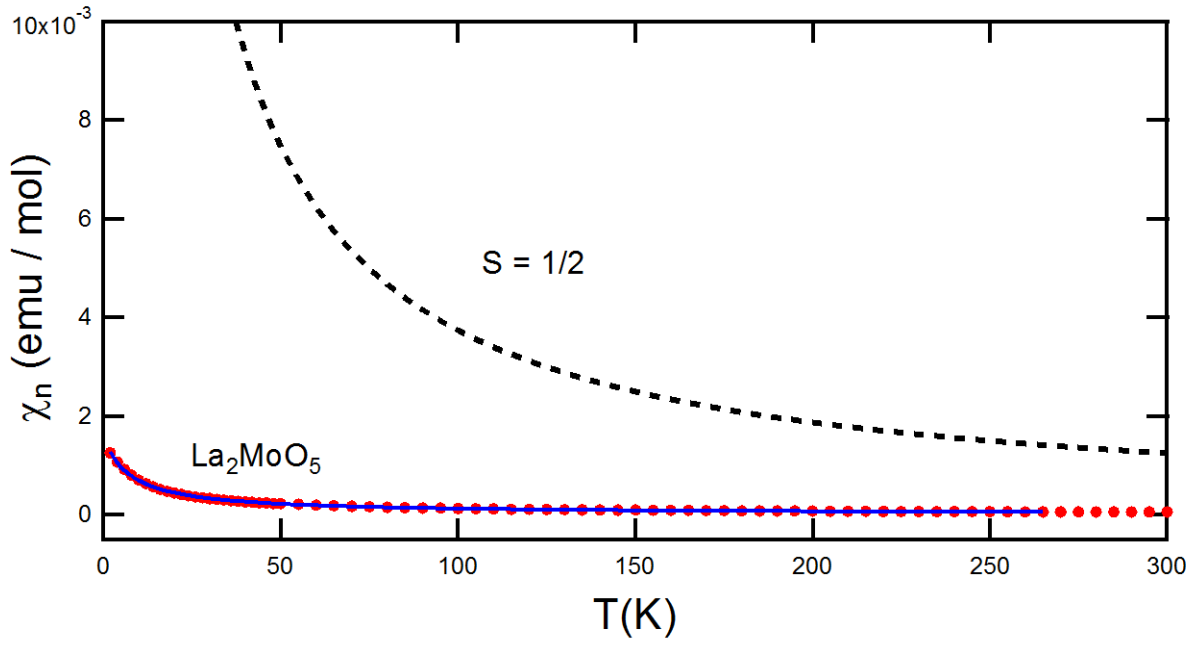

Figure 3.4. The magnetic susceptibility of La_2MoO_5 (red points) obtained in field cooled measurements with B = 5T is much less than expected for an S = ½ ion (dashed line), and indicates this phase is diamagnetic. Fits to the small temperature-dependent susceptibility (blue line) are characteristic of a small amount of a paramagnetic impurity.

Temperature dependent resistivity measurements (Figure 3.5) indicate that La_2MoO_5 is non-metallic with a large resistivity of 2.0 x 10^5 Ω·cm at room temperature that drops by two orders of magnitude on heating to 300 °C. This behavior is consistent with the magnetic susceptibility data, as the complete pairing of electrons generally precludes the observation of metallic behavior. The temperature dependence exhibits Arrhenius behavior, and corresponds to a band gap of 0.49 eV if this compound is behaving as a conventional thermally activated semiconductor following the relationship $\rho = \rho_0 e^{-Eg/2kT}$, or a simple thermal gap of 1.0 eV for an alternate type of thermally activated process such as polaronic hopping – a strong possibility given the very large lattice distortions (oxygen displacement) which accompany the charge disproportionation in this compound.

It is very unusual to find such a small band gap in an oxide semiconductor. For example, the band gaps of the thermodynamically stable compounds of MoO_3 (2.93 eV), Fe_2O_3 (2.2 eV), TiO_2 (3.0 eV), and Cu_2O (2.0 eV) are all much larger. The wide band gaps of oxide semiconductors are typically due to the substantial electronegativity difference between oxygen and the cation, though the energy scales associated with alternate mechanisms for band gap formation in oxide semiconductors without closed shells (ligand field splitting and/or electronic correlations) also tend to be large. The industrially important small gap semiconductors used for infrared detectors, such as InGaAs[128], PbS[129], and InSb[130], incorporate later *p*-block anions that are typically susceptible to oxidation in air and often have high toxicity.[48] The availability of small band gap oxide semiconductors for infrared applications may therefore offer many advantages over existing *p*-block semiconductor systems.

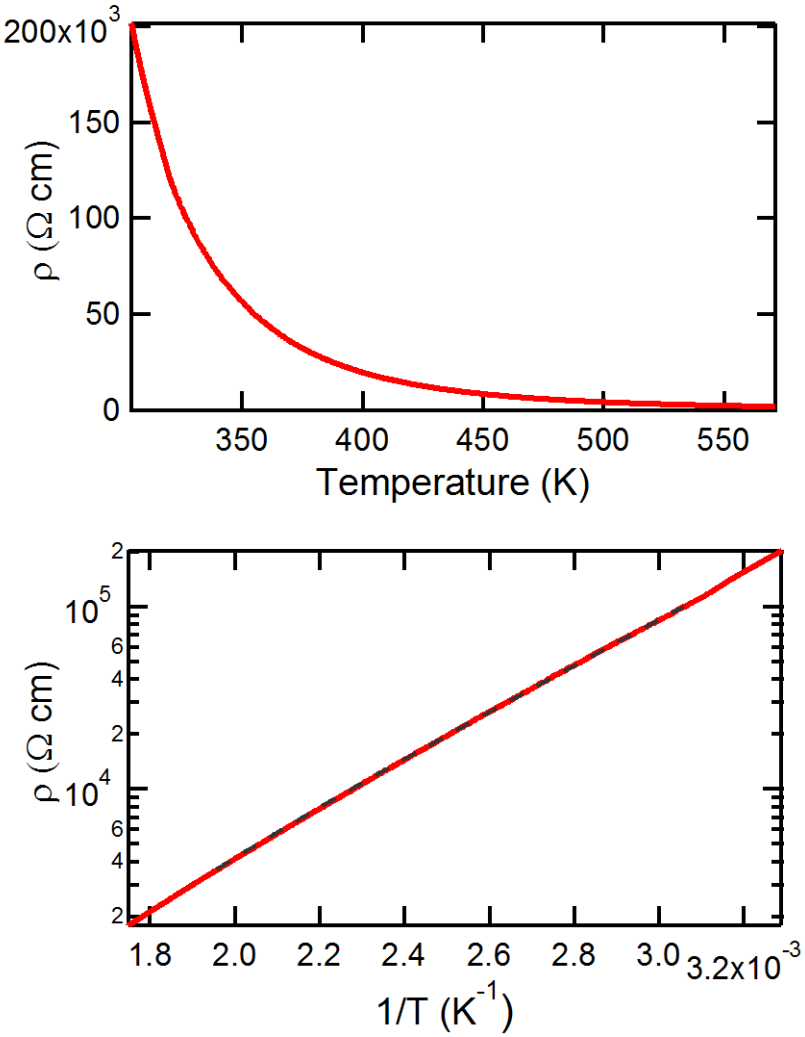

Figure 3.5. The resistivity of La_2MoO_5 decreases exponentially with increasing temperature, as seen in plots against linear axes (top) and in plots rescaled to be linear when this dependence is followed (bottom). A bandgap of 0.49 eV is obtained from fits to this data (dashed black line).

The absorption properties of La_2MoO_5 were directly evaluated using diffuse reflectance data, which were measured over the energy range of 0.5 to 5 eV (Figure 3.6). It is difficult to resolve the band gap of La_2MoO_5 from the present data, but it appears likely that it falls between 0.4 and 0.7 eV. While it is non-trivial to obtain absolute absorption coefficients, it is expected based on a comparison with other oxide semiconductors measured in the same instrument that the absolute absorption between 0.75 – 1.00 eV is strong and that this phase will have a good

cross-section for the absorption of infrared light in this energy range. Unlike conventional oxide semiconductors whose spectra typically exhibit only one or two features associated with absorption across a direct or indirect gap, the absorbance spectra of La_2MoO_5 exhibits many overlapping optical features which cannot be easily resolved. These features cannot be trivially interpreted, and a deeper understanding of the influence of metal-metal bonding on the electronic structure of La_2MoO_5 is therefore required to understand this data.

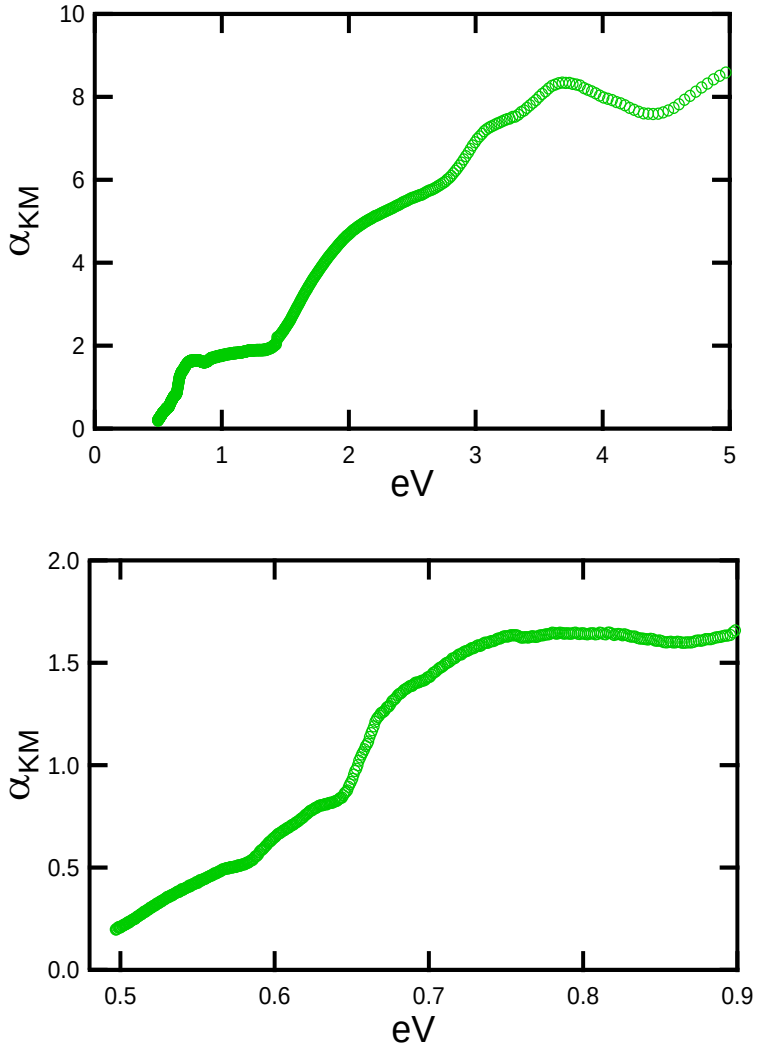

Figure 3.6. Relative absorbance spectra of La_2MoO_5 obtained from a Kubelka-Munk transform of diffuse reflectance data (top), and with an expanded view of the low-energy infrared response (bottom).

Initial insights into electronic structure were obtained through calculations using the LMTO47c code, which is very effective for obtaining insights into the orbital contributions, but which is less robust for the determination of band gaps relative to more conventional plane wave codes. The density of states and band structure obtained in this manner are plotted in Figures 3.7 and 3.8. The dense manifold of orbitals found at energies below -2 eV (relative to the top of the valence band) is assigned to the O 2*p* states that typically make up the valence band of oxide semiconductors, but which do not serve this role in La_2MoO_5. Both the valence and conduction band are comprised of Mo 4*d* states, which are the primary contributor to the active bands between -2 and +4 eV. These *d* electron bands are essentially flat in most reciprocal space directions, but are sometimes strongly dispersed in the *z*-axis direction (*e.g.* G → Z, A → M), likely reflecting the *c*-axis alignment of the polyhedral chains and the Mo-Mo bonds. The lack of dispersion in other directions leads to some very sharp peaks in the density of states associated with the Mo *d* electrons, which approach the high DOS values observed for *f* electron states. It might therefore be expected that the valence electrons in La_2MoO_5 do not behave like typical *d* electrons and may exhibit phenomena such as heavy fermion behavior that are only commonly observed for *f* electron systems. The band gap obtained through these calculations is 0.69 eV, a value which is consistent with the optical measurements, and which is far smaller than typical oxide semiconductors.

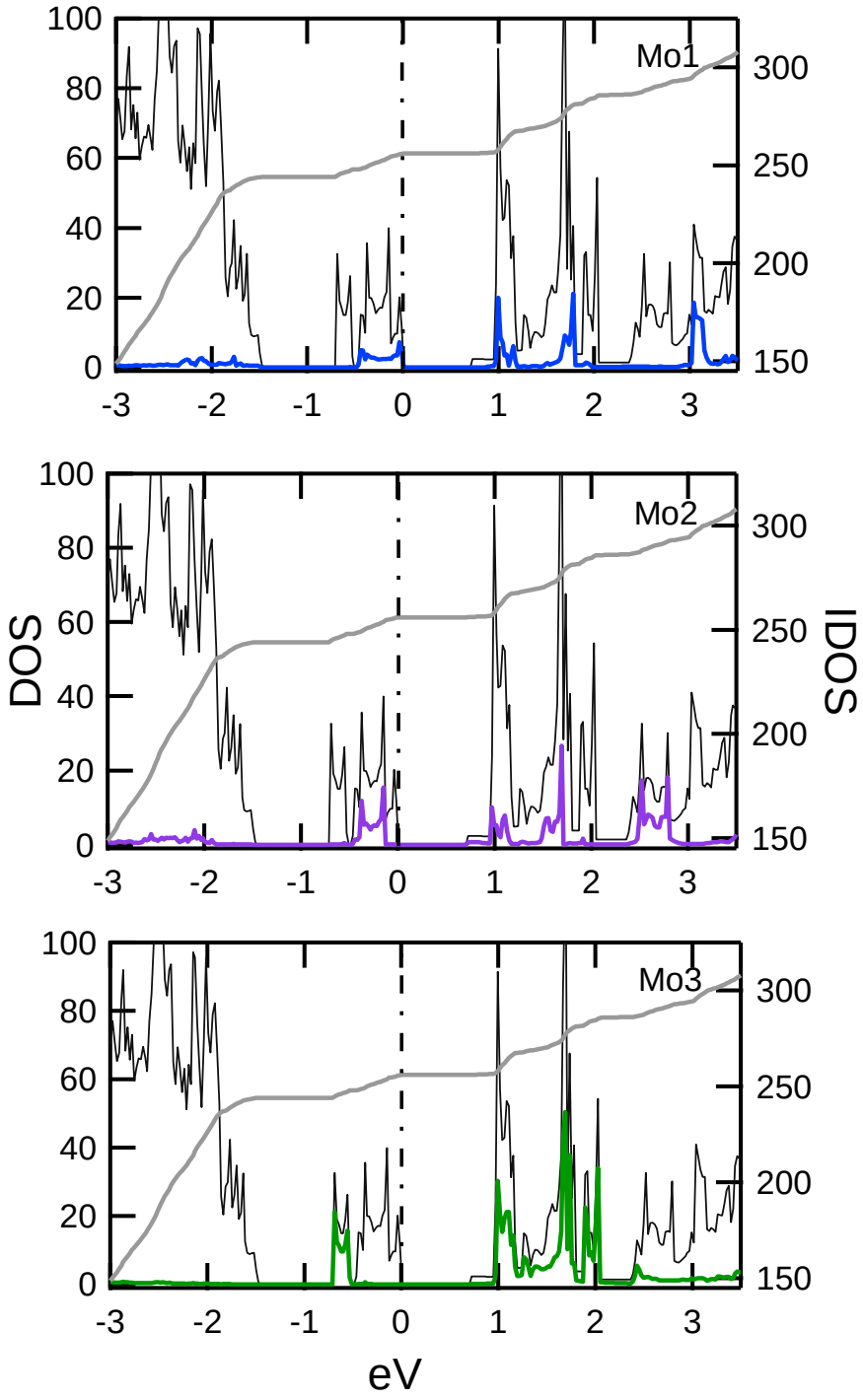

Figure 3.7. Total (black) and Mo *d* orbital site-specific (blue/purple/green) density of states for La_2MoO_5.

An examination of the integrated density of states (IDOS) fully confirms the valence assigned from BVS methods, as the octahedral site (Mo3) is found to have a d^1 configuration while the prismatic sites (Mo1 and Mo2) both have a d^3 configuration (Figure 3.8). The prismatic Mo1 and Mo2 sites have similar but not identical electronic states, reflecting the symmetry breaking that occurs in this $\sqrt{\mathbf{2}} \times \sqrt{\mathbf{2}}$ superstructure. Based on these calculations, the Mo-Mo bonds in Mo_2O_8 can be assigned a bond order of three (triple bond), and those of the Mo_2O_{10} octahedral dimers a bond order of one (single bond).

In order to assign the orbital character of the occupied and unoccupied *d* electron states, "fatbands" calculations were carried out. A condensed description of these results is provided in Figure 3.8, while the full analysis (five individual sets of fatbands for each of the three types of Mo sites) is given in Figures S3-S6. In general, it can be seen that each type of dimeric Mo site gives rise to more than five *d* orbital states. This indicates that a single-ion analysis is incomplete, and that the ten combined molecular orbitals that can be derived from the *d* orbitals on a pair of Mo cations must be considered.

The Mo_2O_{10} dimers are built from Mo cations on the Mo3 site. Although these Mo3 cations can be assigned a d^1 configuration based on their valence, they do not have one single unpaired *d* electron residing in the lowest energy *d* orbital of the t_{2g} manifold, as would typically be expected for an isolated MoO_6 octahedron in the single-ion picture. Instead, the lowest energy t_{2g} orbital (with dz^2 symmetry, when described using the non-standard axis choices most relevant to the dimer shown in Figure 3.3) for the Mo3 site is split into a separate bonding and anti-bonding pairs when the two orbitals of this symmetry (one for each Mo3 in the dimer) are allowed to hybridize. The lower energy bonding orbital contains two paired electrons (one electron from each Mo3 site in the Mo_2O_{10} dimer), and will therefore have a closed shell.

Similarly, the higher energy anti-bonding orbital is completely empty, and will also be diamagnetic in character. These bonding and anti-bonding orbitals are given the labels σ and σ*, using the standard chemistry terminology to describe the direct overlap of their lobes. The ten *d* orbitals associated with the Mo_2O_{10} and Mo_2O_8 dimers can therefore be assigned both single-ion labels (*d*xy, *d*yz, *d*zx, dx^2-y^2, dz^2) and molecular orbital labels (σ, σ *, π, π *, δ, δ *), which are marked on Figure 3.9. The relative energies of these orbitals can be clearly enumerated in most cases, though for highly dispersed orbitals, the midpoint energy of the orbital is an inadequate descriptor of the wide range of energies at which the orbital contributes to the overall density of states.

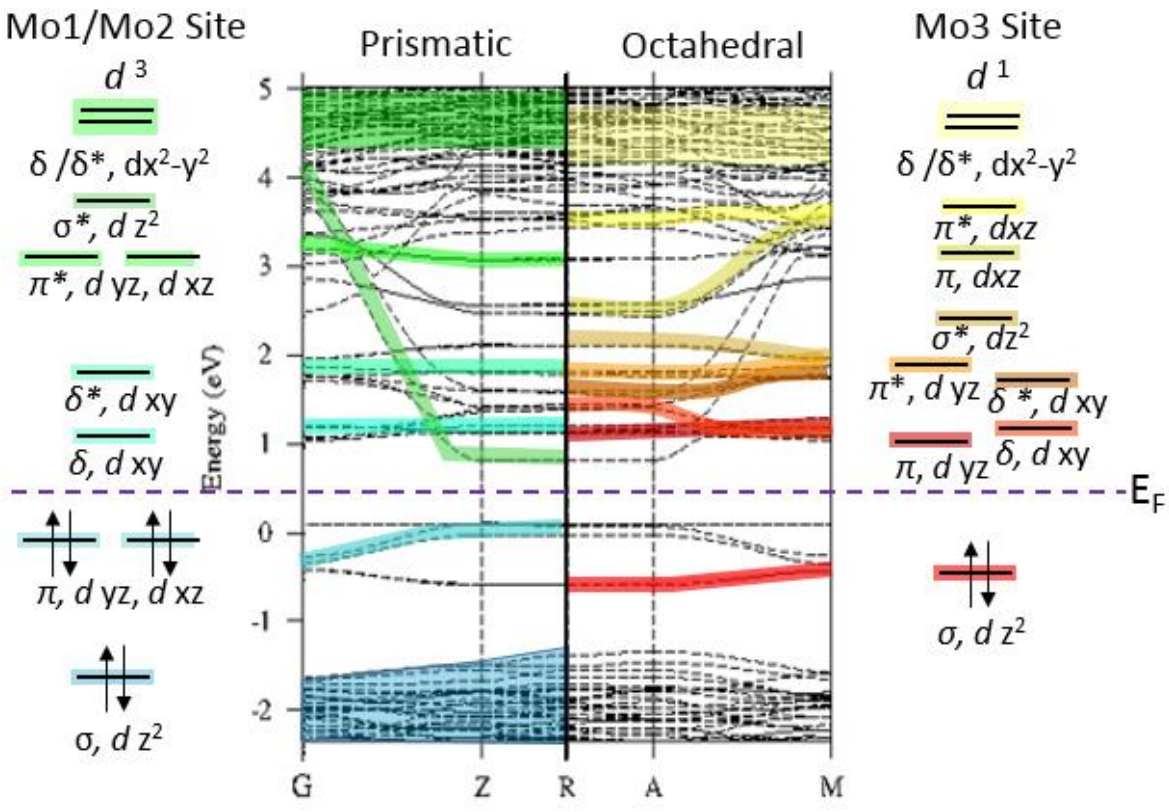

Figure 3.8. LMTO-calculated band structure of La_2MoO_5 showing a band gap of 0.69 eV between the valence and conduction bands. The orbital splitting diagrams were assigned based on "fatbands" plots, provided in the Supporting Information.

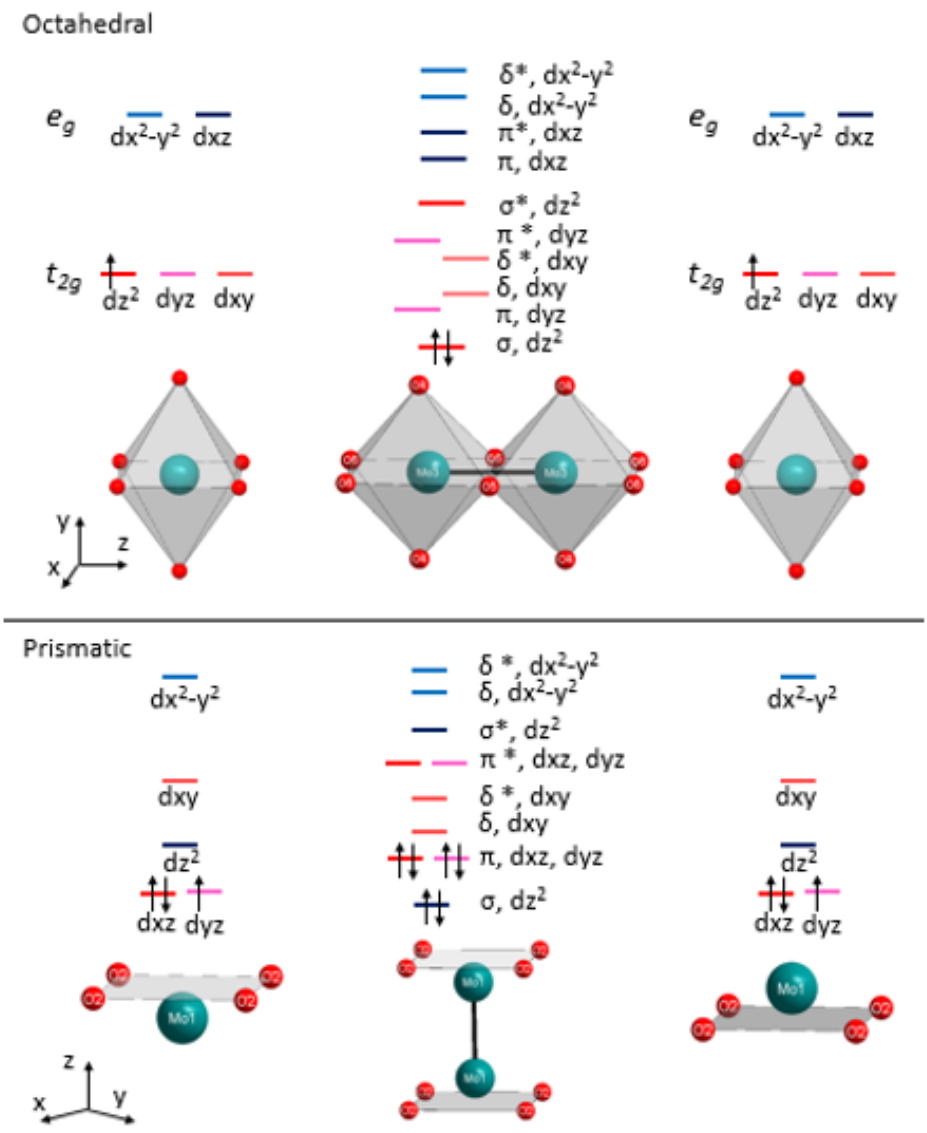

Figure 3.9. Molecular orbital ordering diagram for the *d* electrons involved in forming the metal-metal bond for both the Mo_2O_{10} and Mo_2O_8 dimer types.

Although predictions about the physical properties of La_2MoO_5 made using only the single-ion picture are clearly inaccurate, the single-ion model still provides a good starting point for estimating the energies of the molecular orbitals (MOs), and these MOs are very effective for describing the electronic properties of this phase. For example, in the single ion picture for the Mo3 site, an octahedral ion with the non-standard choice of reference axes given in Figure 3.9 will be split into lower energy triply degenerate t_{2g} (dz^2, *d*yz, *d*xy) and higher energy doubly

degenerate e_g (dx^2-y^2, dxz) states. The higher energies of the e_g orbitals result from the stronger repulsive interactions with the ligand electrons for the *d* orbitals which have lobes oriented towards those ligands, and it is sensible that these repulsions persist even after the *d* orbitals from two different Mo cations hybridize to form MOs. The molecular orbitals observed for La_2MoO_5 maintain the same general arrangement, as the 6 MOs (σ, σ*, π, π*, δ, δ*) derived from t_{2g} states are substantially lower in energy than the 4 MOs (π, π*, δ, δ*) derived from e_g states. The hybridization that results from the metal-metal bonding will result in each single-ion *d* orbital being split into bonding and anti-bonding pairs, with the σ orbitals (dz^2) having a very large splitting, the π orbitals (dxz, dyz) having a smaller but still very substantial splitting, and the δ orbitals (dxy, dx^2-y^2) having minimal splitting. When these two primary factors (relative energies of single ion orbitals and the relative degree of hybridization for molecular orbitals) are considered together, accurate predictions can be made about the relative energies and splitting of the 10 *d* orbital-derived MOs associated with the Mo_2O_{10} dimers.

A similar analysis can be made for the square prismatic Mo_2O_8 dimers. The two types of dimers (with Mo1 and Mo2 sites) have nearly identical local environments, and thus the splitting of the Mo *d* orbitals occurs in the same manner for these two sites. The starting point for understanding the Mo_2O_8 energy levels is the single ion picture, with each Mo cation residing in what is effectively a square planar environment. The relative energies of the 5 *d* orbitals in the square prismatic ligand field environment can be understood by thinking of the prisms as octahedra in which the repulsive interactions in the *z*-axis direction have been removed due to the lack of axial ligands in this direction, resulting in *d* orbitals being stabilized (moving to lower energy) in proportion to their *z*-axis component. Thus the dz^2 orbital is strongly stabilized, the dxz and dyz orbitals are modestly stabilized, and the dxy and dx^2-y^2 orbital energies are

essentially unchanged relative to an ideal octahedron with the difference in their relative energies remaining that of the octahedral crystal field splitting, Δ_O (as shown in Figure S7). Since the prismatic sites have 4-fold rotational symmetry along their *z*-axis, the *d*xz and *d*yz orbitals are necessarily identical in energy and are completely degenerate in the single-ion picture.

The π and π* MOs derived from the *d*xz and *d*yz orbitals do not break the 4-fold symmetry and thus preserve this degeneracy of their parent orbitals. As a result, the *d* orbital states associated with the Mo_2O_8 dimers will form MOs with 8 different energies, in contrast to the 10 non-degenerate MOs that form for the Mo_2O_{10} bioctahedra. Although the dz^2 orbital has only the third-lowest energy in the single-ion picture, the σ-bonding MO derived from this orbital will have the lowest energy among the MOs associated with the Mo_2O_8 dimers and will be fully occupied. The other two fully occupied MOs will be the degenerate π-bonding orbitals derived from the *d*xz and *d*yz single-ion orbitals, which have both the lowest energy in the single ion picture and the second-highest degree of hybridization in the presence of metal-metal bonding. The lowest unoccupied molecular orbital (LUMO) is expected to be the δ-bonding orbital derived from the single-ion *d*xy orbital, followed by the δ*, π*, and σ* anti-bonding orbitals at somewhat higher energies, and the δ and δ* orbitals derived from the dx^2-y^2 orbital at much higher energy.

The initial orbital assignments obtained using simpler LMTO methods on unrelaxed structures were confirmed when further LDA and LDA+U calculations using the projector augmented wave method that incorporated internal structural relaxation were carried out. The band gaps obtained using LDA (indirect 0.50, eV; direct, 0.64 eV) and LDA+U (indirect 0.68, eV; direct, 0.81 eV), and are roughly consistent with both the LMTO result and the experimental onset of absorption. The LDA+U results were then used to directly calculate the optical response

expected for La_2MoO_5 (Figure 3.10) in order to better understand the manner in which metal-metal bonding affects the optical response of this compound.

This optical response is non-trivial to interpret since Mo ions are found in three spatially distinct crystallographic sites with two different types of local coordination geometries. An analysis of the LDA+U results finds that the highest occupied states are mainly on the prismatic Mo1 and Mo2 sites (*d*xz and *d*yz π-bonding states) while the lowest unoccupied states of minimal energy are associated with a number of different orbital states with π and δ character on all three types of Mo sites. As a result, all the possible optically induced transitions among these frontier orbitals involve weakly overlapping *d* electron states with π and δ character. This is reflected in the weak optical response due to dipole allowed transitions calculated for energies below 2.5 eV.

Around 2.5 eV, calculations predict the onset of an intense response originating from strongly coupled σ and σ* states associated with the octahedral dimers of the Mo3 site. A similarly intense response is also seen for the Mo1 and Mo2 sites, though with a higher onset energy of ~3.5 eV that likely reflects the stronger hybridization associated with the much shorter bond length of the prismatic dimers. This intense σ-σ* excitation occurs for dz^2 orbitals aligned along the axis of the Mo-Mo bond in the dimers, and presumably reflects the fact that this specific transition is no longer symmetry-forbidden when the ideal symmetry of each component MoO_6 octahedra is strongly broken in this direction due to the anisotropy induced by dimerization. The optical response associated with this σ-σ* excitation is essentially fully polarized in the *z*-axis direction (Figure S8), reflecting the nature of the orbital contributions.

The fact that the calculated LDA+U optical response (Figure 3.10) appears very different from the experimentally measured optical response (Figure 3.6) can also be ascribed to symmetry breaking effects. The LDA+U calculations suggest a very weak absorption at low energies followed by an abrupt onset of strong absorption around 2.5 eV, in contrast to the experimental data which show a roughly linear increase in the intensity of absorption from the band gap up to the upper limit of the measurements (~5 eV). The DFT calculations were done for a frozen lattice with no account of vibrations, conditions under which the coordination polyhedra should have a reasonably ideal geometry based on the bond lengths (Table 3.3) determined from the average atomic positions (Table 3.2). The experimental optical data was collected at room temperature and the mean displacements for Mo and O ions are expected to be about 0.08 – 0.11 Å at this temperature based on estimates from the relationship $B_{eq} = 8\pi^2\langle u^2\rangle$. The thermal vibrations of these ions are therefore expected to cause very substantial distortions of the local symmetry, and optical transitions which are symmetry forbidden at low temperature should become much more allowed at room temperature. It is therefore anticipated that agreement between theoretical predictions and experimental observations would substantially improve if DFT calculations were carried out for trial structures with thermal displacements of ~0.1 Å, or if the 0 K DFT results were instead compared to optical data collected at cryogenic temperatures for which phonons and their accompanying thermal displacements are effectively suppressed.

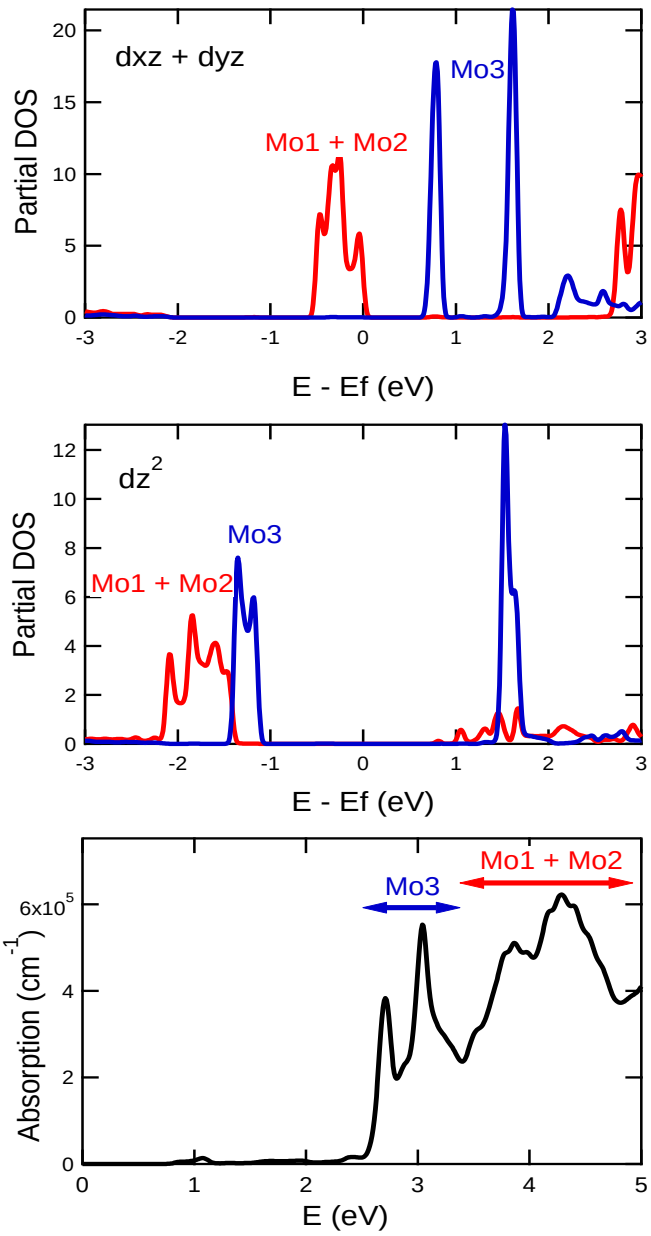

Figure 3.10. Top: Projected *d*xz and *d*yz density of states for the prismatic Mo1 and Mo2 sites (red) and for the octahedral Mo3 sites (blue). Center: Projected dz^2 states. Bottom: Calculated (LDA+U) absorption cross section including contributions from direct, dipole allowed transitions. While most *d*-*d* excitations are predicted to be very weak, strong σ-σ* transitions of the octahedral dz^2 states are clearly seen for photon energies of 2.5 – 3.5 eV.

One curious aspect of the experimentally determined La_2MoO_5 structure is the substantially different refined Mo-Mo bond lengths for the Mo1 site (2.22 Å) and the Mo2 site (2.28 Å), both of which have prismatic local environments that are equivalent and identical in the parent La_2ReO_5 structure type. These two Mo-Mo bond lengths have an unusually large estimated standard deviation of ~0.02 Å that are about 4 times larger than those of the Mo-O or La-O bonds, and which can be confirmed to reflect strong correlations in the refined positions of these two distinct Mo sites by an examination of the correlation matrix of the structure refinement. It is therefore unclear if these differences in bond length are real or reflect an artifact of the refinement. This quandary was addressed through further LDA calculations in which full structure relaxation was carried out by fitting the volume dependence of total energy to the Murnaghan equation of state (Figure S9). The equilibrium lattice parameters obtained in this manner were about 1.5% smaller than then experimentally determined values, as is typically observed for LDA calculations for compounds which do not exhibit strong correlation effects. The Mo-Mo bond lengths calculated for the fully relaxed DFT structure are 2.21, 2.25, and 2.62 Å for the Mo1, Mo2, and Mo3 sites, respectively. The experimental conclusion of a shorter bonds at the Mo1 site than at the Mo2 site is therefore supported by theory, and likely occurs as a result of the slightly different alignment of the two prismatic sites relative to the octahedral chains that occur at the Mo3 site. The different alignments are made possible by the reduction in symmetry of the octahedral Mo3 sites (2-fold) relative to the 4-fold symmetry found in the exclusively square prismatic sites in the parent La_2ReO_5 structure.

3.4. Conclusions

It is demonstrated that the novel structure of La_2MoO_5 corresponds to a superstructure of the parent La_2ReO_5 structure in which charge disproportionation occurs, leading to equal

amounts of Mo^{5+} ions occurring in Mo_2O_8 square prismatic dimers and Mo^{3+} ions occurring in Mo_2O_{10} octahedral dimers. This is the first example Mo charge disproportionation observed in a solid state compound. The presence of direct metal-metal bonding in these dimers results in the lifting of the *d* orbital degeneracy for the Mo cations in the dimers, resulting in 8 different sets of orbital states for the Mo_2O_8 prisms and 10 for the Mo_2O_{10} dimers. Through bond valence sum calculations it is shown that the presence of Mo-Mo bonding results in the weakening of Mo-O bonds. Although the electronic structure associated with La_2MoO_5 is complex, it is demonstrated that its main features can be readily explained within a molecular orbital picture in which the energy states expected for a single-ion configuration hybridize to form bonding (σ, π, δ) and anti-bonding (σ^*, π^*, δ^*) states which are roughly centered about the single-ion levels from which they are derived. This hybridization causes La_2MoO_5 to become a small band-gap semiconductor which has very substantial infrared absorption at room temperature, unlike the vast majority of oxide compounds. The structure-property relationships developed here provide a general framework for interpreting the complex behavior of compounds with metal-metal bonding, and for predictively harnessing the unusual electronic states of these oxide materials for technological applications.

Chapter 4

Observation of vacancies, faults, and modulations in $Ln_5Mo_2O_{12}$ compounds and their influence on physical properties associated with direct Mo-Mo bonding

4.1. Introduction

Compounds with direct metal-metal bonding form a very small but interesting subset of transition metal oxides due to the unusual electronic states that result from the metal-metal bonding. Analyses of the electronic structures of this class of compounds have shown that the degeneracy of the *d* orbital derived states can be mostly or completely lifted as a consequence of the metal-metal bonding, and that the resulting electronic states have a very sharp and narrow density of states that is more commonly associated with *f* electron states. These systems offer the potential for generating interesting and potentially technologically relevant physical properties, as *f* electrons may exhibit unusual behavior including heavy fermion transport and superconductivity associated with these heavy electrons. It has also been previously observed that these compounds may substantially absorb visible and even infrared photons, in contrast to most traditional closed-shell oxide semiconductors.

Among oxide materials, direct metal-metal bonding is found most often in early transition metal compounds, with Mo, Re, and Ru comprising the largest number of known oxides with metal-metal bonding.[12,15] Our recent efforts have focused on obtaining a comprehensive understanding of the metal-metal bonding present in lanthanum molybdenum oxides,[33] and the physical properties that may result from this bonding. This work has included the study of isolated Mo_2O_{10} edge-sharing bioctahedral dimers present in the compound $La_4Mo_2O_{11}$,[28] as well as the discovery of La_2MoO_5, a compound in which charge disproportionation leads to the presence of both Mo-Mo single bonds and triple bonds which are

associated with Mo^{5+} and Mo^{3+} species, respectively. The structure of La_2MoO_5 contains 1-dimensional (1D) chains of both Mo_2O_8 square prisms and Mo_2O_{10} edge-sharing bioctahedra, and for this reason has a very complex electronic structure.[33]

We have therefore chosen to try to synthesize the compound $La_5Mo_2O_{12}$ for further study. This compound, which should have only chains of Mo_2O_{10} edge-sharing bioctahedra based on the structure inferred from previous reports, is particularly interesting in that it represents one of the few examples of Mo-Mo bonding with a non-integer average Mo valence, namely $Mo^{4.5+}$. The presence of unpaired electrons was confirmed in prior studies of polycrystalline $Y_5Mo_2O_{12}$, which was found to have a local magnetic moment corresponding to one unpaired spin per dimer (μ_{eff} = 1.70 μ_B / Mo), with weak interactions between these moments (Curie-Weiss constant of θ = 7.5 K). The first determination of the structure of a $Ln_5Mo_2O_{12}$ (*Ln* = Y, La-Lu) compound was carried out using single crystal diffraction data for $Y_5Mo_2O_{12}$ and $Gd_5Mo_2O_{12}$.[29,100] Although a chemically reasonable structure could be refined in the proposed space group of *C2/m*, it was observed that there were weak but definite violations of the *C*-centering condition in the single crystal diffraction experiments. Curiously, the monoclinic lattice parameters of this compound were in general agreement with those described earlier for a series of compounds reported to have the composition $Ln_4Mo_2O_{10}$, where the investigated trivalent cations in the powder syntheses included the readily accessible lanthanoids from La – Lu as well as Y.[40,41,97] From these prior investigations, it can tentatively be concluded that 1D chains of Mo_2O_{10} dimers should exist for all $Ln_5Mo_2O_{12}$ compounds, and that there are some as-yet unresolved structural complexities in this family of materials that were not resolved in single crystal diffraction studies. Studies of $Ln_5M_2O_{12}$ (*Ln* = Y, Pr, Nd, Sm-Tb; M = Re, Ru) single crystals solved in the *C2/m* space group make use of minority sites to model extra density observed in Fourier

difference maps. These minority sites were refined to an occupancy of 2.27% in $Y_5Re_2O_{12}$ and 4.4% $Ln_5Ru_2O_{12}$.[25,44] Single crystal studies of the Y or Gd $Ln_5Mo_2O_{12}$ compounds solved in the *C2/m* space group do not include minority sites in the final crystal structure, but do make reference that perhaps a more suitable space group to describe all of the observed reflections would be *P2/m*.[44]

A summary of the prior structural information about the Mo-Mo bonding in $Ln_5Mo_2O_{12}$ compounds as well as their Re and Ru analogues is provided in Table 4.1. The number of electrons per transition metal available for the formation of Mo-Mo bonds is 1.5 for Mo, 2.5 for Re, and 3.5 for Ru, though it is possible that some of these electrons may reside in anti-bonding rather than bonding orbitals. An analysis of the bond lengths suggests that the *M-M* bond order is 1.5 when *M* = Mo or Re, but is reduced to 0.5 for *M* = Ru. It can be seen that the variation in *M-M* bond length is small for a given *M* when the *Ln* cation is varied, suggesting that that internal strain provided by smaller *Ln* cations can result in a small but measureable reduction in the *M-M* bond length

In this work, we have synthesized and characterized polycrystalline samples of $Ln_5Mo_2O_{12}$ phases with direct Mo-Mo bonds, as prior powder studies of these phases were carried out on samples synthesized with a 2:1 La:Mo ratio (with the single exception of *Ln* = Y)[29]. The structure of this class of compounds has been reinvestigated through synchrotron X-ray and time-of-flight powder neutron diffraction measurements. Through these studies (and complementary TEM investigations), it is observed that the $Ln_5Mo_2O_{12}$ compounds may exhibit vacancies, faults, and modulations – structural defects which were for the most part previously unrecognized for this class of compounds. Magnetic measurements show that as a result of these defects, it is possible for the Mo valence to be reduced from $Mo^{4.5+}$to $Mo^{4.05+}$, the first

observation of a reduction of the transition metal valence in this general structure type. The reduction is confirmed through the refinement of oxygen vacancies in neutron diffraction data, the observed changes in *Ln*-O and Mo-O bond lengths, the observed mass changes in thermogravimetric analysis (TGA), and the magnetic susceptibility differences between stoichiometric and non-stoichiometric $Ln_5Mo_2O_{12}$ compounds. Density functional theory (DFT) measurements have been carried out and used to assign orbital character to the electronic states in this material, and are analyzed together with optical measurements which provide complementary experimental insights into the electronic states in this family of compounds.

Table 4.1. Bonding in $Ln_5M_2O_{12}$ compounds (*M* = Mo, Ru, Re).

Compound	*d*-electron count	Bond length (Å)	Ref.
$Y_5Mo_2O_{12}$	1.5	2.496	[29]
$Gd_5Mo_2O_{12}$	1.5	2.521	[29]
$Lu_5Re_2O_{12}$	2.5	2.417	[39]
$Yb_5Re_2O_{12}$	2.5	2.419	[39]
$Tm_5Re_2O_{12}$	2.5	2.455	[39]
$Er_5Re_2O_{12}$	2.5	2.430	[39]
$Y_5Re_2O_{12}$	2.5	2.447	[44]
$Ho_5Re_2O_{12}$	2.5	2.436	[39]
$Dy_5Re_2O_{12}$	2.5	2.44	[39]
$Tb_5Re_2O_{12}$	2.5	2.448	[39]
$Tb_5Ru_2O_{12}$	3.5	2.777	[25]
$Gd_5Ru_2O_{12}$	3.5	2.774	[25]
$Eu_5Ru_2O_{12}$	3.5	2.780	[25]
$Pr_5Ru_2O_{12}$	3.5	2.804	[25]

4.2. Experimental

4.2.1. Synthesis

Rare earth oxides (99.99%, Alfa Aesar) of Ln_2O_3 (*Ln* = La, Y, and Lu) and MoO_3 (99.95%, Alpha Aesar) were used as starting materials. The rare earth oxides were dried at 1050 °C in air before weighing in order to eliminate absorbed moisture. Precursors of Ln_2MoO_6 were prepared by weighing out binary precursors in a 2*Ln*:1Mo stoichiometric ratio and then thoroughly mixing and grinding these powders in an agate mortar and pestle. Powders were then placed in dense alumina crucibles (CoorsTek) and heated in air (1050 °C, 12 h) to produce single-phase Ln_2MoO_6 samples, which in some syntheses were mixed with additional Ln_2O_3, and were then used in the synthesis of $Ln_5Mo_2O_{12}$ products. For samples prepared with lanthanum oxide, about 0.5 g of ground powder was placed in a 3 inch quartz boat prepared by cutting a quartz tube (18 mm OD, 16 mm ID) in half lengthwise. The powder sample was spread over approximately 1 in. of the quartz boat to keep powders within the narrow furnace hot zone. The quartz boat was placed within a 1 in. ID quartz tube in a Lindberg/BlueM Mini-Mite furnace under a flowing gas mixture of 5% H_2 / 95% N_2 (60 mL / min, passed through a line drier). After purging with the process gas, the sample was heated to 925 °C and reacted at that temperature for approximately 20 h. For the reactions involving Y and Lu, powder samples of Ln_2MoO_6 were placed in covered dense alumina crucibles inside a mullite tube (3.5” diameter) and heated in a reducing atmosphere of 5% H_2 / 95% N_2 (60 mL/min, not dried) at 1000 °C for 40 h in a Mellen SV Series furnace. All powder samples were observed to be a deep black color upon completion of the reaction.

4.2.2. Powder diffraction

Laboratory X-ray diffraction data were collected using a Bruker D8 Advance diffractometer with a nickel-filtered Cu K_α source. Data for Rietveld refinement were collected with a step size of 0.02° over a 2θ scan range of 7 - 140° using a fixed slit width of 0.3° and Soller slit widths of 2.5°. High resolution, high intensity synchrotron X-ray powder diffraction data were collected for the samples (La, Y, and Lu) at the APS 11-BM beamline. For these measurements, powder samples were packed into 0.8 mm Kapton capillaries. Data were collected with wavelength of 0.41333 Å over a 2θ scan range of 1 – 50° with a step size of 0.001°. Time of flight (TOF) neutron powder diffraction data were collected for *Ln* = La, Y, and Lu oxide phases at the NOMAD beamline located at the Spallation Neutron Source (SNS) at Oak Ridge National Laboratory. Room temperature data were collected on samples packed into 2 mm quartz capillaries. Rietveld refinement of all diffraction data were carried out using the TOPAS v4.2 software (Bruker AXS).

4.2.3. Thermogravimetric analysis

Thermogravimetric analysis (TGA) was used to probe the average oxidation state of Mo in each sample and was performed using a TA Instruments Q5000 IR instrument. Powder samples (10-20 mg) were loaded in 100 μL alumina pans, and were reacted under flowing O_2 (25 mL/min). Samples were heated at a rate of 1 °C / min to 800 °C and held there for approximately 4 h. The mass change difference during oxidation was calculated by comparing the sample mass observed during extended holds at 150 °C before and after oxidation at 800 °C in order to avoid errors associated with buoyancy or with surface-adsorbed moisture.

4.2.4 Magnetic susceptibility measurements

Magnetic measurements were done in a Physical Properties Measurement System (PPMS). The magnetic response was measured over the temperature range of 2 – 300 K with an applied field of 50,000 Oe. Both field-cooled (FC) and zero-field-cooled (ZFC) data were collected while continuously sweeping temperature at a rate of 1.34 K/min.

4.2.5 Diffuse reflectance and bidirectional reflectance spectroscopy

Low energy optical data were collected in a bidirectional reflection spectrometer equipped with an ASD detector (ASD, Inc.) over the range of 0.5 – 3.27 eV (380-2500 nm) with a detector change at 1000 nm and 1800 nm. Data were corrected using the method set forth by Hapke and a refractive index, *n*, estimated from the average refractive index of the starting oxide materials and a particle size estimated from Rietveld refinements with synchrotron data. For these experiments, powder samples were placed in a black dish, with the angle of incidence and reflected light set at 30°. The detector aperature was 5 mm in diameter. Data acquisition was carried out using the RS3 spectral acquisition software from ASD, Inc. Higher energy optical data were collected using a two-beam Perkin-Elmer Lambda 950 UV/VIS/NIR spectrometer with a 60 mm diameter and a spectralon-coated integrating sphere to collect the diffuse reflectance data. Undiluted powder samples were packed into black metal sample holders with a 1.5 mm thick quartz window (16.60 mm in diameter). Ground $BaSO_4$ powder (Alfa Aesar 99.99%) was used as a 100% reflectance standard. The Kubelka−Munk transform was used to calculate relative absorbances from the reflectance data through the relationship $\alpha_{KM} = \alpha/s = (1 - R)^2/(2R)$, where α_{KM} is a relative absorbance, α is the absolute absorbance, s is an generally unknown scattering coefficient, and R is the reflectance measured in the spectrometer.

4.2.6. Theoretical calculations

Density functional theory (DFT) calculations were carried out with the LMTO47c code, which utilizes a linear muffin tin orbital approach within a tight binding approximation and an atomic sphere approximation to model voids within the unit cell with empty spheres. The effects of the Mo-Mo bonds were studied with a "fatbands" analysis to assign Mo *d* orbital contributions to specific bands in the electronic band structure. Lattice parameters and atomic positions from obtained from Rietveld refinements were used directly as input for the program. Integration over k space was implemented with a 4 x 4 x 4 grid that resulted in 24 irreducible k points.

4.3. Results and Discussion

The properties of $Ln_5Mo_2O_{12}$ compounds are expected to be unusual due to the direct Mo-Mo bonding present in 1D chains of edge-sharing Mo_2O_{10} dimers that have been reported to exist within this structure type. Although single crystal samples of $Ln_5Mo_2O_{12}$ for *Ln* = Gd and Y have been prepared by electrodeposition[29], complementary powder studies of $Ln_5Mo_2O_{12}$ compounds for different types of *Ln* choices have only been carried out for samples prepared assuming a significantly different stoichiometry of $Ln_4Mo_2O_{10}$ (or equivalently, Ln_2MoO_5).[40,41,97] This discrepancy occurred because the prior powder studies of these rare earth molybdates were carried out in the late 1970's, well before the first single crystal structure determination was made for $Y_5Mo_2O_{12}$ (1985) or its Re (1982) and Ru (2009) analogues.[25,29,131,132] For this reason, it was judged worthwhile to reinvestigate the synthesis, structure, and properties of this class of Mo compounds using the modern tools developed in the four decades since the prior studies were performed. Furthermore, the optical properties of the $Ln_5Mo_2O_{12}$ compounds have never been previously studied, but are expected to be of interest given the significant absorption of

visible and infrared light that we have found for other oxide compounds with direct Mo-Mo bonding.[33]

Based on this motivation, polycrystalline samples with the nominal stoichiometry of both $Ln_5Mo_2O_{12}$ (5:2) and $Ln_4Mo_2O_{10}$ (4:2), as well as some intermediate compositions, were synthesized for the non-magnetic cations of *Ln* = La, Y, and Lu. All the Mo cations for the reaction were provided using a Ln_2MoO_6 precursor in which the Mo cations are fully oxidized (Mo^{6+}), and the additional rare earth needed to achieve the desired stoichiometric ratio was provided using powders of Ln_2O_3 binary oxides. A high-temperature (925 – 1000 °C) hydrogen reduction of the precursors was carried out under a dry 5% H_2 / 95% N_2 atmosphere in order to produce the reduced molybdate phases with Mo-Mo bonding. Surprisingly, the most pure product was obtained using a 4:2 precursor stoichiometry rather than the 5:2 stoichiometry that matches the composition determined from single crystal diffraction data, as shown for *Ln* = La in Figure 4.1. For this reason, samples used for physical properties characterization were all prepared using a 4:2 precursor stoichiometry.

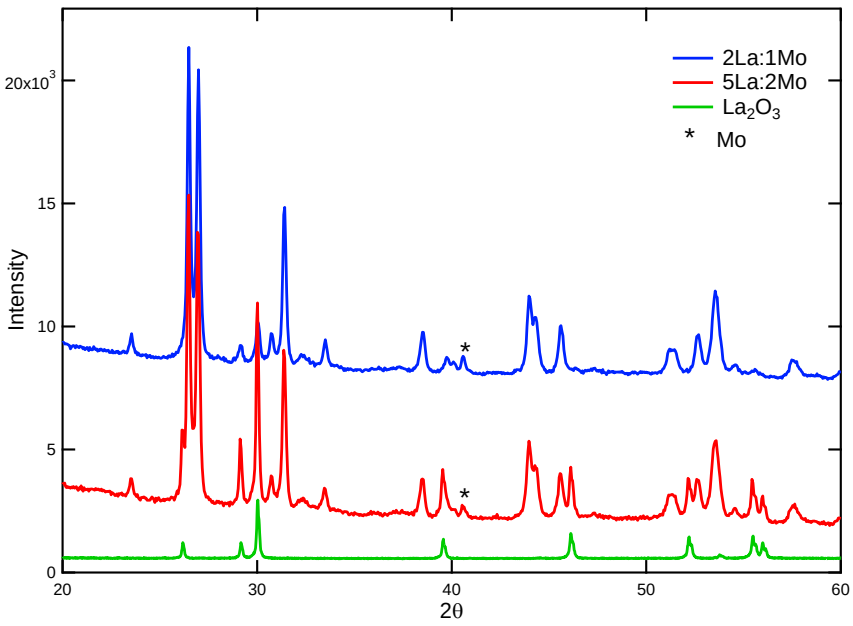

Figure 4.1. Laboratory XRD patterns of reaction products obtained using precursors with La:Mo ratios of 4:2 and 5:2. The 4:2 precursor stoichiometry (blue) results in the most pure product (only a small amount of Mo metal impurity, *), while a 5:2 precursor stoichiometry (red) resulted in an additional impurity of La_2O_3, as can be seen in by a comparison to the measured XRD pattern of La_2O_3 (green).

A close inspection of the X-ray diffraction (XRD) patterns of the reaction products in Figure 4.1 shows that the use of a 4:2 precursor results in a product which is not single phase, but instead contains a small amount of Mo metal (marked with an *). It was not possible to accurately quantify the amount of Mo through the Rietveld refinement of laboratory XRD data due to the small fraction of this phase, the small number of diffraction peaks associated with the simple BCC structure of this phase (a = 3.147 Å), and the high degree of overlap of these peaks with those of other phases. However, the small amount of Mo was generally consistent with the expected 4:2 precursor reaction mechanism (gaseous components omitted) below.

$$5\ La_2MoO_6\ (s) \rightarrow 2\ La_5Mo_2O_{12}\ (s,\ 95.7\ wt\ \%) + Mo\ (s,\ 4.3 wt\ \%) \qquad (1)$$

For *Ln* = Y and Lu, the amount of Mo metal could be quantified through thermogravimetric analysis (TGA) in which the mass change during high temperature oxidation

was followed, with the predicted and observed mass changes shown in Table 4.2. The TGA response showed two distinct features, with the low-T feature (< 400 °C) associated with the oxidation of Mo metal to MoO_3 and the high-T feature associated with the oxidative decomposition of $Ln_5Mo_2O_{12}$ to an overall oxidation product of Ln_2MoO_6 (Figures 4.2 and S2). The amount of Mo metal inferred from the low-T mass gain (1-2 %) was consistent with the proposed 4:2 precursor reaction mechanism. Similarly, the mass gain associated with the second feature was consistent with the proposed stoichiometry of $Ln_5Mo_2O_{12}$ though the overlap of the transitions limited the accuracy of the quantification and other stoichiometries for the $Ln_5Mo_2O_{12}$ phases (such as $Ln_5Mo_2O_{12-\delta}$) could not be ruled out. However, for *Ln* = La, the oxidation the $Ln_5Mo_2O_{12}$ phase occurred at temperatures well below 400 °C, and the two distinct oxidation features could not be resolved in TGA scans.

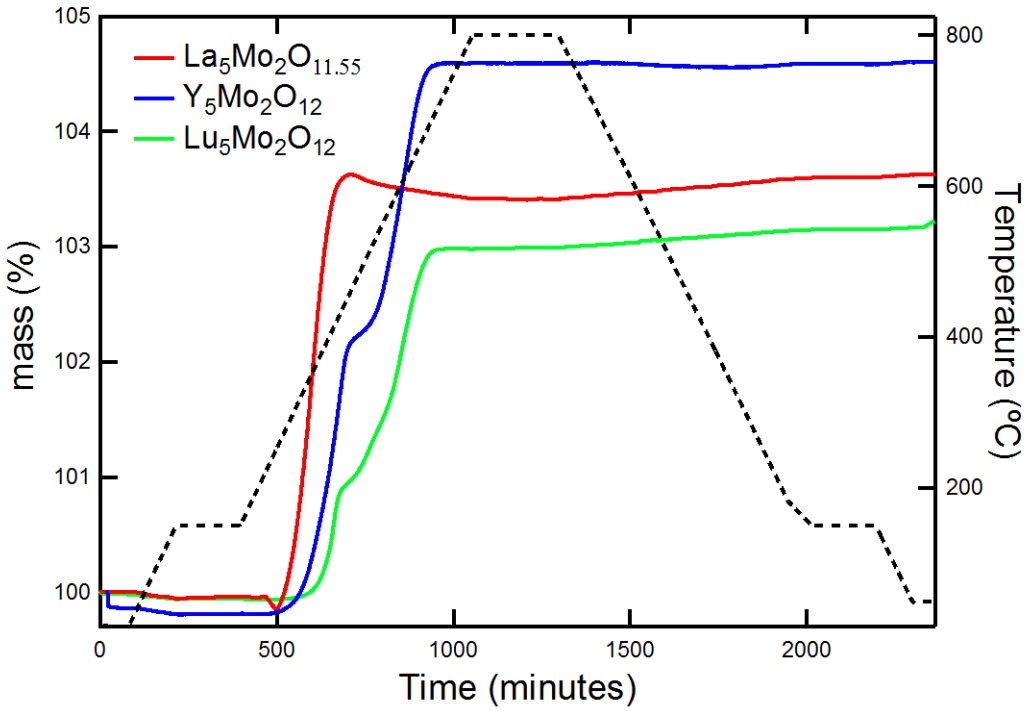

Figure 4.2. TGA data showing the mass changes as each reduced rare earth molybdenum oxide compound is oxidized to Ln_2MoO_6 following the programmed temperature profile (black dashed line). The shoulder in the Y and Lu molybdate data around 700 minutes is attributed to the oxidation of Mo to MoO_3.

Table 4.2. Comparison of predicted and observed mass (%) changes for TGA oxidation experiments of $Ln_5Mo_2O_{12}$ (*Ln* = Y, Lu) and the reduced molybdate sample formula determined from the mass change.

Ln	Predicted Mass %	Observed Mass %	Formula	Predicted Avg Mo^{x+}	Observed Avg Mo^{x+}
Y	5.47%	4.82%	$Y_5Mo_2O_{12.3}$	3.6	3.8
Lu	3.67%	3.26%	$Lu_5Mo_2O_{12.2}$	3.6	3.7

Although both the XRD phase analysis and the TGA results indicated that the 1D chain compound has a composition which is *Ln*-rich relative to the 4:2, *Ln*:Mo, precursor mixture that gave the highest purity reaction products, increasing the *Ln* content of the precursors reduced the purity of the reaction product rather than giving the expected increase in purity. This can most clearly be seen when the XRD products for a sequence of reactions with a variety of precursor compositions spanning the *Ln*:Mo range from 4:2 to 5:2 were tested (Appendix 3: Figure S1). While the use of a 4:2 precursor resulted in Mo metal as the only impurity phase, increasing the *Ln* content of the precursors always resulted in an increasing amount of a second Ln_2O_3 impurity phase in a manner consistent with a kinetically controlled overall reaction scheme in which the direct reaction 5 $Ln_2MoO_6 \rightarrow 2\ Ln_5Mo_2O_{12}$ + Mo is fast, but for which the two-component reaction 5 Ln_2O_3 + 4 Mo $\rightarrow 2\ Ln_5Mo_2O_{12}$ is slow at the reaction temperature (omitting gaseous species from the reaction schemes). The net reaction using a 5:2 or any other precursor stoichiometry which is Ln-rich is therefore approximately described by mechanism (2) for reaction temperatures of 1000 °C and below. It is expected that higher reaction temperatures will permit the production of $Ln_5Mo_2O_{12}$ from Ln_2O_3 and Mo precursors, as these conditions should allow thermodynamic equilibrium to be more quickly reached. However, higher reaction temperatures will also lead to additional experimental challenges (softening of fused quartz

tubes, need to re-investigate the proper process gas to achieve an appropriate pO_2 to stabilize the desired reaction product), and were therefore not investigated in the present study.

$$x\ Ln_2MoO_6\ (s) + y\ Ln_2O_3 \rightarrow 0.4x\ La_5Mo_2O_{12} + 0.2x\ Mo\ (s,\ 3.6\ wt\ \%) + y\ Ln_2O_3 \quad (2)$$

The measured laboratory XRD patterns for $Ln_5Mo_2O_{12}$ (*Ln* = La, Y, and Lu) samples prepared using a 4:2 , *Ln*:Mo, precursor stoichiometry are shown in Figure 4.3. In all cases, the 4:2 precursor could be used to produce samples in which the only impurity phase was a small amount of Mo metal (< 5%), which did not interfere with the structural analysis. The unit cell volume of $Ln_5Mo_2O_{12}$ phases was observed to increase proportionally to the cube of the appropriate rare earth ionic radius taken from the parameterization of Shannon[133] (Ln^{3+}, CN 6), as shown in the top portion of Figure 4.4. No anomalies were observed in the volume plot, indicating that Eu prefers a trivalent rather than divalent state within this structure, and that the $Ln_5Mo_2O_{12}$ structure is compatible with the full range of rare earth radii. In contrast, when the cell lengths in three perpendicular directions (*a*, *b*, and *c**) are plotted against the rare earth radius (Figure 4.4, bottom), it appears that the La compound is anomalous relative to the other rare earth analogues. Structural refinements and physical properties measurements both confirm that this phase is different from other members of this structural family, as will be discussed in detail later.

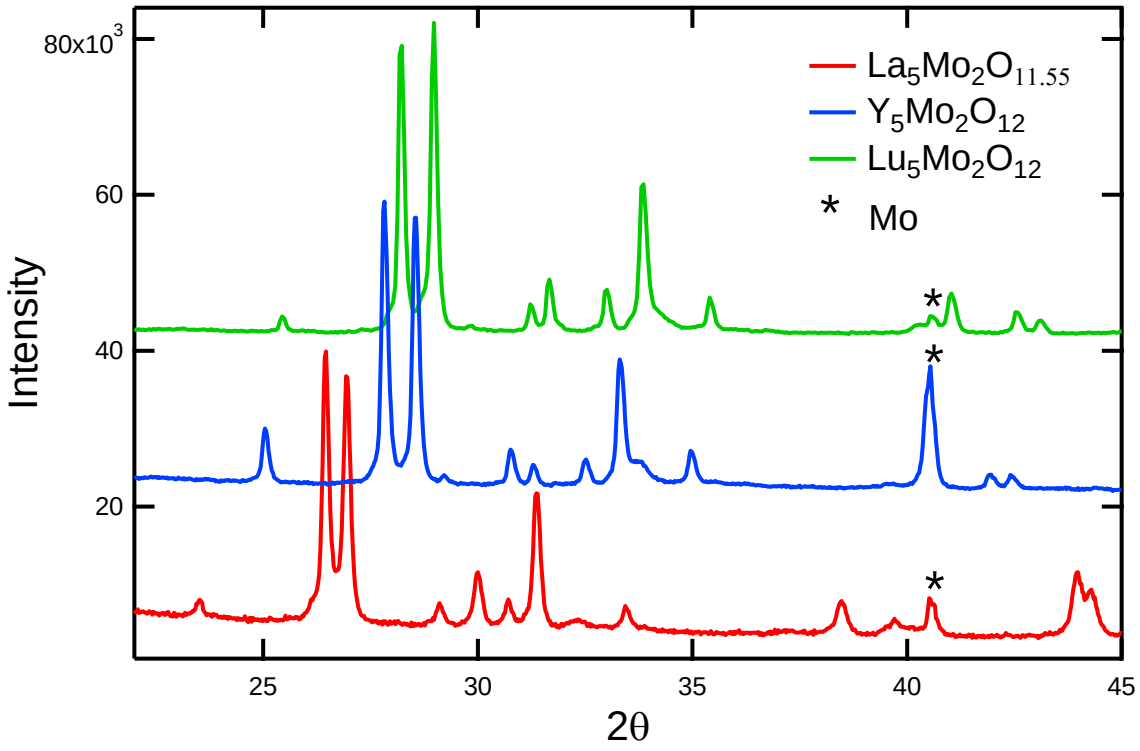

Figure 4.3. Laboratory X-ray diffraction patterns of $Ln_5Mo_2O_{12}$ samples (*Ln*= La, Lu, and Y). Patterns shift appropriately with size of the rare earth ions (La > Y > Lu) and size of the unit cell. The Mo impurity phase (*) is comparable among the three samples, although peaks of the main $Y_5Mo_2O_{12}$ phase overlap with the Mo impurity making the relative intensity of the Mo impurity appear greater.

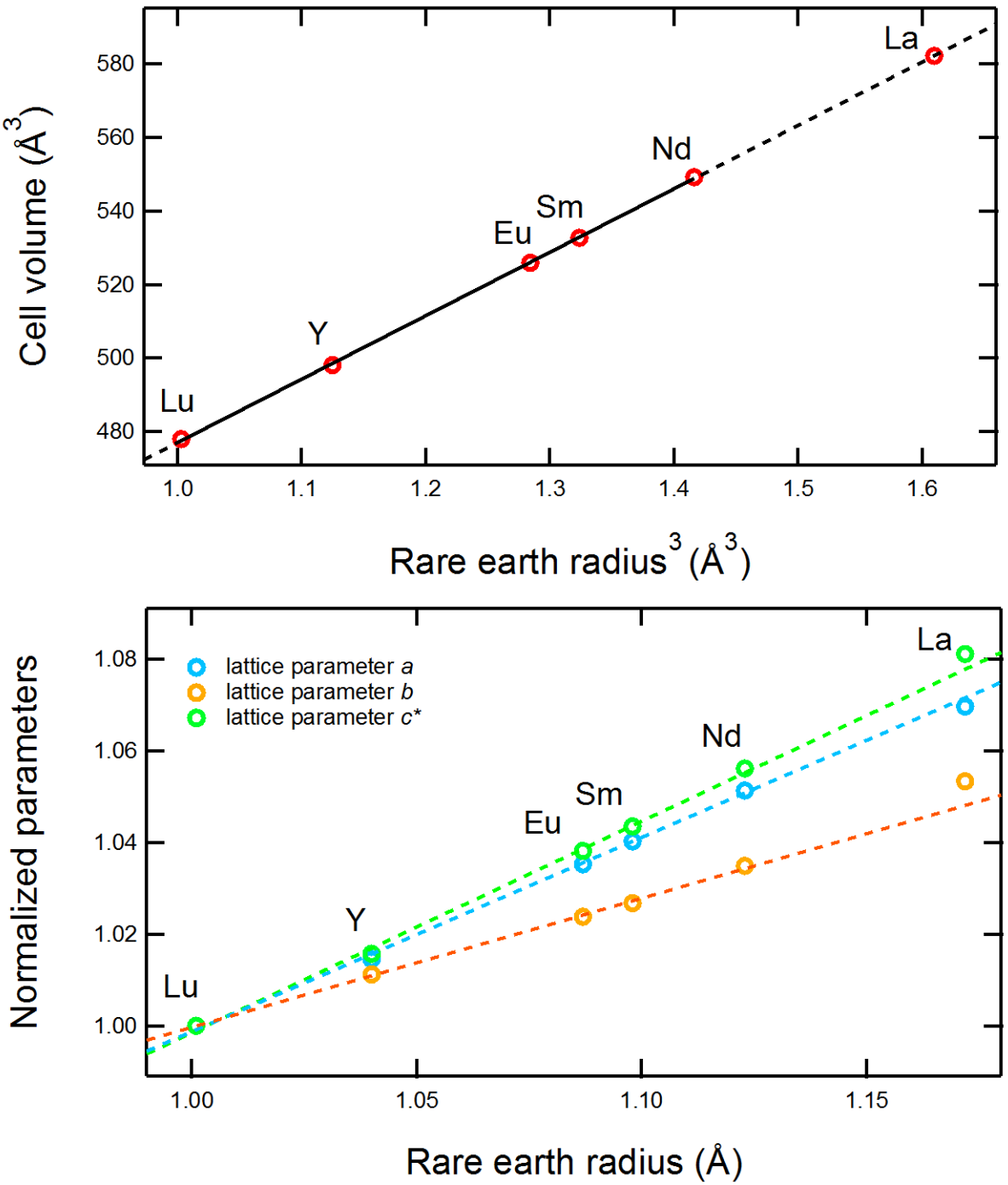

Figure 4.4. (Top) A plot of *C2/m* cell volume versus rare earth radii volume. Data for the Lu-Nd phases were fit (solid black line) to a linear function and extrapolated (dashed black line) to fit the range of the plot. (Bottom) The normalized cell parameters of each $Ln_5Mo_2O_{12}$ phase plotted as a function of rare earth radii. Again, data from the Lu-Nd samples were fit to a linear function (dashed lines) and extended to fit range of the plot.

Subcell description of $Ln_5Mo_2O_{12}$

$Ln_5Mo_2O_{12}$ samples prepared from precursors with 2:1 *Ln*:Mo molar ratios were used for more sensitive structural studies utilizing both synchrotron and time-of-flight neutron diffraction data for *Ln* = La, Y, and Lu. Due to the uncertainty of prior structural investigations, indexing studies were carried out on the synchrotron diffraction data in order to investigate the possibility of alternative symmetry, with the results summarized in (Table 4.3). Unexpectedly, it was found that all three compounds could be indexed to a previously unrecognized orthorhombic unit cell with dimensions of 12.2948(3) x 5.93894(7) x 3.97949(1) Å (volume = 290.575(7) $Å^3$) for the particular case of *Ln* = La. This orthorhombic unit cell was found to correctly predict the positions of all of the most intense diffraction peaks for this phase and can thus be considered to be a subcell, and the previously reported *C2/m* monoclinic unit cell (volume = 581.16(2) $Å^3$) should therefore be reclassified as a supercell. When comparative Pawley refinements of the synchrotron diffraction data were carried out in either the orthorhombic subcell or the corresponding monoclinic subcell (in which the *c*-axis length was reduced to half that of the monoclinic supercell), the differences in the ability to model diffraction peak shapes and also in the resulting refinement R_{wp} values were negligible (Table 4.3), confirming that the unit cells of $Ln_5Mo_2O_{12}$ compounds are metrically orthorhombic. A second possible supercell structure with a primative orthorhombic lattice and a doubled *c*-axis in relation to the *Immm* subcell was also tested, but provided minor improvements in regards to indexing addition supercell peaks. This possible second superstructure is discussed in more detail in later sections.

Table 4.3. Unit cell dimensions for $Ln_5Mo_2O_{12}$ compounds indexed in the orthorhombic subcell/supercell and monoclinic subcell/supercell using synchrotron data.

	R_{wp}	*a* (Å)	*b* (Å)	*c* (Å)	β (°)	Volume (Å^3)
$La_5Mo_2O_{11.55}$						
Immm subcell	14.086	12.2948(3)	5.93894(7)	3.97949(1)	90	290.575(7)
C2/m subcell	13.906	12.9218(3)	5.93895(1)	3.97954(4)	107.917(2)	290.586(8)
C2/m supercell	12.207	12.9218(3)	5.93904(4)	7.95911(7)	107.923(3)	581.16(2)
Pmmn supercell	13.130	12.2950(1)	5.93951(5)	7.9592(2)	90	581.23(1)
C2/m + Pmmn	9.183					
$Y_5Mo_2O_{12}$						
Immm subcell	16.184	11.6370(1)	5.72256(7)	3.74054(4)	90	249.096(5)
C2/m subcell	16.172	12.2169(2)	5.72221(8)	3.74032(5)	107.737(1)	249.046(6)
C2/m supercell	8.173	12.2176(2)	5.72242(7)	7.4806(1)	107.748(2)	498.11(1)
Pmmn supercell	13.111	11.6390(1)	5.72398(8)	7.4824(1)	90	498.49(1)
C2/m + Pmmn	7.325					
$Lu_5Mo_2O_{12}$						
Immm subcell	16.552	11.4662(1)	5.66435(6)	3.68587(4)	90	239.391(4)
C2/m subcell	16.122	12.0479(2)	5.66417(6)	3.68574(5)	107.886(1)	239.364(6)
C2/m supercell	9.086	12.0468(2)	5.66419(5)	7.37149(8)	107.872(1)	478.72(1)
Pmmn supercell	13.636	11.4659(1)	5.66407(6)	7.37148(7)	90	478.732(8)
C2/m + Pmmn	7.572					

The reassignment of the conventional monoclinic cell as a supercell is further supported by an examination of diffraction peak widths, which are consistently narrower for subcell peaks than for supercell peaks. In addition to having increased breadths, the superstructure peaks also exhibit an asymmetry which suggests that stacking faults limit the coherence of the superstructure (Figures 4.5 and S3-6). It is noted that orthorhombic indexing had previously been proposed for a compound with the nominal stoichiometry of "Yb_2ReO_5" (which is believed to correspond to the phase $Yb_5Re_2O_{12}$, based on subsequent structural work) with unit cell dimensions of 7.381 x 5.5598 x 12.206 Å, though these dimensions correspond to a supercell rather than a subcell and at the time were reported to be coincidental rather than reflecting the inherent symmetry of the phase.[39,42] In contrast, the present data clearly indicate that the orthorhombic lattice is the fundamental subcell of $Ln_5Mo_2O_{12}$ compounds.

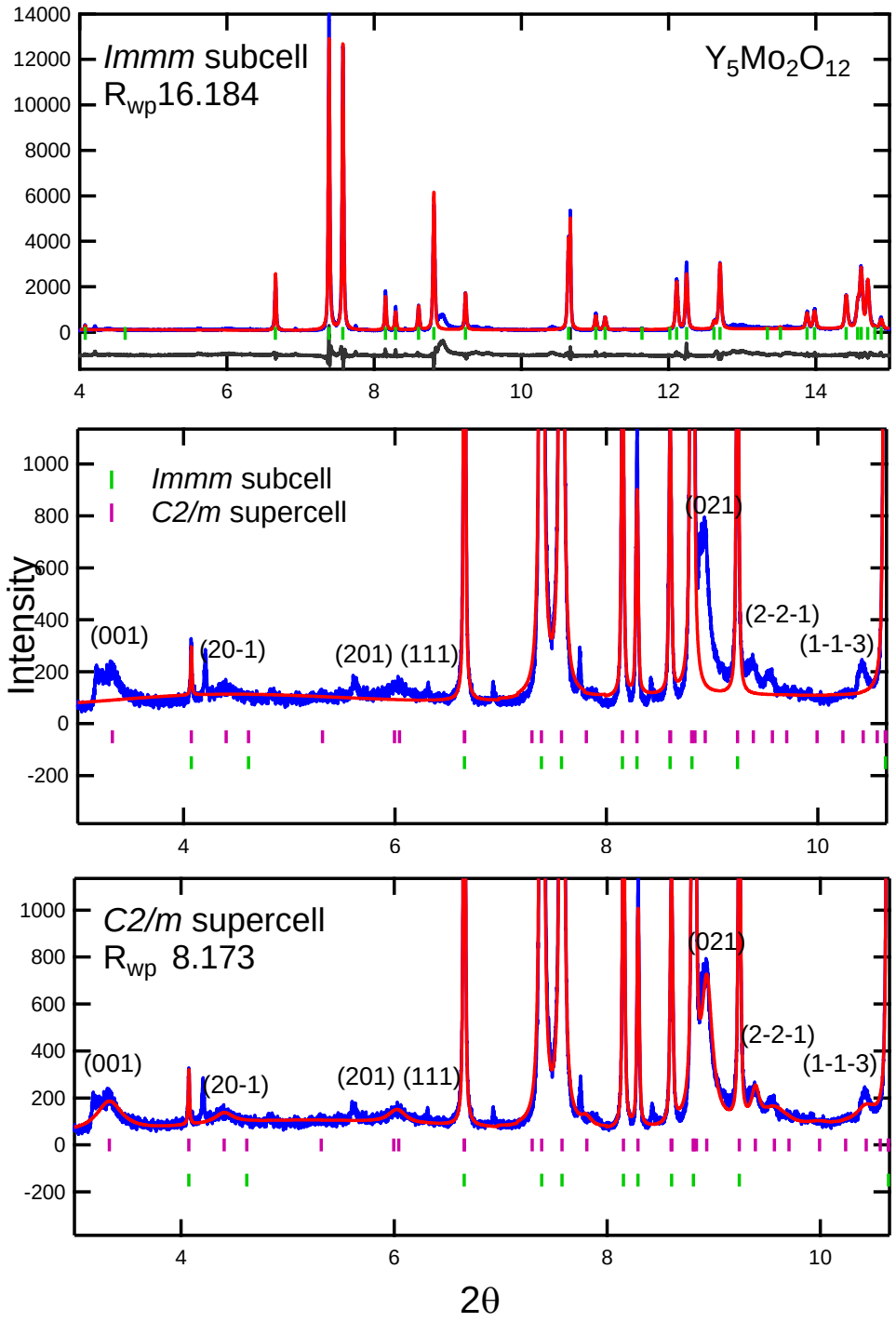

Figure 4.5. (Top) Result of a Pawley fit for $Y_5Mo_2O_{12}$ modeled in the *Immm* subcell. Data is shown in blue and the fit in red. (Middle) The same *Immm* subcell refinement highlighting the broader and unindexed peaks. The hkl indices are provided for some peaks that can be indexed by the *C2/m* supercell. (Bottom) Result of a Pawley fit for $Y_5Mo_2O_{12}$ modeled in the *C2/m* supercell.

The structure of the orthorhombic subcell was solved starting with charge flipping investigations of the synchrotron X-ray diffraction data, which suggested that the unit cell symmetry is *Immm* and which clearly indicated the positions of heavy atoms in solutions using this space group. The positions of oxygen atoms were then identified through a Fourier difference map analysis of neutron diffraction data. The final *Immm* subcell structure refined from the synchrotron diffraction data is given in Tables 4.4 and 4.5 for *Ln* = La, while the electron density maps and coordination polyhedra are given in Figure 4.6. Tables S1-S2 provide similar information for the remaining analogs refined in the *Immm* structure.

Table 4.4. Refinement parameters for $La_5Mo_2O_{12}$ refined in the *Immm* subcell.

Crystal system		Orthorhombic
Space group		*Immm* (#71)
Radiation		Synchrotron
Temperature		RT
λ (Å)		0.41333
Range of collection		$1° < 2\theta < 50°$
		$0.54 < d < 23.68$
Lattice parameters (Å)	*a*	12.29464(8)
	b	5.93891(4)
	c	3.97949(3)
Cell volume ($Å^3$)		290.569(3)
ρ_{calc} (g/cm^3)		6.1587(1)
R_{bragg}		3.83
R_{wp}		21.713

Table 4.5. Atomic coordinates of $La_5Mo_2O_{12}$ refined in the *Immm* subcell using synchrotron data.

	Wyckoff	*x*	*y*	*z*	*occ*	B_{eq}
La1	4f	0.31341(9)	0	½	1	1.2(1)
La2	2c	½	½	0	0.498(1)	0.7(1)
Mo1	4h	½	0.2836(4)	0	0.502(1)	0.7(1)
O1	8h	0.1618(6)	¼	½	1	1.3(2)
O2	4j	½	0	0.328(4)	0.49(1)	1.3(5)
O3	4i	½	½	0.392(5)	0.49(1)	2.4(6)

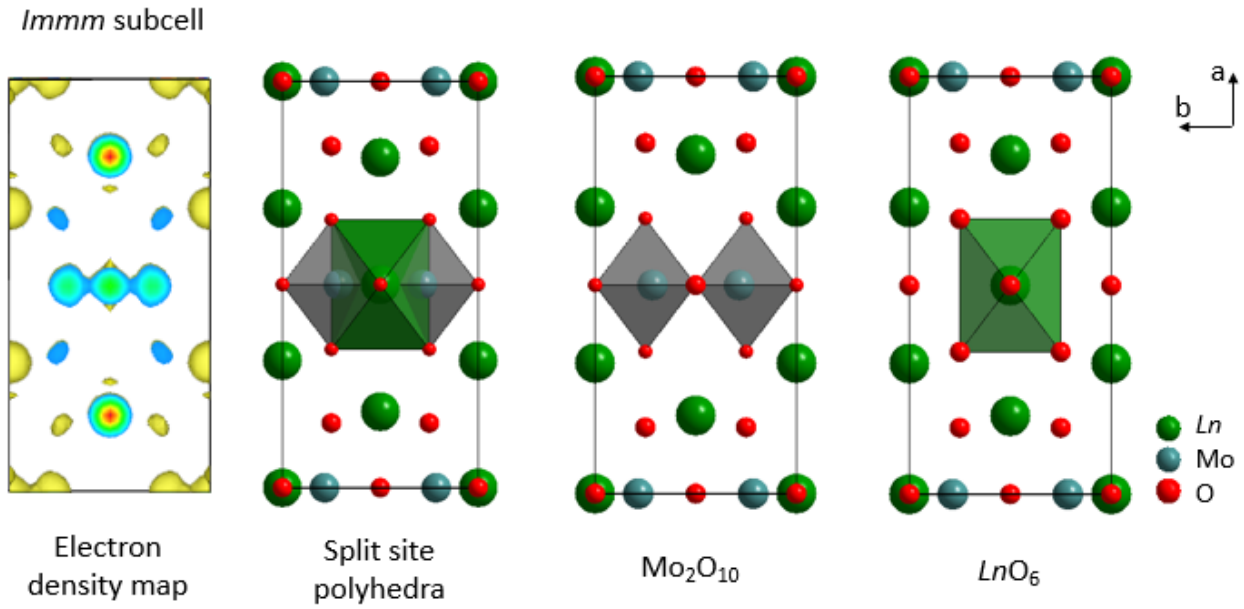

Figure 4.6. (Left to right) Electron density map produced from indexing the orthorhombic subcell. The overlapping polyhedra of the split LnO_6 or Mo_2O_{10} sites. The *Immm* unit cell shown centered with the Mo_2O_{10} dimer unit. The *Immm* unit cell shown centered with the LnO_6 dimer unit.

The close proximity and 50% occupancy of some nearby Mo and La sites as well as for some pairs of O sites indicate that disorder is present within the orthorhombic subcell, and suggest that the conventional *C2/m* monoclinic supercell represents a particular ordering pattern for atomic sites which are disordered in the subcell. A close inspection of the half-occupied sites of the *Immm* subcell and a comparison with their analogues in the conventional C2/*m* monoclinic

cell (Table 4.6) shows that the disorder in the subcell corresponds to two alternative building blocks that can fit within the same position in the *Immm* subcell, resulting in either edge-sharing chains of Mo_2O_{10} dimers or a series of isolated LaO_6 octahedra running repeating along the *b*-axis direction (Figure 4.6). While the subcell electron density results in the apparent superposition of these two structure motifs, the *C2/m* supercell structure reflects the alternation of Mo_2O_{10} and LaO_6 motifs along with a characteristic periodicity of $(½\ 0\ ½)_o$ relative to the orthorhombic subcell (Figure 4.7). Relative to the monoclinic cell vectors of the *C2/m* supercell, this ordering vector is $(0\ 0\ ½)_m$, resulting in the doubling of the *c*-axis period as well as the opportunity for defining all atomic sites to be fully occupied. When specified in terms of the orthorhombic subcell lattice vectors, the unit cell vectors of the *C2/m* monoclinic supercell are $a_m = a_o - c_o$, $b_m = b_o$, and $c_m = 2c_o$, though it should be noted that there is also a translational shift of 0, 0, ½ in the *c*-axis direction between analogous atom positions within the two cells due to their different choices of the unit cell origin.

Table 4.6. Orthorhombic and monoclinic cell site analogs.

Immm subcell	*C2/m* supercell
*Ln*1	*Ln*1
	*Ln*2
*Ln*2	*Ln*3
Mo1	Mo1
O1	O1
	O2
O2	O4
O3	O3

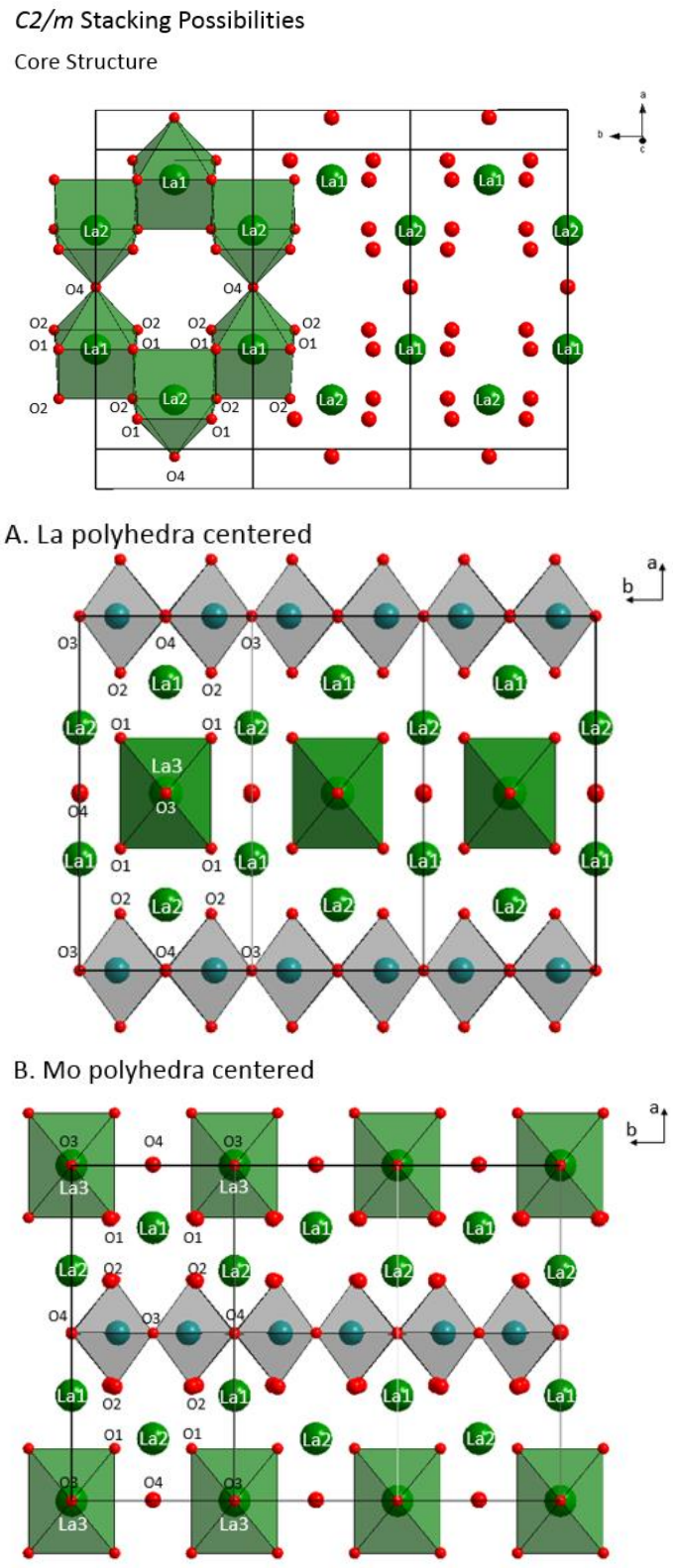

Figure 4.7. The two possible stacking possibilities upon going from the *Immm* subcell to the *C2/m* supercell are depicted.

The subcell structure can be compared to the geometric arrangement of atomic sites and coordination polyhedra within the conventional monoclinic unit cell of $Ln_5Mo_2O_{12}$ compounds, which are shown in Figure 4.6. The relationships between subcell and supercell atomic sites are summarized in Table 4.6. The 1D chains of edge-sharing MoO_6 octahedra with alternating short and long Mo-Mo bond distances of about 2.5 and 3.3 Å, respectively, are aligned parallel to the *b*-axis of the unit cell. The alternating short and long Mo-Mo distances clearly indicates the pattern of bonding and non-bonding interactions between successive Mo cation sites in the 1D chains. The *Ln*3 site, in the monoclinic supercell, is at the center of LnO_6 octahedra which bridge MoO_6 chains through corner-sharing connections at the equatorial O3 site of the Mo_2O_{10} dimers. The other equatorial oxygen site in these dimers, O4, is not shared with these octahedra due to steric constraints and is pinched in. These bonding arrangements result in the O3 sites being pulled out and the O4 sites being pinched in relative to the center line of the MoO_6 octahedral chains, with both displacements occurring parallel to the *c*-axis. Both the O3 and O4 sites in the monoclinic supercell are derived from different half-occupied sites within the *Immm* subcell. Similarly, the alternating 4g Mo and 2c *Ln*3 sites in the monoclinic cell are also derived from half-occupied subcell sites. In contrast, the *Ln*1 and *Ln*2 sites which separate the successive *bc*-planes of octahedral sites (MoO_6 and LaO_6) are fully occupied in the subcell, indicating that they remain in the same orientation relative to both the Mo_2O_{10} dimers and the LnO_6 octahedra of the *Ln*3 sites. This is also the case for the O1 orthorhombic derived sites. The O1 positions are always found at the center of OLn_4 tetrahedra that only have *Ln*1 and *Ln*2 ligands, and thus are also expected to be fully occupied in the supercell. The *Ln*1 and *Ln*2 sites can alternatively be described as occupying the center of LnO_7 monocapped trigonal prisms. The monoclinic O2 site, also derived from the orthorhombic O1 site, occupies terminal positions of

MoO_6 octahedra and LnO_7 monocapped trigonal prisms, though they are found at the apical position of the former and at edge sites of the latter (Figure 4.8), allowing the O2 site to remain fully occupied in the supercell.

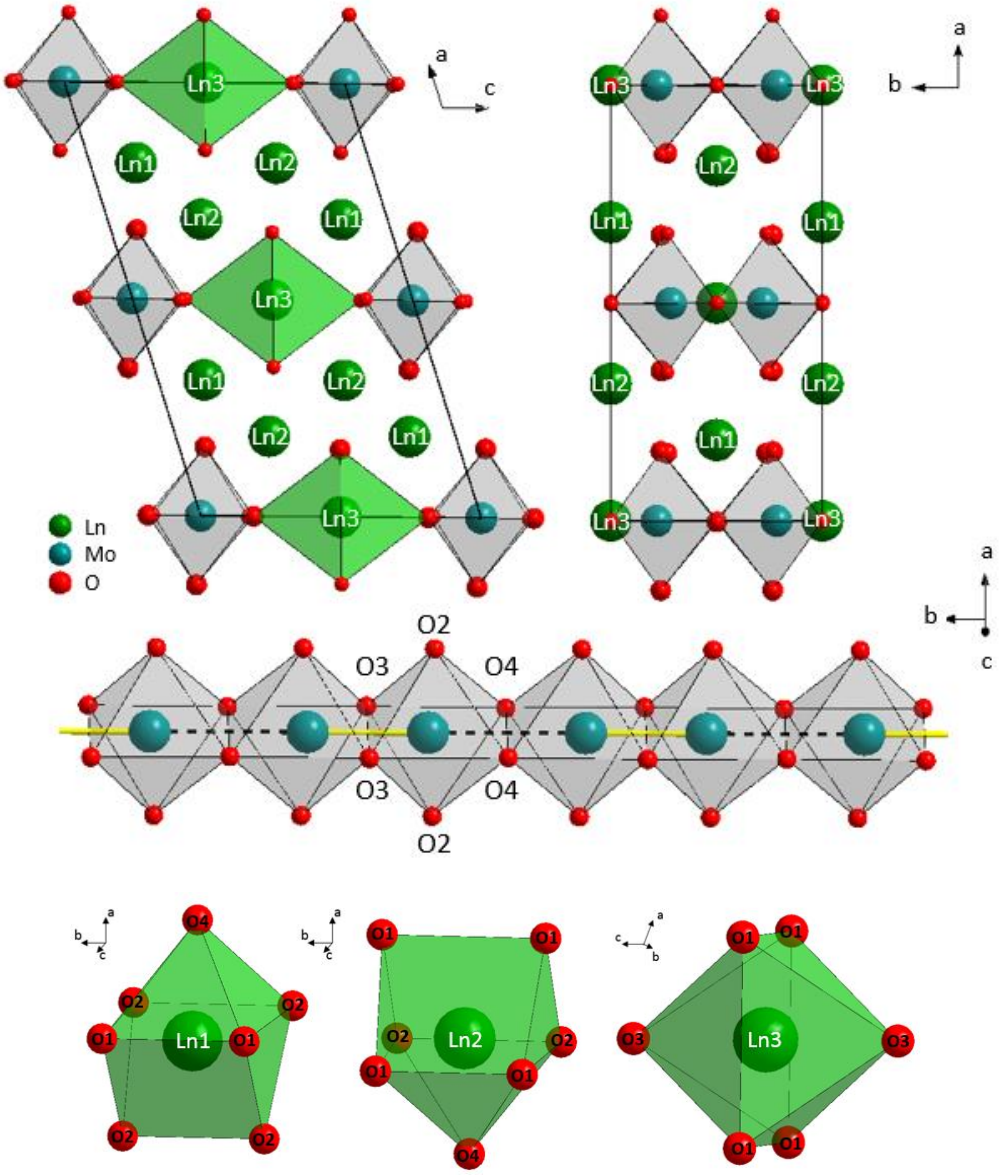

Figure 4.8. (Top) Two viewing directions of the $Ln_5Mo_2O_{12}$ monoclinic supercell crystal structure. Mo centered octahedral chains (gray) are isolated by LnO_6 octahedra (green) in the *c*-axis direction, and by *Ln*O7 monocapped trigonal prisms (not pictured) in the *a*-axis direction. (Bottom) Edge sharing MoO_6 octahedra extend along the *b*-axis of the unit cell alternating short Mo-Mo bonds (yellow) and longer (black) distances between non-bonded Mo atoms. The three *Ln* site polyhedra are also shown for reference.

Supercell description of $Ln_5Mo_2O_{12}$

Although the cell parameters of $Ln_5Mo_2O_{12}$ compounds are intimately tied to that of an *Immm* orthorhombic crystal system, the clear presence of superstructure reflections suggests that the most suitable space group for structural refinements should be one associated with a superstructure, such as the monoclinic *C2/m* setting that was previously reported in prior single crystal studies for Mo-, Re-, and Ru-containing members of this structural family.[25,29,39] However, it is possible and perhaps even likely that the *C2/m* space group does not fully capture the symmetry of this system and that an alternate symmetry description (such as a 3+1 dimensional commensurate superspace group or the use of representational analysis to describe additional symmetry elements within a conventional 3D space group) is needed to fully describe the symmetry of these compounds. The assignment of symmetry beyond that of the *C2/m* space group requires detailed information about systematic absences which are generally impossible to definitively resolve from powder diffraction data and are therefore beyond the scope of the present work. Furthermore, the fits to single crystal diffraction data for Mo, Re, and Ru compounds with this structure type described in previous reports were generally good, suggesting that the *C2/m* structural model effectively captures the main features of this structure type. Future single crystal diffraction experiments on these phases that for the first time explicitly test for the presence of symmetry beyond those of the 230 conventional 3D space groups represent the best approach for conclusively resolving the symmetry of the $Ln_5Mo_2O_{12}$ phases, but are beyond the scope of this work. In this study, our analysis has focused on carrying out Rietveld and Pawley refinements using a either the conventional *C2/m* space group used to describe this structure type in the past or an alternative *Pmmn* symmetry description corresponding to different ordering of structural building blocks.

A close examination of the synchrotron diffraction pattern of $Y_5Mo_2O_{12}$ clearly shows that there are numerous diffraction peaks beyond those predicted by the *Immm* subcell resulting in a doubling of the *c*-axis relative to that of the orthorhombic subcell, and many of the extra peaks which are visible can be indexed by the *C2/m* supercell (Figures 4.5 and 4.9) corresponding to extra periodicity with a vector of $(½\ 0\ ½)_o$ relative to the orthorhombic subcell. It is clear that the breadths of the supercell peaks (all l = odd reflections when indexed in the *C2/m* cell) are far larger than those of the subcell peaks. The peak widths of the supercell reflections could be quantitatively modeled by inferring stacking faults normal to the *ab*-plane, and when the coherence length in this *c** direction was refined using an approach previous proposed by P. Stephens[134], a coherence length of 26.3(2) Å was refined for $Y_5Mo_2O_{12}$ (APS data). Additional tests in which the coherence length was refined in the *a** direction produced little improvement compared both to not refining any coherence length or refining this length in the *c** direction.

Although Rietveld refinements using the *C2/m* description of the $Y_5Mo_2O_{12}$ structure (Figure 4.9) improved the quality of the overall fit to synchrotron diffraction data relative to the *Immm* subcell and accurately reproduced the observed intensity of subcell peaks, there were very substantial errors in the modeled intensity of some supercell peaks using the conventional *C2/m* structural model. As such, the *C2/m* description is believed to give a close but imperfect approximation of the structure of this $Y_5Mo_2O_{12}$ sample. Since stacking faults are expected to have their origin in the nearly interchangeable blocks of Mo_2O_{10} dimers and LnO_6 octahedra, there are multiple possibilities for the precise nature of this fault. Because the superstructure peaks are generally much weaker than the subcell peaks, the overall refinement R_{wp} is not very sensitive to the manner in which the superstructure is modeled – a challenge common to both

powder and single crystal diffraction experiments. One likely alternate superstructure is that formed with a $(0\ 0\ ½)_o$ basis vector, which simply results in a doubling of the *c*-axis length relative to the orthorhombic subcell lattice. Tests using Pawley fits indicated that a substantial improvement in the quality of the fit is possible when this alternate lattice is used as a secondary phase together with a *C2/m* phase (Figure S7).

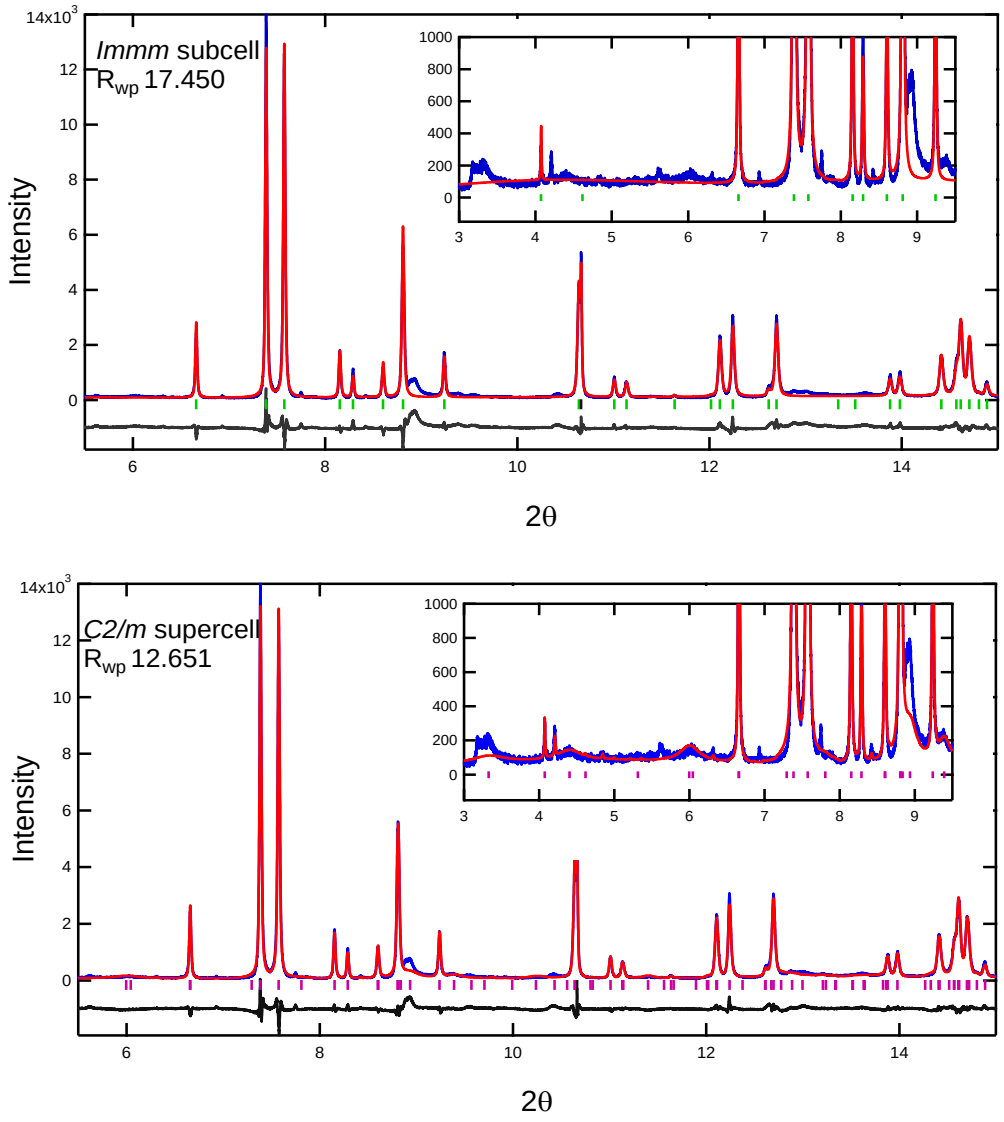

Figure 4.9. Comparison of the *Immm* subcell and *C2/m* supercell structural models (red) to the synchrotron data (blue). The difference pattern (black), tick marks for corresponding models, and r_{wp} are given for reference. Insets show modeling of one of the more intense supercell peaks.

Attempts to find a model structure with this alternate $(0\ 0\ ½)_o$ basis vector were carried out using Isodistort to generate and evaluate possible superstructures.[135] It was found that a probable space group for this alternative stacking sequence is *Pmmn*, with unit cell dimensions of 11.6390(1) Å x 5.72398(8) Å x 7.4824(1) Å for *Ln* = Y. The atomic site information for this *Pmmn* structural model is given in Table S3. The structures of the *Pmmn* and *C2/m* $Y_5Mo_2O_{12}$ polymorphs are compared in Figure 4.10. Both of these structures have blocks of Mo_2O_{10} and LnO_6 units alternating in the *c*-axis direction, and differ in only the relative alignment of layers of these blocks perpendicular to the *bc*-plane. It can be seen that fully coherent interfaces can be formed between these blocks normal to the *a** direction (referenced to either cell), and thus it is possible that coherent intergrowths of both polymorphs will form for $Y_5Mo_2O_{12}$ samples. It should be noted that if both polymorphs are coherently intergrown and their domain sizes are small, it will be impossible to accurately model the resulting diffraction pattern through a two-phase refinement of the *Pmmn* and *C2/m* polymorphs. The two best options for modeling structures of this type are (1) stochastic modeling based on stacking fault probabilities, as implemented in the DIFFAX and FAULTS software packages, or (2) explicit modeling of a single phase which is a superstructure containing coherent interfaces between blocks of these two polymorphs.[136,137] It is indeed found that while this *Pmmn* structure appears plausible, its inclusion in Rietveld refinements did not significantly improve the quality of the fit to diffraction patterns for any of the $Ln_5Mo_2O_{12}$ phases tested (Figures S8-10). While this might reflect the absence of long-range coherence of the *Pmmn* phase (*ie* if it is only present in the immediate vicinity of stacking faults), it might also indicate that the $(0\ 0\ ½)_o$ basis vector is important but gives rise to an alternate crystal structure, or that the $(0\ 0\ ½)_o$ basis vector is unimportant and that it was incorrectly assigned due to its ability to fortuitously index unidentified impurity peaks.

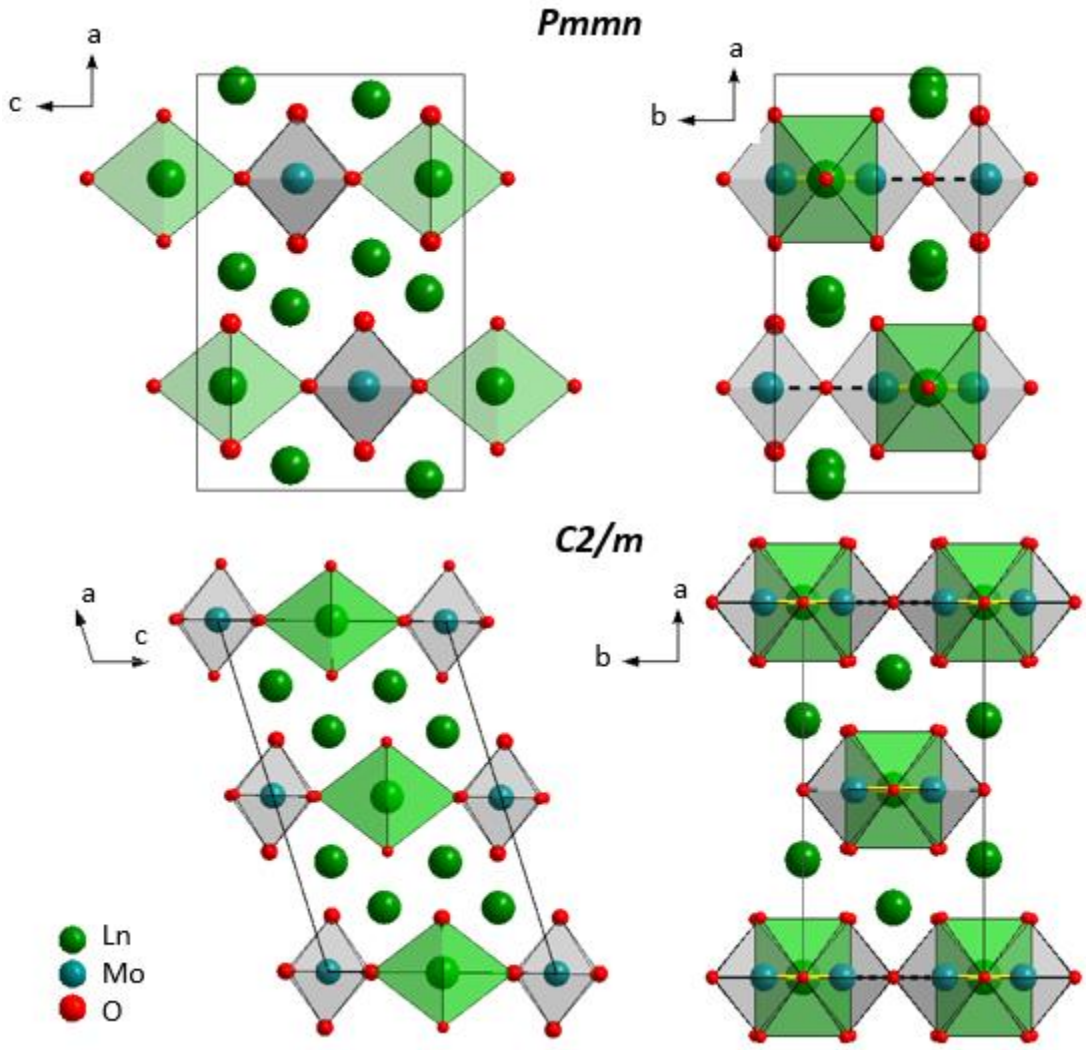

Figure 4.10. Comparison of *Pmmn* (top) and *C2/m* (bottom) supercells along several viewing directions.

Another potential source of faults in the $Y_5Mo_2O_{12}$ structure is a shear vector of (0,½,0) applied to layers of Mo_2O_{10} and LaO_6 units (organized in *bc*-planes). This *b*-axis shear corresponds to switching the pattern of dimerization between pairs of MoO_6 octahedra (swapping the positions of the non-bonded and bonded Mo-Mo neighbors), as well as switching the connection point for the bridging LaO_6 octahedra (changing the connection point from the O3 to the O4 site). The presence of this type of faulting might be indirectly inferred from a close inspection of Rietveld refinements of the $Y_5Mo_2O_{12}$ synchrotron diffraction data (Figure 4.11),

which shows that although most subcell peak intensities are very effectively modeled, the intensity of 0*k*0 reflections is systematically underestimated. This indicates a substantial error in describing the distribution of electron density parallel to the *b*-axis within the average structural model, and as such, hints at the presence of stacking faults of this type. However, there is no direct evidence for this type of faulting at the present time.

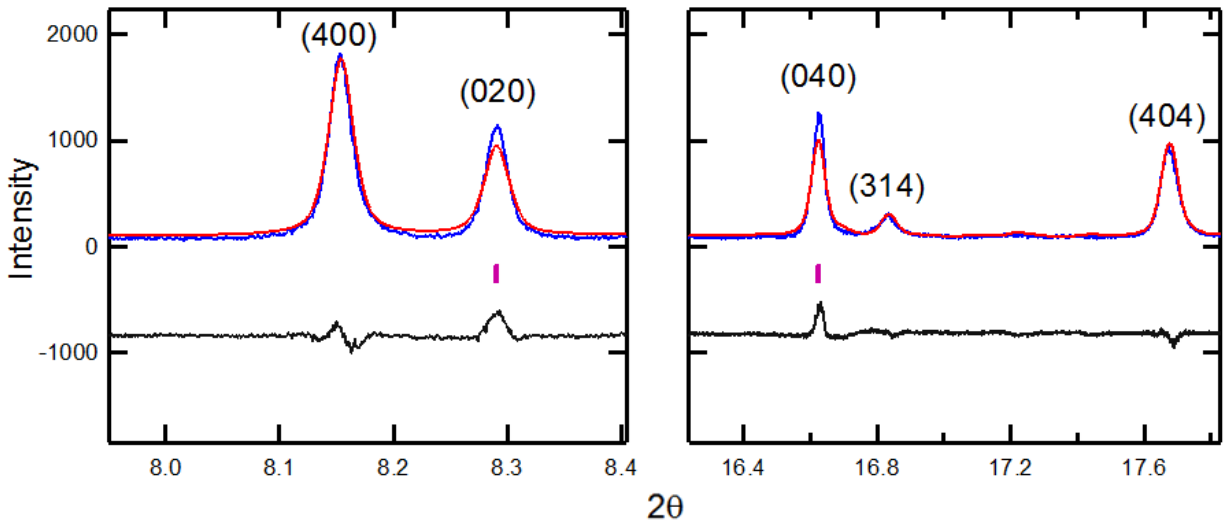

Figure 4.11. Synchrotron X-ray diffraction data showing the 0*k*0 peaks are ineffectively modeled for the $Y_5Mo_2O_{12}$ structure refined in the *C2/m* supercell.

Although stacking faults are clearly important as they are responsible for the very substantial broadening of supercell diffraction peaks (all *l* = odd reflections when indexed in the *C2/m* supercell), a comprehensive model for stacking faults is not available at this time and is beyond the scope of the present work. The *C2/m* superstructure represents the best structural approximation available for our $Ln_5Mo_2O_{12}$ samples, and was therefore used to model time-of-flight powder neutron diffraction data for compounds with *Ln* = La, Y, and Lu. The structures refined from this data are given in Tables 4.7 and 4.8, while selected bond distances are reported in Tables 4.9 and S4. There were no major errors in the fits to the neutron diffraction data,

though it is still possible that an improved treatment of stacking faults could further improve the minor differences between the observed and refined peak intensities (Figure S11).

Table 4.7. Crystallographic parameters of $Ln_5Mo_2O_{12}$ compounds refined from time-of-flight neutron diffraction data collected at 300 K.

		$La_5Mo_2O_{12-\delta}$	$Y_5Mo_2O_{12}$	$Lu_5Mo_2O_{12}$
formula weight (g/mol)		1070.44	828.44	1258.73
crystal system		monoclinic	monoclinic	monoclinic
space group		*C2/m*	*C2/m*	*C2/m*
Z		2	2	2
radiation		neutron (TOF)	neutron (TOF)	neutron (TOF)
temperature		300 K	300 K	300 K
range of collection (Å)		0.4 < d < 3	0.4 < d < 3	0.4 < d < 3
coherence length (Å)		12.3 (2)	20.5 (2)	14.1(8)
unit cell dimensions	*a*	12.907(2)	12.238(2)	12.0393(7)
	b	5.9552(6)	5.7269(6)	5.6607(3)
	c	7.9646(8)	7.4830(8)	7.3659(4)
	β(°)	108.05(1)	107.907(7)	107.759(8)
cell volume ($Å^3$)		582.0(1)	499.0(1)	478.08(5)
ρ_{calc} (g/cm^3)		6.112(1)	5.513(1)	8.744(1)
R_{bragg}		2.548	3.386	3.39
R_{wp}		6.394	7.929	6.039

Table 4.8. Refined atomic coordinates, occupancies, and displacement parameters for $Ln_5Mo_2O_{12}$ type compounds refined from time-of-flight neutron data collected at 300 K.

	Wykcoff	*X*	*y*	*z*	*occ*	B_{eq}
$La_5Mo_2O_{11.55}$						
La1	4i	0.3124(7)	0	0.162(1)	1	0.26(7)
La2	4i	0.3171(9)	0	0.635(1)	1	0.26(7)
La3[a]	2c	0	0	½	0.82/0.18(4)	0.37(8)
Mo1[a]	4g	0	0.2173(8)	0	0.82/0.18(4)	0.37(8)
O1	8j	0.342 (1)	0.261(1)	0.427(2)	1	0.13(5)
O2	8j	0.1560(9)	0.2625(9)	0.073(2)	1	0.13(5)
O3 [a]	4i	-0.001(2)	0	0.810(1)	0.72/0.16(3)	0.72(9)
O4 [a]	4i	0.0001(2)	½	0.169(1)	0.72/0.16(3)	0.72(9)
$Y_5Mo_2O_{12}$						
Y1	4i	0.3144(5)	0	0.173(1)	1	0.54(9)
Y2	4i	0.3059(6)	0	0.636(1)	1	0.75(9)
Y3 [a]	2c	0	0	½	0.88/12(2)	0.30(5)
Mo1[a]	4g	0	0.2208(6)	0	0.88/12(2)	0.30(5)
O1	8j	0.3427(5)	0.246(1)	0.420(1)	1	0.70(3)
O2	8j	0.1620(5)	0.253(1)	0.074(1)	1	0.70(3)
O3 [a]	4i	-0.005(1)	0	0.7947(8)	0.88/12(2)	0.60(5)
O4 [a]	4i	0.0001(1)	½	0.1838(9)	0.88/12(2)	0.60(5)
$Lu_5Mo_2O_{12}$						
Lu1	4i	0.3136(3)	0	0.1747(9)	1	0.22(6)
Lu2	4i	0.3051(3)	0	0.6317(8)	1	0.17(6)
Lu3 [a]	2c	0	0	½	0.92/0.08(1)	0.14(3)
Mo1 [a]	4g	0	0.2188(4)	0	0.92/0.08(1)	0.14(3)
O1	8j	0.3457(2)	0.2460(7)	0.4251(9)	1	0.28(3)
O2	8j	0.1656(2)	0.2539(7)	0.0896(8)	1	0.28(3)
O3 [a]	4i	0.0086(6)	0	0.7966(4)	0.92/0.08(1)	0.24(4)
O4 [a]	4i	-0.0003(8)	½	0.1905(6)	0.92/0.08(1)	0.24(4)

[a] Sites have corresponding minority site related by (0, 0, ½)

Table 4.9. Mo-O and Mo-Mo bond distances refined from neutron data collected at 300 K.

site 1	site 2	mult	*Ln* = La	*Ln* = Y	*Ln* = Lu
Mo1	O2	x2	1.933(1)	1.896(6)	1.910(3)
	O3	x2	1.982(1)	1.977(6)	1.971(4)
	O4	x2	2.156(9)	2.109(6)	2.123(4)
	Mo (short)	x1	2.588(7)	2.529(7)	2.477(4)
	Mo (long)	x1	3.362(7)	3.196(6)	3.180(4)

Initial attempts to refine the monoclinic structure without explicitly modeling the larger widths of the supercell peaks gave rise to substantial errors in the determined crystal structure. An examination of Fourier difference maps (Figure 4.12) for refinements carried out in this manner indicated the presence of highly occupied minority sites (approximately 60/40 distribution between majority and minority sites) for a number of atomic sites (Ln3, Mo, O3, O4) which were shifted displaced from the majority sites by a monoclinic vector of $(0\ 0\ ½)_m$. For this reason, these minority site positions are exactly those that would be expected if stacking faults are present. Similar minority sites have been previously proposed in the single crystal structure refinement of $Y_5Re_2O_{12}$ and $Ln_5Ru_2O_{12}$ compounds.[25,44] However, we find that the occurrence of highly occupied minority sites is a refinement artifact, despite the fact that the Rietveld refinements indicated a nearly equal occupancy between the majority and minority sites. The influence of these minority sites on the modeled diffraction intensity is to uniformly reduce the supercell (l = odd) peak intensities. This reduction of supercell intensity greatly improves the refinement quality when the supercell peak intensities are modeled as being sharp. However, when the supercell peaks are broadened by properly incorporating the supercell coherence length of ~25 Å, the maximum intensity of the supercell peaks is suppressed as a result of this broadening and the refined majority/minority distribution is closer to 85/15. It is therefore expected that the non-zero refined minority site occupancy is indicative of the presence of stacking faults, but provides a much less robust means of quantifying the stacking fault abundance than the refined coherence length associated with the superstructure peaks.

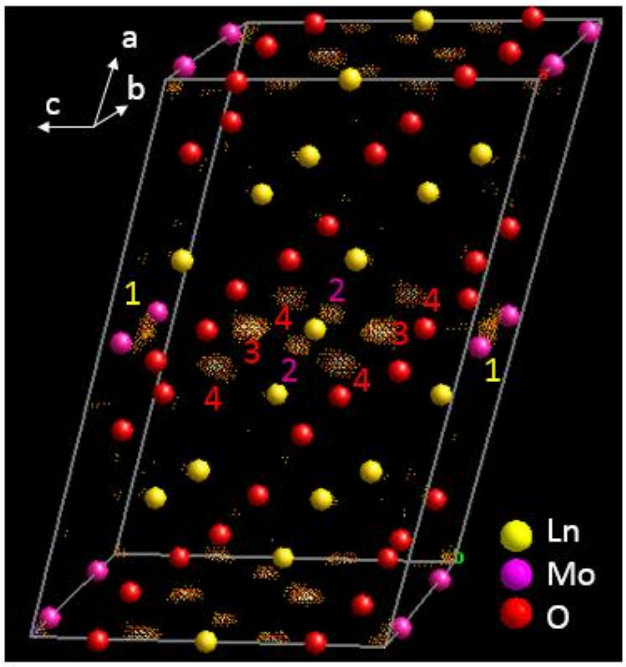

Figure 4.12. A Fourier difference map generated from a Rietveld refinement of the $Ln_5Mo_2O_{12}$ structure, modeled without minority sites, using neutron data collected at 300 K. Positive density is represented by yellow-orange clouds. The significant amount of density corresponds to a shift of the layers that contain MoO_6 and LnO_6 octahedra by ½ in the *c*-axis direction. The final structural model included the minority sites *Ln*3a, Mo1a, O3a, and O4a sites corresponding to sites labeled 1, 2, 3, and 4 respectively.

While Rietveld refinements utilizing neutron diffraction data support the assignment of $Y_5Mo_2O_{12}$ and $Lu_5Mo_2O_{12}$ as stoichiometric phases, they clearly indicate that $La_5Mo_2O_{11.55}$ has a substantial oxygen deficiency. The oxygen deficiency was clearly associated with the oxygen sites that are affected by the modulation (O3/O4) rather than those which were fully occupied in the subcell (O1/O2). However, it could not be clearly resolved if vacancies preferentially occurred at the O3 site, the O4 site, or a mixture of the two. While it is often challenging to refine accurate site occupancies from powder diffraction data due to correlations between occupancies and displacement parameters, the wide range of time-of-flight neutron diffraction data used in this refinement (dmin ~ 0.4-3 Å) should effectively eliminate these correlations. Furthermore, there are a variety of other indications that the stoichiometry of $La_5Mo_2O_{11.55}$

refined from the time-of-flight neutron diffraction data is accurate. As noted before, the anomalous behavior of this phase was hinted at by the deviation of its lattice parameters from the trends exhibited for the other samples in this series (Figure 4.4). The oxygen-deficiency of $La_5Mo_2O_{11.55}$ also results in a reduction in the average Mo oxidation state to a value of 4.05+ ($d^{1.95}$), which should lead to longer Mo-O bond lengths relative to $Y_5Mo_2O_{12}$ and $Lu_5Mo_2O_{12}$, both of which have an average Mo oxidation state of 4.5+ ($d^{1.5}$). These differences were more quantitatively evaluated through a bond valence sum (BVS) analysis.

In the BVS method, the contribution of each Mo-O bond to the overall Mo valence, *v*, can be estimated as $v = \sum_i v_i$ where v_i is the valence contribution from the i^{th} Mo-O bond with $v_i = e^{(R_0 - R_i)/b}$. In this equation, R_i is the experimentally determined Mo-O bond distance for the i^{th} bond, while the parameters R_0 and b are characteristic parameters determined from analyses of bond lengths available in crystallographic literature. Although the parameters for R_0 and b are typically specific for a single cation valence, Zocchi *et al.* have previously proposed a universal set of R_0 and b parameters that are applicable for Mo oxidation states from 3+ to 6+.[80] These parameters of R_0 = 1.8788 Å and b = 0.3046, were used to calculate the Mo valence for the La, Y, and Lu phase (Table 4.10), resulting in estimated Mo oxidation states of 3.9+ for $La_5Mo_2O_{11.55}$, a value that is 0.4 valence units smaller than the value of about 4.25+ obtained for both $Y_5Mo_2O_{12}$ and $Lu_5Mo_2O_{12}$. For all three compounds, the calculated Mo oxidation states are slightly smaller than those predicted by their stoichiometries. The underestimation of the Mo valence by the bond valence method has been previously observed in other molybdate compounds with direct Mo-Mo bonds, and is ascribed to the direct Mo-Mo bond drawing electron density away from the Mo-O bonds, thereby leading to longer bond distances than in molybdenum oxides without direct metal-metal bonding.[33] The BVS results are therefore fully

consistent with the proposed stoichiometry of $La_5Mo_2O_{11.55}$ within the accuracy of the BVS method, and further support the conclusion that Mo in this compound is reduced relative to other rare earth analogues.

Table 4.10. Bond valence sum analysis.

	Atom 1	Atom 2	Mult	Bond length	Valence/bond	Site Valence
$La_5Mo_2O_{11.55}$	Mo1	O2	2	1.933	0.837	3.90
		O3	2	1.982	0.713	
		O4	2	2.156	0.403	
$Y_5Mo_2O_{12}$	Mo1	O2	2	1.897	0.942	4.27
		O3	2	1.977	0.724	
		O4	2	2.109	0.470	
$Lu_5Mo_2O_{12}$	Mo1	O2	2	1.910	0.903	4.18
		O3	2	1.971	0.739	
		O4	2	2.123	0.449	

Further evidence for the distinct nature of $La_5Mo_2O_{11.55}$ comes from thermogravimetric analysis (TGA) data collected during thermal oxidation carried out with a maximum temperature of 800 °C, with the data for *Ln* = La, Y, and Lu (Figure 4.2). As discussed before, the oxidative decomposition of $La_5Mo_2O_{11.55}$ occurred at temperatures about 200 °C lower than for the other rare earths, a very large difference that is tentatively ascribed to oxygen vacancies giving rise to enhanced mobility of O^{2-} anions with the solid oxide lattice. Although thermogravimetric analysis often allows oxidation states to be determined with high precision, that is not the case for the present samples. The sample containing $La_5Mo_2O_{11.55}$ was a multiphase mixture which contained both Mo metal and a $Ln_5Mo_2O_{12}$ phase, as well as a small amount of La_2MoO_6 based on the analysis of XRD patterns. The oxidation of Mo metal could not be fully separated from the oxidation of the $Ln_5Mo_2O_{12}$ phase, making estimates of the mass fraction of Mo metal from TGA impossible. Attempts made to determine the amount of Mo metal in samples through

quantitative phase analysis using Rietveld refinement had fairly high uncertainties due to the nearly complete overlap between the peaks from Mo metal and those from the $Ln_5Mo_2O_{12}$ phases. Working within these limitations, the average Mo oxidation state in $La_5Mo_2O_{11.55}$ was coarsely estimated to be 3.9+ from the TGA data, a result which is consistent with the oxidation state of 4.05+ expected based on the composition refined from neutron diffraction data but which is far from the oxidation state of 4.5+ that would be expected in the absence of vacancies.

More conclusive evidence for the presence of oxygen vacancies in $La_5Mo_2O_{11.55}$ comes from the comparison of the magnetic susceptibility data for this compound with that of $Lu_5Mo_2O_{12}$ (Figure 4.13). In both of these three compounds, the rare earth species has a non-magnetic closed shell configuration, and thus the magnetic susceptibility provides direct insights into the electronic configuration of the Mo cations. Plots of the magnetic susceptibility clearly show that the magnetic response is about ten times stronger for $Lu_5Mo_2O_{12}$ than $La_5Mo_2O_{11.55}$, indicating a different electronic configuration for these two compounds. For bioctahedral Mo_2O_{10} dimers, the *d* orbital degeneracy should be fully lifted, resulting in the formation of ten non-degenerate molecular orbitals. The Mo oxidation state of 4.5+ for $Lu_5Mo_2O_{12}$ results in a total of three *d* electrons per dimer, and one unpaired electron per dimer when these electrons are in their ground state configuration. Thus each dimer should have S = ½, with an expected effective moment of $\mu_{eff} = 1.73\ \mu_B$ per dimer or $0.865\ \mu_B$ per Mo cation. Field-cooled magnetic susceptibility data for $Lu_5Mo_2O_{12}$ were fit to a modified Curie-Weiss law of $\chi = \chi_0 + C/(T-\theta)$ with a Curie constant *C* of 0.259(1) emu/(mol K), a Curie-Weiss θ of -11.0(1) K, and a refined temperature independent susceptibility of $\chi_0 = -6.73(6) \times 10^{-4}$ emu/mol. Based on the Curie constant, the uncorrected effective moment of this sample is $\mu_{eff} = 1.44\ \mu_B$ per dimer. The effective moment after correcting for the mass of secondary phases is $\mu_{eff} = 1.52\ \mu_B$ per dimer, a

value which is fully consistent with the expected magnetic moment, and is in good agreement with the effective moment (1.70 μ_B) and Weiss constant (7.5 K) previously measured for powders of $Y_5Mo_2O_{12}$.[29]

If the composition of the La-containing phase was precisely $La_5Mo_2O_{11.5}$, the full reduction of $Mo^{4.5+}$ to Mo^{4+} should add another electron to each dimer, resulting in four total *d* electrons per dimer and no unpaired electrons in the non-degenerate molecular orbitals associated with these dimers, thereby resulting in the absence of magnetism. However, the stoichiometry of $La_5Mo_2O_{11.55}$ refined from neutron diffraction data suggests that the Mo valence is not completely reduced to 4+, and is consistent with the Curie-Weiss paramagnetism observed for this phase. Fitting the data to a modified Curie-Weiss law gives C = 0.029(1) emu/(mol K), θ = -6.9(6) K, and χ_0 = -6.33(6) x 10^{-4} emu/mol. By comparing the ratio of C obtained for *Ln* = Lu and *Ln* = La, the magnetic data can be used to estimate a stoichiometry of $La_5Mo_2O_{11.56}$, a value that is in very close agreement with the stoichiometry of $La_5Mo_2O_{11.55}$ refined from time-of-flight neutron diffraction data. The Weiss constant is weakly antiferromagnetic for both $Lu_5Mo_2O_{12}$ and $La_5Mo_2O_{11.55}$. While the dilution of spins in $La_5Mo_2O_{11.55}$ reduces the value of θ as expected, the change is small suggesting that the interactions between spins in successive Mo_2O_{10} dimers along the *b*-axis chains is very weak, and that longer-range interactions between spins provide the dominant magnetic interactions for this phase.

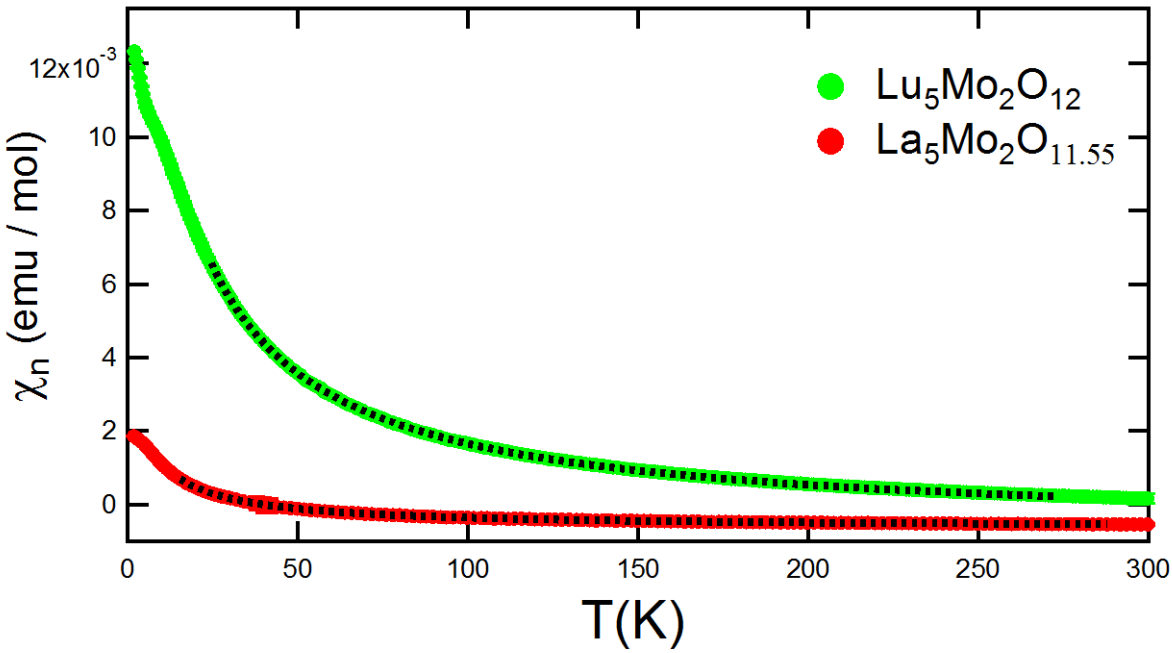

Figure 4.13. Magnetic susceptibility of $Lu_5Mo_2O_{12}$ (green) and $La_5Mo_2O_{11.55}$ (red) obtained from field cooled measurements with B = 5 T. The La-Mo-O phase exhibits about $1/10^{th}$ the moment of $Lu_5Mo_2O_{12}$. Fits to the data with the Curie-Weiss law are shown in black.

Optical absorption spectra (Figure 4.14) also confirm that the electronic configuration of $La_5Mo_2O_{11.55}$ is very different from those of $Y_5Mo_2O_{12}$ and $Lu_5Mo_2O_{12}$, two compounds which have nearly indistinguishable responses. Diffuse reflectance data were collected using two different methods to span different energy ranges, with lower energy data (0.5 – 3 eV) collected in a bidirectional reflectance geometry and higher energy (1 – 5 eV) data collected in an integrating sphere geometry. The data are generally complex, as is expected for compounds with Mo-Mo bonding, with the dominant optical feature of the $Ln_5Mo_2O_{12}$ compounds occurring at energies just below the visible light portion of the electromagnetic spectrum. For both the Y and Lu compounds, this feature is centered at about 1.25 eV, while the corresponding response in the La compound is shifted about 0.25 eV lower in energy. There is no evidence for a band gap in any compound over the range of accessible energies, and the absorption remains substantial

across this entire range. All three compounds show multiple additional broad optical features between 1 and 5 eV.

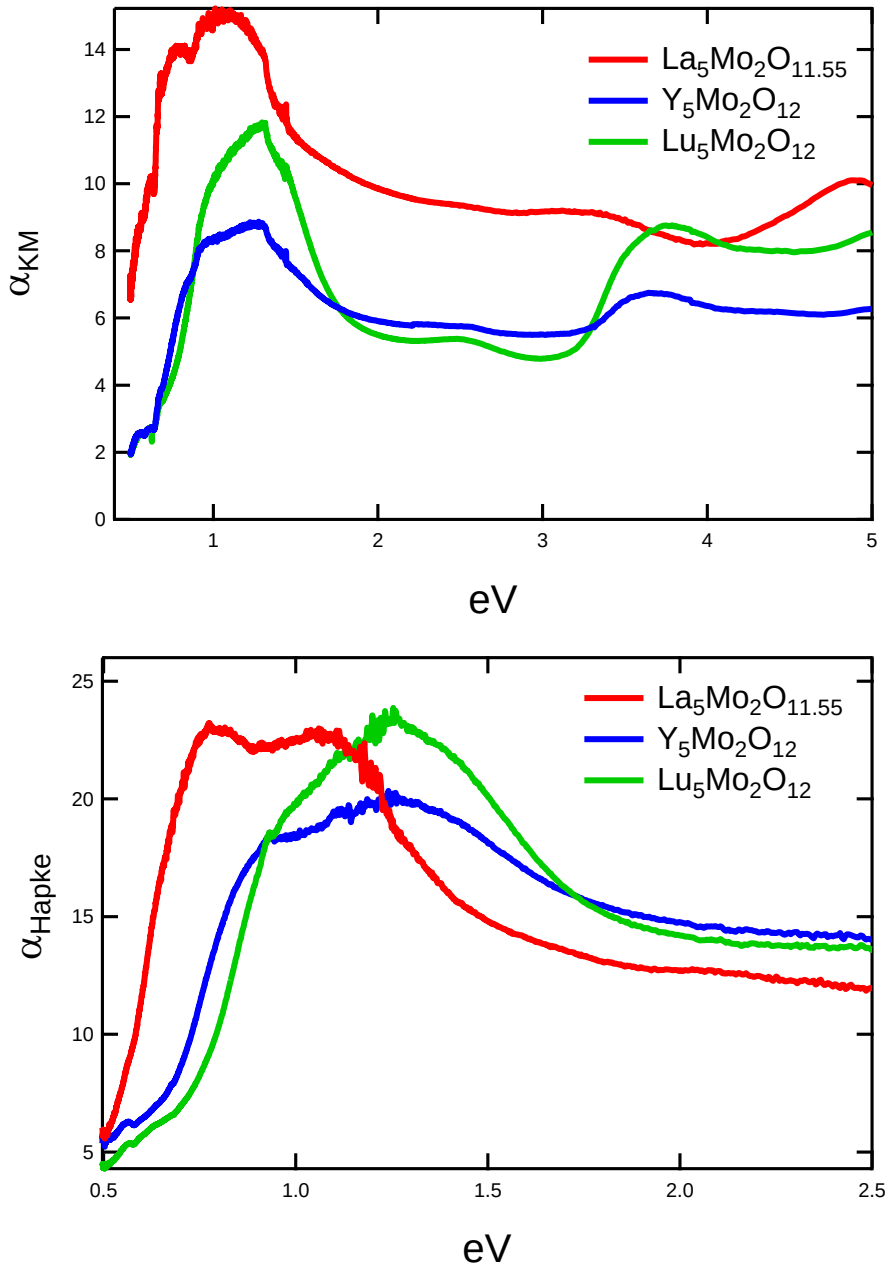

Figure 4.14. (Top) Relative absorbance spectra of $Y_5Mo_2O_{12}$, $Lu_5Mo_2O_{12}$, and $La_5Mo_2O_{11.55}$ obtained from a Kubelka-Munk transform of diffuse reflectance data. For *Ln* = La, Lu an absorbance offset of +0.65 was applied to data below 1.45eV to account for a change in instrument detector at 860 nm. (Bottom) Relative absorbance spectra of $Y_5Mo_2O_{12}$, $Lu_5Mo_2O_{12}$, and $La_5Mo_2O_{11.55}$ obtained from a Hapke transform of bidirectional reflectance data with n = 1.9 (estimated from n of Ln_2O_3 and MoO_3).

In order to better understand the origin and magnitude of these optical features (and especially their relationships to the orbitals affected by Mo-Mo bonding), the electronic structure of these compounds were investigated through density functional theory calculations, starting with linear muffin-tin orbital (LMTO) type calculations which are especially useful for providing insights about bonding. The band structure and density of states plots for $Y_5Mo_2O_{12}$ are shown in Figures 4.15 and 4.16, and are representative of the behavior of fully stoichiometric compounds in this series. As is observed for other compounds with direct metal-metal bonding,[22,33,45,46] there are many sharp peaks in the density of states with very narrow widths that are commonly observed for *f* electron states, but which are atypical for *d* electron states. LMTO calculations for the fully stoichiometric Lu and La $Ln_5Mo_2O_{12}$ analogs are provided in Figures S12-16.

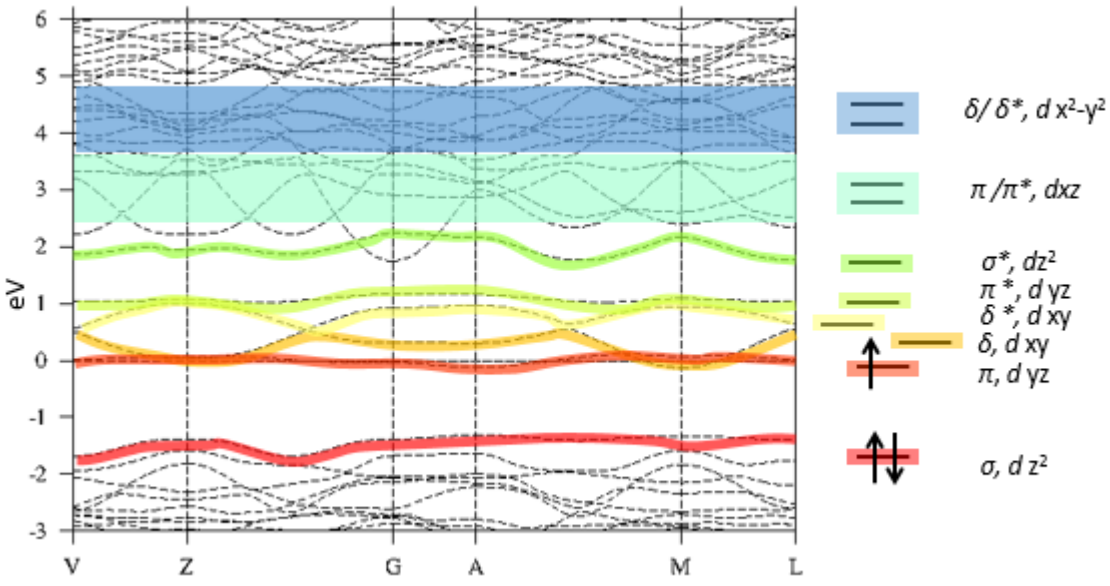

Figure 4.15. Electronic band structure of $Y_5Mo_2O_{12}$ calculated using the LMTO method. The orbital splitting assignments were based on the analysis of "fatband" plots provided in the supporting information. The Fermi level is set at 0 eV.

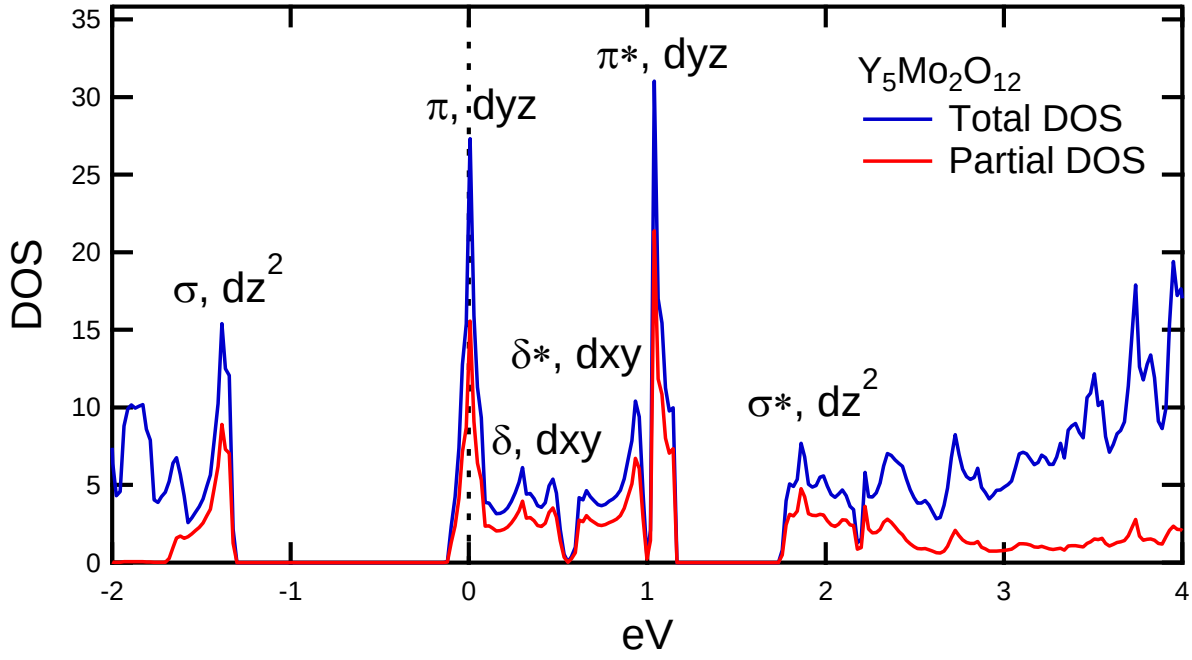

Figure 4.16. The total DOS (blue) for $Y_5Mo_2O_{12}$ is provided along with the Mo *d* orbital partial DOS shown in red. The orbital assignments were based on interpretation of the integrated DOS and the fatband analysis of the electronic structure.

A close examination of the density of states with the integrated density of states (IDOS) confirms the Mo valence assigned with bond valence sum analysis for the fully stoichiometric $Ln_5Mo_2O_{12}$ compounds. BVS estimated the single Mo cation valence to be 4.5+ with 1.5 electrons available for Mo-Mo bonding. Each peak observed in the DOS has an equal step size in the IDOS indicating that Mo *d* orbital degeneracy is completely lifted by the formation of the Mo-Mo bond across edge sharing octahedra. The first peak associated with the Mo *d* orbitals, -1.5 eV, can accommodate 2 of the 3 *d* electrons available per dimer for bonding, and the third electron goes on to partially fill the next highest energy level peak which crosses the Fermi level at 0 eV. Based on these calculations and interpretation of the electronic structure, a bond order of 1.5 can be assigned to the fully stoichiometric $Ln_5Mo_2O_{12}$ phases. In the oxygen deficient structure $La_5Mo_2O_{11.55}$, two $Mo^{4.05+}$ ($d^{1.95}$) cations would almost completely fill the second lowest energy orbital, resulting in a bond order closer to 2. This band structure also supports the

observed magnetic susceptibility behavior measured for the fully stoichiometric (*Ln* = Lu) and oxygen deficient *(Ln* = La*)* structures. Another observation that can be made about the DOS for the fully stoichiometric $Ln_5Mo_2O_{12}$ compounds is that the Mo *d* orbitals contribute both to the valence and conduction band edges, which is unusual for transition metal oxides where O 2*p* states are usually the primary contributor to the valence band.

As we have previously demonstrated, the character of the bands associated with the Mo_2O_{10} dimers can be intuitively explained based on simple molecular orbital assignments. The two sets of triply degenerate t_{2g} orbitals expected for two isolated MoO_6 octahedra are split into six non-degenerate orbitals in the context of a Mo_2O_{10} dimer with direct Mo-Mo bonding. The orientation of the Mo_2O_{10} dimer used for analysis is represented in Figure 4.17. These bonding orbitals (σ, π, δ) are lower in energy than the anti-bonding orbitals ($\sigma*$, $\pi*$, $\delta*$), and for $Y_5Mo_2O_{12}$, the relative energies of these orbitals are simply determined by the relative degree of hybridization ($\sigma > \pi > \delta$), as labeled in Figure 4.15 and schematically illustrated in Figure 4.17. Similarly, the Mo-Mo bonding lifts the degeneracy of e_g orbitals to produce a second set of orbitals with π and δ symmetry, though for these e_g-derived orbitals both the π and π^* orbitals are found to be lower in energy than the δ and δ^* orbitals, as is expected since the axial Mo-O2 bond lengths associated with the δ bonds are 0.1 – 0.2 Å shorter than the equatorial Mo-O3 and Mo-O4 bond lengths associated with the π bonds.

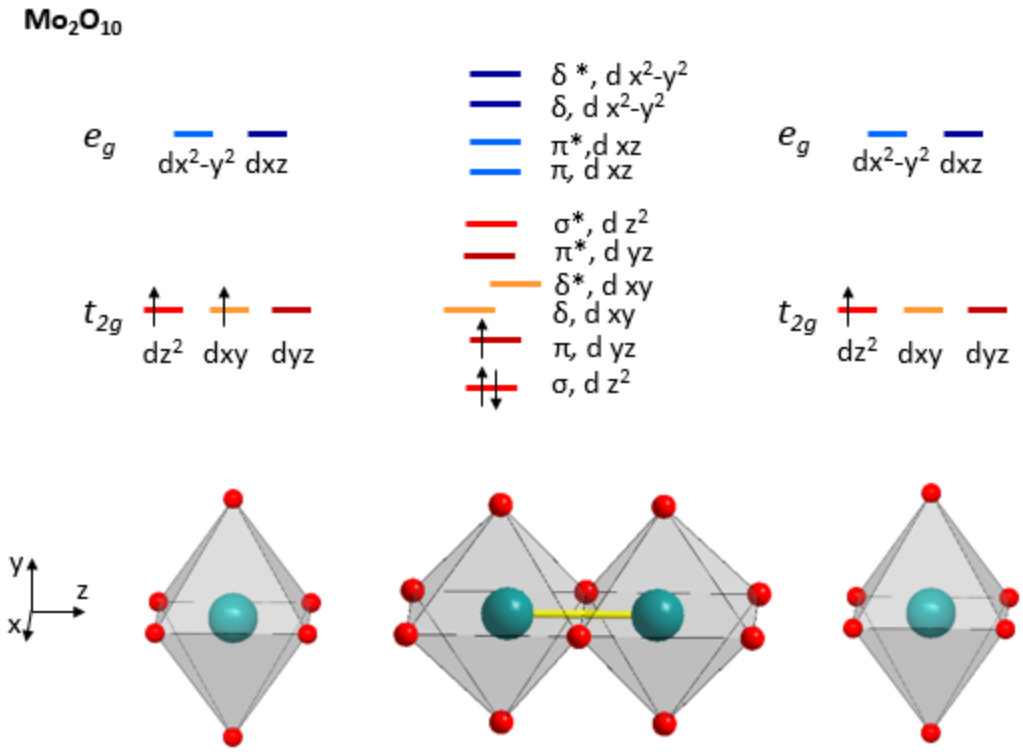

Figure 4.17. Molecular orbital ordering diagram for the Mo *d* electrons involved in forming the metal-metal bond (yellow) across the MoO_6 edge sharing octahedra.

Based on the LMTO calculations, it can be seen that the lowest energy *d* orbital states are the σ-bonding states derived from the dz^2 orbital, which are completely filled. The next lowest energy states are the π-bonding states derived from a *dyz* orbital, and Fermi level (E_F) of this compound is predicted to fall in the middle of these states, and as such, this compound is not predicted by DFT to have a band gap. Prior single crystal measurements on $Y_5Mo_2O_{12}$ have shown that this compound has activated transport with an activation energy of 0.29 eV, and this compound is therefore experimentally found to be a semiconductor.[29] In the context of the calculated band structure, this is not surprising. The Mo_2O_{10} dimers are organized into one-dimensional chains (and exhibit the characteristic U-shaped density of states expected for 1D chains), and thus should be susceptible to Peierls distortions.[138-140] Additionally, E_F falls in the

middle of states which form a very narrow band (width of ~0.25 eV, about ten time narrower than typical t_{2g} manifolds), and might therefore be expected to have a poor mobility. Finally, it has been previously observed for the compound La_2MoO_5 that there is a strong possibility for polaronic transport in compounds with 1D-chains of Mo-Mo bonded dimers, as the preferred local geometry is strongly sensitive to the electron configuration. Based on the results of these LMTO calculations, it can be tentatively inferred that the dominant feature around 1.25 eV is associated with π-π^* transitions. Also, σ-σ^* transitions have previously found to be important in compounds with dimeric units with Mo-Mo bonding, and it is likely that this is the origin of the broad optical feature observed at an energy of about 3.5 eV.

Higher level DFT calculations using GGA/HSE methods can be used to make more quantitative predictions about absorption spectrum and optical constants of this system. GGA calculations were carried out for both the hypothetical stoichiometric compound $La_5Mo_2O_{12}$ and for hypothetical analogs with ordered oxygen vacancies having the precise stoichiometry of $La_5Mo_2O_{11.5}$. The calculated imaginary dielectric constant ε_2 for stoichiometric $La_5Mo_2O_{12}$ is shown in Figure 4.18 together with the calculated absorption spectrum, $\alpha(E)$ for this compound. There are two strong features in the calculated ε_2 associated with metal-metal bonding, a feature at 1.0 eV that corresponds to a π-π^* transition, and a higher energy feature at 3.5 eV that corresponds to σ-σ^* transition. The energy of π-π^*transition closely matches that of the strongest feature in the optical spectrum. The σ-σ^* transition at 3.5 eV is not matched by a sharp feature in the experimental data, though it likely corresponds to a broad transition seen at this energy. While there is good energy correspondence between the major features predicted from DFT calculations and the optical data, the background absorption at other energies is significantly higher in the experimental data than in the DFT calculations. There are two likely

reasons for this. The first that dynamic vibrations are not incorporated into the DFT calculations, and the substantial atomic vibrations that occur at room temperature (~0.1 Å) will strongly break the local octahedral symmetry and thus increase the intensity of symmetry-forbidden transitions relative to the 0 K predictions. The second reason is that DFT calculations only model the subset of *d-d* transitions which correspond to excitations between energy levels would be accessible if the electron count of the system was increased. In contrast, DFT calculations are insensitive to *d-d* transitions which involve excited states where the orbital configurations which do not correspond to the ground state of a higher electron filling. It is therefore possible that the extra intensity observed outside of the σ-σ* and π-π* transitions in experimental is derived from *d-d* transitions which cannot be modeled by DFT.

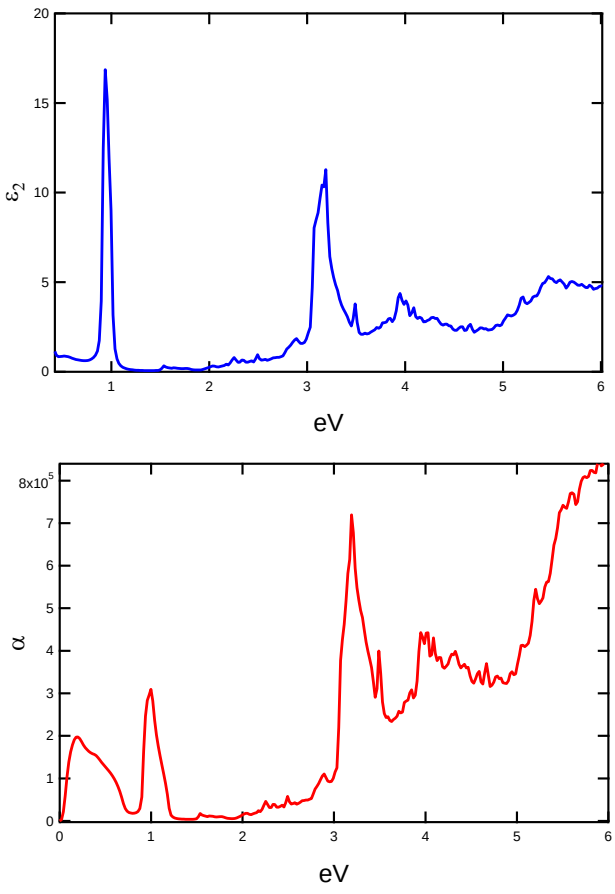

Figure 4.18. DFT calculated ε_2 versus energy (top), and the calculated absorbance spectra (bottom) for a fully stoichiometric $La_5Mo_2O_{12}$ compound.

DFT calculations were also used to investigate the nature of the oxygen vacancies in $La_5Mo_2O_{11.55}$. Since the neutron diffraction measurements unambiguously indicated that the oxygen vacancies reside at either the O3 or the O4 site, different trial structures were constructed in which vacancies were formed entirely at the O3 site (1/4 of O3 sites were vacant), entirely at the O4 site (1/4 of O4 sites were vacant), or at both sites (1/8 of the O3/O4 sites were vacant). Although persistent structures corresponding to local energy minima could be formed in this manner, the lowest energy structure formed during our investigations was one in which a substantial reconstruction of the Mo_2O_{10} dimers occurred, in a manner related to the disproportionation of La_2MoO_5. This lowest energy defect structure is shown in Figure 4.19. The unit cell of this structure is expanded by 4X relative to the *b*-axis direction of the conventional *C2/m* monoclinic cell. Rather than having four Mo_2O_{10} dimers in this quadruple cell, it is observed that the reconstruction results in the formation of three distinct coordination environments for the Mo cations as well as three Mo dimer environments.

Similar to the tetragonal La_2MoO_5 cell containing Mo_2O_8 square prismatic dimers, one of the three Mo dimer sites generated by the lowest energy DFT structural model is a Mo_2O_8 square prismatic dimer. The second dimer is also a Mo_2O_8 dimer, but the unit is formed by an edge sharing MoO_4 tetrahedra and MoO_6 octahedra. The last Mo-Mo dimeric unit is analogous to the fully stoichiometric $Ln_5Mo_2O_{12}$ parent structure. The Mo-Mo bond distances vary with the dimer unit. The Mo atoms in the square prismatic sites are separated by 2.27 Å while the Mo-Mo distance in the second Mo_2O_8 dimer share a 2.38 Å bond. The Mo_2O_{10} edge sharing dimers are separated by 2.49 Å. The different bond strengths suggest different bond orders for the different types of Mo-Mo bonds. BVS analysis using the calculated Mo-O bond distances and the parameters for R_0 = 1.8788 Å and b = 0.3406 suggest that Mo atoms in the Mo_2O_8 square

prismatic dimers have an oxidation state of approximately 3+, while the remaining 3 Mo atoms have an oxidation state of about 4.33+, resulting in an overall Mo^{4+} phase. This is somewhat unexpected due to differing coordination environments (tetrahedra vs octahedra) and the differing Mo-Mo bond lengths (tetrahedra-octahedra vs bioctahedra), and is attributed to both the method chosen for removal of oxygen atoms and the level of the DFT code used for study. Higher level calculations are expected to deal with the amount of electron localization in a more appropriate fashion, but represent an ongoing effort to understand the oxygen deficient structure that has so far only been observed in the La analog.

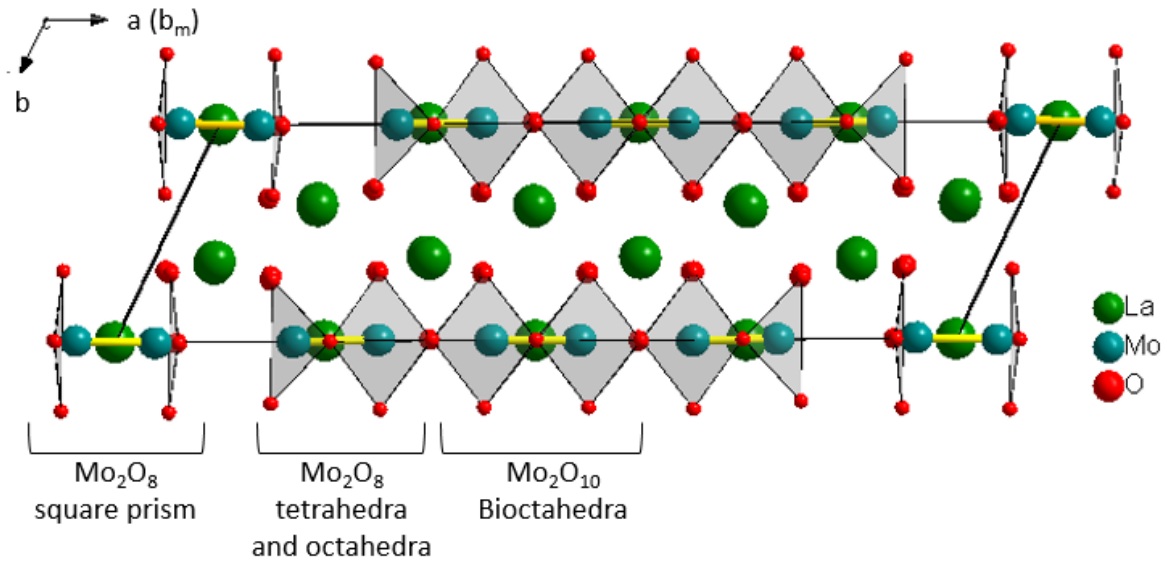

Figure 4.19. DFT generated oxygen deficient $La_5Mo_2O_{11.5}$ crystal structure showing the resulting Mo-O polyhedra in gray. The three resulting dimer environments are highlighted. The *a*-axis of the modeled cell is representative of the monoclinic *b*-axis in the *C2/m* supercell.

4.4. Conclusions

It has been shown that the crystal structure of powder samples of $Ln_5Mo_2O_{12}$ (*Ln* = La, Y, and Lu) is best modeled in the monoclinic *C2/m* space group, but metrically belongs to an orthorhombic *Immm* subcell. Faulting within the *C2/m* model causes substantial broadening of the supercell peaks making structural modeling particularly challenging. Neutron diffraction data were instrumental in characterizing the large amount of site disorder across the series of compounds, and also in detecting the oxygen deficiency in $La_5Mo_2O_{11.55}$. Refined bond distances and bond valence sum analyses highlight the effects of the oxygen deficiency on the Mo cation valence compared between the fully stoichiometric and oxygen deficient compounds. BVS estimates that Mo is in the 4.5+ oxidation state for the fully stoichiometric phases, and a substantial amount of oxygen deficiency results in a Mo oxidation state closer to 4.05+. Magnetic data provide additional evidence for this conclusion, as the predicted S = ½ response is observed for the fully stoichiometric $Lu_5Mo_2O_{12}$, and a magnetic susceptibility approximately equivalent to $1/10^{th}$ that of an S = ½ material is observed for the $La_5Mo_2O_{11.55}$ phase. Optical data reveal that these phases absorb strongly in the infrared region. The strongest features in the optical data are determined from DFT to be due to π-π* (1.25 eV) and σ-σ* (3.5 eV) transitions, which is related to the Mo *d* orbital splitting and lack of orbital degeneracy induce by the formation of the Mo-Mo bond. DFT-type calculations demonstrate that Mo-Mo bonds result in an electronic structure that deviates from the single ion prediction of *d* orbital splitting for an isolated MoO_6 octahedra. Instead, the electronic structure can be described with a molecular orbital scheme that is the result of hybridizing the Mo *d* orbitals for each octahedra that participate in forming the edge sharing Mo_2O_{10} dimer units. The six t_{2g} orbitals, from both Mo atoms in the single ion model, hybridize to from the bonding (σ, π, δ) and anti-bonding (δ*, π*,

σ*) states associated with forming the Mo-Mo bond. This type of structure-property analysis provides a good starting point to developing a better understanding of the effects direct *M*-*M* bonding in solid state structures and in particular the family of $Ln_5M_2O_{12}$ (*M* = Mo, Re, and Ru) compounds.

Chapter 5

Conclusions

Through the work presented in this dissertation, the influence of Mo-Mo bonding within dimeric environments on the electronic structures and select physical properties of oxide compounds has been evaluated. Of the three structural families studied, $La_4Mo_2O_{11}$, La_2MoO_5 and $Ln_5Mo_2O_{12}$, Mo dimers are either found in isolated (0D) Mo_2O_{10} bioctahedra, in chains (1D) of Mo_2O_8 square prisms/Mo_2O_{10} bioctahedra, or chains (1D) of Mo_2O_{10} bioctahedra, respectively. In the case of the oxygen deficient $La_5Mo_2O_{11.5}$ compound we have been able to use the results of experimental magnetic studies and the results of DFT calculations to propose a model of how Mo-Mo dimer environments might distort to accommodate an oxygen vacancy in the structure. While it is clear that different static environments for the Mo-Mo dimers have been observed, the disproportionation into a mixture of Mo^{5+} and Mo^{3+} environments with the same local stoichiometry seen for La_2MoO_5 perhaps indicates that dynamic changes in the coordination environment of Mo cations may also occur. This is perhaps hinted at by the similar transport behavior observed for the $La_4Mo_2O_{11}$, La_2MoO_5, and $Ln_5Mo_2O_{12}$ molybdates, all of which follow Arrhenius type behavior (Figure 5.1) with an activation energy of about E_a = 0.25 eV. The common nature of the transport activation energy suggests that the energy scale is set not by the band gap, but by some polaronic process that might indicate exceptionally strong electron-lattice coupling.

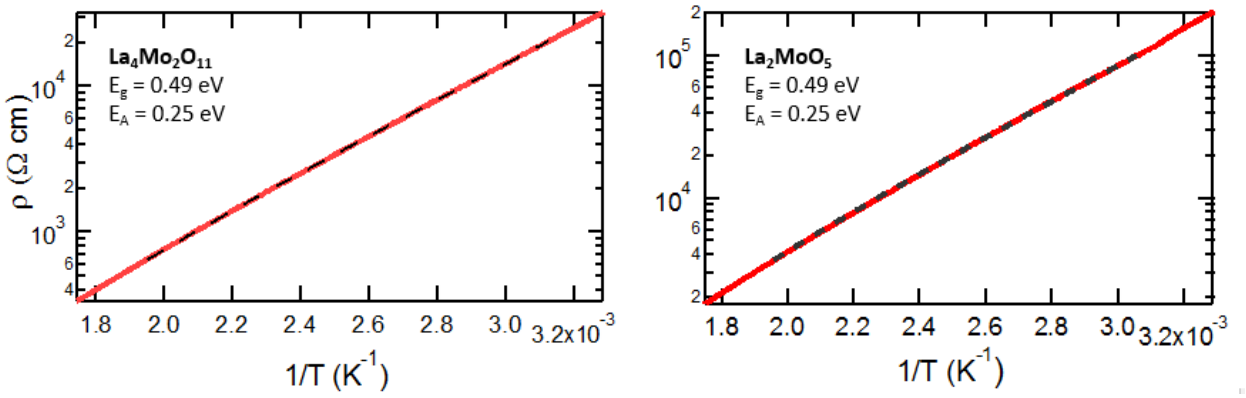

Figure 5.1. Comparison of the electronic transport data for $La_4Mo_2O_{11}$ with isolated Mo_2O_{10} dimers and La_2MoO_5 with 1D chains of either Mo_2O_8 or Mo_2O_{10} dimers.

In all cases, the electronic states of these compounds investigated through DFT have been found to be very complex, with most or all of the degeneracy of the *d* orbital states being lifted through the formation of molecular orbitals with σ, π, and δ symmetry. In the case of bioctahedral Mo_2O_{10} dimers, the *d* orbital degeneracy is fully lifted. For each dimer, there are 6 lower energy molecular orbitals derived from atomic octahedral ligand field t_{2g} states, which in order of increasing energy are approximately σ, π, δ, δ*, π*, and σ*. There are 4 higher energy orbitals derived from the higher energy e_g states (corresponding to states associated with the two *d* orbitals oriented directly toward ligands), which in order of increasing energy are approximately π, π*, δ, and δ*. However, the energetic order of these orbitals can be perturbed by up to ~ 3 eV due to differences in Mo-O bond lengths along the different axial directions, since shorter Mo-O distances result in greater repulsions between the electrons in Mo *d* orbitals and the ligand electrons, thus pushing certain orbitals to higher average energies. For square prismatic Mo_2O_8 dimers, the situation is somewhat different for two reasons. First, the tetrahedral symmetry allow two pairs of MOs (π/π, and π*/π*) to have identical energies if this square prism has true 4-fold symmetry along the axis of the Mo-Mo bond. Second, only one *d* orbital has lobes that point directly at the four ligands, resulting in 8 lower energy MO orbitals (σ, π/π, δ, δ*, π*/π*, and σ*) and 2 higher energy MO orbitals (δ, δ*) (Figure5.2). These principles can be readily extended to other ligand

geometries surrounding Mo-Mo bonding units, and to transition metals other than Mo which participate in metal-metal bonds.

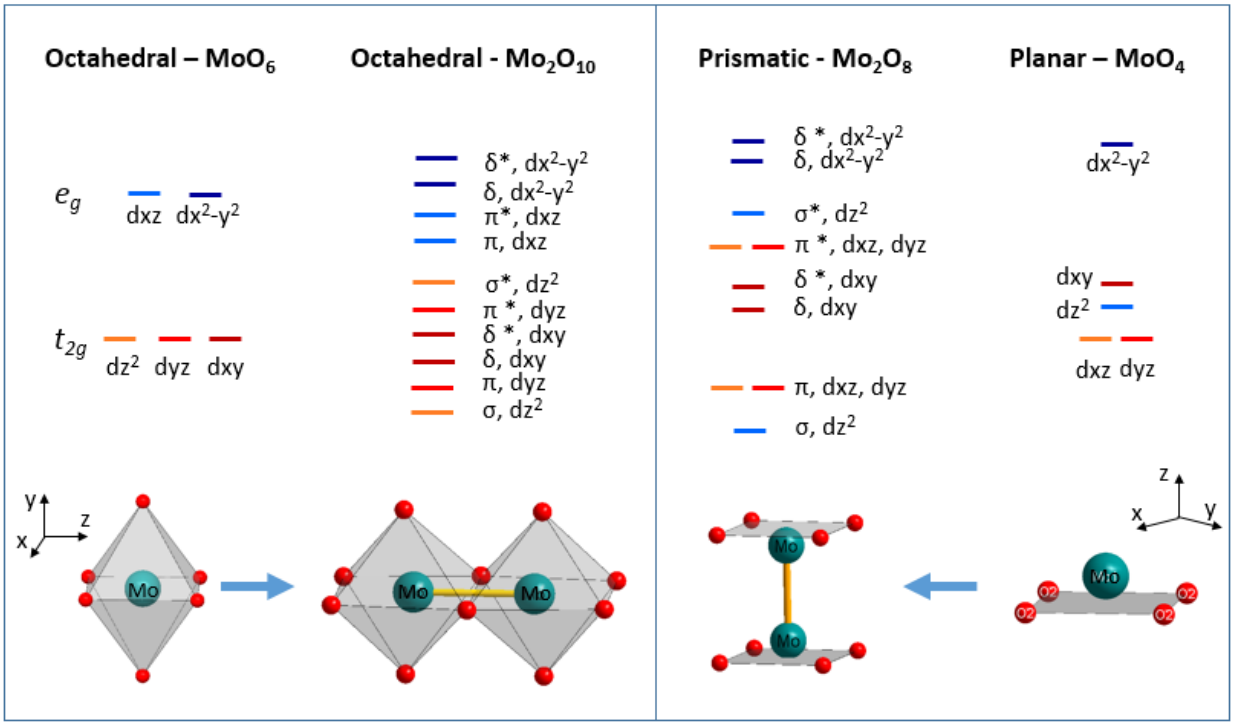

Figure 5.2. Schematic illustration comparing of the Mo *d* orbital molecular orbital splitting in either a bioctahedral Mo_2O_{10} unit or a prismatic Mo_2O_8 unit.

As a result of the lifting of the *d* orbital degeneracy, the effective magnetic moments of compounds with Mo-Mo bonding are typically small or zero (Figure 5.3). For bioctahedral Mo_2O_{10} dimers, any integer number of valence electrons (per Mo) will lead to a S = 0 (per dimer) ground state. This is the situation that is experimentally observed for both $La_4Mo_2O_{11}$ and La_2MoO_5. The maximum effective moment of μ_{eff} = 1.73 μ_B / dimer that can be theoretically expected for bioctahedral Mo_2O_{10} dimers is possible when each the Mo cations have a half-integer number of valence electrons, as has been experimentally observed for $Lu_5Mo_2O_{12}$ (this work) and $Y_5Mo_2O_{12}$ (prior work), both of which have 1.5 e^- / Mo cation due to the 4.5+ average oxidation state for the Mo cations. We have discovered the first intermediate case for the compound $La_5Mo_2O_{11.55}$, a compound where oxygen vacancies increase the electron total to 1.95 e^- / Mo cation, reducing the local moment to 0.48 μ_B / dimer. If the oxygen vacancy

concentration can be continuously tuned by the low temperature oxidation of this phase, then it will be possible to continuously tune the magnetic moment in the 1D dimeric chains of this system, offering an interesting possibility for studying magnetic interactions and excitations within this this quantum magnetic system.

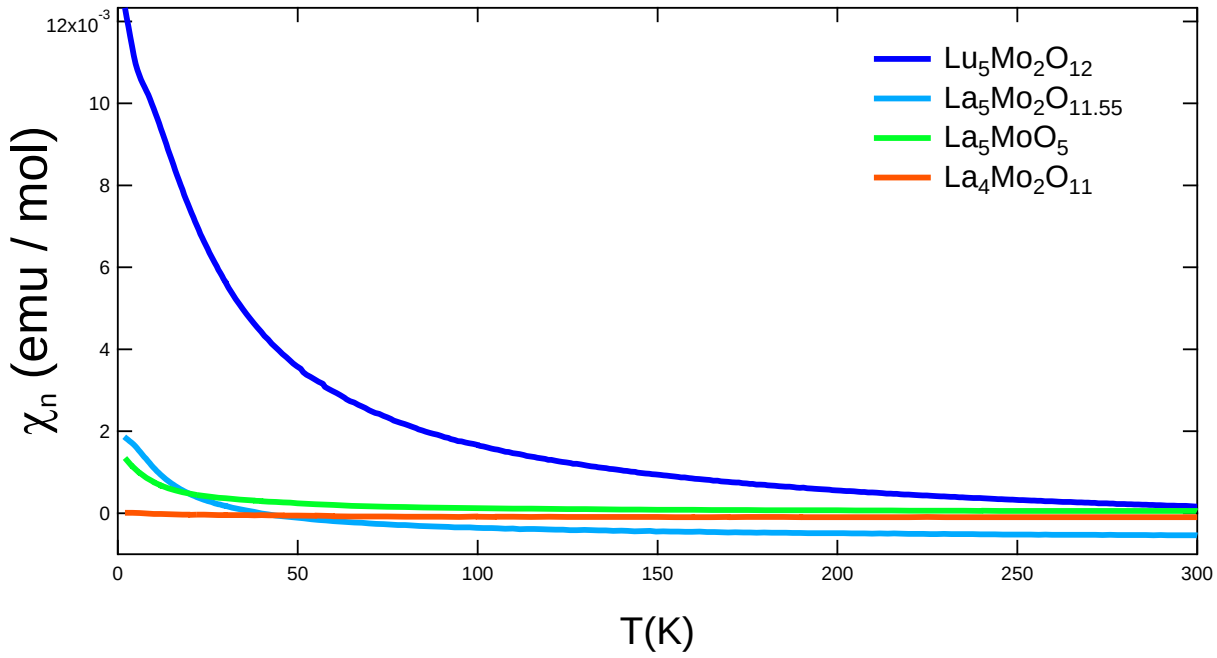

Figure 5.3. Field-cooled magnetic susceptibility measurements of powder $La_4Mo_2O_{11}$, La_2MoO_5, $La_5Mo_2O_{11.55}$ and $Lu_5Mo_2O_{12}$ samples conducted in a field of 5T.

The unusual electronic structure of these molybdenum oxides also leads to very unusual optical properties. While most oxides have large band gaps (> 2.5 eV), the lifting of the degeneracy allows smaller band gaps to be realized for compounds with Mo-Mo bonding. It has proven to be challenging to experimentally determine the band gaps of these systems. At this point in time, the best estimates of the band gap have come from high level HSE-type DFT calculations. In this manner, a direct band gap of 2.2 eV is predicted for $La_4Mo_2O_{11}$ (HSE) while a gap of 0.81 eV is predicted for La_2MoO_5 (LDA+U). Due to their non-integer electron counts and 1D chain geometry, it is not expected that DFT will predict a band gap for $Lu_5Mo_2O_{12}$ or , and $La_5Mo_2O_{11.55}$, though these compounds are not expected to truly be metals due to the gap-opening mechanisms available to them. In all cases, optical response of the compounds with

Mo-Mo bonding starts at infrared energies of ~0.5 eV or lower. This suggests that it is experimentally possible to observe *d-d* transitions (in a manner analogous to other transition metal systems with unpaired *d* electrons) that occur at energies lower than the band gap of these systems, as is possible since they correspond to electronic transitions to final states which are not represented in the band picture of solids (since the excited state does not correspond to the ground state for a different electron filling). Through a comparison of DFT and experimental data, it is found that all of these compounds exhibit a relatively strong σ-σ^* transition at energies of 3 – 4 eV, while those compounds with more than 1 e^- / Mo cation also exhibit a relatively intense π- π^* transition which can occur at energies as low as 1 eV ($La_5Mo_2O_{12}$, occurring within bioctahedral Mo_2O_{10} dimers) and as high as 3 eV (La_2MoO_5, occurring within square prismatic Mo_2O_8 dimers). While most *d-d* transitions are strongly symmetry forbidden, these particular transitions have a substantial component of their electrical dipole oriented along the direction of the Mo-Mo bond, the one axis where the symmetry of the isolated octahedral cation environment is most strongly broken due during the construction of dimeric units. For all of the compounds studied in this work there are numerous additional optical transitions apparent over the spectral ranges probed in this work (0.5 – 5 eV). The assignment of these features is still in progress.

We have recently been working on methods for estimating the absolute optical coefficients of powder samples from comparative (self-referencing, SR) diffuse reflectance measurements collected using both integrating sphere (IS) and bidirectional reflectance (BR) geometries. Using these newly-developed methods together with external information about the particle size, it is possible to estimate the complex refractive index of these compounds. Near-perfect matching of the BR and IS data generally occurs for $La_4Mo_2O_{11}$ and La_2MoO_5 if we use a constant value 1.91 for the real part of the refractive index, *n*. This value is reasonable as it is roughly reproduced by averaging the literature values of *n* previously reported for La_2O_3 and MoO_3. The correspondence between the BR and IS data for $La_5Mo_2O_{12}$, $Y_5Mo_2O_{12}$, and $Lu_5Mo_2O_{12}$ is generally good, but is noticeably deficient in the vicinity of the ~1 eV optical feature associated with the π-π^* transition. It is believe that this is due to the assumption of

a constant *n* value for these compounds being particularly bad in the vicinity of this strong oscillator, since strong variations in *n* generally occur in the vicinity of oscillators. This hypothesis is supported by DFT calculations on the hypothetical stoichiometric compound $La_5Mo_2O_{12}$, which indicate strong variations in *n* in this energy range. Using the value of 1.91 for *n* obtained through self-referenced diffuse reflectance measurements and the (coarsely) estimated particle size of ~5 μm obtained in SEM studies, it is possible to estimate the absolute absorbance coefficients of these compounds. As seen below in Figure 5.4, even the most intense σ-σ* and π-π* optical transitions appear to correspond to rather low optical cross-sections, with $\alpha_{SR} \sim 1.5 \times 10^3$ cm^{-1}. The transitions around 4-5 eV are much weaker than those predicted for *p-d* transitions and this would suggest that the absorbance is currently being underestimated by this method.

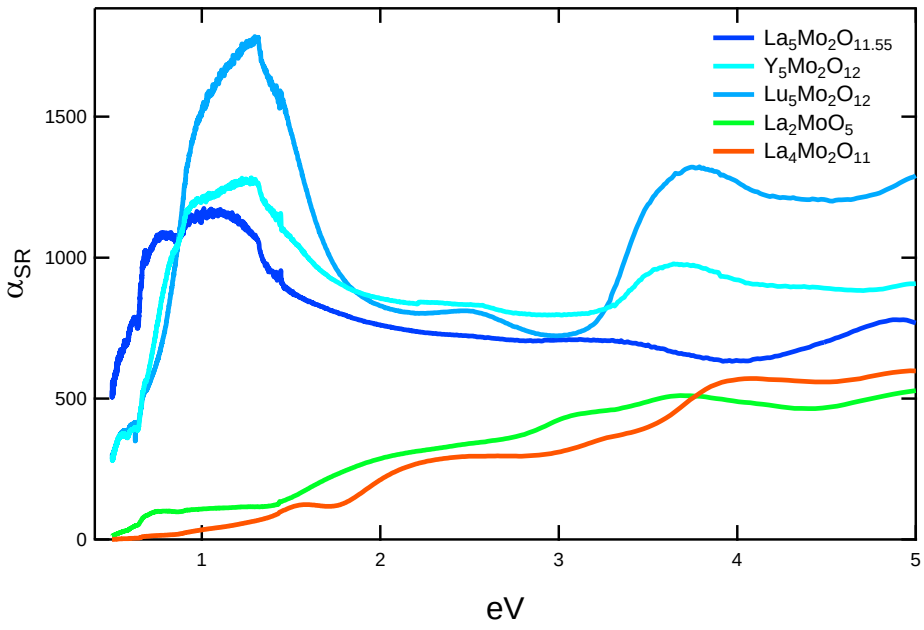

Figure 5.4. Self- refined absorbance plotted as a function of energy for several rare earth molybdates with Mo-Mo bonds. A value of *n* = 1.91 and a particle size of 5 microns were used to refine integrating sphere data against bidirectional reflectance data.

The discovery of the first metal-metal quadruple bond in molecular systems occurred almost 50 years ago. Since that time, a small number of solid state oxides with direct *M-M* bonds have also been discovered. In this work, we have discovered one new compound (La_2MoO_5) with Mo-Mo bonds, and as

well as discovering for the first time the appropriate orthorhombic subcell description for the $Ln_5Mo_2O_{12}$ family of compounds as well as the first members of this family with oxygen vacancies. A general framework for describing the complex electronic structures of these compounds using simple molecular orbital concepts has been developed. It has been shown that many effective predictions about the physical properties of compounds with Mo-Mo bonding can be made within this context. We have undertaken the first detailed optical studies of solid state compounds with direct metal-metal bonding, and have found a wealth of features within the optical spectra. The origin of some of the dominant optical features (σ-σ^* and π-π^*) have been assigned, and some initial estimates of the absolute absorption coefficients have been made. As such, this work represents a promising beginning to our efforts to obtain a comprehensive understanding of transition metal oxides with direct metal-metal bonding. It is believed that the work provided in this dissertation provides a strong basis to begin studying more complex Mo-Mo bonding environments and other transition metal oxides with *M-M* bonds following the same methodologies.

Appendix1

Chapter 2 Supporting Information

Table S1. Refinement parameters for $La_4Mo_2O_{11}$ studied with X-ray and TOF neutron diffraction.

Crystal system		Tetragonal	
Space group		*P4₂/n* (# 86)	
Radiation		X-ray	neutron (TOF)
Temperature		298 K	300 K
λ (Å)		1.541	1.333 (center)
Range of collection		7°< 2θ <140°	0.41< *d* < 3.61
Lattice parameters (Å)	*a*	13.00025(9)	12.9899(4)
	c	5.65705(5)	5.6531(2)
Cell volume ($Å^3$)		956.07 (2)	953.90(6)
ρ_{calc} (g/cm^3)		6.4158(1)	6.4305(4)
R_{bragg}		1.95	1.65
R_{wp}		4.13	3.12

Table S2. Structure of $La_4Mo_2O_{11}$ refined from TOF neutron data collected at 300 K.

Atom	Wyck	*x*	*y*	*z*	B_{eq}
La1	8g	0.1176(1)	0.1814(1)	-0.0027(4)	0.56(2)
La2	8g	0.3026(1)	0.6124(1)	0.0768(2)	0.55(2)
Mo1	8g	0.02426(1)	0.5910(1)	0.0756(3)	0.59(2)
O1	8g	0.6477(2)	0.2032(2)	-0.0028(4)	0.70(3)
O2	8g	0.0297(2)	0.3071(2)	0.7036(4)	0.66(3)
O3	8g	0.1258(2)	0.5465(2)	0.2839(4)	0.85 (3)
O4	8g	0.1596(2)	0.0432(2)	0.3224(3)	0.70(3)
O5	8g	-0.0011(2)	0.0855(2)	0.6891(4)	0.84(3)
O6	2b	¼	¼	¾	0.58(6)
O7	2a	¼	¼	¼	0.57(6)

Table S3. Select La-O bond distances (Å) in $La_4Mo_2O_{11}$**.**

Atom1	Atom2	Length	Atom1	Atom2	Length
La1	O6	2.389(2)	La2	O1	2.370(3)
CN 8	O7	2.407(2)	CN 8	O2	2.433(3)
	O2	2.476(3)		O1	2.454(3)
	O4	2.498(3)		O4	2.500(3)
	O3	2.568(3)		O1	2.515(3)
	O2	2.593(3)		O3	2.572(3)
	O4	2. 627(3)		O3	2.717(3)
	O5	2.639(3)		O5	2.894(3)

Table S4. Bond valence sum analysis of $La_4Mo_2O_{11}$ calculated using several R_0 and b parameters found in literature.

			Chen	**Zocchi**	**Refined This work**	**Brese/ Brown [77,78]**	
		Source	**[79]**	**[80]**			**Ideal**
		Valence	5	3-6	5	6	5
		b	0.37	0.305	0.37	0.37	N/A
		R_0	1.878	1.879	1.9079	1.907	N/A
		Bond					
Mo1	O3	1.860	1.05	1.06	1.14	1.14	0.83
	O4	1.901	0.94	0.93	1.02	1.02	0.83
	O2	1.952	0.82	00.79	0.89	0.89	0.83
	O5	1.970	0.78	0.74	0.85	0.84	0.83
	O5	2.059	0.61	0.55	0.66	0.66	0.83
	O1	2.208	0.41	0.34	0.44	0.44	0.83
		Total *v*	**4.61**	**4.41**	**5.00**	4.99	5

Table S5. Ideal Mo-O bond distances based on literature values for Mo (CN = 6).

Author	*v*	R_0	*b*	CN = 6 *v*/bond	CN = 6 Distance
Chen [1]	6	1.900	0.37	1.00	1.900
Chen [1]	5	1.878	0.37	0.83	**1.945**
Chen [1]	4	1.856	0.37	0.67	2.006
Chen [1] Chen [1]	3	1.834	0.37	0.50	2.090
Brown [4]	6	1.907	0.37	1.00	1.907
Brese [3]	6	1.907	0.37	1.00	1.907
Zocchi [2]	6	1.8788	0.3046	1.00	1.879
Zocchi [2]	5	1.8788	0.3046	0.83	**1.934**
Zocchi [2]	4	1.8788	0.3046	0.67	2.002
Zocchi [2]	3	1.8788	0.3046	0.50	2.090

Table S6. Comparison of Average Mo-O bond distance to the Ideal Mo-O bond distance for Mo^{5+} with CN = 6.

Source	*v*	R_0	*b*	CN	*v*/bond	Ideal R	Exp. R	ΔD
Chen [1]	5	1.8780	0.37	6	0.83	**1.946**	1.990	0.04
Zocchi [2]	5	1.8788	0.3046	6	0.83	**1.934**	1.990	0.06

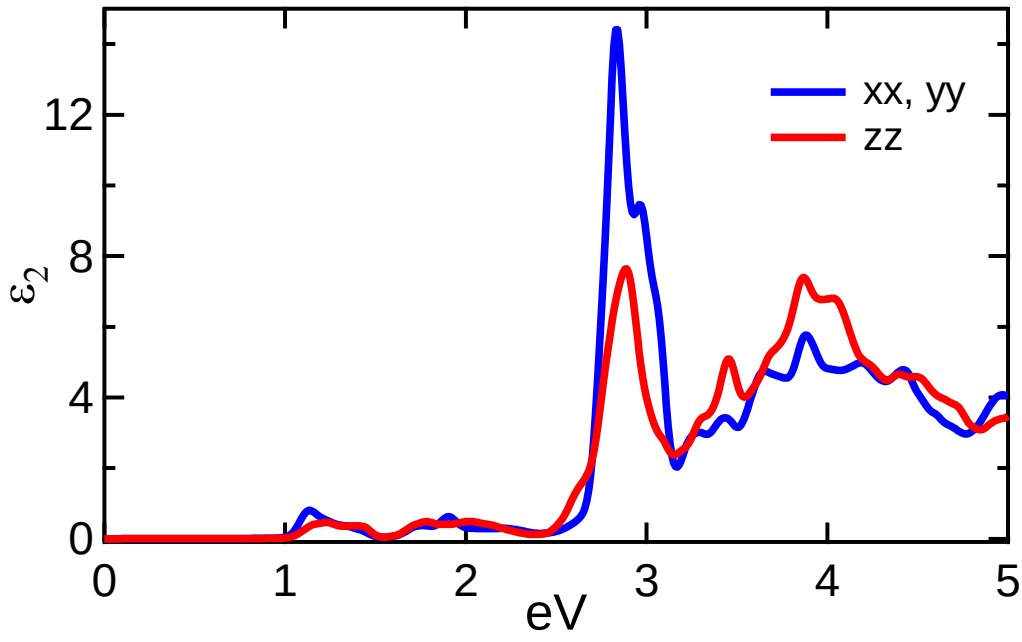

Figure S1. Calculated polarized absorption for $La_4Mo_2O_{11}$ along the x, y, and z directions.

$La_4Mo_2O_{11}$ Mo *d* orbital Fatband Analysis

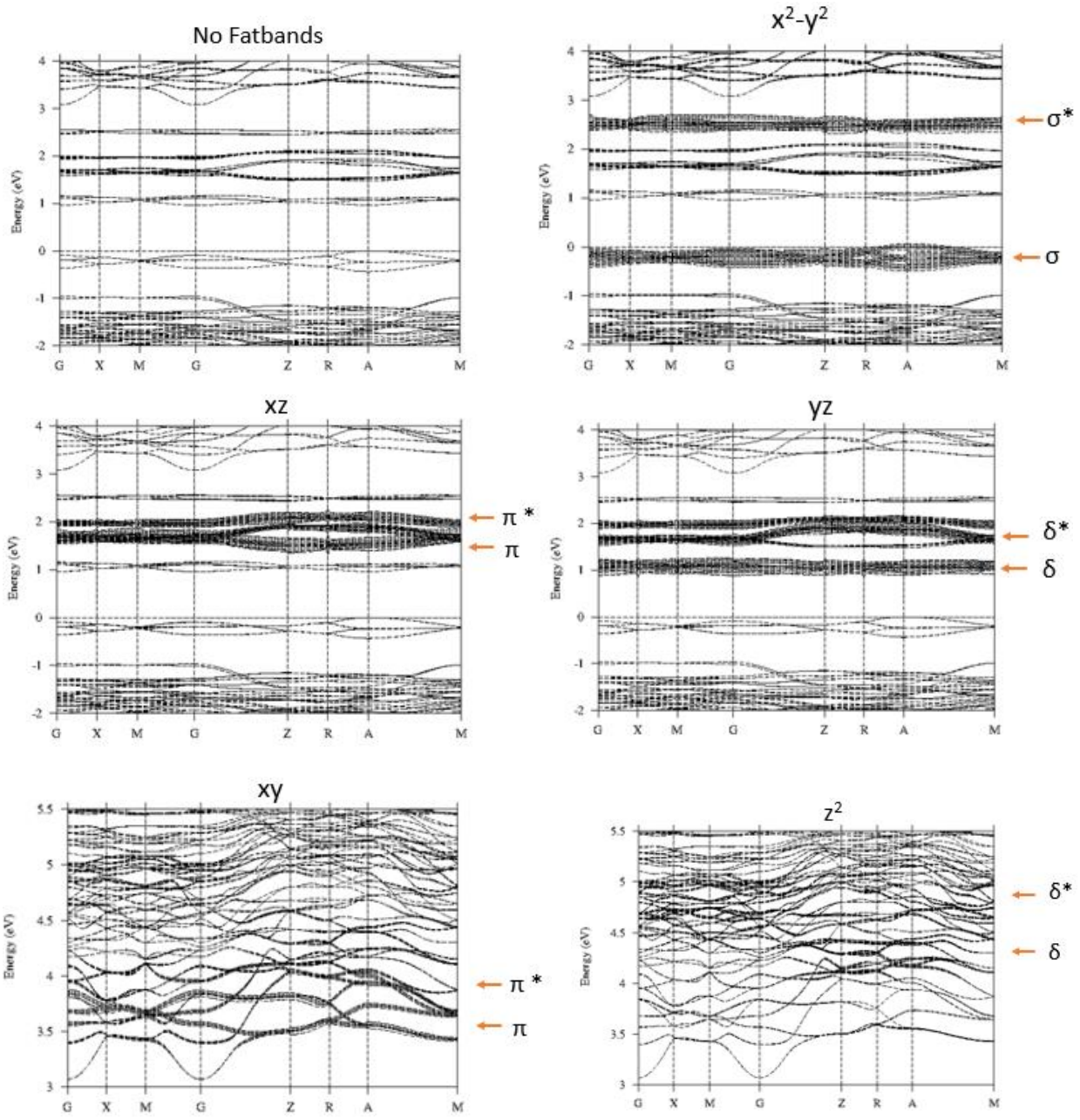

Figure S2. Individual fatband calculations representing each of the five Mo *d* orbital contributions to the electronic band structure.

Appendix 2

Chapter 3 Supporting Information

Rietveld refinement of La_2MoO_5 subcell (*I4/m*) setting

While the correct unit cell and space group (*P4/m*) are discussed in the main text, the results of the structural refinement for La_2MoO_5 in the incorrect approximant subcell space group of *I4/m* (corresponding to the La_2ReO_5 structure type) are provided below to illustrate the limitations of this structure refinement. The relatively high quality of the fit to this incorrect structural model is evident in Figure 1 of the main text. The present La_2MoO_5 lattice parameters are both slightly larger than those of the Re analogue, La_2ReO_5, which has a = 8.935Å, c = 6.011 Å.

Table S1. Structure of La_2MoO_5 refined in *I4/m* subgroup using lab X-ray data.

Phase		La_2MoO_5
Crystal system		Tetragonal
Space group		*I4/m*
Radiation		Cu K_α
λ (Å)		1.541
Range of collection		$7° < 2\theta < 140°$
Lattice parameters (Å)	*a*	8.9587(2)
	c	6.0518(1)
Cell volume ($Å^3$)		485.55(2)
ρ_{calc}(g/cm^3)		6.030(2)
R_{bragg}		2.67
R_{wp}		6.98

Site	Wyck.	*x*	*y*	*z*	occ.	B_{eq}
La1	8h	0.1811(2)	0.3943(2)	0	1	2.48(4)
Mo1	4e	0	0	0.1983(4)	1	1.506)
O1	4d	0	0.5	0.25	1	1.9(2)
O2	16i	0.103(1)	0.202 (2)	0.279(2)	0.80 (1)	1.9(2)

TGA product analysis

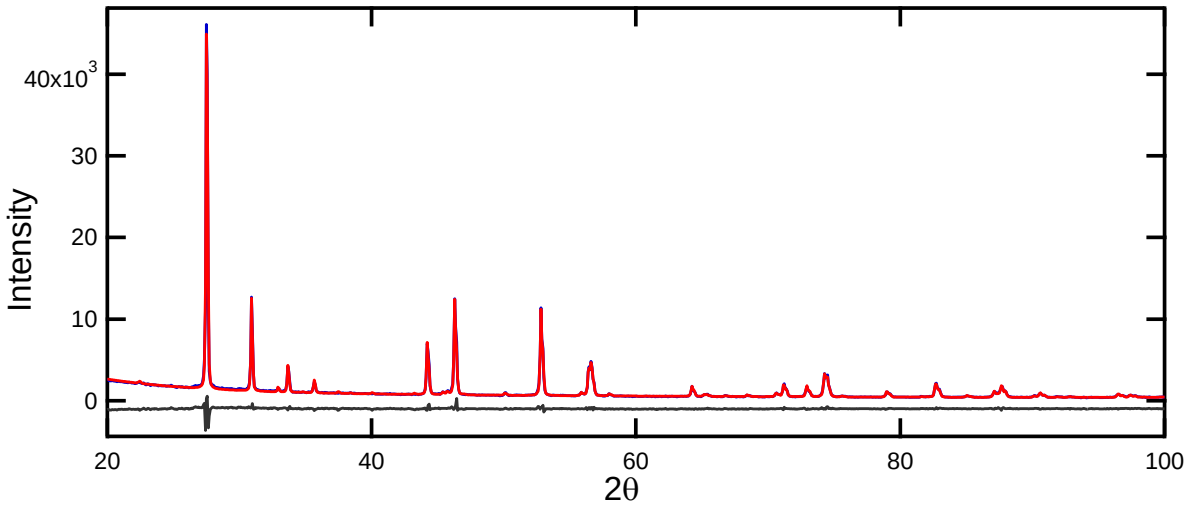

Figure S1. Structure refinement of the TGA product from laboratory X-ray data is very well described with a single tetragonal La_2MoO_6 phase. No evidence for impurity phases was seen.

Table S2. Rietveld refinement of La_2MoO_6 (TGA product) using lab X-ray data.

Phase		La_2MoO_6
Crystal system		Tetragonal
Space group		*I4₁/acd* (origin 2)
Radiation		Cu K_α
λ (Å)		1.541
Range of collection		$7° < 2\theta < 140°$
Lattice parameters (Å)	*a*	5.80346(8)
	c	32.0287(7)
Cell volume (Å^3)		1078.73(4)
ρ_{calc}(g/cm^3)		5.7848(2)
R_{bragg}		2.19
R_{wp}		5.19

Site	Wyck.	*x*	*y*	*z*	B_{eq}
La1	16d	0	0.25	0.03863(8)	0.50(4)
Mo2	8a	0	0.25	0.375	0.73(9)
O1	32g	0.322(7)	0.082(7)	0.0893(5)	1.7(3)
O2	16e	0.231(7)	0	0.25	1.7(3)

Neutron powder diffraction results for La_2MoO_5

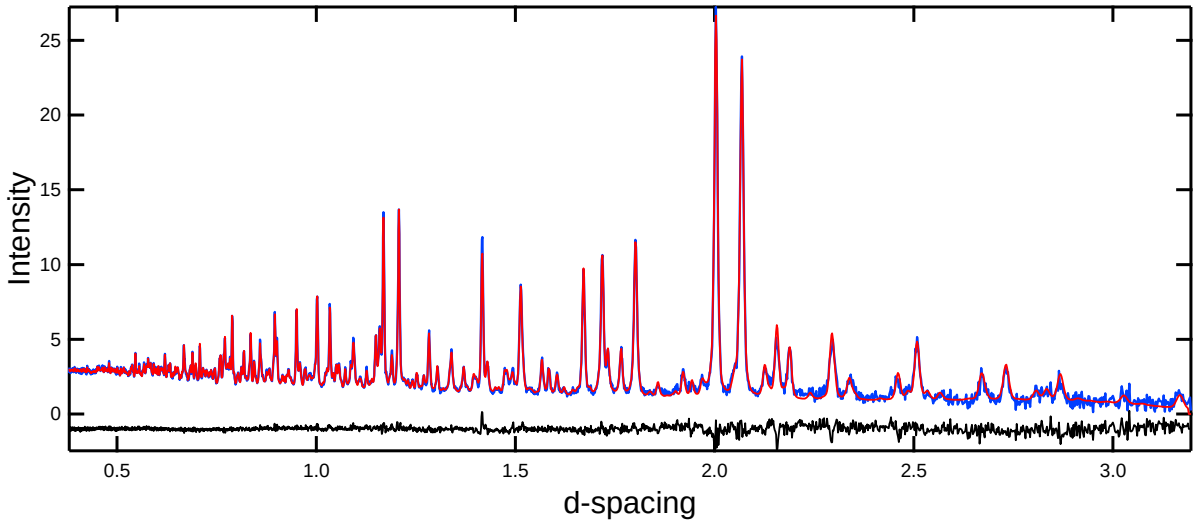

Figure S2. Fit to 300K powder neutron diffraction data collected on a sample of tetragonal La_2MoO_5 in the correct *P4/m* structure model.

Table S3. Lanthanum-oxygen bond distances in La_2MoO_5 (*P4/m*) refined using 300 K neutron data.

Atom 1	Atom 2	Mult	Distance (Å)
La1	O2	x2	2.484(7)
	O2	x2	2.507(7)
	O3	x2	2.444(7)
	O4	x2	2.632(7)
La2	O1	x2	2.505(6)
	O1	x2	2.529(6)
	O3	x2	2.405(6)
	O5	x1	2.571(6)
La3	O2	x2	2.381(6)
	O3	x2	2.415(6)
	O4	x2	2.636(7)
	O6	x1	2.452(9)
La4	O1	x2	2.436(6)
	O3	x2	2.384(6)
	O4	x2	2.665(7)
	O6	x1	2.444 (8)

X-ray diffraction results for La_2MoO_5 (synchrotron and laboratory)

Table S4. Results of Rietveld refinement for La_2MoO_5 using powder X-ray diffraction data.

Note that unit cell parameters are reported for both lab and synchrotron data, while the atom positions are only given for synchrotron data.

Crystal system		Tetragonal	
Space group		*P4/m* (#83)	
Z		8	
Radiation		Cu K_α	Synchrotron
Temperature		RT	RT
λ (Å)		1.5410	0.41333
Range of collection		7° < 2θ < 140°	1° < 2θ < 50°
Lattice parameters (Å)	*a*	12.6694(1)	12.66871(6)
	c	6.05187(5)	6.05048(3)
Cell volume (Å^3)		971.41(2)	971.08(1)
ρ_{calc} (g/cm^3)		6.2051(2)	6.20727(7)
R_{bragg}		1.38	3.07
R_{wp}		3.70	12.557

Atom	Wyck	*x*	*y*	*z*	B_{eq}
La1	4j	0.2074(2)	0.1094(2)	0	0.67(3)
La2	4j	0.3018(2)	0.3890(2)	0	0.67(3)
La3	4k	0.2716(2)	-0.0967(2)	½	0.70(5)
La4	4k	0.3879(2)	0.2207(2)	½	1.45(6)
Mo1	2g	0	0	0.3167(3)	0.72(8)
Mo2	2h	½	½	0.3167(3)	0.88(9)
Mo3	4i	0	½	0.2196(3)	1.10(4)
O1	8l	0.3553(8)	0.538(1)	0.766(2)	0.97(8)
O2	8l	-0.053(1)	0.8538(8)	0.780(2)	0.97(8)
O3	8l	0.2352(9)	0.749(1)	0.244(2)	0.97(8)
O4	8l	0.036(1)	0.6472(8)	0.242(2)	0.97(8)
O5	4j	0.474(1)	0.877(1)	½	0.97(8)
O6	4k	0.486(1)	-0.103(1)	0	0.97(8)

Bond valence sum analysis

Bond valence sum (BVS) calculations were carried out to better understand the bonding in La_2MoO_5. First, BVS methods were used to calculate the Mo valence at each crystallographic Mo site. The total Mo site valence (v) is the sum of the valences (s_i) associated with each of the i individual bonds to coordinating oxygen ligands. These individual bond valences can be calculated from the experimentally determined bond lengths, R_i, through Eqn. (1), where R_0 and b are tabulated empirical parameters based on an analysis of literature compounds with known valence.

$$v = \sum_i s_i = \sum_i e^{(R_0 - R_i)/b} \qquad (1)$$

The experimental bond distances (R_i) could be accurately determined through the Rietveld refinement of powder neutron diffraction data (Table 3). However, the best choice of R_o and b was less clear. This is a common dilemma when assigning valences since the parameters of Ro and b are often valence-specific, and the thus the choice of an expected valence can affect the valence calculated using BVS methods. The canonical BVS work of Brown and Altermatt [78] and Brese and O'Keefe [77] conveniently report the same values for R_0 and b, but this analysis was only done for compounds with 6+ Mo and is unlikely to be appropriate for the present case of La_2MoO_5, whose average Mo valence is 4+. Still, a first calculation with these parameters suggests that the prismatic sites have 3+ Mo and the octahedral site has 5+ Mo. Later work by Chen [79] determined different values of R_0 for each Mo valence while keeping the standard value of b (0.37) for all sites. A different parameterization by Zocchi [80] allowed b to vary so that a common set of R_0 and b values could be used for Mo all valences from 3+ to 6+. While somewhat different results are obtained for all parameterizations, it is found for all of these parameterizations that very different valences exist at the prismatic and octahedral sites, and the difference in valence is 1.5 – 2.0 valence units (v.u.). This strongly supports the assignment of the prismatic sites as Mo 3+ and the octahedral site as Mo 5+. In order to provide an unbiased estimate, the valences reported in the manuscript also calculated by fixing b to 0.37 and refining R_0 so that the average Mo valence in the compound is exactly 4+. The overall valences for each Mo site are provided in Table S5, while the separate calculations used for each individual bond to obtain this overall result are provided in Table S6.

Table S5. Comparison of Mo site valences calculated with different BVS parameterizations.

	Source	**Expt.**	**Refined**	**Brese**	**Chen**	**Chen**	**Chen**	**Chen**	**Zocchi**
		Ideal	-	**[77,78]**	**[79]**	**[79]**	**[79]**	**[79]**	**[80]**
	Valence	N/A	N/A	6	6	**5**	4	**3**	6,**5**,4,**3**
	b	N/A	0.37	0.37	0.37	0.37	0.37	0.37	0.3046
	***R*₀**	N/A	1.9084	1.907	1.900	1.878	1.856	1.834	1.8788
Polyhedron	**Atom**								
Prism	Mo1	3	3.04	3.03	2.97	2.80	2.64	**2.49**	**2.60**
Prism	Mo2	3	3.17	3.16	3.10	2.92	2.75	**2.59**	**2.74**
Oct	Mo3	5	4.89	4.87	4.78	**4.51**	4.25	4.00	**4.30**
	***v*(avg)**	4	4.00	3.98	3.91	3.68	**3.47**	3.27	**3.48**
	***v*(oct)-*v*(prism)**	2	1.78	1.78	1.74	1.64	1.55	1.46	1.63

Table S6. Comparison of individual Mo bond valences calculated with different BVS parameterizations.

		Source	**Ideal**	**Refined**	**[77,78]**	**[3]**	**[3]**	**[3]**	**[3]**	**[4]**
		Valence	N/A	N/A	6	6	5	4	3	6,5,4,3
		b	N/A	0.37	0.37	0.37	0.37	0.37	0.37	0.3046
		R_0	N/A	1.9084	1.907	1.900	1.878	1.856	1.834	1.8788
Atom	**Atom**	**Bond (Å)**								
Mo1 (prism)	O2	2.010 x4	0.75	0.76	0.76	0.74	0.70	0.66	0.62	0.65
Mo2 (prism)	O1	1.994 x4	0.75	0.79	0.79	0.78	0.73	0.69	0.65	0.68
Mo3 (oct)	O4	1.866 x2	0.83	1.12	1.12	1.10	1.03	0.97	0.92	1.04
	O5	2.000 x2	0.83	0.78	0.78	0.76	0.72	0.68	0.64	0.67
	O6	2.135 x2	0.83	0.54	0.54	0.53	0.50	0.47	0.44	0.43

While the accuracy of the BVS method in general is typically very modest (~0.1 v.u.), a closer look at the specific values in Table S5 (highlighted in bold) which were calculated using the assigned valences of 3+ for the prismatic site and 5+ for the octahedral site shows that the valences in La_2MoO_5 are all underestimated by a very large amount (0.3 – 0.5 v.u.). This means that the bond lengths experimentally observed for La_2MoO_5 are systematically longer than expectations for these specific combinations of Mo site valence and coordination number. It can therefore be concluded that direct Mo-Mo bonding weakens the Mo-O ligand bonds.

More quantitative prediction about the expected bond lengths for these sites can be obtained by reversing the BVS process and using the BVS parameterization to make predictions about the average Mo-O bond lengths using Eqn. (2) and (3). The Mo1 and Mo2 sites have a valence of v = 3 and a coordination number of CN = 4, while the Mo3 site has v = 5 and CN = 6. For comparison, calculations have been carried out for all of the sets of Mo BVS parameters (Tables S7 and S8), and the subset of values directly relevant to the present compound highlighted in yellow. When the ideal average bond distances (R) calculated using BVS methods are compared to the experimentally measured bond distances, it can be seen that the experimental distances are longer by about 0.05 Å. This suggests that the participation of electrons in the Mo-Mo bonding results in less electron density in the Mo-O bonds, and an increase in the overall Mo-O bond lengths. It is therefore expected that the presence direct metal-metal bonding will generally weaken the *M-X* bonding to ligands, and thus represents a method for tuning bond strength in a useful manner that might allow, for example, the activity of heterogeneous catalysts to be tuned.

$$s_i = v/\mathrm{CN} \qquad (2)$$

$$R = R_0 - b*\ln(s_i) \qquad (3)$$

Table S7. Ideal Mo-O bond distance (Å) as a function of bond valence, sorted by reference.

				CN = 6		CN = 4	
Author	**Valence**	***R₀***	***b***	***v*/CN**	**Ideal *R***	***v*/CN**	**Ideal *R***
Chen [3]	6	1.900	0.37	1.00	1.900	1.50	1.750
Chen [3]	5	1.878	0.37	0.83	**1.945**	1.25	1.795
Chen [3]	4	1.856	0.37	0.67	2.006	1.00	1.856
Chen [3]	3	1.834	0.37	0.50	2.090	0.75	**1.940**
Brown [78]	6	1.907	0.37	1.00	1.907	1.50	1.757
Brese [2]	6	1.907	0.37	1.00	1.907	1.50	1.757
Zocchi [4]	6	1.8788	0.3046	1.00	1.879	1.50	1.755
Zocchi [4]	5	1.8788	0.3046	0.83	**1.934**	1.25	1.811
Zocchi [4]	4	1.8788	0.3046	0.67	2.002	1.00	1.879
Zocchi [4]	3	1.8788	0.3046	0.50	2.090	0.75	**1.966**

Table S8. Ideal Mo-O bond distance (Å) as a function of bond valence, sorted by Mo valence.

				CN = 6		CN = 4	
Author	**Valence**	***R₀***	***b***	**v/bond**	**Ideal *R***	**v/bond**	**Ideal *R***
Brese [2]	6	1.907	0.37	1.00	1.907	1.50	1.757
Brown [1]	6	1.907	0.37	1.00	1.907	1.50	1.757
Chen [3]	6	1.900	0.37	1.00	1.900	1.50	1.750
Zocchi [4]	6	1.8788	0.3046	1.00	1.879	1.50	1.755
Chen [3]	5	1.878	0.37	0.83	**1.945**	1.25	1.795
Zocchi [4]	5	1.8788	0.3046	0.83	**1.934**	1.25	1.811
Chen [3]	4	1.856	0.37	0.67	2.006	1.00	1.856
Zocchi [4]	4	1.8788	0.3046	0.67	2.002	1.00	1.879
Chen [3]	3	1.834	0.37	0.50	2.090	0.75	**1.940**
Zocchi [4]	3	1.8788	0.3046	0.50	2.090	0.75	**1.966**

Table S9. Comparison of BVS-predicted average Mo-O bond distance (Ideal *R*) to the experimental distance (Exp. R), and their observed differences (ΔR).

Source	**Valence**	***R₀***	***b***	**CN**	**v/bond**	**Ideal R**	**Exp. *R***	**Δ*R***
Chen [3]	3	1.834	0.37	4	0.75	1.940	2.002	0.062
Zocchi [4]	3	1.8788	0.3046	4	0.75	1.966	2.002	0.036
Chen [3]	5	1.878	0.37	6	0.83	1.945	2.000	0.055
Zocchi [4]	5	1.8788	0.3046	6	0.83	1.934	2.000	0.066

La_2MoO_5 Electronic Band Structure

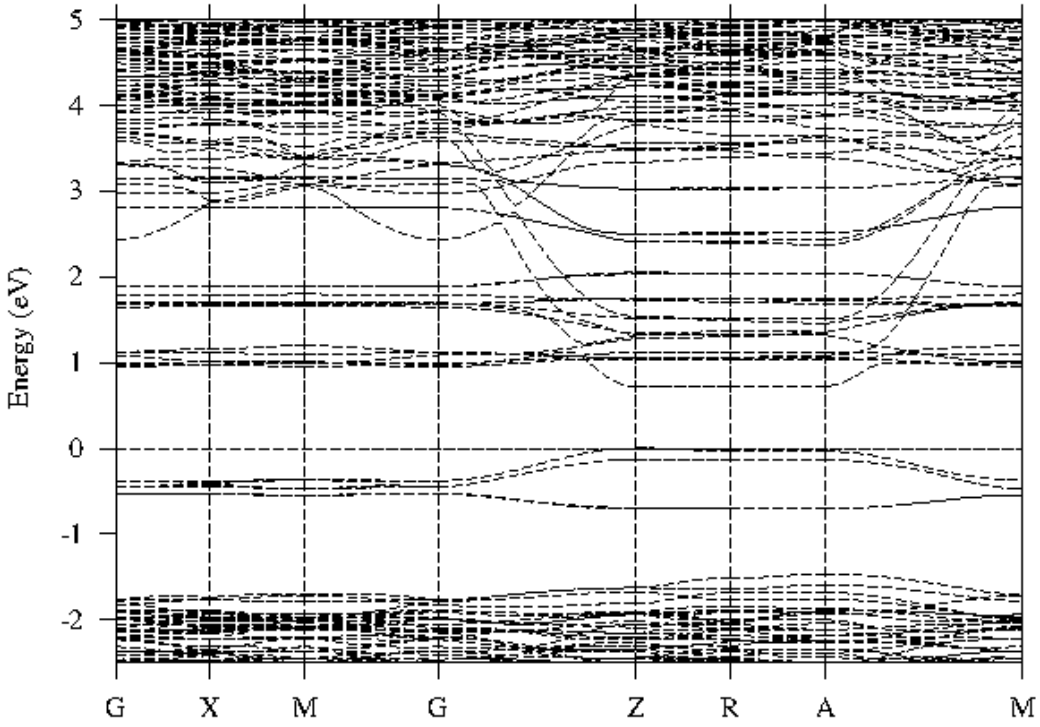

Figure S3. Electronic band structure (LMTO) calculated using refined lattice parameters and atom positions from room temperature neutron diffraction data. An energy of 0 eV is assigned to the top of the valence band.

La_2MoO_5 Mo1 Site Fatband Analysis

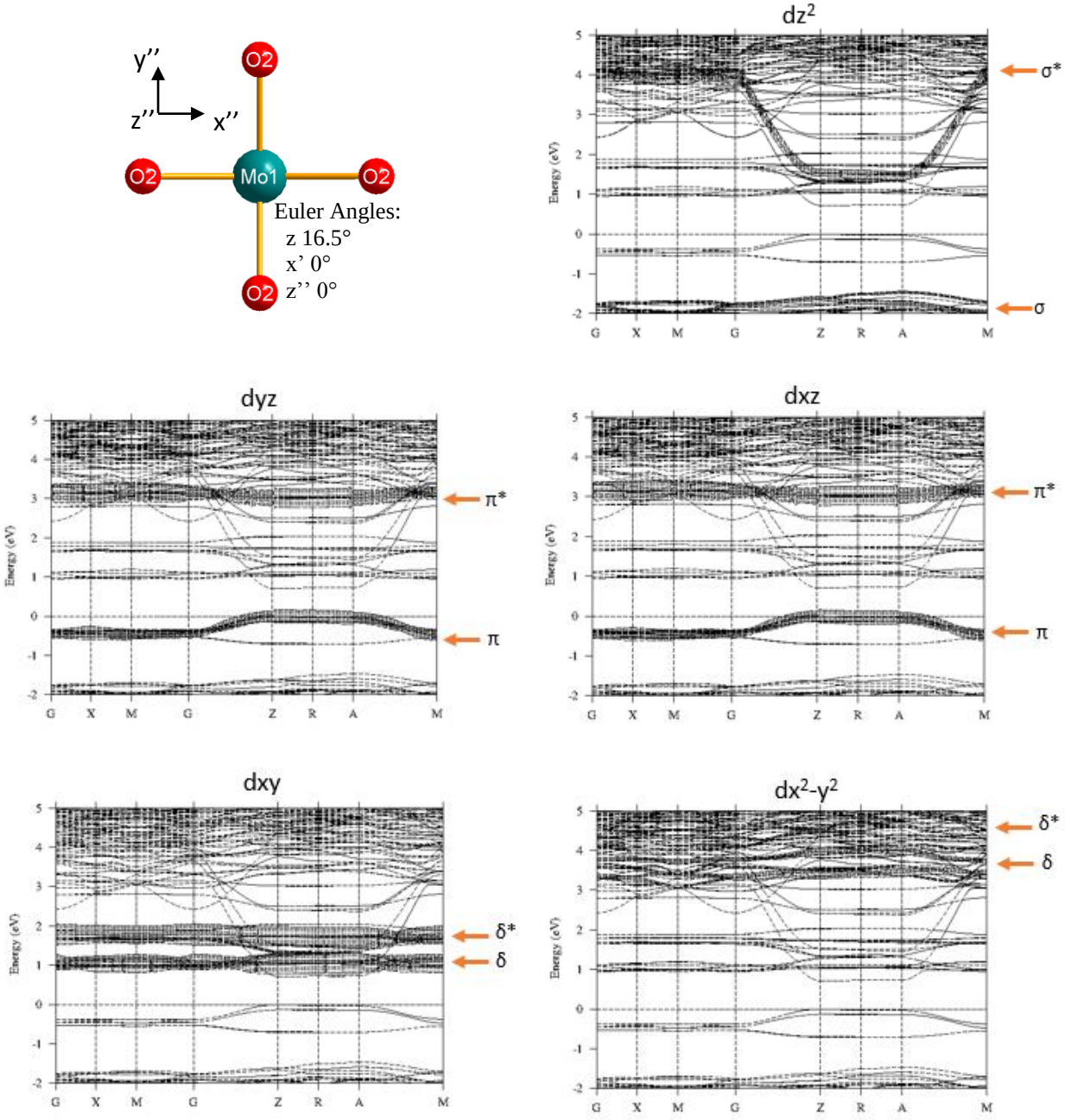

Figure S4. Individual *d* orbital contributions for the prismatic Mo1 site projected as "fatbands" in the electronic structure.

La_2MoO_5 Mo2 Site Fatband Analysis

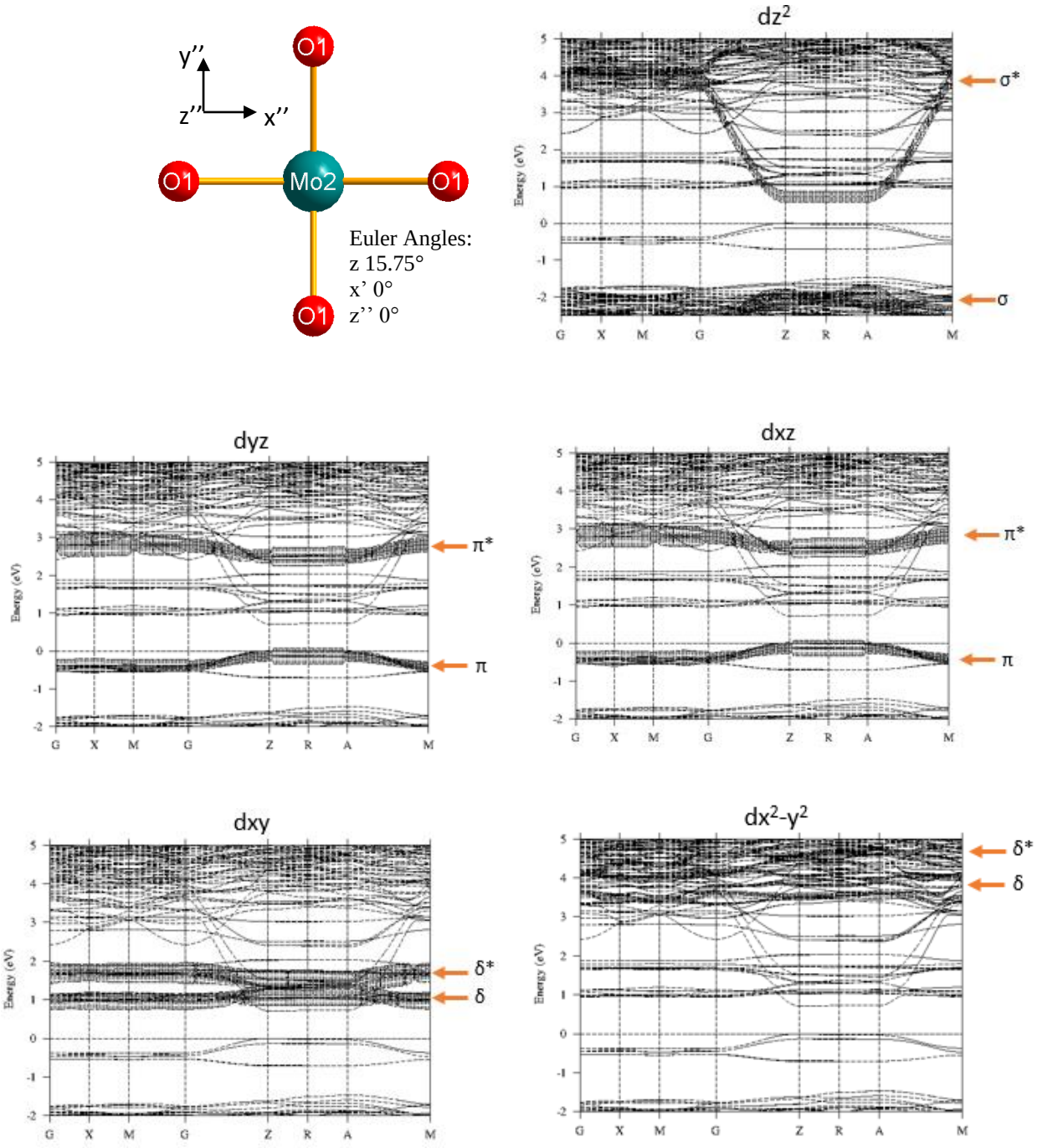

Figure S5. Individual *d* orbital contributions for the prismatic Mo2 site projected as "fatbands" in the electronic structure.

La_2MoO_5 Mo3 Site Fatband Analysis

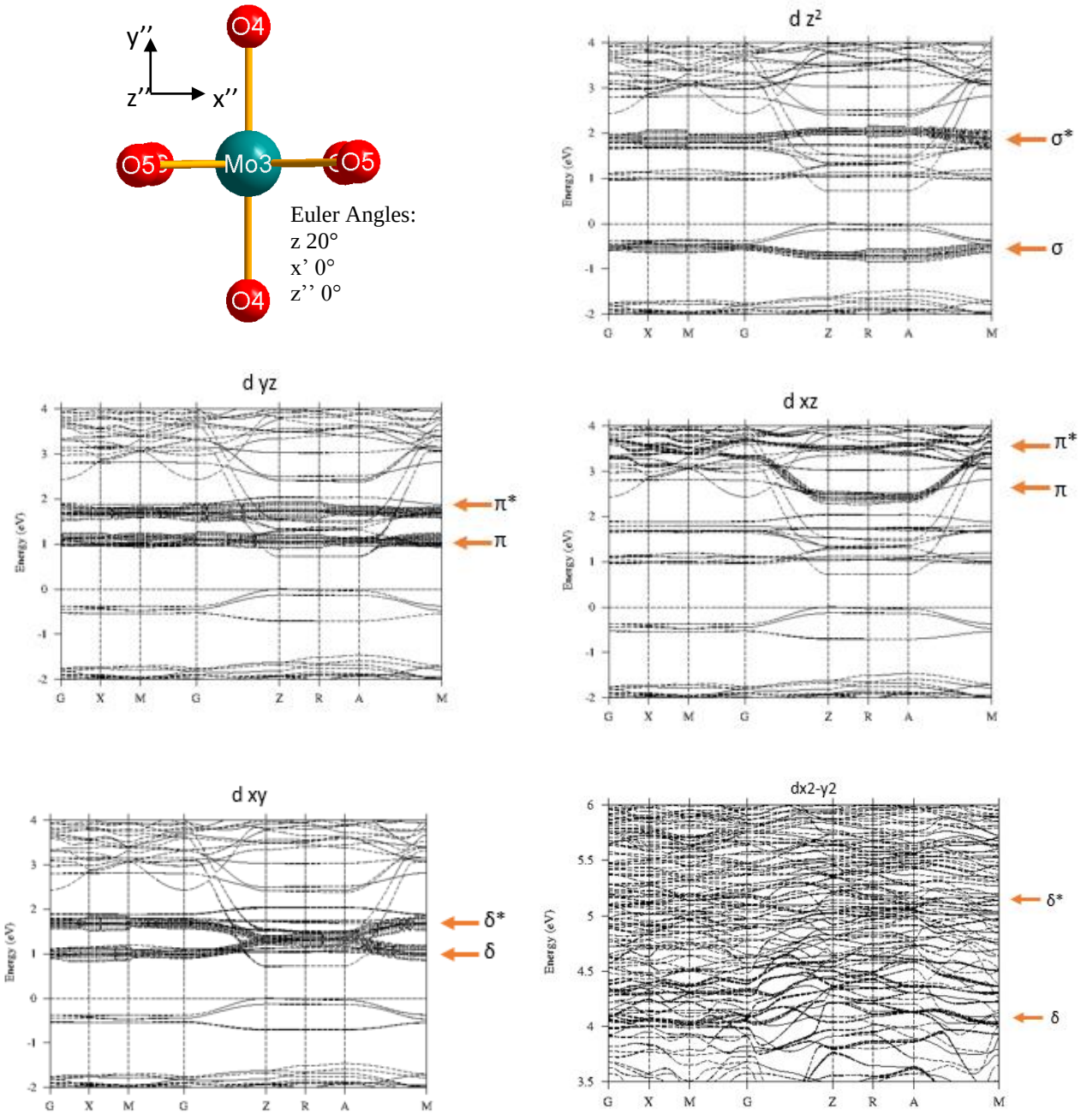

Figure S6. Individual *d* orbital contributions for the octahedral Mo3 site projected as "fatbands" in the electronic structure.

Assignment of orbital character from both single ion and molecular orbital (dimeric) point of view

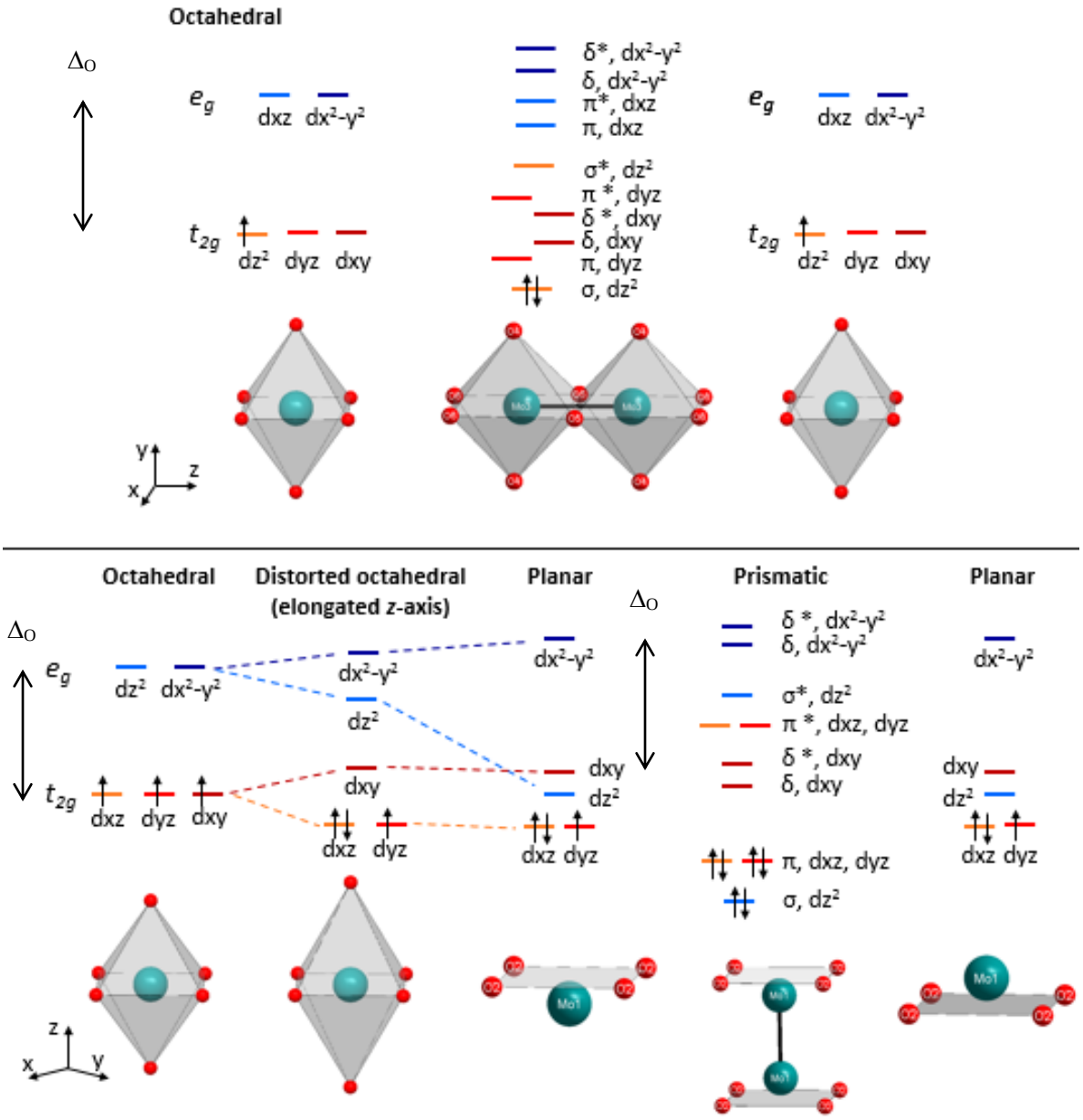

Figure S7. Molecular orbital ordering diagram depicting evolution of the spitting of the Mo *d* orbitals on going from a single ion to the metal-metal bonded dimer for both Mo_2O_{10} (top) and Mo_2O_8 (bottom). In the case of the Mo_2O_8 prismatic dimers, the orbital splitting is shown beginning with an undistorted MoO_6 octahedra that becomes distorted as the *z*-axis elongates and eventually forms the square planar MoO_4 members of the dimer. Note that the energy difference between the dxy and dx^2-y^2 orbital (Δ_O in an octahedral picture) remains essentially unchanged when distorting to a square planar type environment.

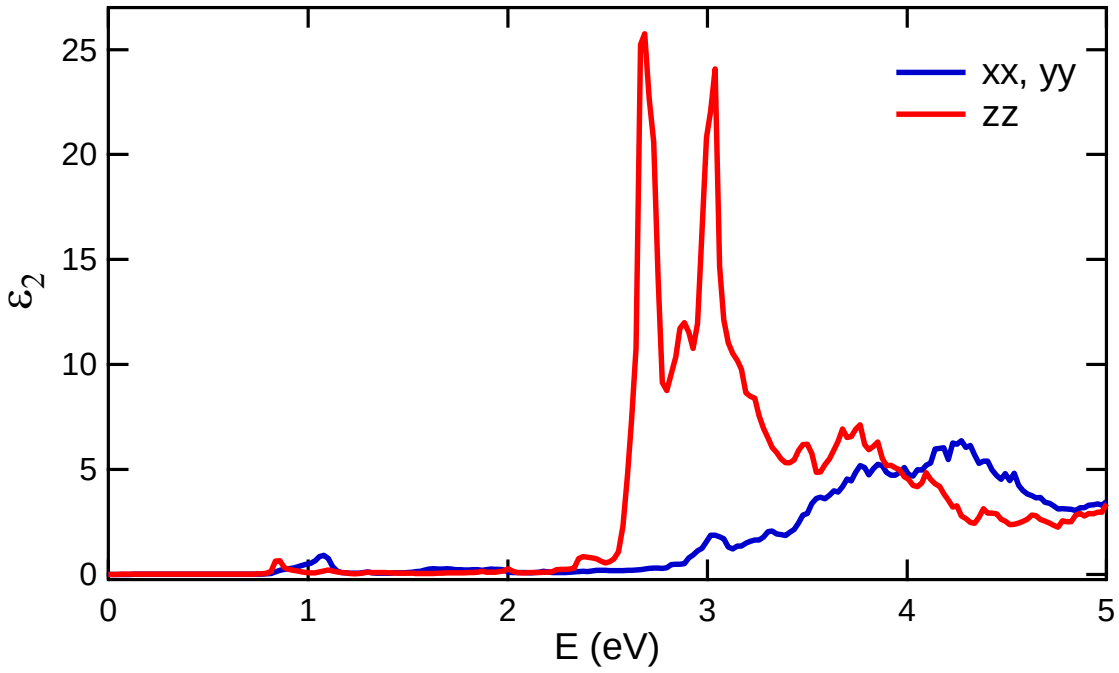

Figure S8. Calculated polarized absorption of La_2MoO_5 along the *x*, *y*, and *z* directions. The *x* and *y* directions are equivalent by symmetry in the tetragonal space group.

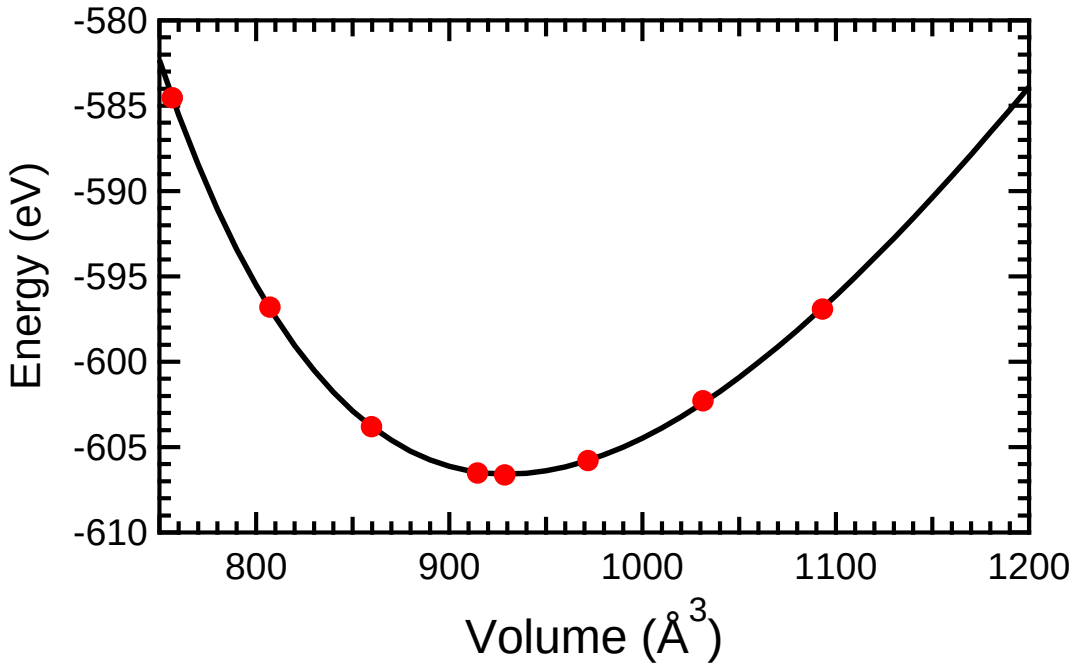

Figure S9. Fit of the calculated total energy for selected volumes (red circles) with relaxed internal coordinates and *c*/*a* ratios to the Murnaghan equation of states (line). Fit parameters are E_0=-606.582 eV, V_0=929.723 A^3, B_0=146 GPa and B_0'=4.67.

Appendix 3

Chapter 4 Supporting Information

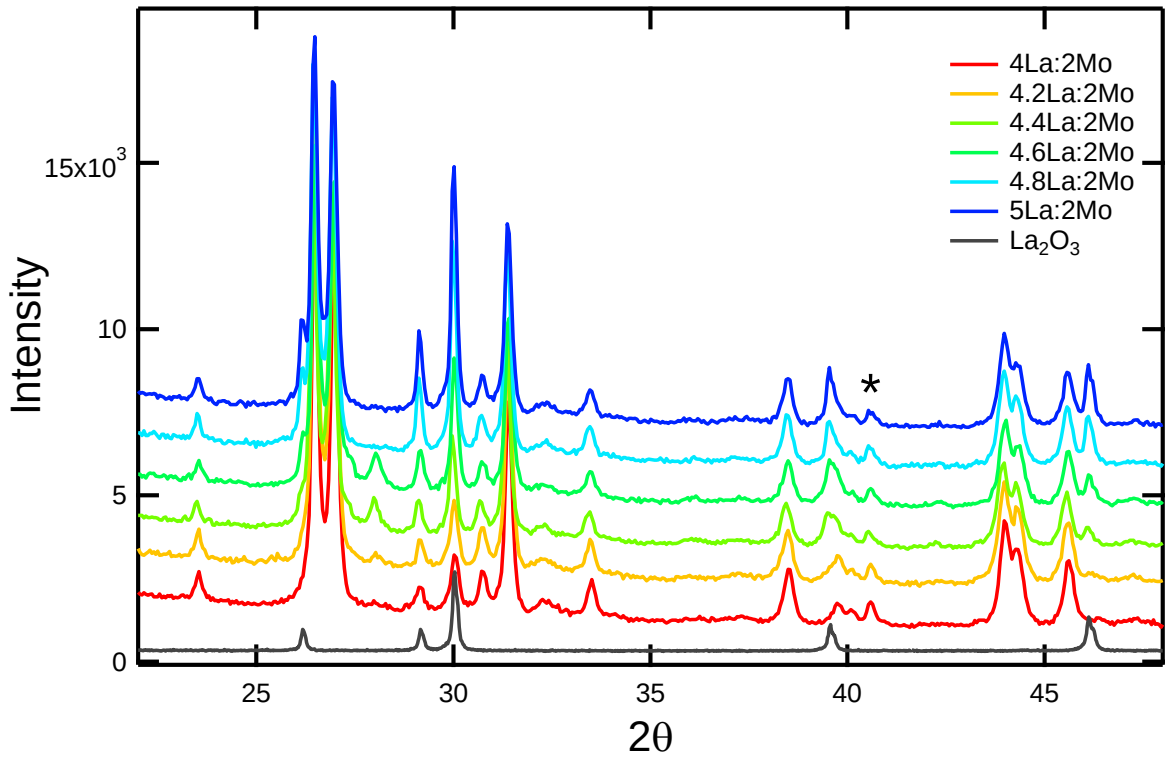

Figure S1. Laboratory X-ray diffraction data comparing the products of syntheses conducted with different starting ratios of 4+x La: $2Mo^{6+}$. Data for La_2O_3 (gray) is shown for reference. The position of the Mo impurity is indicated with an asterisk (*).

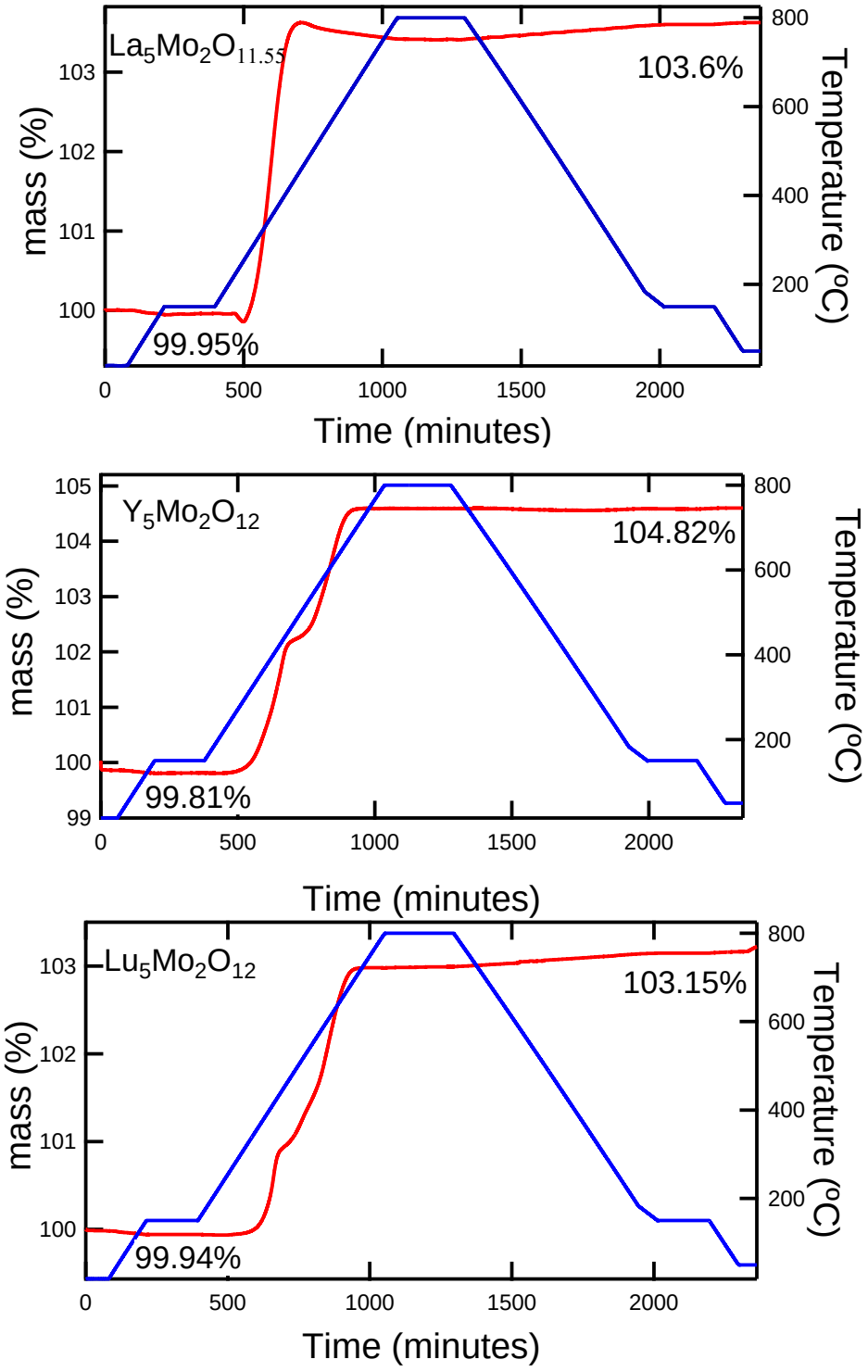

Figure S2. Individual results for the TGA oxidation experiments. The average oxidation state of Mo in each compound was calculated from the observed mass % (red) recorded at extended holds of 150°C before and after the complete oxidation of the powder sample. The temperature profile is shown in blue.

$Lu_5Mo_2O_{12}$ –Pawley Refinements

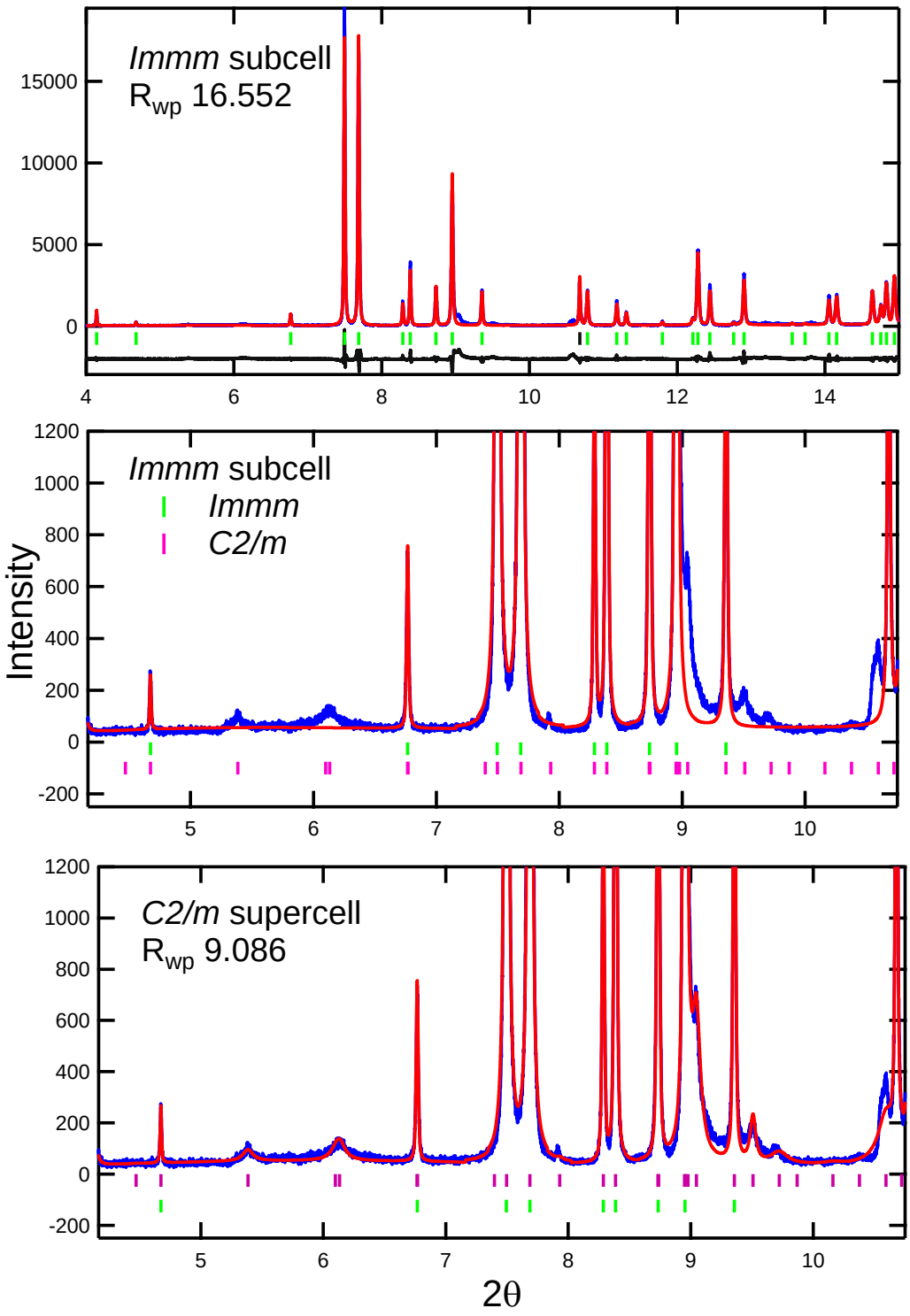

Figure S3. Pawley fits of the $Lu_5Mo_2O_{12}$ structure modeled in the subcell and supercell. Zoomed regions compare the fit of *Immm* subcell vs *C2/m* supercell.

$Lu_5Mo_2O_{12}$ –Pawley Refinements continued

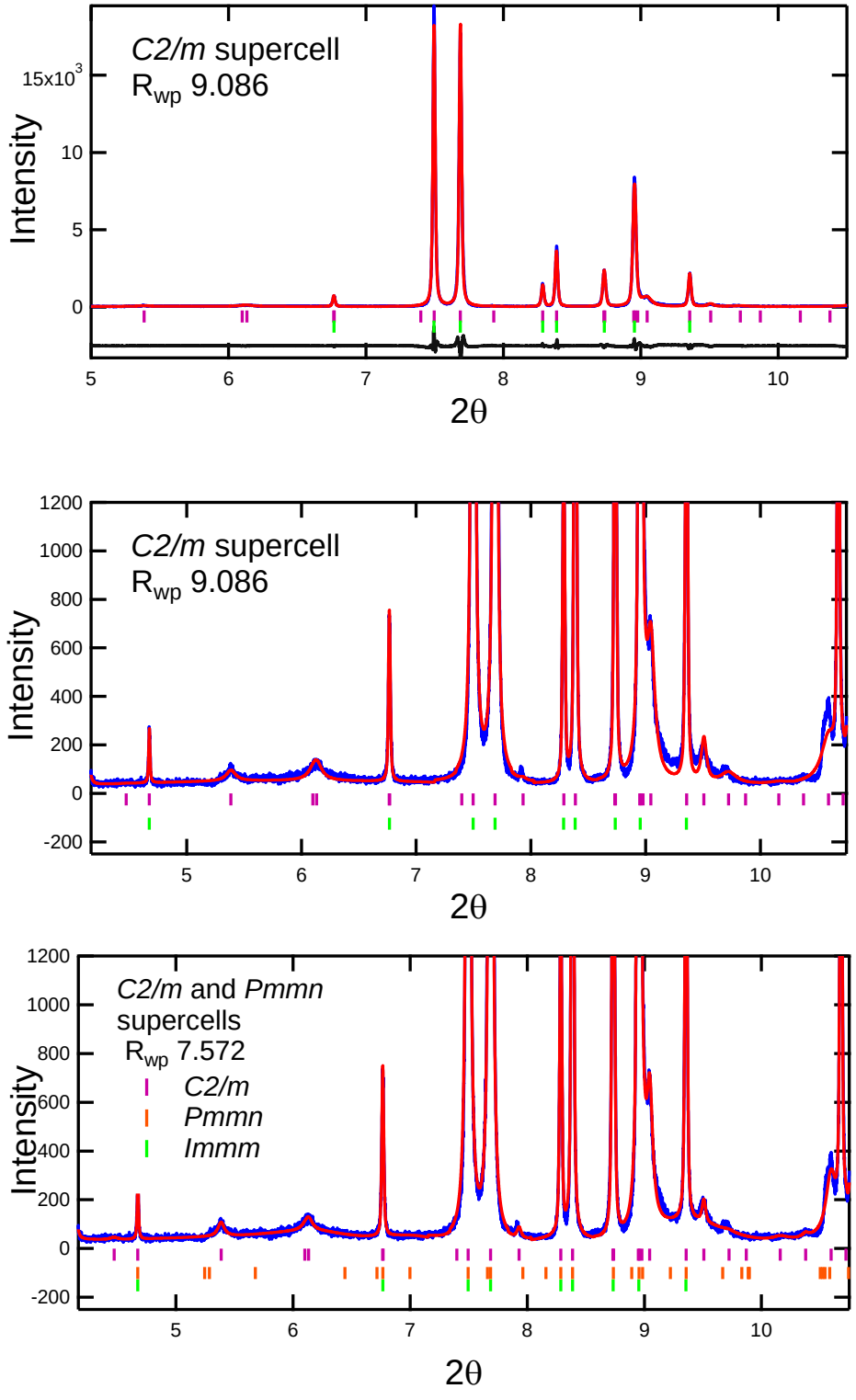

Figure S4. Comparison of Pawley fitting with the *C2/m* and *C2/m* combined with *Pmmn* supercell structures refined using a synchrotron data.

$La_5Mo_2O_{12}$ –Pawley Refinements

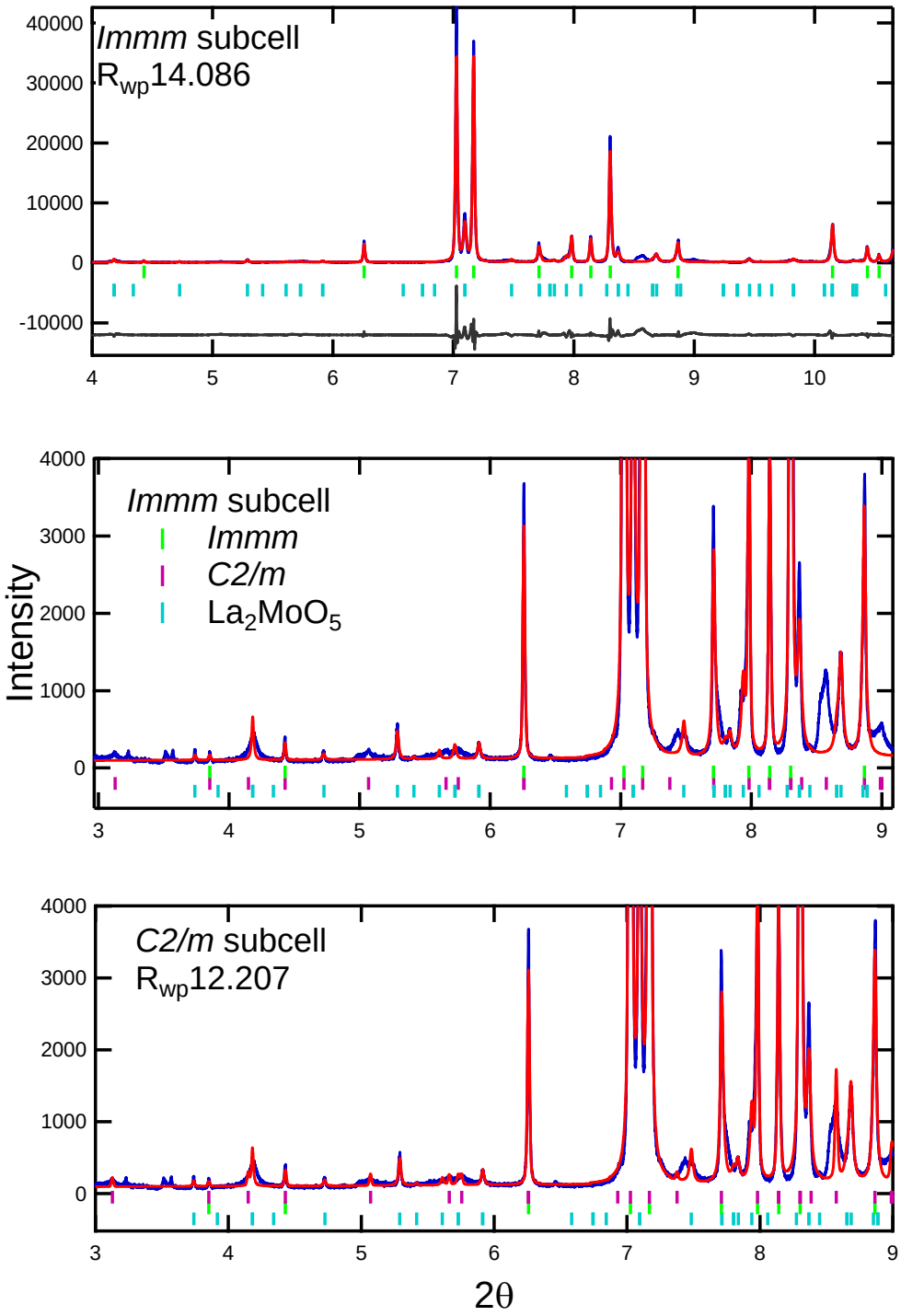

Figure S5. Pawley fits of the $La_5Mo_2O_{12}$ structure modeled in the subcell and supercell. Zoomed regions compare the fit of *Immm* subcell vs *C2/m* supercell. Indexing for the substantial La_2MoO_5 impurity phase is also provided.

$La_5Mo_2O_{12}$ –Pawley Refinements continued

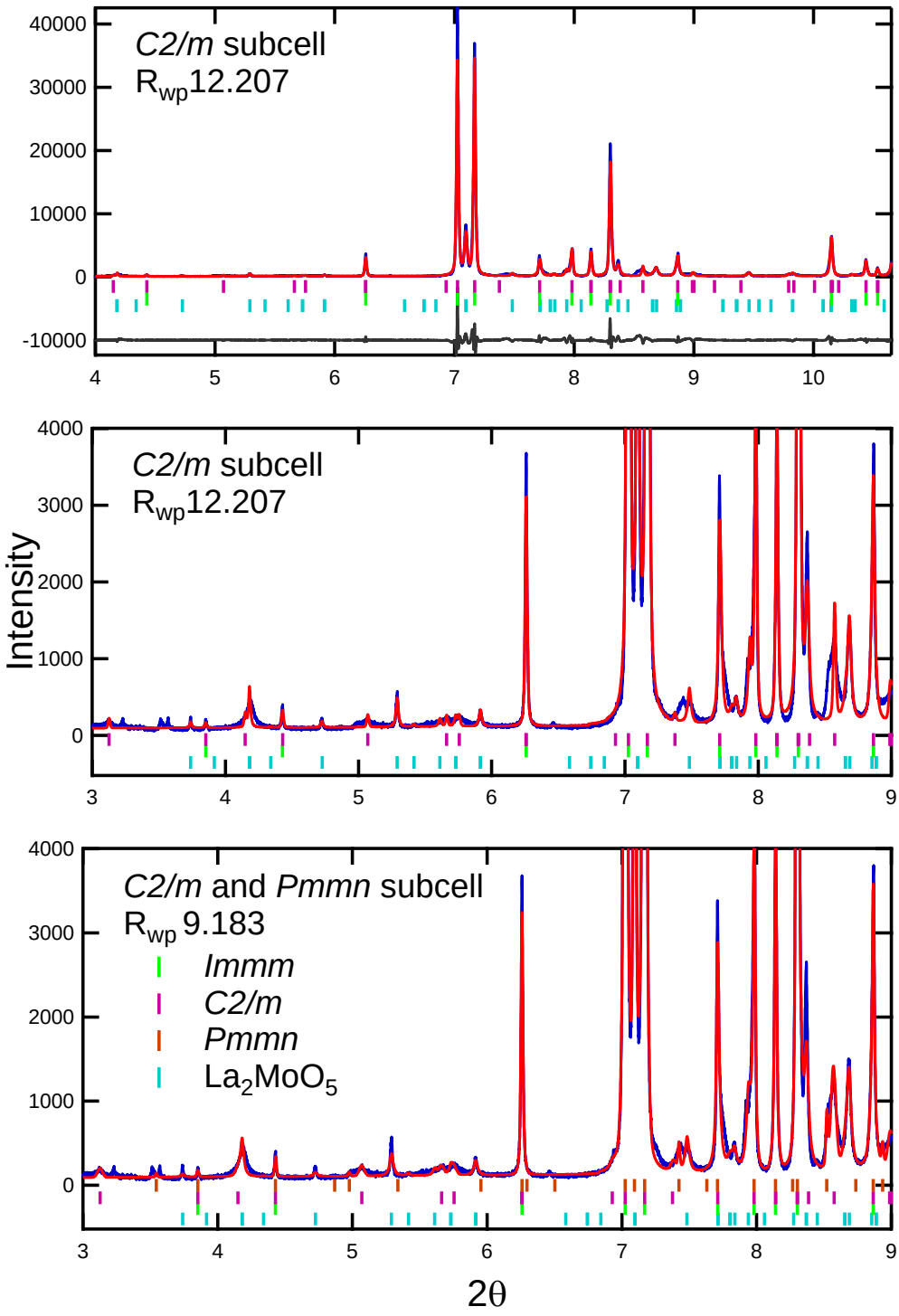

Figure S6. Comparison of Pawley fitting with the *C2/m* and *C2/m* combined with *Pmmn* supercell structures refined using a synchrotron data. Indexing for the substantial La_2MoO_5 impurity phase is also provided.

Table S1. Rietveld refinement parameters for $Ln_5Mo_2O_{12}$ (*Ln* = Y, Lu) refined in the *Immm* subcell using synchrotron data.

Ln		Y	Lu
Crystal system		Orthorhombic	Orthorhombic
Space group		*Immm* (#71)	*Immm* (#71)
Radiation		Synchrotron	Synchrotron
Temperature		RT	RT
λ (Å)		0.41333	0.414176
Range of collection		$1° < 2\theta < 50°$	$1° < 2\theta < 50°$
		$0.54 < d < 23.68$	$0.54 < d < 23.68$
Lattice parameters (Å)	*a*	11.6379(1)	11.46653(9)
	b	5.72314(6)	5.66482(5)
	c	3.74085(4)	3.68608(3)
Cell volume ($Å^3$)		249.160(5)	239.432(3)
ρ_{calc} (g/cm^3)		5.525(2)	8.7298(1)
R_{bragg}		4.21	4.93
R_{wp}		17.450	18.390

Table S2. Atomic coordinates of $Ln_5Mo_2O_{12}$ (*Ln* = Y, Lu) refined in the *Immm* subcell using synchrotron data.

	Wyckoff	*x*	*y*	*z*	*occ*	B_{eq}
$Y_5Mo_2O_{12}$						
Y1	4f	0.31122(6)	0	½	1	1.63(7)
Y2	2c	½	½	0	0.497(1)	1.78(9)
Mo1	4h	½	0.2803(2)	0	0.503(1)	0.89(8)
O1	8h	0.1593(3)	¼	½	1	0.90(9)
O2	4j	½	0	0.622(2)	0.465(6)	0.90(9)
O3	4i	½	½	0.624(2)	0.537(6)	0.90(9)
$Lu_5Mo_2O_{12}$						
Lu1	4f	0.31002(5)	0	½	1	1.46(7)
Lu2	2c	½	½	0	0.494(2)	1.26(8)
Mo1	4h	½	0.2796(3)	0	0.506(2)	0.62(8)
O1	8h	0.1584(4)	¼	½	1	0.7(1)
O2	4j	½	0	0.625(5)	0.464(8)	0.7(1)
O3	4i	½	½	0.614(3)	0.536(7)	0.7(1)

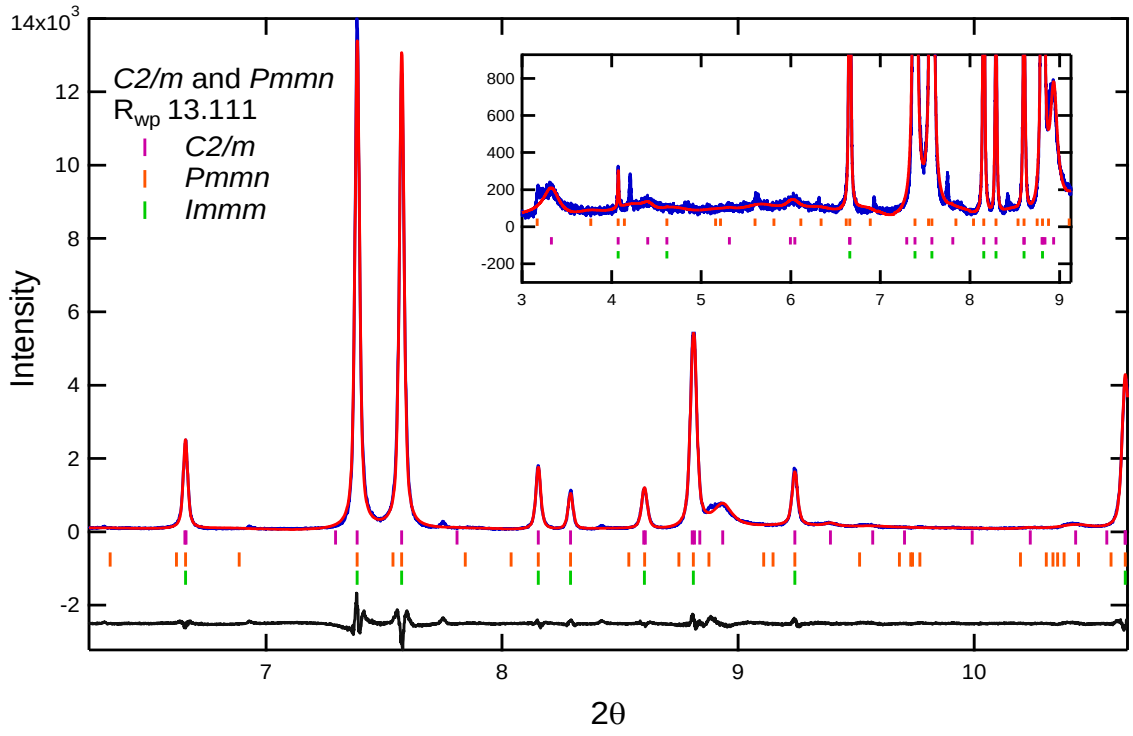

Figure S7. The $Y_5Mo_2O_{12}$ structure modeled (Pawley fit) with both possible *C2/m* and *Pmmn* supercells. Corresponding tick marks represent indexing in both supercells and the subcell indexing is also provided for reference.

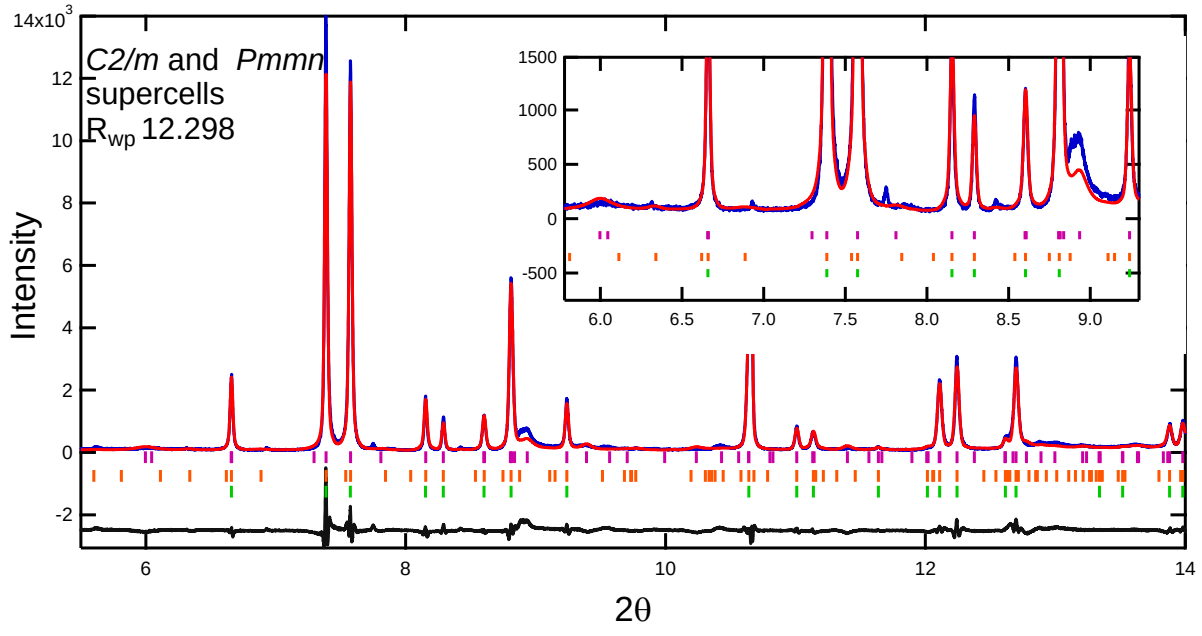

Figure S8. Results of a two phase Rietveld refinement using the both *C2/m* supercell and the *Pmmn* supercell showing the fit is only marginally improved compared to the single phase *C2/m* structural model. Tick marks are provided for reference.

$Lu_5Mo_2O_{12}$ –Rietveld Refinements

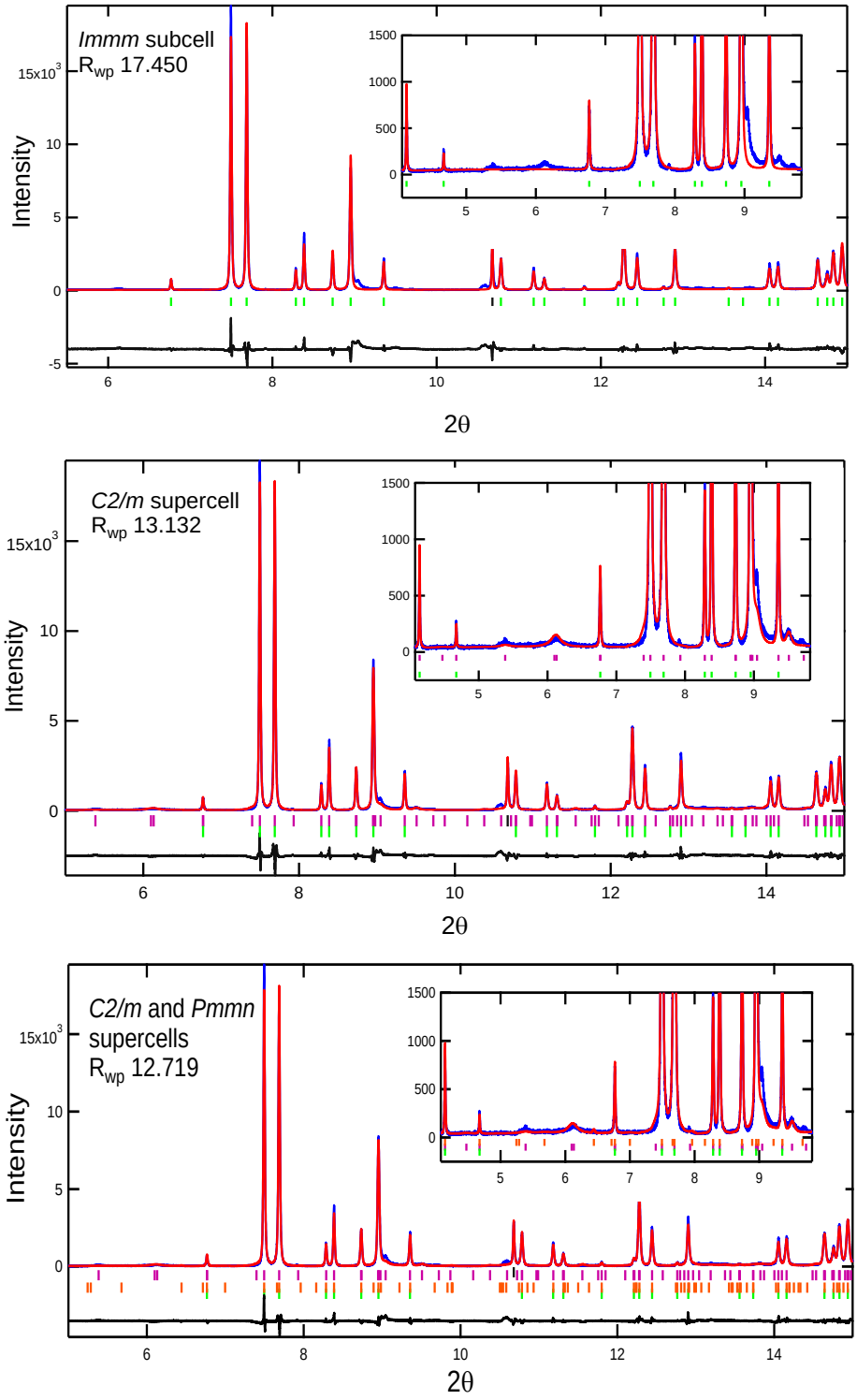

Figure S9. Comparison of Rietveld refinements results for $Lu_5Mo_2O_{12}$ refined with different structural models. Ticks for sub and supercells follow the same color scheme as previous plots.

$La_5Mo_2O_{12}$ –Rietveld Refinements

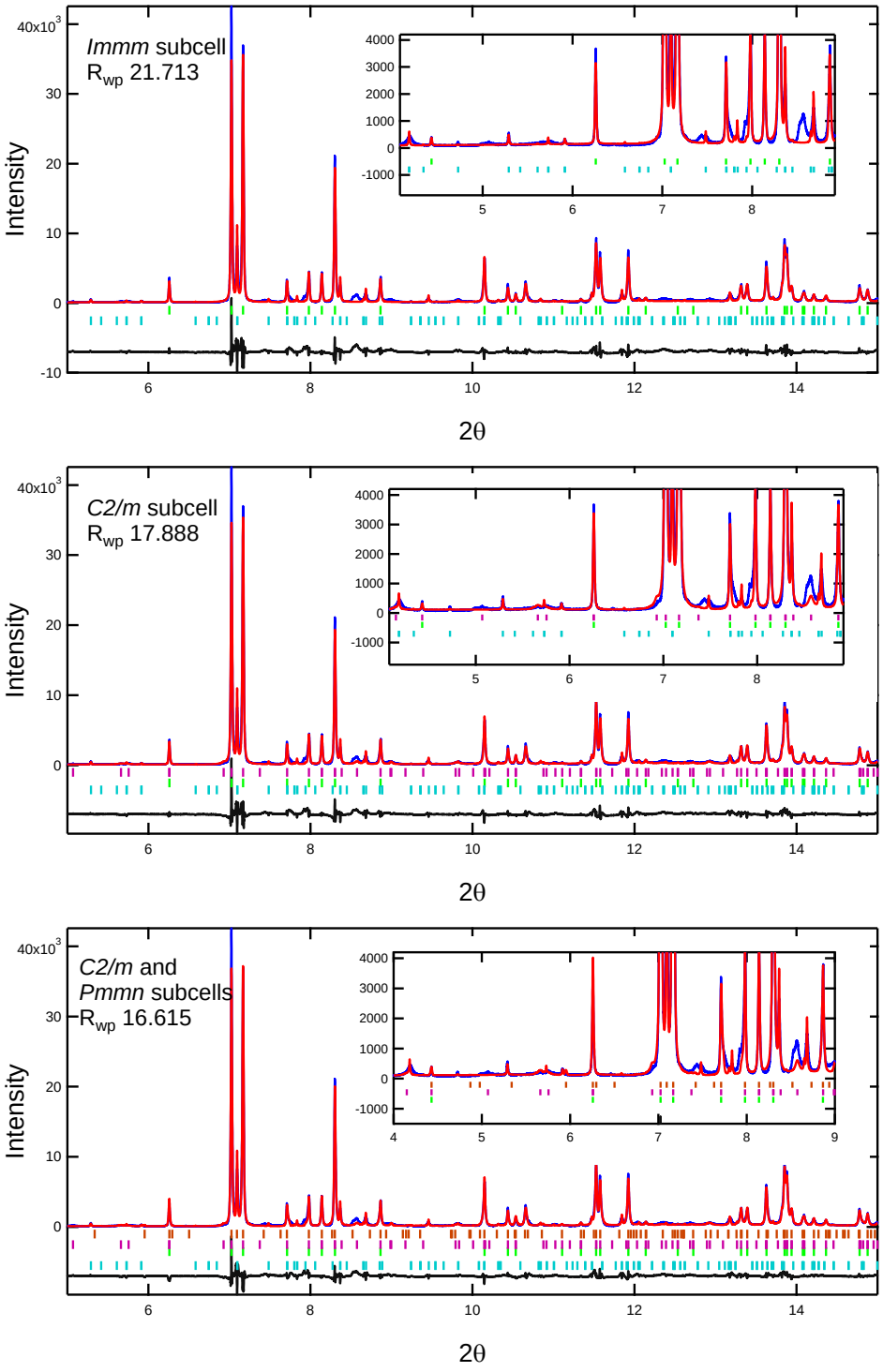

Figure S10. Comparison of Rietveld refinements results for $La_5Mo_2O_{12}$ refined with different structural models. Ticks for sub and supercells follow the same color scheme as previous plots.

Table S3. Atomic positions determined for the *Pmmn* supercell are provided for $Y_5Mo_2O_{12}$.

space group	*a* (Å)	*b* (Å)	*c* (Å)	volume (Å^3)
Pmmn	11.6396(1)	5.72324(8)	7.4820(1)	498.42(3)
Site	Wyckoff	*x*	*y*	*z*
Y1	4f	0.5264	¼	0.1490
Y2	4f	0.5594	¼	0.6514
Y3	2a	¼	¼	0.1151
Mo1	4e	¼	0.0328	0.625
O1	8g	0.9013	0	0.875
O2	8g	0.9063	0	0.375
O3	2a	¼	¼	0.8375
O4	2a	¼	¼	0.4130
O5	2b	¼	¾	0.4247
O6	2b	¼	¾	0.8269

Table S4. Rare earth oxygen bond distances refined from neutron data collected at 300K.

	atom 1	atom 2	mult	distance (Å)
$La_5Mo_2O_{11.55}$	La1	O4	x1	2.41(4)
		O2	x2	2.48(1)
		O2	x2	2.48(2)
		O1	x2	2.55(1)
	La2	O1	x2	2.36(1)
		O4	x1	2.39(3)
		O1	x2	2.41(1)
		O2	x2	2.65(2)
	La3	O1	x4	2.41(1)
		O3	x2	2.48(1)
$Y_5Mo_2O_{12}$	Y1	O4	x1	2.25(2)
		O1	x2	2.27(1)
		O2	x2	2.298(8)
		O2	x2	2.42(1)
	Y2	O1	x2	2.262(9)
		O1	x2	2.29(1)
		O4	x1	2.34(1)
		O2	x2	2.52(1)
	Y3	O3	x2	2.223(7)
		O1	x4	2.336(7)
$Lu_5Mo_2O_{12}$	Lu1	O4	x1	2.21(1)
		O2	x2	2.225(4)
		O1	x2	2.249(8)
		O2	x2	2.468(8)
	Lu2	O1	x2	2.224(8)
		O1	x2	2.253(4)
		O4	x1	2.315(9)
		O2	x2	2.417(8)
	Lu3	O3	x2	2.155(4)
		O1	x4	2.280(3)

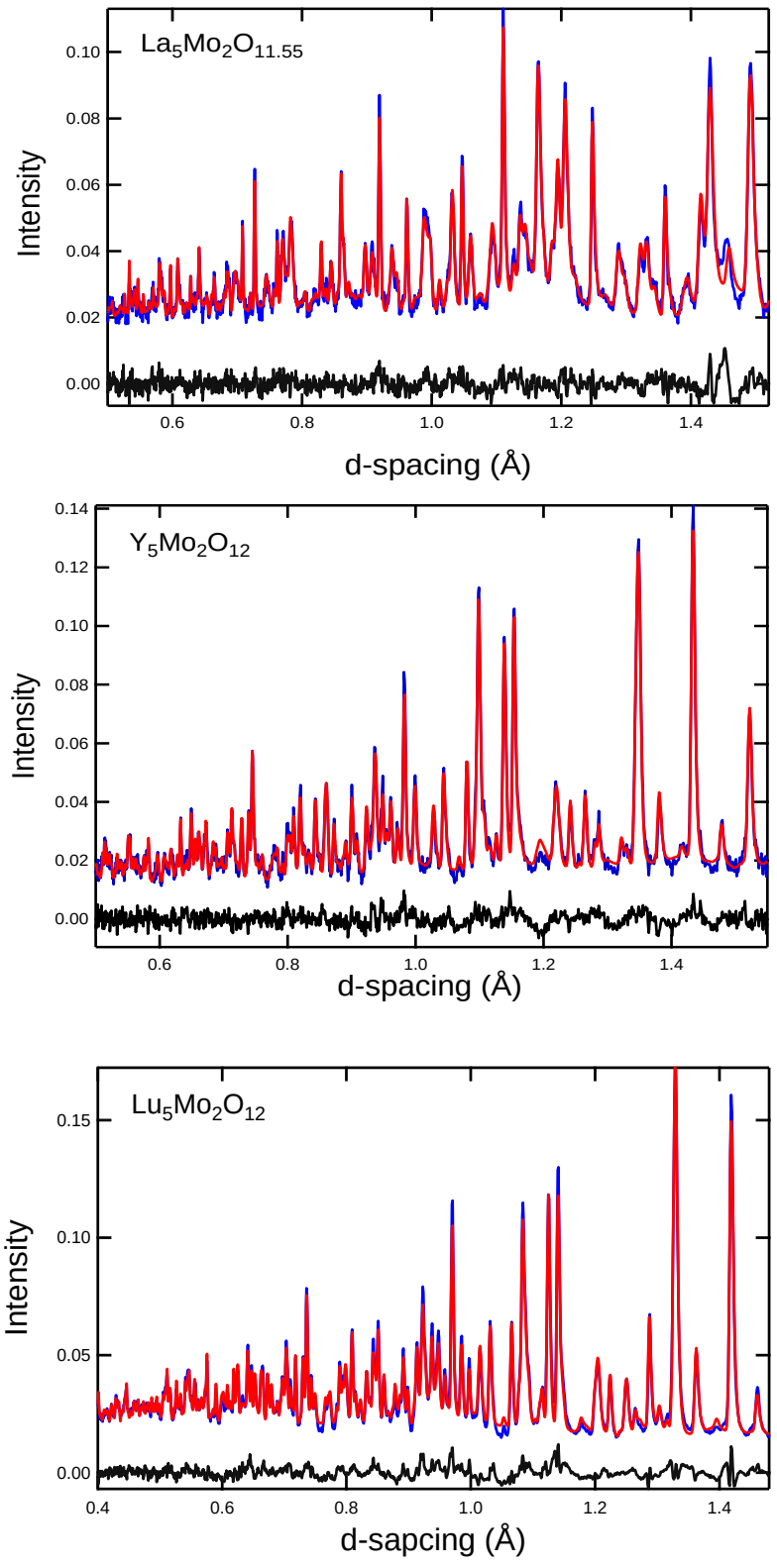

Figure S11. Rietveld refinement of *Ln*$_5$Mo$_2$O$_{12}$ compounds refined from TOF neutron data collected at 300 K.

$Y_5Mo_2O_{12}$ Electronic Band Structure

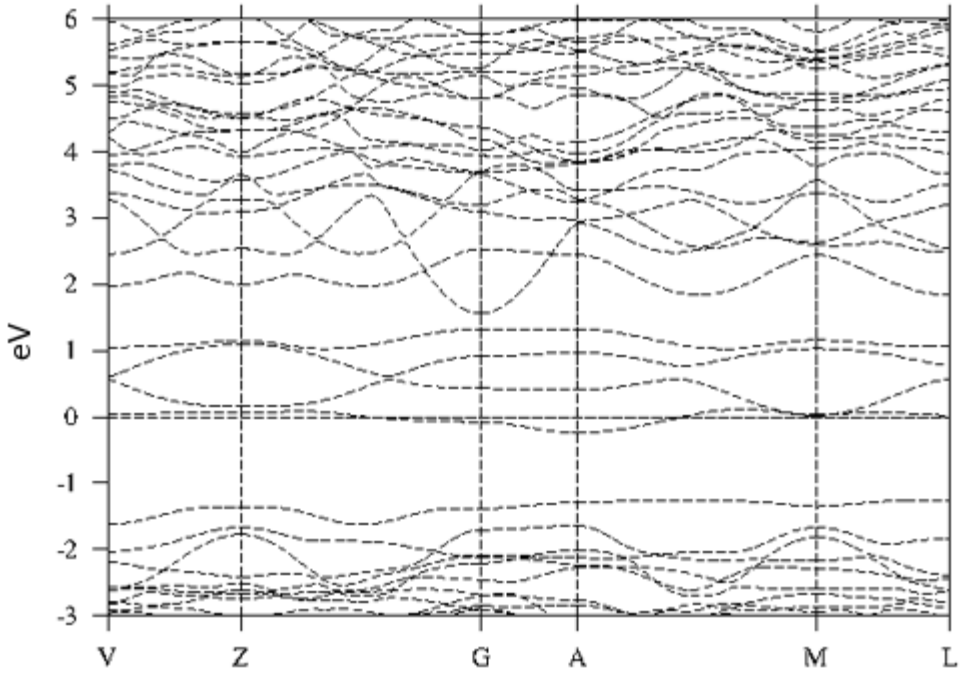

Figure S12. The electronic band structure of $Y_5Mo_2O_{12}$ (LMTO) calculated with the refined lattice parameters and atom positions for the majority site structure obtained from neutron diffraction data collected at room temperature.

$Y_5Mo_2O_{12}$ Mo1 Site Fatbands Analysis

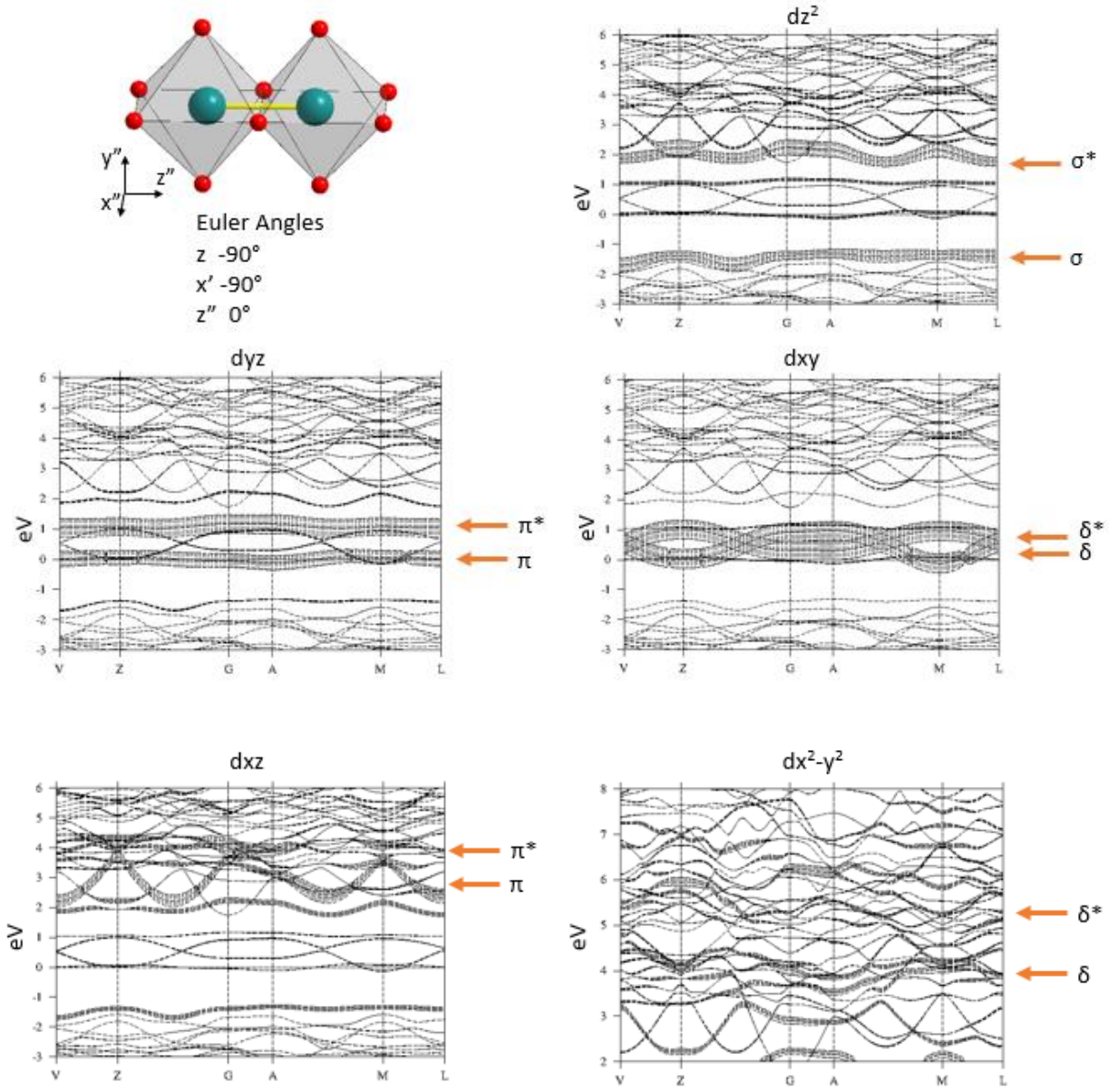

Figure S13. Individual *d* orbital contributions for the octahedral Mo1 site projected as "fatbands" in the electronic structure.

$La_5Mo_2O_{12}$ Mo1 Site Fatbands Analysis

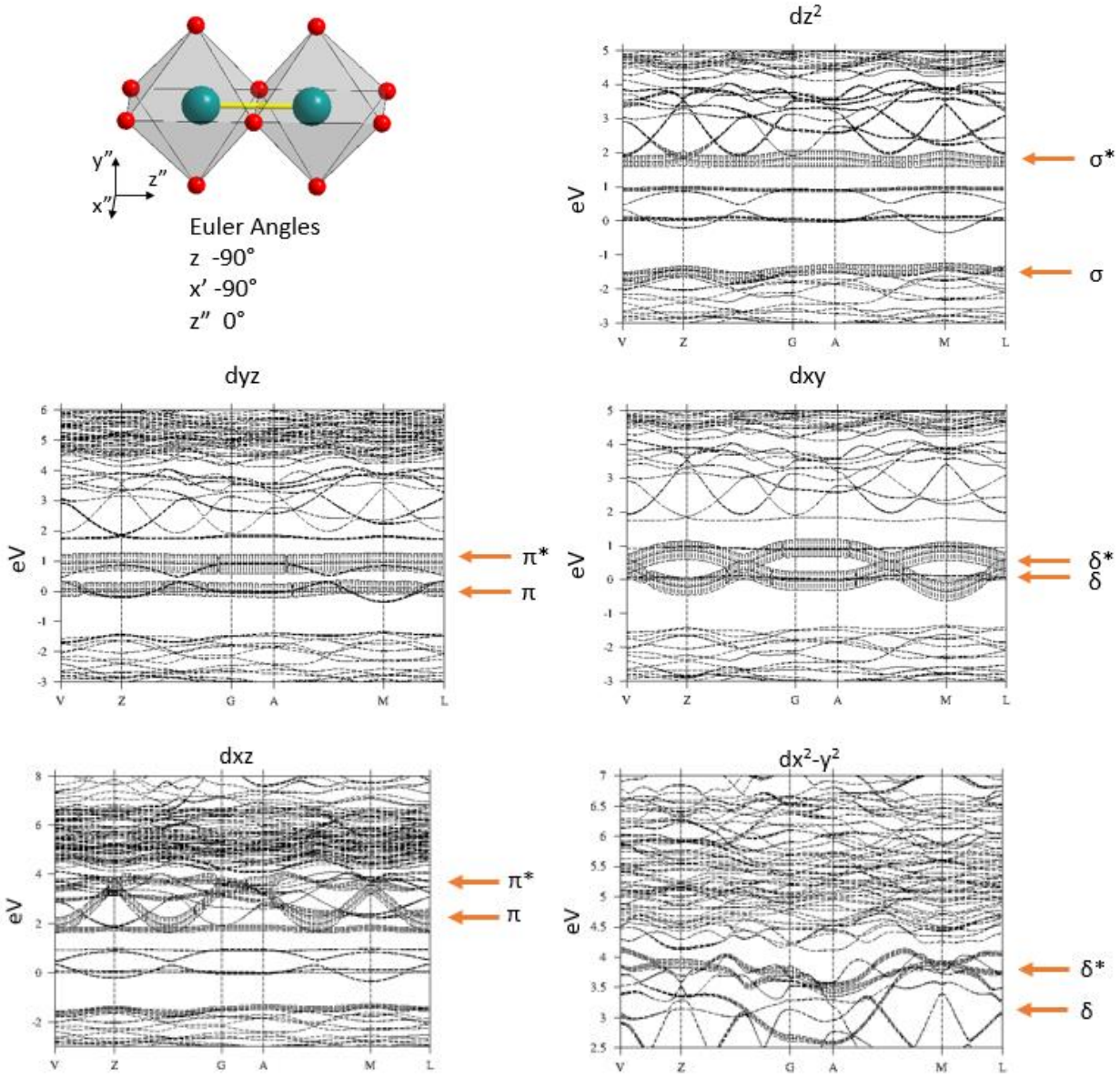

Figure S14. Individual *d* orbital contributions for the octahedral Mo1 site projected as "fatbands" in the electronic structure of $La_5Mo_2O_{12}$. The calculations were completed for the fully stoichiometric cell due to program limitations

$Lu_5Mo_2O_{12}$ Mo1 Site Fatbands Analysis

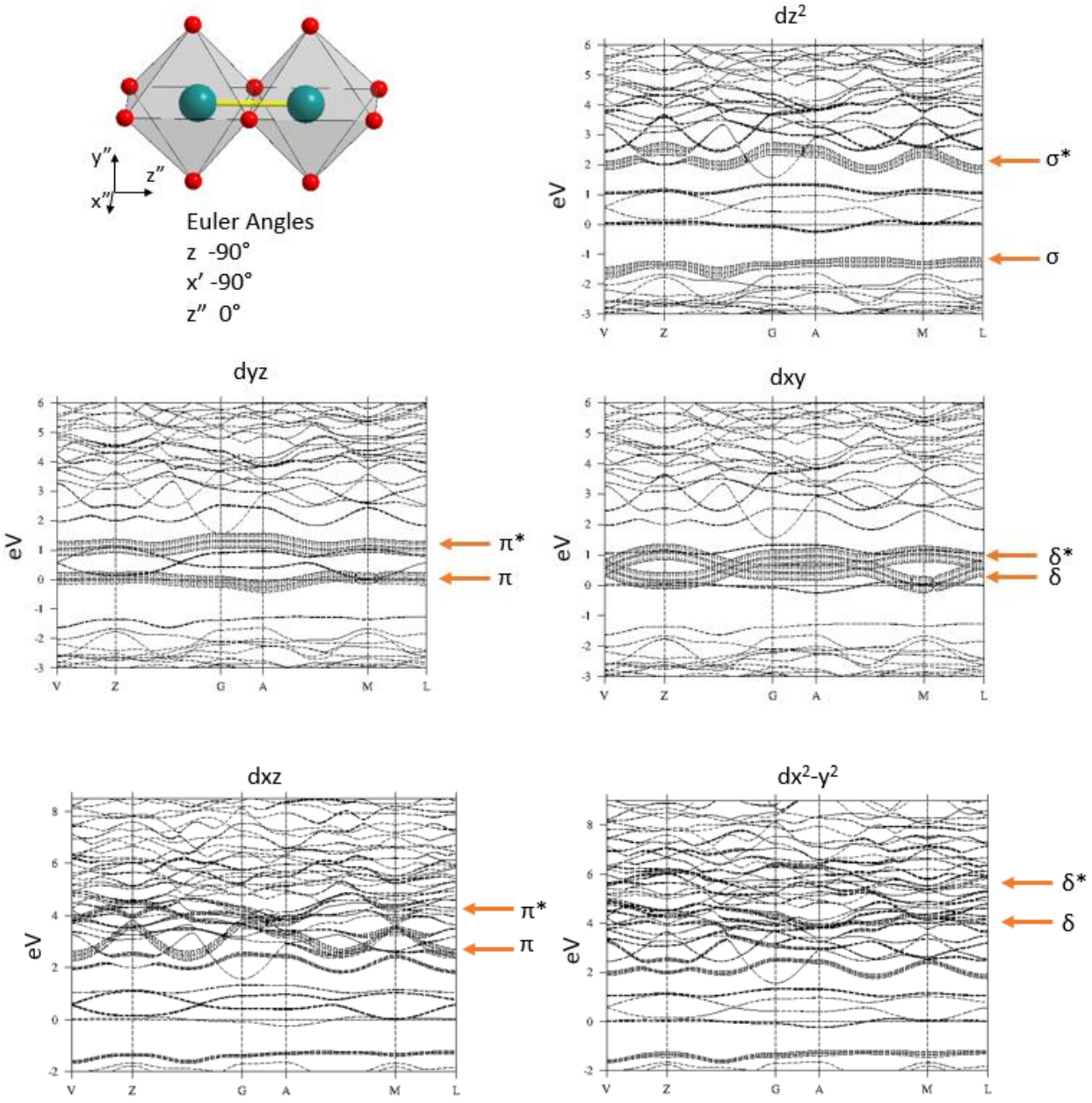

Figure S15. Individual *d* orbital contributions for the octahedral Mo1 site projected as "fatbands" in the electronic structure of $Lu_5Mo_2O_{12}$.

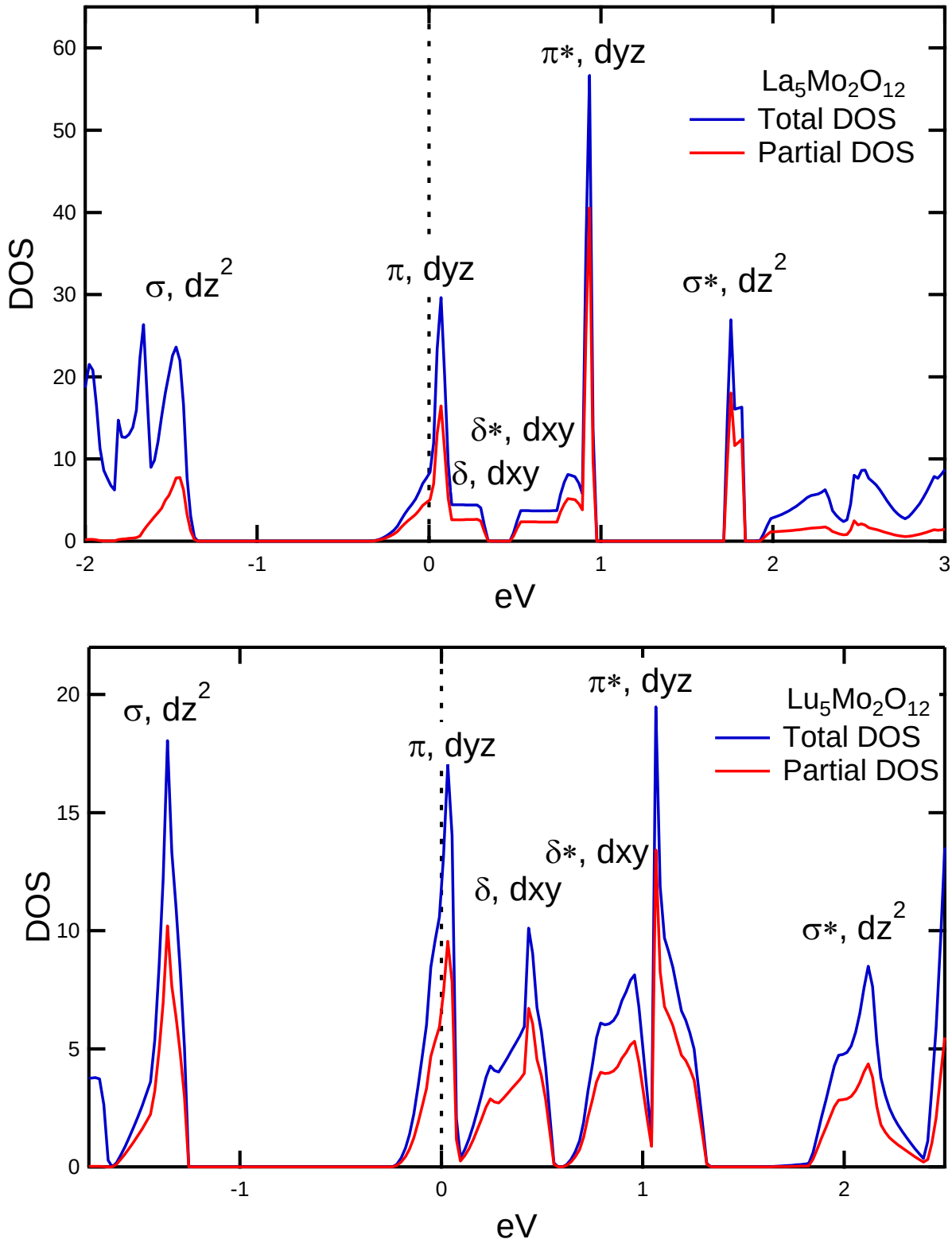

Figure S16. The calculated DOS plots for $Lu_5Mo_2O_{12}$ and $La_5Mo_2O_{12}$ majority site structures (blue) with the Mo *d* orbital partial DOS shown in red.

References

(1) Rao, C. Transition Metal Oxides. *Annu. Rev. Phys. Chem.* **1989**, *40*, 291-326.

(2) Cheong, S. W. Transition metal oxides: The exciting world of orbitals. *Nature Materials* **2007**, *6*, 927-928.

(3) Kamihara, Y.; Hiramatsu, H.; Hirano, M.; Kawamura, R.; Yanagi, H.; Kamiya, T.; Hosono, H. Iron-Based Layered Superconductor: LaOFeP. *J. Am. Chem. Soc.* **2006**, *128*, 10012-10013.

(4) Goodenough, J. B. Perspective on Engineering Transition-Metal Oxides. *Chem. Mater.* **2014**, *26*, 820-829.

(5) Miessler, G.; Fischer, P.; Tarr, D.: *Inorganic Chemistry*; 5 ed.; Prentice Hall, 2013. pp. 696.

(6) Griffith, J.; Orgel, L. Ligand-Field Theory. *Q. Rev. Chem. Soc.* **1957**, *11*, 381-393.

(7) Tokura, Y.; Nagaosa, N. Orbital Physics in Transition-Metal Oxides. *Science* **2000**, *288*, 462-468.

(8) Rao, C. N. R.: Transition metal oxides : crystal chemistry, phase transition, and related aspects. Subba Rao, G. V., Ed.; U.S. Dept. of Commerce, National Bureau of Standards : for sale by the Supt. of Docs., U.S. Govt. Print. Off.: Washington :, 1974.

(9) Valenzuela, R. Novel Applications of Ferrites. *Physics Research International* **2012**.

(10) West, A.: *Basic Solid State Chemistry*; 2nd ed.; John Wiley & Sons Ltd., 1999.

(11) Mugavero, S. J.; Gemmill, W. R.; Roof, I. P.; zur Loye, H. C. Materials discovery by crystal growth: Lanthanide metal containing oxides of the platinum group metals (Ru, Os, Ir, Rh, Pd, Pt) from molten alkali metal hydroxides. *J. Solid State Chem.* **2009**, *182*, 1950-1963.

(12) McCarley, R. E. Metal-clusters and extended metal-metal bonding in metal oxide systems. *ACS Symposium Series* **1983**, *211*, 273-290.

(13) Cotton, F.; Walton, R.: *Multiple Bonds between Metal Atoms*; 2 ed.; Oxford University Press: New York, 1993.

(14) Cotton, F. A. Multiple metal-metal bonds. *Journal of Chemical Education* **1983**, *60*, 713.

(15) Lewis, J.: Metal-metal interaction in transition metal complexes. In *Pure and Applied Chemistry*, 1965; Vol. 10; pp 11.

(16) Falvello, L. R.; Foxman, B. M.; Murillo, C. A. Fitting the Pieces of the Puzzle: The δ Bond. *Inorg. Chem.* **2014**, *53*, 9441-9456.

(17) Murillo, C. A. The magic of the delta bonds: How to modulate electronic communication in pairs-of-pairs containing multiple bonded Mo-2 species. *Inorganica Chimica Acta* **2015**, *424*, 3-13.

(18) Rogers, D. B.; Shannon, R. D.; Sleight, A. W.; Gillson, J. L. Crystal Chemistry of Metal Dioxides with Rutile-Related Structures. *Inorg. Chem.* **1969**, *8*, 841-849.

(19) Kucharczyk, D.; Niklewski, T. Accurate X-ray determination of the lattice-parameters and the thermal-expansion coefficients of VO_2 near the transition temperature. *J. Appl. Crystallogr.* **1979**, *12*, 370-373.

(20) Gulino, A.; Parker, S.; Jones, F. H.; Egdell, R. G. Influence of metal-metal bonds on electron spectra of MoO_2 and WO_2. *Journal of the Chemical Society-Faraday Transactions* **1996**, *92*, 2137-2141.

(21) Tkachenko, E.; Fedorov, P. Lower rare-earth molybdates. *Inorg. Mater.* **2003**, *39*, S25-S45.

(22) Xu, J.; Sonne, M.; Pryds, N.; Kleinke, H. Thermoelectric properties of molybdenum oxides $LnMo_8O_{14}$ (Ln = La, Ce, Pr, Nd and Sm). *J. Alloys Compd.* **2010**, *489*, 353-356.

(23) Gougeon, P.; Gall, P.; McCarley, R. Structure of $Gd_4Mo_{18}O_{32}$. *Acta Crystallogr. C* **1991**, *C47*, 2026-2029.

(24) Wilhelmi, K.; Lagervall, E.; Muller, O. Crystal structure of $Nd_4Re_2O_{11}$. *Acta Chem. Scand.* **1970**, *24*.

(25) Bharathy, M.; Gemmill, W. R.; Fox, A. H.; Darriet, J.; Smith, M. D.; Hadermann, J.; Remy, M. S.; zur Loye, H. C. Synthesis and magnetic properties of rare earth ruthenates, $Ln_5Ru_2O_{12}$ (Ln = Pr, Nd, Sm-Tb). *J. Solid State Chem.* **2009**, *182*, 1164-1170.

(26) Moini, A.; Subramanian, M.; Clearfield, A.; DiSalvo, F.; McCarroll, W. Structure and properties of $La_2Mo_2O_7$: A quasi-two-dimensional metallic oxide with strong Mo-Mo bonds. *J. Solid State Chem.* **1987**, *66*, 136-143.

(27) Gall, P.; Gougeon, P. $La_5Mo_6O_{21}$: a novel ternary reduced molybdenum oxide containing $\{MoIV\}_3$ clusters and isolated MoV centres. *Acta Crystallogr. C* **2005**, *61*, 169-170.

(28) Gall, P.; Gougeon, P. Structure of $La_4Mo_2O_{11}$ containing isolated Mo_2O_{10} cluster units. *Acta Crystallogr. C* **1992**, *48*, 1915-1917.

(29) Torardi, C.; Fecketter, C.; McCarroll, W.; DiSalvo, F. Structure and Properties of $Y_5Mo_2O_{12}$ and $Gd_5Mo_2O_{12}$: Mixed Valence Oxides with Structurally Equivalent Molybdenum Atoms. *J. Solid State Chem.* **1985**, *60*, 332-342.

(30) Gall, P.; Barrier, N.; Gautier, R.; Gougeon, P. Synthesis, Structural Trends, and Physical and Electronic Properties of the Reduced Molybdenum Oxides $R_4Mo_4O_{11}$ (R) Nd-Tm and Y) Containing Infinite Chains of Trans-Edge-Shared Octahedral Clusters. *Inorg. Chem.* **2002**, *41*, 2879-2885.

(31) Ledesert, M.; Labbe, P.; McCarroll, W.; Leligny, H.; Raveau, B. $La_5Mo_4O_{16}$ - A new structural type related to perovskite with extremely short Mo-Mo bonds *J. Solid State Chem.* **1993**, *105*, 143-150.

(32) Loftland, S.; Scabarozi, T.; Ramanujachary, K.; McCarroll, W. Unusual magnetic properties of $La_5Mo_4O_{16}$. *J. Magn. Magn. Mater.* **2003**, *260*, 184-187.

(33) Colabello, D. M.; Camino, F. E.; Huq, A.; Hybertsen, M.; Khalifah, P. G. Charge Disproportionation in Tetragonal La_2MoO_5, a Small Band Gap Semiconductor Influenced by Direct Mo-Mo Bonding. *J. Am. Chem. Soc.* **2015**, *137*, 1245-1257.

(34) Hibble, S.; Cooper, S.; Hannon, A.; Patat, S.; McCarroll, W. Structure of $LaMo_2O_5$ containing both isolated Mo_6O_{18} clusters and sheets of fused triangular Mo-3 clusters. *Inorg. Chem.* **1998**, *37*, 6839-6846.

(35) Gall, P.; Gautier, R.; Halet, J.; Gougeon, P. Synthesis, physical properties, and theoretical study of $R_{16}Mo_{21}O_{56}$ compounds (R) La, Ce, Pr, and Nd) containing bioctahedral Mo_{10} clusters and single Mo atoms. *Inorg. Chem.* **1999**, *38*, 4455-4461.

(36) Gall, P.; Gougeon, P. Structure of $La_5Mo_{32}O_{54}$ Containing trans Bicapped Mo8 Octahedral Clusters and Tricluster Mo7-Mo10-Mo7 Chain Fragments. *Acta Crystallogr. C* **1993**, *49*, 1580-1584.

(37) Gall, P.; Gougeon, P.; Ramanujachary, K. V.; McCarroll, W. H.; Greenblatt, M. Anomalous metal-insulator transitions in reduced molybdenum oxides, $A_4Mo_{18}O_{32}$ (A = Ca, Y, Gd-Yb) with Mo-n (n = 2, 4, 6) cluster chains. *J. Solid State Chem.* **1997**, *134*, 45-51.

(38) Gougeon, P.; Gall, P.; Halet, J.; Gautier, R. Structural trends and the electronic structure of the rare-earth oxomolybdates RMo_5O_8 (R = La,Ce, Pr, Nd, Sm, Eu and Gd) containing chains of bioctahedral Mo_{10} clusters. *Acta Crystallogr. B* **2003**, *B59*, 472-478.

(39) Jeitschko, W.; Heumannskamper, D.; Rodewald, U.; Schriewer-Pottgen, M. Preparation and Crystal Structure of Rare Earth Rhenates: the Series $Ln_5Re_2O_{12}$ with Ln = Y, Gd±Lu, and the Praseodymium Rhenates Pr_3ReO_8, $Pr_3Re_2O_{10}$, and $Pr_4Re_2O_{11}$. *Z. Anorg. Allg. Chem.* **2000**, *626*, 80-88.

(40) Manthiram, A.; Gopalakrishnan, J. Preparation and structure of some Ln_2MoO_5 oxides. *P. Indian Acad. Sci.* **1978**, *8*, 267-273.

(41) Manthiram, A.; Gopalakrishnan, J. Studies of some Ln_2MoO_5 oxides. *J. Less-Common Met.* **1979**, *68*, 167-174.

(42) Muller, O.; Roy, R. A crystal-chemical study of some new rare earth-rhenium oxides. *Mater. Res. Bull.* **1969**, *4*, 349-360.

(43) Manthiram, A.: Lower Valence Molybdenum Oxides. In *Reviews in Inorganic Chemistry*, 1984; Vol. 6.

(44) Chi, L.; Britten, J. F.; Greedan, J. Synthesis, structure and magnetic properties of the S=1/2; one-dimensional antiferromagnet, $Y_5Re_2O_{12}$. *J. Solid State Chem.* **2003**, *172*, 451-457.

(45) Khalifah, P.; Nelson, K.; Jin, R.; Mao, Z.; Liu, Y.; Huang, Q.; Gao, X.; Ramirez, A.; Cava, R. Non-Fermi-liquid behaviour in $La_4Ru_6O_{19}$. *Nature* **2001**, *411*, 669-671.

(46) Khalifah, P.; Cava, R. Metal-metal bonding in the $KSbO_3$-type oxides $La_4Ru_6O_{19}$ and $La_3Ru_3O_{11}$: A mechanism for band gap formation in t_{2g} states. *Phys. Rev. B* **2001**, *64*.

(47) Rogalski, A. Infrared detectors: an overview. *Infrared Physics & Technology* **2002**, *43*, 187-210.

(48) Rogalski, A. Infrared dectectors: status and trends. *Prog. Quant. Electron.* **2003**, *27*, 59-210.

(49) Minnich, A. J.; Dresselhaus, M. S.; Ren, Z. F.; Chen, G. Bulk nanostructured thermoelectric materials: current research and future prospects. *Energy & Environmental Science* **2009**, *2*, 466-479.

(50) Zebarjadi, M.; Esfarjani, K.; Dresselhaus, M. S.; Ren, Z. F.; Chen, G. Perspectives on thermoelectrics: from fundamentals to device applications. *Energy & Environmental Science* **2012**, *5*, 5147-5162.

(51) Tritt, T. M.; Subramanian, M. A. Thermoelectric materials, phenomena, and applications: A bird's eye view. *MRS Bull.* **2006**, *31*, 188-194.

(52) Mahan, G. D.; Sofo, J. O. The best thermoelectric. *P. Natl. Acad. Sci. USA* **1996**, *93*, 7436-7439.

(53) He, T.; Calvarese, T. G.; Chen, J. Z.; Rosenfeld, H. D.; Small, R. J.; Krajewski, J. J.; Subramanian, M. A.: *Origin of low thermal conductivity in alpha-Mn: Enhancing the ZT of $YbAl_3$ and $CoSb_3$ through Mn addition*, 2005.

(54) Pecharsky, V.; Zavalij, P.: *Fundamentals of Powder Diffraction and Structural Characterization of Materials*; Second Edition ed.; Springer, 2008.

(55) Smart, L.; Moore, E.: *Solid State Chemistry An Introduction*; Third Edition ed.; CRC Press: Boca Raton, FL, 2005.

(56) Rietveld, H. M. A profile refinement method for nuclear and magnetic structures. *J. Appl. Crystallogr.* **1969**, *2*, 65-&.

(57) Coats, A. W.; Redfern, J. P. Thermogravimetric analysis. A review. *Analyst* **1963**, *88*, 906-924.

(58) *Design Quantum Physical Property Measurement System PPMS MultiVu Application User's Manual*: San Diego, CA, 2008.

(59) Kubelka, P.; Munk, F. *Fur Tekn. Physik* **1931**, *12*, 593.

(60) Andersen, O.; Pawlowska, Z.; Jepsen, O. Illustration of the linear-muffin-tin-orbital tight-binding representation: Compact orbitals and charge density in Si. *Phys. Rev. B* **1986**, *34*, 5253-5269.

(61) Skriver, H.: *The LMTO Method Muffin-Tin Orbitals and Electronic Structure*; Springer-Verlag Berlin Heidleberg: Germany, 1984; Vol. 41.

(62) Saha-Dasgupta, T. DFT Electronic Structure Calculations by Muffin Tin Orbital Based Basis.

(63) Waltersson, K. The crystal structure of $La_4[Re_2]O_{10}$, a flourite-related structure containing rhenium doublets. *Acta Crystallogr. B* **1976**, *32*, 1485-1489.

(64) Ehrenberg, H.; Hartmann, G.; Wltschek, G.; Fuess, H.; Morgenroth, W.; Krane, H. The crystal structure of $Tm_5Re_2O_{12}$. *Acta Crystallogr. B* **1999**, *B55*, 849-852.

(65) Bramnick, K.; Abakumov, A.; Shpanchenko, R.; Antipov, E.; VanTendeloo, G. Synthesis and structure of $Ln_4Re_{6-x}O_{19}$ (Ln=Ce, Pr, Nd) complex oxides. *J. Alloys Compd.* **1998**, *278*, 98-102.

(66) Gautier, R.; Andersen, O.; Gougeon, P.; Halet, J.; Canadell, E.; Martin, J. Electronic Structure, Electrical and Magnetic Properties of RMo_8O_{14} Compounds (R = La, Ce, Pr, Nd, Sm) Containing Bicapped Mo_8 Clusters. *Inorg. Chem.* **2002**, *41*, 4689-4699.

(67) Kihlborg, L. Least Squares Refinement of the Structure of $Mo_{17}O_{47}$. *Acta Chem. Scand.* **1963**, *17*, 1485-1487.

(68) Kresse, G.; Joubert, D. From ultrasoft pseudopotentials to the projector augmented-wave method. *Phys. Rev. B* **1999**, *59*, 1758-1775.

(69) Kresse, G.; Furthmuller, J. Efficient iterative schemes for ab initio total-energy calculations using a plane-wave basis set. *Phys. Rev. B* **1996**, *54*, 11169-11185.

(70) Blochl, P. Projector augmented-wave method. *Phys. Rev. B* **1994**, *50*, 17953-17979.

(71) Ceperley, D.; Alder, B. Ground State of the Electron Gas by a Stochastic Method. *Phys. Rev. Lett.* **1980**, *45*, 566-569.

(72) Perdew, J.; Zunger, A. Self-interaction correction to density-functional approximations for many-electron systems. *Phys. Rev. B* **1981**, *23*, 5048-5079.

(73) Onida, G.; Reining, L.; Rubio, A. Electronic excitations: density-functional versus many-body Green's-function approaches. *Reviews of Modern Physics* **2002**, *74*, 601-659.

(74) Heyd, J.; Peralta, J. E.; Scuseria, G. E.; Martin, R. L. Energy band gaps and lattice parameters evaluated with the Heyd-Scuseria-Ernzerhof screened hybrid functional. *Journal of Chemical Physics* **2005**, *123*.

(75) Marsman, M.; Paier, J.; Stroppa, A.; Kresse, G. Hybrid functionals applied to extended systems. *J. Phys.: Condens. Matter* **2008**, *20*.

(76) Lagervall, E.; Lofgren, P.; Waltersson, K.; Wilhelmi, K. Crystal-Structures of $La_4[Re_2]O_{10}$ and $Nd_4[Re_2]O_{11}$- Fluorite-Related Structures Containing Rhenium Doublets. *Acta Crystallogr. A* **1975**, *31*, S88.

(77) Brese, N.; O'Keeffe, M. Bond-Valence Parameters for Solids. *Acta Crystallogr. B* **1991**, *B47*, 192-197.

(78) Brown, I.; Altermatt, D. Bond-Valence Parameters Obtained from a Systematic Analysis of the Inorganic Crystal Structure Database. *Acta Crystallogr. B* **1985**, *B41*, 244-247.

(79) Chen, M.; Zhou, Z.; Hu, S. Bond valence parameters linearly dependent on the molybdenum oxidation states. *Chin. Sci. Bull.* **2002**, *47*, 978-981.

(80) Zocchi, F. Some considerations about equations correlating valence and length of a chemical bond. *Solid State Sci.* **2001**, *3*, 383-386.

(81) Rodl, C.; Bechstedt, F. Optical and energy-loss spectra of the antiferromagnetic transition metal oxides MnO, FeO, CoO, and NiO including quasiparticle and excitonic effects. *Phys. Rev. B* **2012**, *86*.

(82) Adler, D.; Feinleib, J. Electrical and optical properties of narrow-band materials. *Physical Review B-Solid State* **1970**, *2*, 3112-3134.

(83) Reinen, D. Farbe und konstitution bei anorganischen festoffen .8 B. Die lichtabsorption des zweiwertigen nickels in den mischkristallen $Mg_{1-x}Ni_xO$. *Berichte Der Bunsen-Gesellschaft Fur Physikalische Chemie* **1965**, *69*, 82-&.

(84) Figgis, B.; Hitchman, M.: *Ligand Field Theory and its Applications*; 1 ed.; Wiley-VCH, 1999. pp. 376.

(85) Tanabe, Y.; Sugano, S. On the absorption spectra of complex ions 1. *J. Phys. Soc. Jpn.* **1954**, *9*, 753-766.

(86) Tanabe, Y.; Sugano, S. On the absorption of complex ions .2. *J. Phys. Soc. Jpn.* **1954**, *9*, 766-779.

(87) Sasaki, A.; Wakeshima, M.; Hinatsu, Y. Magnetic and transport properties of lanthanide rhenates $Ln_4Re_6O_{19}$ (Ln = La, Pr, Nd). *J. Phys.: Condens. Matter* **2006**, *18*, 9031-9046.

(88) Kreisel, K.; Yap, G.; Dmitrenko, O.; Landis, C.; Theopold, K. The Shortest Metal-Metal Bond Yet: Molecular and Electronic Structure of a Dinuclear Chromium Diazadiene Complex. *J. Am. Chem. Soc.* **2007**, *129*, 14162-14163.

(89) Cotton, F. Stong Homonuclear Metal-Metal Bonds. *Acc. Chem. Res.* **1969**, *2*, 240-247.

(90) Nguyen, T.; Sutton, A.; Brynda, M.; Fettinger, J.; Long, G.; Power, P. Synthesis of a Stable Compound with Fivefold Bonding Between Two Chromium(I) Centers. *Science* **2005**, *310*, 844-847.

(91) Cuthbert, H.; Greedan, J.; Vargas-Baca, I.; Derakhshan, S.; Swainson, I. Syntheis, Structure, and Unexpected Magnetic Properties of $La_3Re_2O_{10}$. *Inorg. Chem.* **2007**, *46*, 8739-8745.

(92) Besse, J.; Baud, G.; Chevalier, R. Structure Cristalline d'Oxydes Doubles de Rhenium. II. L'Oxyde de Lanthane-Rhenium $La_6Re_4O_{18}$. *Acta Crystallogr. B* **1978**, *B34*, 3532-3535.

(93) Sleight, A. L., JM. Charterization and Crystal Structure of $La_4Re_6O_{19}$, a New Metal Cluster Compound. *Inorg. Chem.* **1968**, *7*, 108-111.

(94) Wlschek, G.; Paulus, H.; Ehrenberg, H.; Fuess, H. Crystal Structure and Magnetic Properites of Sm_2ReO_5. *J. Solid State Chem.* **1997**, *132*, 196-201.

(95) Jeitschko, W.; Heumannskamper, D.; Schriewer-Pottgen, M.; Rodewald, U. Preparation, Crystal Structures, and Properties of Rhenates with Multiple Re-Re Bonds: Ln_2ReO_5 (Ln=Sm, Eu, Gd), $Ln_3Re_2O_9$ (Ln=Pr, Nd, Sm), and $Ln_4Re_6O_{19}$ (Ln=La-Nd). *J. Solid State Chem.* **1999**, *147*, 218-228.

(96) Xue, J.; Antonio, M.; Soderholm, L. Polymorphs of Ln_2MoO_6: A Neutron Diffraction Investigation of the Crystal Structures of La_2MoO_6 and Tb_2MoO_6. *Chem. Mater.* **1995**, *7*, 333-340.

(97) Kerner-Czeskleba, H.; Tourne, G. Preparation de nouveaux oxydes de molybdene IV et de lanthanide de formule Ln_2MoO_5. *Mater. Res. Bull.* **1978**, *13*, 271-278.

(98) Hubert, P.; Laffitte, M. Monomolybdites des terres rares Ln_2MoO_5 (Ln = La a Lu + Y). *C. R. Seances Acad. Sei., Ser. C* **1977**, *285*, 567-570.

(99) Shi, F.; Meng, J.; Ren, Y. Structure and physical properties of new phase oxide La_2MoO_5. *Solid State. Commun.* **1995**, *95*, 745-747.

(100) McCarroll, W.; Darling, C.; Jakubicki, G. Synthesis of Reduced Complex Oxides of Molybdenum by Fused Salt Electrolysis. *J. Solid State Chem.* **1983**, *48*, 189-195.

(101) Dudarev, S.; Botton, G.; Savrasov, S.; CJ, H.; Sutton, A. Electron-energy-loss spectra and the structural stability of nickel oxide: An LSDA1U study. *Phys. Rev. B* **1998**, *57*, 1505-1509.

(102) Vaugier, L.; Jiang, H.; Biermann, S. Hubbard U and Hund exchange J in transition metal oxides: Screening versus localization trends from constrained random phase approximation. *Phys. Rev. B* **2012**, *86*, 165105.

(103) Murnaghan, F. The compressibility of media under extreme pressures. *P. Natl. Acad. Sci. USA* **1944**, *30*, 244-247.

(104) Oszlanyi, G.; Sueto, A. Ab initio structure solution by charge flipping. *Acta Crystallogr. A* **2004**, *60*, 134-141.

(105) Pearson, R. The Second-Order Jahn-Teller Effect. *J. Mol. Struct.* **1983**, *103*, 25-34.

(106) Sleight, A. W. Valency, valence degeneracy, ferroelectricity, and superconductivity. *Prog. Solid State Chem.* **2009**, *37*, 251-261.

(107) Robin, M. B.; Day, P.: Mixed Valence Chemistry-A Survey and Classification. In *Adv. Inorg. Chem. Radiochem.*; Emeléus, H. J., Sharpe, A. G., Eds.; Academic Press, 1968; Vol. Volume 10; pp 247-422.

(108) Pickett, W.; Quan, Y.; Pardo, V. Charge states of ions, and mechanisms of charge ordering transitions. *J. Phys.: Condens. Matter* **2014**, *26*, 274203.

(109) Orosel, D.; Balog, P.; Liu, H.; Qian, J.; Jansen, M. Sb_2O_4 at high pressures and high temperatures. *J. Solid State Chem.* **2005**, *178*, 2602-2607.

(110) Sleight, A. W.; Gillson, J. L.; Bierstedt, P. E. High- temperature superconductivity in $BaPB_{1-x}Bi_xO_3$ system. *Solid State. Commun.* **1975**, *17*, 27-28.

(111) Cava, R. J.; Batlogg, B.; Krajewski, J. J.; Farrow, R.; Rupp, L. W.; White, A. E.; Short, K.; Peck, W. F.; Kometani, T. Superconductivity near 30 K without copper - The $Ba_{0.6}K_{0.4}BiO_3$ perovskite. *Nature* **1988**, *332*, 814-816.

(112) Cava, R. J.; Batlogg, B.; Espinosa, G. P.; Ramirez, A. P.; Krajewski, J. J.; Peck, W. F.; Rupp, L. W.; Cooper, A. S. Superconductivity at 3.5 K in $BaPb_{0.75}Sb_{0.25}O3$: why is Tc so low? *Nature* **1989**, *339*, 291-293.

(113) Retuerto, M.; Emge, T.; Hadermann, J.; Stephens, P.; Li, M.; Yin, Z.; Croft, M.; Ignatov, A.; Zhang, S.; Yuan, Z.; Jin, C.; Simonson, J.; Aronson, M.; Pan, A.; Basov, D.; Kotliar, G.; Greenblatt, M. Synthesis and Properties of Charge-Ordered Thallium Halide Perovskites, $CsTl^{+0.5}Tl^{3+0.5}X_3$ (X = F or Cl): Theoretical Precursors for Superconductivity? *Chem. Mater.* **2013**, *25*, 4071-4079.

(114) Kotliar, G.; Yin, Z. Rational material design of mixed-valent high-T-c superconductors. *EPL* **2013**, *101*, 27002.

(115) Woodward, P.; Cox, D.; Moshoppoulou, E.; Sleight, A.; Morimoto, S. Structural studies of charge disproportionation and magnetic order in $CaFeO_3$. *Phys. Rev. B* **2000**, *62*, 844-855.

(116) Huynh, M.; Bediako, D.; Nocera, D. A Functionally Stable Manganese Oxide Oxygen Evolution Catalyst in Acid. *J. Am. Chem. Soc.* **2014**, *136*, 6002-6010.

(117) Zaghrioui, M.; Bulou, A.; Lacorre, P.; Laffez, P. Electron diffraction and Raman scattering evidence of a symmetry breaking at the metal-insulator transition of $NdNiO_3$. *Phys. Rev. B* **2001**, *64*, 081102.

(118) Zhao, Q.; Darriet, J.; Whangbo, M.; Ye, L.; Stackhouse, C.; zurLoye, H. Intriguing Interconnections Among Phase Transition, Magnetic Moment, and Valence Disproportionation in 2H-Perovskite Related Oxides. *J. Am. Chem. Soc.* **2011**, *133*, 20981-20994.

(119) Kojima, N. Gold valence transition and phase diagram in the mixed-valence complexes, M-2 (AuX2)-X-I (AuX4)-X-III (M = Rb, Cs; X = Cl, Br, and I). *B. Chem. Soc. Jpn.* **2000**, *73*, 1445-1460.

(120) Bland, S.; Angst, M.; Adiga, S.; Scagnoli, V.; Johnson, R.; Herrero-Martin, J.; Hatton, P. Symmetry and charge order in Fe_2OBO_3 studied through polarized resonant X-ray diffraction. *Phys. Rev. B* **2010**, *82*, 115110.

(121) Akrap, A.; Angst, M.; Khalifah, P.; Mandrus, D.; Sales, B.; Forro, L. Electrical transport in charge-ordered Fe_2OBO_3: Resistive switching and pressure effects. *Phys. Rev. B* **2010**, *82*, 165106.

(122) Attfield, J.; Bell, A.; Rodriguez-Martinez, L.; Greneche, J.; Cernik, R.; Clarke, J.; Perkins, D. Electrostatically driven charge-ordering in Fe_2OBO_3. *Nature* **1998**, *396*, 655-658.

(123) Radaelli, P. G.; Horibe, Y.; Gutmann, M. J.; Ishibashi, H.; Chen, C. H.; Ibberson, R. M.; Koyama, Y.; Hor, Y.-S.; Kiryukhin, V.; Cheong, S.-W. Formation of isomorphic Ir^{3+} and Ir^{4+} octamers and spin dimerization in the spinel $CuIr_2S_4$. *Nature* **2002**, *416*, 155-158.

(124) Takubo, K.; Hirata, S.; Son, J.; Quilty, J.; Mizokawa, T.; Matsumoto, N.; Nagata, S. X-ray photoemission study of $CuIr_2S_4$: Ir^{3+}-Ir^{4+} charge ordering and the effect of light illumination. *Phys. Rev. Lett.* **2005**, *95*, 246401.

(125) Verwey, E. Electronic Conduction of Magnetite (Fe_3O_4) and its Transition Point at Low Temperatures. *Nature* **1939**, *144*, 327-328.

(126) Senn, M. S.; Wright, J. P.; Attfield, J. P. Charge order and three-site distortions in the Verwey structure of magnetite. *Nature* **2012**, *481*, 173-176.

(127) Goff, R.; Wright, J.; Attfield, J.; Radaelli, P. G. Resonant x-ray diffraction study of the charge ordering in magnetite. *J. Phys.: Condens. Matter* **2005**, *17*, 7633-7642.

(128) Yuan, Z. K. B.; Sharpe, A.; Shields, A. High spped photon detection in the near infrared. *Appl. Phys. Lett.* **2007**, *91*, 041114-041111.

(129) Hines, M.; Scholes, G. Colloidal PbS Nanocrystals with Size-Tunable Near-Infrared Emission Observation of Post-Synthesis Self-Narrowing of Particle Size Distribution. *Adv. Mater.* **2003**, *15*, 1844-1849.

(130) Phelan, R.; Calawa, A.; Rediker, R.; Keyes, R.; Lax, B. Infrared InSb Laser Diode in High Magnetic Fields. *Appl. Phys. Lett.* **1963**, *3*, 143-145.

(131) Baud, G.; Besse, J. P.; Capestan, M.; Chevalier, R. Oxides doubles de rhenium a valence mixte. *Annales De Chimie-Science Des Materiaux* **1982**, *7*, 615-621.

(132) Baud, G.; Besse, J. P.; Chevalier, R. Synthesis and structural study of the double oxide $Dy_5Re_2O_{12}$. *Materials Chemistry and Physics* **1983**, *8*, 93-99.

(133) Shannon, R. Revised Effective Ionic Radii and Systematic Studies of Interatomie Distances in Halides and Chaleogenides *Acta Crystallogr. A* **1976**, *32*, 751-757.

(134) Her, J. H.; Stephens, P. W.; Gao, Y.; Soloveichik, G. L.; Rijssenbeek, J.; Andrus, M.; Zhao, J. C. Structure of unsolvated magnesium borohydride $Mg(BH_4)_2$. *Acta Crystallogr. B* **2007**, *63*, 561-568.

(135) Campbell, B. J.; Stokes, H. T.; Tanner, D. E.; Hatch, D. M. ISODISPLACE: a web-based tool for exploring structural distortions. *J. Appl. Crystallogr.* **2006**, *39*, 607-614.

(136) Treacy, M.; Deem, M.; Newsam, J. *DIFFaX v1.812*2005.

(137) Cabanas, M.; Ormazabal, J.; Reynaud, M.; Carvajal, J.: FAULTS manual. Energigune, C., Ed., 2015.

(138) Eyert, V.; Horny, R.; Hock, K. H.; Horn, S. Embedded Peierls instability and the electronic structure of MoO2. *J. Phys.: Condens. Matter* **2000**, *12*, 4923-4946.

(139) Eyert, V. The metal-insulator transitions of VO_2: A band theoretical approach. *Annalen der Physik* **2002**, *11*, 650-704.

(140) Hirsch, J. E. Effect of coulomb interactions on the peierls instability. *Phys. Rev. Lett.* **1983**, *51*, 296-299.